MAGNETIC AND SPECTROSCOPIC PROPERTIES OF HETEROMETALLIC LANTHANIDE COMPOUNDS AND TOWARDS UTILIZING SYNCHROTRON MÖSSBAUER SPECTROSCOPY FOR MAGNETIC RELAXATION MEASUREMENTS

A Dissertation

by

COURTNEY MARIE DICKIE

Submitted to the Office of Graduate and Professional Studies of
Texas A&M University
in partial fulfillment of the requirements for the degree of

DOCTOR OF PHILOSOPHY

Chair of Committee,	Michael Nippe
Committee Members,	François P. Gabbaï
	Timothy Hughbanks
	Artem G. Abanov
Head of Department,	Simon W. North

August 2018

Major Subject: Chemistry

ABSTRACT

Single-molecule magnets (SMMs) have attracted considerable attention for their fascinating properties and exciting potential applications in next generation high-density data storage and quantum computing. SMMs are a class of paramagnetic compounds defined by a bistable magnetic ground state and an energy barrier (U) to reorientation of their molecular spin. Towards the utilization of SMMs in devices, the development of methods for the control of magnetic properties via external stimuli is required. A major objective of this research project has been the development of lanthanide-based SMMs featuring a redox-active transition metal center, with the ultimate goal of utilizing the redox properties of the transition metal to modulate the magnetization dynamics at the nearby lanthanide center.

Early results in developing mixed d-block/f-block systems led to the isolation of the dysprosium-isocarbonyl compound, $[(\mathrm{thf})_5\mathrm{Dy}((\mu\text{-OC})\mathrm{W(CO)_2Cp})_3]\cdot\mathrm{thf}$. Notably, this was the the first structurally characterized dysprosium-isocarbonyl compound. The static and dynamic magnetic properties of $[(\mathrm{thf})_5\mathrm{Dy}((\mu\text{-OC})\mathrm{W(CO)_2Cp})_3]\cdot\mathrm{thf}$ were characterized, revealing field-induced slow relaxation only in a magnetically dilute sample (12:1 Y^{3+}:Dy^{3+}) with $U_{\mathrm{eff}} = 12.6$ cm^{-1}. However, due to instability towards oxidation/reduction, these isocarbonyl compounds were determined to be unsuitable for redox-switchability applications. A possible route to improved magnetization dynamics is through the development of low-coordinate lanthanide-isocarbonyl compounds. Towards this goal, the new, bulky tungsten hydride compound, $\mathrm{HWCp^{BIG}(CO)_3}$ ($\mathrm{HCp^{BIG}} = \mathrm{HC_5(4\text{-}}n\mathrm{\text{-}Bu\text{-}C_6H_4)_5}$) was isolated. Gratifyingly, $\mathrm{HWCp^{BIG}(CO)_3}$ is soluble in non-coordinating solvents, including hexanes and toluene.

The highly reversible redox properties of ferrocence, $\mathrm{FeCp_2}$, make it ideal for use in redox-switchability applications. Towards this goal, dysprosium(III) and erbium(III) bis(diamidoferrocene) complexes have been developed and their dynamic magnetic properties investigated. The Dy^{3+} compound exhibits either "on/off" or "slow/fast" switching in the presence or absence of a dc field, respectively. The Er^{3+} compound exhibits "on/off" functionality in the presence of a dc field. UV-vis-NIR spectroscopy, ^{57}Fe Mössbauer spectroscopy, and electrochemical studies support the presence of electronic communication between the mixed-valent Fe ions in both solution and in the solid state. This molecular level study is intended to provide the foundation for future switchable solid materials based on the redox properties of ferrocene/ferrocenium.

The cyclopentadienide (Cp^-) substitution chemistry of chromocene was investigated as a synthetic route for the generation of transition metal precursors for d-block/f-block complexes. The reaction between chromocene and two equivalents of $K(N(SiMe_3)_2)$ generated the polymeric species, $[CpCr(N(SiMe_3)_2)_2K]_\infty$. Carrying out the reaction in the presence of cryptand-222 afforded the mononuclear compound $[K(crypt\text{-}222)][CpCr(N(SiMe_3)_2)_2]$. Despite the similar coordination environments and only slight differences in geometric parameters, the polynuclear species showed no evidence of slow relaxation whereas the mononuclear cryptand species displayed field-induced slow relaxation with U_{eff} = 9.8(6) cm^{-1} (H_{dc} = 1000 Oe). Notably, this is only the third reported mononuclear chromium(II)-based compound to display field-induced slow relaxation and first example that is not square planar at the Cr^{2+} center.

Another major objective of this research project was the development of new techniques for the characterization of SMMs. Mössbauer spectroscopy presents an exciting opportunity to study magnetization dynamics at higher temperatures than currently achievable through ac magnetometry, as the lifetime of the Mössbauer spectroscopy measurement is 5-6 orders of magnitude shorter. In this first of its kind study, the magnetization dynamics of Dy^{3+}-based hexafluoroacetylacetonate compounds were studied by ^{119}Sn and ^{161}Dy synchrotron Mössbauer spectroscopy. In the zero-field ^{119}Sn Mössbauer spectra, no measurable magnetic hyperfine field from the Dy^{3+} center was detected at the nearby diamagnetic Sn center. While detailed analyses of the collected ^{161}Dy Mössbauer spectra are currently ongoing, early observations suggest a relationship between the loss of count rate (intermediate relaxation regime) and the relaxation times/U_{eff} determined through ac magnetometry studies. It remains to be determined whether or not ^{161}Dy synchrotron Mössbauer spectroscopy can be utilized to extract relaxation times and calculate U_{eff} in Dy^{3+}-based SMMs.

DEDICATION

To my parents, for their endless encouragement and support.

ACKNOWLEDGMENTS

After five years of work, I'm thrilled to have completed this Ph.D. dissertation! I really can't say at the moment whether it has been a long or short journey. There were certainly times when it felt like it would never end, but looking back on it now the entire journey went by incredibly too fast.

I want to first thank my research advisor, Dr. Michael Nippe, for his mentorship and support throughout my PhD. I had the very unique experience of being Michael's first graduate student and starting up the lab. What an exciting journey it has been! It makes me feel super proud to look back and see how far the group has come in just a few short years!

I would like to acknowledge my Committee Members: Dr. François Gabbaï and Dr. Timothy Hughbanks from the Department of Chemistry, and Dr. Artem Abanov from the Department of Physics & Astronomy for all of their advice. I'd like to thank Dr. Nattamai Bhuvanesh and Dr. Joe Reibenspies for the training and support in the X-ray Diffraction Laboratory. I'd especially like to thank Dr. Bhuvanesh for solving several of the structures presented in this dissertation.

I'd like to acknowledge Adam Burkhard (B.S. 2017) for his contributions to this work. Adam worked with me in the lab as a undergraduate researcher for two years during the middle of my PhD (2015-2017). I was pretty tired at times in the middle of my PhD and Adam's relentless enthusiasm really kept me motivated during that time. Not only is Adam a talented researcher, he is also a great friend. I wish him great success in pharmacy school!

I'd like to thank our synchrotron Mössbauer spectroscopy collaborators at Beamline 3-ID at the Advanced Photon Source (Argonne National Laboratory): Dr. Ercan Alp, Dr. Wenli Bi, and Dr. Michael Hu, for all the training and assistance with the ^{119}Sn and ^{161}Dy Mössbauer spectroscopy measurements and data analysis. In addition to traveling to Argonne National Laboratory for the synchrotron Mössbauer experiments, I also attended a great Nuclear Resonant Scattering workshop where I learnt a ton about synchrotron Mössbauer spectroscopy and data fitting using CONUSS. I would especially like to acknowledge Dr. Wenli Bi for the fits of the ^{161}Dy Mössbauer spectra in

Chapter 6.

Past and present Nippe group members: thank you for being the best lab mates and colleagues I could ever ask for, because of all y'all it has been a pleasure to come to lab everyday. I'll dearly miss our coffee breaks, of which I'm sure we've taken far too many over the years. A special thank you to Corey Burns and Siyoung Sung - I'll never forget those grueling days of setting up the lab and getting our projects started, because of our teamwork we pushed through! Thanks to Corey, the amount of feminist punk on my playlists has increased considerably. Thank you to Siyoung for his support and friendship, I've always enjoyed our deep conversations that have covered just about every topic. Thank you to Trevor Latendresse for not only being a fellow "magnetizer" in the group but for also being my football buddy at the Aggie games. I want to acknowledge Branford Wilkins for being the most positive and optimistic person I've ever met. I'll always remember us struggling with the big liquid N_2 dewar - I'd always joke "hey, who put the two milers in charge of the liquid nitrogen?". Thank you to Gabrielle Risica for the always humbling experience of kicking my butt in the lap pool, I still can't believe how fast you swim. Thank you to Jeremy Meeder, your positive attitude and laughter always brightened my day during this past year. Thank you to Dr. Apoorva Upadhyay for all of the support and advice during the final year of my PhD! I'd like to acknowledge the past Nippe group members who have contributed very positively to my time in graduate school: Dr. Davinder Kumar, Soomin Park, Marcos Gil-Sepulcre, and Emily Brackhahn. I feel very fortunate to have worked with such awesome people!

I'd like to thank my undergraduate research advisor, Dr. Glen Briand, at Mount Allison University for giving me the opportunity to work in his lab. My undergraduate research experience is what inspired me to pursue my PhD. I remember sitting in Glen's office the summer before my final year of my B.Sc. and Glen recommending Texas A&M University for graduate studies. I'm pretty sure I said something along the lines of "Glen, no way would I ever move to Texas". And well, here I am. All jokes aside, I've loved my time here at Texas A&M University and I'm really happy that I decided to pursue my PhD here. I'll dearly miss all of the people and the great fun that was college football season. I think the only thing I won't miss about this place is the relentless

Texas summer heat.

I want to acknowledge the Department of Chemistry at Texas A&M University for all the support. I'd like to especially acknowledge Sandy Horton and Dr. Joanna Goodey-Pellois of the graduate office for all of their support and advice for navigating graduate school.

I'd like to give a shout out to the Texas A&M Graduate and Professional Student Council (GPSC) for being an important part of my graduate school experience. I spent several years as a member of the GPSC: a couple of years as a Delegate and this past year as VP of Information. I loved every minute of my time on GPSC and serving the graduate student community. I'd especially like to thank this year's Executive Committee for all of their encouragement and support while I was finishing my PhD and for keeping me honest by always asking how my writing was going. It was a ton of fun working with all of you this year. I admire all of you and know you are all destined for great success!

Thank you to Dr. Williams and the thesis and dissertation support group at Texas A&M University for all of the support, encouragement, and advice during the final year of my PhD. Thank you for helping me set goals and holding me accountable for them. The thought of writing an entire dissertation was overwhelming in October and now here it is!

I want to acknowledge my parents for their endless support and encouragement along this journey, I couldn't have made it this far without them. Thank you for everything! I've lived far away from home for about 9 years now so I'm looking forward to being a little closer to home so we can see each other more often!

I'd like to thank all of my friends at Texas A&M University and in Bryan-College Station for all of their encouragement and for making the past five years some of the best of my life. I'll miss you all dearly! While there are more great memories than I could ever fit in this section, some of the best times I had here were standing in the blazing heat watching Aggie football games with all my friends. I'd especially like to thank my roommates during my PhD: Dr. Aaron Clubb, Dr. George Peabody, and Zac Perry, for always being there to listen and for sitting through many hockey games on TV. I'd also like to acknowledge my intramural softball, kickball, soccer, basketball, and hockey teams for getting me out of the lab and contributing to my sanity.

Finally, I would especially like to thank my best friend and partner, Francisco, for all of his support and encouragement over the past four years. I couldn't imagine making it through this journey without him by my side. I'd also like to thank my cat, Washburne, for always making my day a lot brighter!

In summary, thank you to everyone who contributed to the past five years. I'm really grateful that we crossed paths. On to the next Chapter!

CONTRIBUTORS AND FUNDING SOURCES

Contributors

This work was supervised by a dissertation committee consisting of Professor Michael Nippe, Professor François P. Gabbaï, and Professor Timothy Hughbanks of the Department of Chemistry and Professor Artem G. Abanov of the Department of Physics & Astronomy.

The X-ray structures for compounds **3-1**, **4-1**, and **4-2** were solved by Dr. Nattamai S. Bhuvanesh of the Department of Chemistry at Texas A&M University. The ferrocene diamine precursor in Chapter 4, fc[HNSi(*t*-Bu)Me$_2$]$_2$, was prepared by Alexander L. Laughlin of the Department of Chemistry and Biochemistry at the University of California, Los Angeles. The ^{57}Fe Mössbauer data in Chapter 4 were collected and fit by Joshua D. Wofford of Professor Lindahl's group (Texas A&M University, Department of Chemistry). Shaoyang Wang and Yanpu Zhang from Prof. Lutkenhaus's group st the Department of Chemical Engineering at Texas A&M University assisted with the UV-Vis-NIR spectroscopy measurements in Chapter 4.

Adam Burkhard from the Department of Chemistry at Texas A&M University contributed to the syntheses in Chapter 3 and assisted with the synthesis and purification of some of the 5-organostannane-2,2-bipyridine compounds in Chapter 6.

The ^{119}Sn and ^{161}Dy synchrotron Mössbauer studies in Chapter 6 were carried out in collaboration with Dr. Esen Ercan Alp, Dr. Wenli Bi, Dr. Ayman Said, and Dr. Michael Hu at the Advanced Photon Source (APS) at Argonne National Laboratory (Argonne, IL). All of the ^{161}Dy Mössbauer spectra were fit by Dr. Wenli Bi.

The results from Chapter 2 in this dissertation have been published in Dickie, C. M. and Nippe, M. *Inorg. Chem. Front.* **2016**, *3*, 97-103. Chapter 4 of this dissertation has been published in Dickie, C. M.; Laughlin, A. L.; Wofford, J. D.; Bhuvanesh, N. S.; Nippe, M. *Chem. Sci.* **2017**, *8*, 8039-8049.

All other work in this dissertation was completed by the student, under the advisement of Dr.

Michael Nippe of the Department of Chemistry.

Funding Sources

Graduate study was supported by two fellowships from the Natural Sciences and Engineering Research Council (NSERC) of Canada: the NSERC Postgraduate Scholarship Master's (2013–2014) and the NSERC Postgraduate Scholarship - Doctoral (2016–2018).

This work was made possible through generous start-up funds from the Department of Chemistry at Texas A&M University, the Welch Foundation, and the National Science Foundation.

TABLE OF CONTENTS

LIST OF FIGURES

FIGURE Page

LIST OF TABLES

1. INTRODUCTION TO MOLECULAR MAGNETISM

1.1 Introduction to Single-molecule Magnets

Single-molecule magnets (SMMs) have been attracting considerable attention for potential exciting applications in high density data storage, molecular spintronics, and quantum computing.[1,2]. Single-molecule magnets are a fascinating class of paramagnetic molecules featuring a bistable magnetic ground state and magnetic anisotropy; manifesting in an energy barrier, U_{eff}, to reorientation of their molecular spin.[3–5] The height of this energy barrier is influenced by the magnetic anisotropy of the system and is tunable through changes in ligand field. If the energy barrier is large enough, relaxation may be sufficiently slow to observe magnetic hysteresis, "magnetic memory", below a certain blocking temperature, T_{B}.

SMMs represent a promising "bottom up" approach in the development of well-defined nanoscale magnetic materials of uniform shape, size, and composition. At an approximate size of 1 nm, SMMs have the potential to allow for data storage densities of up to 31 terabit/cm^2. To relate this to the macroscopic world, the surface of a quarter could hold approximately 18 GB of memory storage if covered in a layer of SMMs (Figure 1.1). Huge strides have been made in the field of molecular magnetism in recent years. From the compound that coined the term "single-molecule magnet" in 1993, $Mn_{12}O_{12}(OAc)_{16}(H_2O)_4$ ($Mn_{12}Ac$), with a blocking temperature of 4 K,[6] to a recently published dysprosiocenium compound in 2017, $[Dy(Cp^{ttt}{}_2)][B(C_6F_5)_4]$, with a blocking temperature of 60 K; a new benchmark in the field.[7,8] This development marks a 56 K increase in blocking temperature over a 25-year period, moving operating temperatures closer towards the liquid nitrogen temperature regime (77 K). Compared to other fields, the study of SMMs is still in its infancy. Advancements still need to be made in terms of our understanding of molecular interactions and magnetization dynamics.

In bulk magnets, individual moments organized into domains, respond in unison to external stimuli. Within a domain, all spins are either parallel (or antiparellel) to minimize magnetic en-

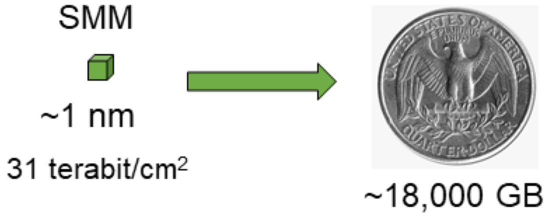

Figure 1.1: Covering the surface of a quarter with a layer of SMMs gives the possibility of 18,000 GB of storage. The SMM size is assumed to be approximately 1 nm^2.

ergy. In the absence of an external field, domain orientations are random (magnetization = 0) and in the presence of a field, the domains align with the field, with transition from one domain to another occurring through the domain walls. One strategy towards the miniaturization of magnetic materials is through a "top down" approach, ie. making bulk magnetic materials smaller. However, an inherent problem with this strategy is the difficulty achieving monodispersity in size. An alternative is a "bottom up", or molecular, approach to generating nanoscale magnetic materials. Advantages of the bottom up approach include: monodispersity and consistency in particle size and the ability to tune properties using chemistry.[3]

The discovery of SMMs has allowed several quantum phenomena to be observed for the first time in magnetic materials, as SMMs are small and monodisperse enough.[3,9] SMMs have also presented exciting opportunities in the areas of ultra high density data storage, molecular spintronics, and quantum computing.[1,10]

1.1.1 Characterization techniques for single-molecule magnets

The properties of molecular magnets are typically characterized through magnetometry and susceptometry studies using a Superconducting QUantum Interference Device (SQUID). The SQUID can reach applied fields of up to 7 T and very low temperatures of 1.8 K (or 0.5 K for microSQUID); allowing for the characterization of magnetic properties at very low temperatures with the utilization of liquid helium. In a SQUID, two superconducting coils are separated by insulating layers to form Josephson junctions. The SQUID is able to detect magnetic fields as small as 10^{-15} T.[3]

Static magnetic properties are measured using dc fields. If magnetization (*M*) depends linearly on field (*H*), then $M = \chi_V H$, where χ_V is the dimensionless volume susceptibility. The susceptibility depends on both a paramagnetic component, χ_{para}, and a diamagnetic component, χ_{dia} (Equation 1.1). The diamagnetic component arises from interaction of the magnetic field with paired electrons; it is negative and small in magnitude relative to the paramagnetic component. The χ_{para} is calculated through applying a correction to the experimentally determined χ to account for the inherent diamagnetism of the compound and the sample holder.

The temperature times susceptibility product, χT is a useful metric for highlighting deviations from the paramagnetic behavior of non-interacting spins. According to the Curie Law (Equation 1.2), non-interacting spins should have constant χT.[3] Provided that the magnetic fields are small and the temperature is not too low, χ is independent of magnetic field, as to satisfy the relationship $g\mu_B H << k_B T$. The Landé g-factor for lanthanide ions may be approximated from the quantum numbers *S*, *L*, and *J* (Equation 1.3).

$$\chi = \chi_{\text{para}} + \chi_{\text{dia}} \tag{1.1}$$

$$\chi = \frac{M}{H} = \frac{Ng^2\mu_B^2 J(J+1)}{2k_B T} = \frac{C}{T} \tag{1.2}$$

$$g_J = 1 + \frac{S(S+1) - L(L+1) + J(J+1)}{2J(J+1)} \tag{1.3}$$

From the temperature dependence of χT, information on magnetic exchange interactions in the system may be obtained. A plot of χT vs *T* obeying the Curie Law yields a straight line parallel to the *T* axis. The Curie Law remains valid provided the energy level splitting is small with respect to *kT* (at 300 K, *kT* approx 200 cm^{-1}) and only one *J* state is populated. For Ln(III) complexes at rt, the measured $\chi_M T$ coincides with the expected value for the free ion (Curie Law); as long as the ground *J* multiplet is isolated from the excited states.[4,5] A decrease in χT with decreasing

T can be indicative of thermal depopulation of the Stark sublevels (generated from ligand field splitting of the ground J state) or antiferromagnetic interactions. An increase in χT with decreasing temperature may be indicative of ferromagnetic coupling.

For example in Dy^{3+}, the f-electron configuration is $4f^9$, resulting in a ground multiplet of $^6H_{15/2}$, with $S = 5/2$ and $L = 5$. The estimated g-value from Equation 1.3 is $g_J = 4/3$. Substituting these values into the Curie Law (Equation 1.2) gives an expected room temperature $\chi_M T$ value of 14.17 cm^3 K mol^{-1}.

The effective magnetic moment, μ_{eff}, is useful for the characterization of static magnetic properties (Equation 1.4). It is calculated from the experimentally determined susceptibility and is expressed in units of Bohr magneton (μ_B). The field dependence of μ_{eff} is useful for determining magnetic saturation.

$$\mu_{\text{eff}}^2 = \frac{3k_B T\chi}{N\mu_B^2} = g^2(J(J+1)) \tag{1.4}$$

A common characterization method for magnetic memory in bulk magnets and SMMs is the hysteresis loop; a measure of the field dependence of the magnetization of the compound when cycled through fields in positive and negative directions at certain scan rate. When a field is applied, the sample is magnetized up to a certain saturation point, where all spins are aligned with the field. Then the applied magnetic field is brought back to zero. If there is "magnetic memory", a remnant magnetization will be observed under zero field. A field in the opposite direction is required to bring the magnetization of the sample back to zero; defined as the coercive field. The highest temperature at which an opening in the hysteresis is observed is referred to as the blocking temperature, T_B. Magnets may be referred to as hard or soft based on the value of the coercive field: hard magnets have high coercive field and soft magnets have low coercive fields. Waist restricted hysteresis is often observed in SMMs due to efficient quantum tunnelling of the magnetization at zero field.

Dynamic magnetic properties of molecular magnets are studied with ac susceptibility measurements using small (typically 2 Oe) oscillating magnetic fields. Ac susceptibility measurements can either be done in the absence of a dc field (zero-field) or in the presence of a static dc field parallel to the oscillating field. Magnetization dynamics and relaxation times are investigated through varying the frequency (ω) of the oscillating field. The formula for ac susceptibility is given in equation 1.5, where τ is the relaxation time, ω is the oscillation frequency of the ac field, χ_T is the isothermal susceptibility, and χ_S is the adiabatic susceptibility.[3] At low frequencies, $\omega\tau << 1$, the measured susceptibility corresponds to a static one where the spin system is in thermal equilibrium with the lattice. At high frequencies, $\omega\tau >> 1$, the spin system is uncoupled with the lattice.[3] If χ_S and χ_T are real; then the real (χ') and imaginary (χ") components of the ac susceptibility are given by Equation 1.6 and 1.7, respectively.[3] χ' is referred to as the in-phase (real) component and χ" as the out-of-phase (imaginary) component of the ac susceptibility. The typical frequency dependencies of χ' and χ" are shown in Figure 1.2.

$$\chi_\omega = \chi_S + \frac{\chi_T - \chi_S}{1 + i\omega\tau} \tag{1.5}$$

$$\chi' = \frac{\chi_T - \chi_S}{1 + \omega^2\tau^2} + \chi_S \tag{1.6}$$

$$\chi" = \frac{(\chi_T - \chi_S)\omega\tau}{1 + \omega^2\tau^2} \tag{1.7}$$

The relaxation time (τ) is typically a distribution of times rather than a single value. The parameter α is added to account for the distribution, with a larger α indicating a wider distribution of relaxation times (Equation 1.8).[3]

$$\chi_\omega = \chi_S + \frac{\chi_T - \chi_S}{1 + (i\omega\tau)^{1-\alpha}} \tag{1.8}$$

The out-of-phase (χ") component may be plotted vs the in-phase (χ') component of the ac susceptibility in a Cole-Cole (Argand) plot. A plot of χ" vs χ' transforms as a semi-circle, with the top of the semi-circle satisfying $\omega^{-1} = \tau$. The semi-circle Cole-Cole plots are fit using least

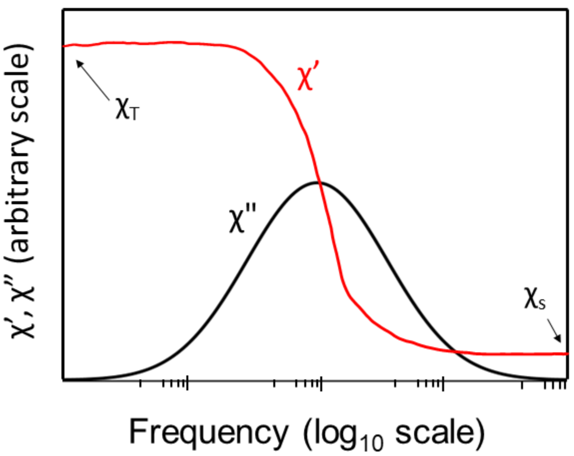

Figure 1.2: Typical frequency dependence behavior of the in-phase (χ') and out-of-phase (χ") components of the ac susceptibility. The isothermal susceptibility, χ_{T} at $\omega\tau << 1$ corresponds to thermal equilibrium of the spin system with the lattice, whereas the adiabatic susceptibility, χ_{S} at $\omega\tau >> 1$ corresponds to complete uncoupling of the spin with the lattice.

squares regression to the generalized Debye Equation (Equations 1.9 and 1.10) for the in-phase (χ') and out-of-phase (χ") components of the ac susceptibility to obtain the parameters χ_{T} (isothermal susceptibility), χ_{S} (adiabatic susceptibility), α (distribution) and τ (relaxation time).[3] From an Arrhenius plot of the natural logarithm of the relaxation times (ln τ) vs inverse temperature (T^{-1}), the parameters accounting for the different relaxation pathways maybe fit to extract a barrier height, U_{eff}, for thermal relaxation.

$$\chi'_{\omega} = \chi_{\mathrm{S}} + (\chi_{\mathrm{T}} - \chi_{\mathrm{S}})\frac{1 + (\omega\tau)^{1-\alpha}\sin(\pi\alpha/2)}{1 + 2(\omega\tau)^{1-\alpha}\sin(\pi\alpha/2) + (\omega\tau)^{2-2\alpha}} \tag{1.9}$$

$$\chi_{\omega}" = (\chi_{\mathrm{T}} - \chi_{\mathrm{S}}) + \frac{(\omega\tau)^{1-\alpha}\cos(\pi\alpha/2)}{1 + 2(\omega\tau)^{1-\alpha}\sin(\pi\alpha/2) + (\omega\tau)^{2-2\alpha}} \tag{1.10}$$

1.1.2 Evaluating single-molecule magnets

There are two very important parameters to consider for the evaluation of performance and comparing SMMs, the barrier height, U, and the magnetic blocking temperature, T_{B}. Single-molecule magnets are defined by a bistable magnetic ground state and an energy barrier, U, to reorientation of their molecular spin. For lanthanide-based SMMs, the energy barrier U represents the transition between the two levels of the $\pm\, m_J$ ground state (Figure 1.3).

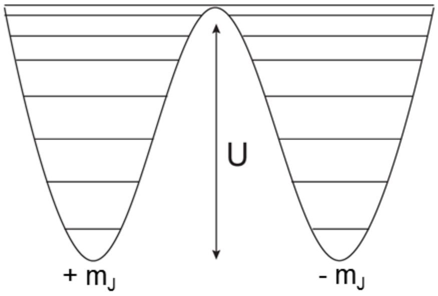

Figure 1.3: Schematic of the thermal relaxation barrier, U, between bistable $\pm\, m_J$ ground states in Ln^{3+} complexes.

The Arrhenius plot, generated with relaxation times extracted from the Cole-Cole plots, is fit with Equation 1.11; accounting for the four main pathways for magnetic relaxation: Direct, Quantum Tunneling of the Magnetization (QTM), Raman, and Orbach.

$$\tau^{-1} = AH^{n_1}T + \tau_{\mathrm{QTM}}^{-1} + CT^{n_2} + \tau_0^{-1}\exp\left(\frac{-U_{\mathrm{eff}}}{k_{\mathrm{B}}T}\right) \tag{1.11}$$

Two phonon relaxation processes more common, especially at higher temperatures, due to the phonon density of states. The two phonon processes are the Orbach and Raman pathways. Orbach relaxation is the "over-the-barrier pathway" characterized by the thermal barrier height U_{eff} (Figure 1.3). It is a two phonon process that is temperature dependent. Orbach relaxation has an exponential dependence on temperature, appearing linear in the Arrhenius plot of ln τ vs T^{-1}, with a slope of $U_{\mathrm{eff}}/k_{\mathrm{B}}$ and a y-intercept equal to τ_0. The barrier height, U_{eff} and τ_0 are determined from fitting the Arrhenius plot to Equation 1.11. Additionally, U_{eff} and τ_0 may be approximated roughly from the linear region of the Arrhenius plot (Equation 1.12). It is common that the true barrier, U, is not accessible due relaxation occurring through low-lying excited states, therefore $U_{\mathrm{eff}} < U$. The parameter τ_0 is the attempt time; the inverse of the attempt frequency. For thermal relaxation through a real excited state, τ_0 should range from 10^{-9} to 10^{-12}.[11] A larger attempt time suggests relaxation via other pathways, such as QTM. The U_{eff} value is expressed in cm^{-1}.[11]

$$\tau^{-1} = \tau_0^{-1}\text{exp}\left(\frac{-U_{\text{eff}}}{k_{\text{B}}T}\right) \tag{1.12}$$

Raman relaxation is a temperature dependent ($\propto T^{n_2}$) two phonon process that occurs via a virtual intermediate state. The Raman parameter C is treated as free fit parameter when fitting the Arrhenius plot with Equation 1.11. The typical value of n_2 = 7 (non-Kramers), 9 (Kramers), or 5 (Kramers ion in the presence of low-lying excited states).[12] Raman relaxation is distinguished from Orbach relaxaton in that the Raman pathway produces curvature in the Arrhenius plot.

Direct relaxation is a pathway between the ground states that involves only one-phonon.[12] Direct relaxation only occurs in the presence of a dc field and is both field and temperature dependent (Equation 1.13). Since the density of phonon states equivalent to the energy difference between the ground states (approximately 1 cm^{-1}) is very low, direct relaxation does not occur under zero dc field.[12] However, applying a field lifts the degeneracy of the ground state sublevels, increasing the energy difference, leading to more direct relaxation (more available phonons). Therefore, direct relaxation becomes more prominent with increasing fields. The direct relaxation parameter, A, is treated as a free-fit parameter in the fitting of the field dependence of τ (Equation 1.13), where n_1 = 2 (non-Kramers ions or Kramers ions in presence of hyperfine interactions) or 4 (Kramers ions).[12]

$$\tau^{-1} = AH^{n_1}T + \tau_{\text{QTM}}^{-1} + D \tag{1.13}$$

$$\tau_{\text{QTM}}^{-1} = \frac{B_1}{1 + B_2H^2} \tag{1.14}$$

Quantum tunnelling is a through-the-barrier relaxation pathway.[9] The field dependence is given by Equation 1.14, where B_1 and B_2 are free-fit parameters. QTM is mitigated by introducing a field bias, either through application of an external dc field or through exchange coupling, which biases one side of the potential well thereby lifting the degeneracy. QTM is problematic in SMMs; as fast

QTM limits relaxation times, especially at low T. QTM is facilitated by dipole-dipole interactions between paramagnetic centers and the presence of transverse anisotropy. QTM may be minimized through magnetic dilution with an isostructural diamagnetic analogue to decrease dipole-dipole interactions.[13]

Blocking temperature, T_B is a more ambiguous parameter than the barrier height U_{eff}, due to the many different definitions and methods for determining T_B. The most ubiquitous way to determine T_B is through the highest temperature in which an opening in the hysteresis loop is observed. The trouble with this definition is that hysteresis loops are scan rate dependent, with faster scan rates often leading to larger openings in hysteresis loops. It therefore becomes difficult to compare blocking temperatures for compounds that were characterized using different scan rates. To further complicate matters, there really is no standard scan rate in the field. An alternative definition of T_B that has been proposed is the highest temperature at which relaxation times are longer than 100 s (0.01 Hz).[3] An advantage of this definition is that it is universal and not dependent on a scan rate. A less common method is the magnetic blocking temperature from field cooled (FC) - zero field cooled (ZFC) measurements. Blocking temperatures in this thesis will be reported in K and the method used (and scan rate if applicable) will be noted.

It should be noted that many different criteria exist in terms of what comprises a single-molecule magnet. Some possible criteria include slow relaxation under zero dc field, slow relaxation under an applied field, or the presence of magnetic hysteresis. For consistency, SMM will be used to describe only those compounds that display slow relaxation (out-of-phase signal below 1000 Hz) under zero field. Slow relaxation under applied dc fields will be referred to as "field-induced slow relaxation". An energy barrier U_{eff} does not necessarily mean that hysteresis will be observed. In fact, often due to efficient QTM at low temperatures, no opening in the hysteresis is observed, even in compounds with large U_{eff} values. However, the presence of hysteresis (and a blocking temperature) typically indicates an appreciable energy barrier to spin reversal.

1.2 Transition Metal-based SMMs to Lanthanide-Based SMMs

The term single-molecule magnet was coined by Sessoli et al. in 1993, describing a Mn_{12} acetate compound, $[Mn_{12}O_{12}(OAc)_{16}(H_2O)_4]$ (referred to as $Mn_{12}Ac$), that displayed magnetic hysteresis (of molecular origin) below a blocking temperature of 4 K and U_{eff} = 42 cm^{-1}.[6] $Mn_{12}Ac$ is made up of an external ring of 8 Mn(III) ions (S = 2) and an internal tetrahedron of 4 Mn(IV) ions, corresponding to an S = 10 ground state. The large uniaxial anisotropy originates from a Jahn-Teller distortion that favors the tetragonally elongated geometry.

The energy barrier for magnetization reversal in 3d-based SMMs is described by the expression $U_{\text{eff}} = |D|S^2$ (integer spin) or $U_{\text{eff}} = |D|(S^2 - 0.25)$ (non-integer spin), where S is total spin of the molecule and D is the axial zero-field splitting parameter. Following the discovery of magnetic hysteresis in $Mn_{12}Ac$, attempts at increasing U_{eff} largely focused on the development of molecules with large total spin, S. The development of $[Mn_6O_2(sao)_6(O_2CPh)_2(EtOH)]$ (Mn_6) with S = 12 supported this trend, with U_{eff} = 62 cm^{-1}.[14] However, this strategy culminated in the development of $[Mn_{19}O_8(N_3)_8(HL)_{12}(MeCN)_6]^{2+}$, $[Mn_{19}]$, with a huge S = 83/2 ground state.[15] If maximizing spin was a valid approach to increasing U_{eff}, then it would be anticipated that $[Mn_{19}]$ would have a larger U_{eff} value than Mn_{12} or Mn_6. Despite the large S value, $[Mn_{19}]$ was found to have a barrier height of only U_{eff} = 2.8 cm^{-1} and no opening in the hysteresis loop. This low U_{eff} is a manifestation of the near zero axial zero-field splitting parameter, D, which has since been described in seminal theoretical work by Neese and Pantazis (2010) to vary nearly inversely with S.[16] Following this discovery, focus in the field has shifted to complementary efforts aimed at increasing anisotropy. These efforts have spurred the development of single-ion magnets of the d- and f-block.

The current record U_{eff} value for a transition metal-based SMM is 413 cm^{-1}, held by a mononuclear two-coordinate cobalt imido complex, $[(sIPr)Co^{II}NDmp]$ (sIPr = 1,3-bis(2,6-diisopropylphenyl)-4,5-dihydro-imidizole-2-ylidene, Dmp = 2,6-dimesitylphenyl), reported by Yao et al. in 2017.[17]

In 2003, Ishikawa et al. reported the first monometallic single-molecule magnets and the first examples of lanthanide-based single-ion magnets: the double-decker lanthanide(III) phthalocyanate complexes, $[LnPc^2]^{+/0/-}$ (Ln = Tb, Dy).[18] Slow magnetic relaxation was observed in the yttrium(III) diluted Tb(III) phthalocyaninate complex $[Bu_4N][Tb_{0.02}Y_{0.98}Pc_2]$, with an effective barrier of U_{eff} = 230 cm^{-1}. The current record SMM is a dysprosiocenium compound, $[Dy(Cp^{ttt}{}_2)][B(C_6F_5)_4]$ with T_B = 60 K and U_{eff} = 1277 cm^{-1}.[7,8]

1.3 Electronic Structure of Lanthanide(III) ions

To understand the magnetic properties, the electronic structure of lanthanide(III) ions must first be considered. The prequisites for an SMMs are (1) *a bistable ground state* and (2) *magnetic anisotropy*. Trivalent lanthanide ions are attractive candidates for SMMs due to their large inherent single-ion anisotropy. Since the 4f-orbitals do not contribute appreciably to bonding, the "core-like" character of the 4f-orbitals leads to large unquenched orbital momentum. Exceptions are lanthanide ions of the $^1S_0$ and $^8S_{7/2}$ ground states (ie. La^{3+}, Ce^{4+}, Eu^{2+}, Gd^{3+}) because of the orbitally non-degenerate ground state (S).[4] Early trivalent lanthanide ions are not ideal for SMMs on account of their antiparallel orientation of spins with respect to the angular orbital momentum.[4]

In transition metals, spin-orbit coupling acts as a perturbation on ligand field effects. However there is a fundamental difference in lanthanide ions: ligand field effects act as a small perturbation on spin-orbit coupling.[12] The origin of the ground state in lanthanide ions is $[2J + 1]$ m_J microstates that form the spin-orbit coupled ground state term $^{2S+1}L_J$.[4] To obtain SMMs with the most desirable magnetization dynamics the ground state should ideally be the largest magnitude $\pm m_J$ state with a large energy separation from the exited $\pm m_J$ states.[19]

Dysprosium(III)-based SMMs are by far the most ubiquitous, greatly outnumbering all of the other reported Ln-based SMMs combined.[13,20,21] The reason Dy^{3+} SMMs are so prominent is two-fold: (1) high single-ion magnetic anisotropy and (2) Dy^{3+} is a Kramers ion (odd number of electrons); meaning the ground state will always be bistable (satisfies the first requirement for SMM). Tb^{3+} also has high single ion anisotropy and has produced SMMs with high U_{eff} values and blocking temperatures (refs).[18,22,23] However, there are fewer reported Tb^{3+} SMMs likely because Tb^{3+} is not a Kramers ion. Depending on the geometry, the ground state may or may not be bistable, and rigorously axial symmetry is required to achieve a bistable ground state. Other Ln^{3+} ions that have been used for SMMs include Er^{3+} and Ho^{3+}.

The f-orbital electron densities of trivalent lanthanide ions have different shapes depending on the filling of the f-orbitals, according to Hund's Rules.[24 19] The shapes of the f-orbital electron density varies from spherical to oblate or prolate. Filling of the highest magnitude m_l results in oblate electron density. Lanthanide (III) ions with oblate electron density include: Tb^3 and Dy^{3+}. The oblate shape can be visualized as taking a sphere and squishing it at the poles and in the extreme case could be described as a pancake. As the lower magnitude m_l orbitals are filled, the electron density becomes more prolate in shape, ie. Er^{3+} and Yb^{3+}. Gd^{3+} has 7 f-electrons, resulting in isotropically filled orbitals and a spherical f-electron density.

To achieve desirable magnetic properties, the ground state should ideally be the largest magnitude m_J value.[19] For oblate f-electron densities, an axial ligand field leads to large anisotropy and the stabilization of the highest magnitude m_J level as the ground state. For ions with prolate f-electron density, an equatorial ligand field should lead to high anisotropy and the largest magnitude m_J ground state. These preferential ligand fields for oblate vs prolate ions are based on the minimization of electrostatic interactions between f-electron density and the ligand field.[19]

1.4 Lanthanide(III)-based Single-Molecule Magnets

The first reported monometallic SMMs and the first examples of lanthanide-based SMMs were the phthalocyanate (Pc) "double decker" sandwich complexes, $[Bu_4N][LnPc_2]$, of Tb^{3+} and Dy^{3+} reported by Ishikawa et al. in 2003.[18] The compounds possess a square antiprismatic geometry and D_{4d} symmetry at the metal center. The strong axial ligand field provided by the two phthalocyanate ligands is ideal for the oblate ions Tb^{3+} and Dy^{3+}. In the Tb^{3+} compound, the strong axial ligand field promoted the ground state to be the highest magnitude m_J state, $m_J = \pm 6$ and a large energy separation between the ground m_J state and the first excited $m_J = \pm 5$ state. Magnetically diluted compounds (due to the prominence of QTM) in the form of $[Bu_4N][Ln_{0.02}Y_{0.098}Pc_2]$ were found to have $U_{\mathrm{eff}} = 230$ cm^{-1} for Tb^{3+} and $U_{\mathrm{eff}} = 28$ cm^{-1} for Dy^{3+}. At the time, 230 cm^{-1} was the record U_{eff} for an SMM. It was later discovered that upon one-electron ligand-based oxidation of the Tb^{3+} compound to form the charge neutral compound, $TbPc_2$, the barrier increased to $U_{\mathrm{eff}} =$

410 cm^{-1}, without dilution.[22,25] The change in behavior has been postulated to be the result of the delocalization of the unpaired electron density of the ligand interacting with the highly anisotropic Tb^{3+} center. Due to the relative ease of functionalization of the Pc ligands, many variants have been investigated, rendering it the most studied Ln-based SMM platform.[13]

In 2011, Rinehart et al. reported an especially intriguing bimetallic Tb^{3+} compound bridged by a [N$_2$]$^{3-}$ radical.[26,27] Typically, exchange coupling is either non-existent or very weak in lanthanide ions due to the contracted nature of the f-orbitals. However, the spin density from the [N$_2$]$^{3-}$ bridging ligand is diffuse enough to couple strongly with the Tb^{3+} centers, resulting in strong exchange coupling. The strong magnetic anisotropy of the Tb^{3+} centers combined with the exchange coupling ability of the [N$_2$$^{3-}$] radical bridge led to magnetic hysteresis at 14 K and T_B (100 s relaxation time) = 13.9 K with a large coercive field. At the time, this was a record high temperature for magnetic hysteresis and blocking temperature. The success of this compound arises from the mitigation of the QTM relaxation pathway. Notably, lanthanide-based SMMs tend to have considerable QTM, especially at low T. The [N$_2$$^{3-}$] radical bridge serves as a field bias, shifting the degenerate m_J sublevels to different energies, thereby minimizing the probability of the QTM pathway.

The pentagonal bipyramidal geometry (D$_{5h}$ local symmetry around the metal ion), with strong axial ligands and weak equatorial ligands, has been found to be an effective geometry for achieving desirable magnetization dynamics with the oblate Dy^{3+} ion. In 2016, Chen et al. reported a pentagonal bipyramidal compound, $[\mathrm{Dy(Cy_3PO)_2(H_2O)_5}]\mathrm{Br_3\cdot(2Cy_3PO)}$, with U_{eff} = 377 cm^{-1} and T_B (200 Oe/s scan rate) = 20 K, setting a new record at the time.[28] The near perfect D$_{5h}$ local symmetry surrounding the Dy^{3+} center formed by the axial OPR$_3$ ligands (O–Dy–O = 179 ° and 175 °) and the five weak equatorial water molecules highly quench the transverse anisotropy and therefore QTM. Shortly after the report by Chen et al., several other Dy^{3+}-based SMMs with D$_{5h}$ local symmetry (pentagonal bipyramidal geometry) were reported. The compressed pentagonal bipyramidal complex, [Dy(bbpen)Br] (H$_2$bbpen = N,N'-bis(2-hydroxybenzyl)-N,N'-bis(2-methylpyridyl)ethylenediamine), reported by Liu et al. in 2016 broke a record at the time with U_{eff} = 712 cm^{-1}.[29] Later that same year, Ding et al. reported the pentagonal bipyramidal complex, $[Dy(O^tBu)_2(py)_5][BPh_4]$ with anionic axial ligands and neutral equatorial ligands.[30] This compound increased the record to U_{eff} = 1261 cm^{-1}. Even though the quenching of transverse anisotropy has mitigated QTM in this series of pentagonal bipyramidal complexes, zero field QTM is still observed in the magnetic hysteresis loops, limiting the remnant magnetization (magnetic memory).

For minimizing the transverse anisotropy the ideal symmetry would be either C_∞ or D_∞ (axial ligands only). Ab intio calculations by Chilton in 2015 predicted a U_{eff} value around 1800 cm^{-1} and hysteresis above liquid N_2 temperatures for the proposed (hypothetical) complex $[Dy(N(SiMe_3)_2)_2]^+$.[31,32] Calculations indicated a large decrease in U_{eff} as a result of bending (N–Dy–N < 180 °) and equatorial solvent coordination (generation of a transverse field).

Two-coordinate complexes of trivalent lanthanide complexes are extremely challenging to synthesize. The most truly axial Dy^{3+} compound reported to date is a dysprosiocenium compound, $[Dy(Cp^{ttt}{}_2)][B(C_6F_5)_4]$, reported independently by Goodwin et al. and Guo et al. in 2017.[7,8] It is the first example of a rare-earth metallocenium compound and was reported to have a blocking temperature of T_B (39 Oe/s scan rate) = 60 K, smashing the previous record of 20 K. The FC/ZFC measurements and the temperature at which relaxation is 100 s corroborate with T_B = 60 K. The remnant magnetization and coercive field are also much higher than in the pentagonal bipyramidal complexes, a manifestation of less zero field QTM in the dysprosiocenium compound. The compound also set a new record for barrier height, U_{eff} = 1277 cm^{-1}. Notably, this still falls short of what has been predicted to be achievable by Chilton through ab initio calculations, likely a result of the not truly axial symmetry (< 180 °).

For the Ln^{3+} ions with prolate f-election density, ie. Er^{3+}, an equatorial ligand field leads to more desirable dynamic magnetic properties.[19] An Er^{3+} n^8-cyclooctatrienide (COT) complex, $[K(18\text{-}c\text{-}6)][Er(COT_2)]\cdot 2thf$, was reported by Meihaus et al. with a blocking temperature of 10 K (scan rate = 7.2 Oe/s and 100 s relaxation time).[33] The predominantly equatorial field imposed by the COT ligands stabilizes the $m_J = \pm$ 15/2 ground state. Similarly, the equatorial three-coordinate compound $Er(N(SiMe_3)_2)_3$ was reported to have U_{eff} = 85 cm^{-1} under zero dc field; whereas the

Dy^{3+} (oblate) congener displayed no evidence of slow relaxation.[34]

1.5 Redox-switchable Magnetization Dynamics

An exciting potential application of single-molecule magnets is in high density data storage and next-generation computing devices. The utilization of SMMs in devices necessitates the development of methodologies that allow for the control of dynamic magnetic properties reversibly via external stimuli. Redox active SMMs present the opportunity to modulate magnetization dynamics through the use of an electric potential as the external stimulus. Other examples of possible external stimuli that have been explored include light, temperature, pressure, chemical, and dc field.[35–40]

1.5.1 Redox-switchable magnetization dynamics in transition metal-based complexes

In redox-switchable transition metal-based SMMs, magnetization dynamics are altered through the modulation of exchange coupling interactions. These can be grouped into two general categories, based on whether or not the redox chemistry is (1) *metal-based*,[41–43] or (2) *ligand-based.*[44,45] In multinuclear transition metal complexes, generation of a spin on a previously diamagnetic metal center may allow for the facilitation of exchange coupling interactions and the observation of slow magnetic relaxation. The generation of a ligand-based radical may also facilitate exchange coupling between multiple metal centers, thereby turning "on" slow relaxation and/or SMM behavior.

The first redox-switchable SMM was reported by Freedman et al. in 2008.[41] It features four $[(PY5Me_2)Mn]^{2+}$ units coordinated to a central pentagonal bipyramidal $[Re(CN)_7]^{3-/4-}$ unit. In the form $[(PY5Me_2)_4Mn_4Re(CN)_7](PF_6)_5{\cdot}6H_2O$ the S = 1/2 Re(IV) center facilitates exchange coupling with the four $[(PY5Me_2)Mn]^{2+}$ units to form a high spin, S = 21/2, ground state with significant zero-field splitting. This compound displayed slow relaxation under zero field with U_{eff} = 33 cm^{-1}. The spontaneous one-electron reduction to Re(III) through work-up at rt yielded $(PY5Me_2)_4Mn_4Re(CN)_7](PF_6)_4{\cdot}6H_2O$. The Re(III) center is S = 0 (diamagnetic) and only simple paramagnetism arising from the four isolated S = 5/2 Mn(II) centers was observed. Redox switchability in this set of compounds arises from the loss of spin at the Re center; turning off exchange coupling and therefore SMM behavior. Thermal stability of this compound (oxidized species) is a challenge, with spontaneous reduction occurring during rt workup. In another example, the compound $[\mathrm{Mn^{III}(salphen)Ru^{II}(DMAP)_4(CN)_2}](\mathrm{PF_6})$ is a simple paramagnet, however oxidation of the diamagnetic Ru(II) center to paramagnetic Ru(III) turns on ferromagnetic coupling and slow relaxation under zero dc field.[43]

Other systems feature redox switchable magnetization dynamics through the generation of a ligand-based radical. Fortier et al. reported redox switchable behavior in a paramagnetic dinuclear Co(II) complex, $\mathrm{dmp_2Nin(Co[N(SiMe_3)_2])_2}$.[44] It was discovered that ligand-centered reduction and oxidation of the nindigo ligand generated a ligand-based radical. The ligand-based radical facilitated coupling between the high-spin Co(II) centers (S = 3/2); enabling field-induced slow relaxation. However, the reduced ligand compound suffered from thermal instability. Similarly, Ma et al. reported a dinuclear Co(II) complex, $[\mathrm{Co_2(tphz)(tpy)_2}]^{4+/3+/2+}$ with the redox-active ligand tphz (tetrapyridophenazine). One electron reduction switched the compound from a spin-crossover complex to a compound which displayed field-induced slow relaxation. A further one-electron reduction produced a diamagnetic compound.[46]

In same cases, reduction oxidation may improve magnetic properties in an existing transition metal-based SMMs. For example, Newton et al. developed a series of $\mathrm{Mn_{13}}$ Keggin-type clusters in three different redox states. In this series of compounds, the SMM behavior improved (larger coercive field) with each successive one-electron oxidation.[47]

1.5.2 Redox-switchable magnetization dynamics in lanthanide-based complexes

While there are several examples of redox switchability of the magnetization dynamics in transition metal-based complexes, there are comparatively few examples featuring lanthanide based-SMMs. Notably, the first reported class of lanthanide ion-based SMMs, the $\mathrm{Tb^{3+}}$ phthalocyanine double-decker complexes, display redox-switchable behavior, undergoing changes in magnetization dynamics (increased U_{eff} value) and hysteretic behavior upon electrochemical generation of a ligand-based radical.[18,25]

Aside from the Tb^{3+} phthalocyanate complexes and our Ln^{3+} bis(ferrocene)diamine complexes, $K(thf)_5[Ln(fc[NSi(t\text{-}Bu)Me_2]_2)_2]/[Ln(fc[NSi(t\text{-}Bu)Me_2]_2)_2]$ (Ln = Dy^{3+}, Er^{3+}), highlighted in Chapter 4 and in Dickie et al. 2017,[48] there is only one previously reported Ln(III)-based compound with proven redox controllability of the magnetization dynamics and slow relaxation. In that example, an intramolecularly attached $Ru^{2/3+}$ redox-switch was utilized to modify the magnetic relaxation dynamics of a Dy^{3+}-based SIM.[49] It was determined that the oxidation of Ru^{2+} to Ru^{3+} enhanced slow magnetic relaxation. It is believed that the enhancement occurs either through perturbations of the ligand field or the addition of another spin-carrier to the system. However, one drawback is the limited thermal stability at room temperature.

1.6 Outlook

Many of the redox-switchable systems suffer from limited thermal stability of at least one of the redox states. Additionally, there are relatively few reported examples of switchable magnetization dynamics in lanthanide-based compounds. Our report of redox switchability in Dy^{3+} and Er^{3+} bisferrocene diamide complexes was the first report of redox switchability in Ln^{3+} complexes to utilize the reversible redox chemistry of ferrocene/ferrocenium in the ligand scaffold. Notably both of the redox states are thermally stable.

The field of single-molecule magnetism is rapidly advancing. A major challenge thus far in the field has been low blocking temperatures, necessitating the use of costly liquid helium. With recent advances, blocking temperatures are beginning to approach temperatures which are achievable with liquid N_2. Towards the application of SMMs in devices, there have been many studies investigating the attachment of SMMs to different surface substrates, including silicon,[50] graphite,[51] and gold.[52–55]

2. SYNTHESIS AND MAGNETIZATION DYNAMICS OF A DYSPROSIUM-ISOCARBONYL COMPOUND

2.1 Introduction

Compounds containing both lanthanide (f-block) and transition metal (d-block) components are of interest synthetically and for their physical properties. In the field of molecular magnetism, compounds combining f-block and d-block ions have been extensively studied for their magnetic properties, including exchange coupling between metal centers.[56–59] Heteronuclear mixed lanthanide-transition metal compounds are attractive building blocks for SMMs; the lanthanide ion provides high single-ion anisotropy and the transition metal lends its desirable redox and exchange coupling properties. A majority of d-block/f-block compounds feature bridging oxygen-based ligands, with the coordination environment around the Ln^{3+} ion often composed entirely of oxygen donor atoms.[60]

In lanthanide(III)-based single-molecule magnets, quantum tunneling of the magnetization (QTM), a through-the-barrier relaxation pathway, often dominates at low temperatures. This manifests in low blocking temperatures and limits applicability. Hence, many Dy(III) compounds display only field and/or dilution induced slow magnetic relaxation and either waist-restricted or no hysteresis.[13,56,61] One approach to circumvent QTM in lanthanide-based SMMs is to utilize strong exchange coupling between lanthanide ions through radical bridges.[26,27,62] Similarly, spin exchange interactions between a 4f ion and a 3d ion,[61,63,64] or another 4f ion,[65,66] may limit zero-field QTM by altering the Dy(III) ion energy levels, thereby mitigating this undesirable relaxation pathway. However, it has been shown that these interactions may either quench or enhance magnetic properties.[64]

In this regard, lanthanide-transition metal isocarbonyl compounds are attractive candidates for molecular magnetism studies. This class of compounds allows for synthetic flexibility; the cy-

---

The data in this chapter is reproduced from Ref. 78, Dickie, C. M.; Nippe, M. Magnetization dynamics of a heterometallic Dy-isocarbonyl complex. *Inorg. Chem. Front.* **2016**, *3*, 97-103, with permission from from the Chinese Chemical Society (CCS), Peking University (PKU), and the Royal Society of Chemistry.

clopentadienide (Cp^-) moiety may be substituted with electron withdrawing or electron donating groups. Furthermore, the identity of the transition metal may be changed, altering the redox properties, ligand field strength, and charge localization. In addition, the presence of the transition metal ion allows for the possibility to introduce an additional spin to the system and redox-switching functionality: using redox chemistry to change magnetic properties. Redox control utlizing electric potential as an external stimulus is very exciting for potential applications of SMMs in devices. Additionally, with paramagnetic transition metal ions there is the possibility of exchange coupling through the isocarbonyl bridge.

From a synthetic point of view, lanthanide-isocarbonyl complexes are interesting precursors to lanthanide-transition metal bonds via photolysis. This principle has been demonstrated with isocarbonyl compounds of actinide (An) ions. Ward et al. demonstrated the formation of a direct An–cobalt bond (An = U, Th) via photolytic CO elimination from the isocarbonyl precursor $N[(o\text{-}NCH_2P^iPr_2)C_6H_4]_3An(\mu\text{-}OC)Co(CO)_3$, in which the N_4P_3 ligand stabilizes the An–Co bond through the secondary P coordination sphere.[67]

The synthesis of molecular and polymeric lanthanide-isocarbonyl complexes via salt elimination reactions between lanthanide halide salts and alkali metal salts of transition metal carbonyl compounds has been previously reported.[68–74] However, structural data is not available for these early complexes. The lack of structural information presents questions as to whether these compounds are ionic or feature bridging isocarbonyl moieties. In the case of anionic transition metal carbonyl fragments, there are four categories of possible binding modes highlighted in Figure 2.1.[75] In 1984, Pasynskii et al. reported an isocarbonyl compound formed from the reaction between $[CpMo(CO)_3]_2$ and lanthanum metal activated by $HgCl_2$ (La/Hg) to form the structurally characterized lanthanum-molybdenum isocarbonyl species $[(thf)_5La((\mu\text{-}OC)Mo(CO)_2Cp)_3]thf$.[76] In 2014, Sobaczynski et al. reported the structure of an yttrium-isocarbonyl complex prepared via an alkane elimination reaction between $Y(CH_2SiMe_3)_3(thf)_2$ and the tungsten hydride compound $HW(CO)_3Cp$.[77] The structure showed the CO bridging in an isocarbonyl ($\mu(\sigma)$-OC) fashion in $(thf)_5Y((\mu\text{-}OC)W(CO)_2Cp)_3$.

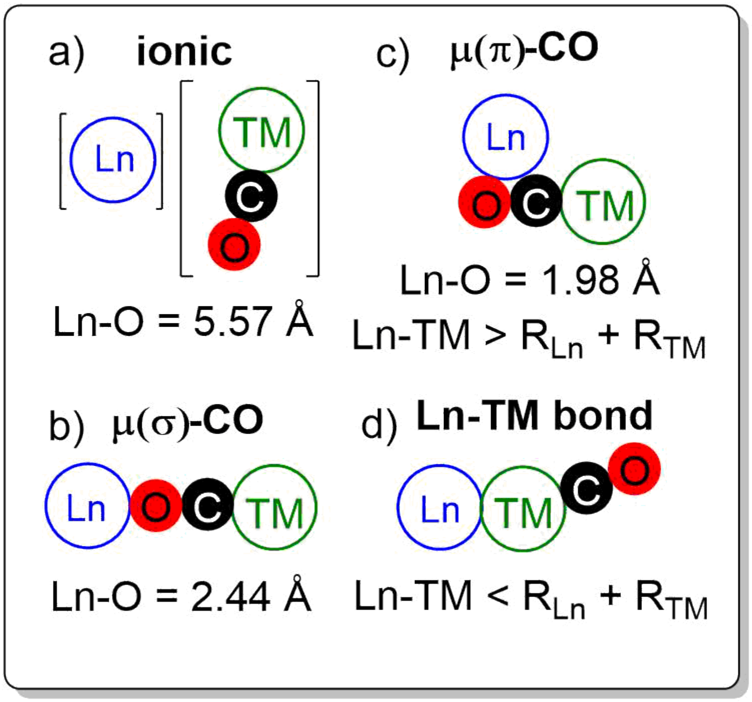

Figure 2.1: Possible bonding modes in Ln-TM carbonyl complexes. Isocarbonyl σ-bonding is highlighted in (b). Adapted from Beletskata et al. (1993).

In this study, Dy^{3+}-isocarbonyl compounds of tungsten were investigated. Dy^{3+} was selected as the paramagnetic ion; on account of its bistable ground state independent of the ligand field (Kramers ion) and high single ion anisotropy. Herein, I report the synthesis and characterization of the first structurally characterized dysprosium-isocarbonyl compound, $(thf)_5Dy((\mu\text{-}OC)W(CO)_2Cp)_3$ **2-1**. The compound was prepared via an amine elimination reaction between $[Dy(N(SiMe_3)_2)_3]$ and $[HW(CO)_3Cp]$. Temperature dependent slow magnetic relaxation was observed in dilute samples of **2-1·thf** Dy:Y (1:12), with a barrier height (U_{eff}) of 12.6 cm^{-1} (18.1 K) under a 400 Oe applied dc field. The results in this Chapter have been published in *Inorg. Chem. Front.* **2016**, *3*, 97-103.[78]

Following our report of this dysprosium-isocarbonyl compound, Pugh et al. reported a dinuclear Dy^{3+}-metallocene compound with bridging isocarbonyl ligands to a Fp moeity, $[Cp^{\star}_2Dy(\mu\text{-}Fp)]_2$, $(Fp^-) = [CpFe(CO)_2]^-)$.[79]

2.2 Experimental

2.2.1 General considerations

Unless otherwise stated, all reactions and manipulations were carried out under anaerobic and anhydrous conditions in an argon-filled glovebox (Vigor). Tetrahydrofuran (thf) and toluene were dried and deoxygenated using a solvent purification system (JC Meyer Solvent System) and stored over molecular sieves. $HW(CO)_3Cp$ was purchased from Sigma-Aldrich and used as received. $[Dy(N(SiMe_3)_2)_3]$ and $[Y(N(SiMe_3)_2)_3]$ were prepared as previously described and recrystallized from toluene prior to use.[34,80] Elemental analyses were carried out by ALS Environmental (Tucson, AZ). IR spectra were recorded on a Mattson ATI Genesis FT-IR spectrometer fitted with a PIKE Technologies MIRacle ATR sampling accessory.

2.2.2 Synthesis

Synthesis of $[(thf)_5Dy((\mu\text{-}OC)W(CO)_2Cp)_3]\cdot thf$ (2-1·thf). A solution of $HW(CO)_3Cp$ (63.0 mg, 0.189 mmol) in thf (3 mL) was added to a stirring solution of $Dy(N(SiMe_3)_2)_3$ (39.0 mg, 0.0606 mmol) in thf (3 mL) and the reaction mixture was stirred for 1.5 h at rt. The solution was filtered through Celite and concentrated in vacuo. Very air-sensitive yellow block shaped crystals of **2-1·thf** (41.7 mg, 43 %) were obtained from the concentrated thf solution after 24 h at –30 °C. Anal. calcd for $C_{42}H_{51}DyW_3O_{13.5}$ (**2-1** –0.5 thf): C, 33.95; H, 3.46. Found: C, 33.45; H, 3.49. IR: ν_{max} cm^{-1} = 2010s, 1894s, 1790br, 1680 br, 1602br [all ν(CO)]. Unit cell parameters (110 K): $P\bar{1}$, a = 11.1291(8) Å, b = 11.2334(8) Å, c = 20.7030(16) Å, α = 97.367(4) °, β = 101.318(4) °, γ = 92.721(4) °, V = 2509.9(3) Å^3.

Modified synthesis of $[(thf)_5Y((\mu\text{-}OC)W(CO)_2Cp)_3]\cdot thf$ (2-2·thf). Prepared analogously to $(thf)_5Dy((\mu\text{-}OC)W(CO)_2Cp)_3\cdot thf$ (**2-1·thf**). Yellow block shaped crystals of **2-2·thf** were formed from a concentrated thf solution after 24 h at –30 °C. Yield: 64 %. Product was confirmed by comparing unit cell parameters to those of previously reported structure.[77]

Synthesis of $[(thf)_5Dy_{0.08}Y_{0.92}((\mu\text{-}OC)W(CO)_2Cp)_3]\cdot thf$. A solution of **2-1·thf** (7.28 mg, 0.00457 mmol) in thf (3 mL) and a solution of **2-2·thf** (83.2 mg, 0.0547 mmol) in thf (10 mL) were mixed. Yellow block shaped crystals were obtained after 48 h at –30 °C. Yield: 77 %. Unit cell parameters (110 K): $P\bar{1}$, a = 11.21 Å, b = 11.32 Å, c = 20.83 Å, α = 97.4 °, β = 101.2 °, γ = 92.8 °, V = 2562 Å^3.

2.2.3 X-ray crystallography

Single crystal X-ray diffraction measurements were carried out using a Bruker-AXS APEX-II CCD area detector diffractometer (Mo K_α radiation, λ = 0.71069 Å) (NSF-CHE-9807975, NSF-CHE-0079822 and NSF-CHE-0215838). Crystals were mounted on nylon loops and cooled in a nitrogen stream (110(2) K). Bruker AXS APEX II software was used for data collection and reduction.[81] Absorption corrections were applied using SADABS.[82] Space group assignments were determined by examination of systematic absences, E-statistics, and successive refinement of the structures. Structures were solved using direct methods and refined by least-squares refinement on F^2 followed by difference Fourier synthesis.[81,83–86] All hydrogen atoms were included in the final structure factor calculation at idealized positions and were allowed to ride on the neighbouring atoms with relative isotropic displacement coefficients. Thermal parameters were refined anisotropically for most non-hydrogen atoms. There is partial disorder of some of the carbon atoms of one of the Cp ligands. Crystallographic data for **2-1·thf** is given in Table 2.1. The structure of isostructural Y^{3+} analogue **2-2·thf** was confirmed by unit cell determination to match the previously reported unit cell.[77]

2.2.4 Magnetic measurements

Magnetic samples were prepared by adding crushed crystalline sample to a high-purity 7 mm x 5mm NMR tube and covering with a layer of eicosane. The tube was flame sealed under vacuum and the eicosane was melted in a water bath at 39 °C, evenly dispersing it throughout the sample. The sample was loaded into a straw affixed to the end of the sample rod. Magnetic measurements were carried out using a Quantum Design MPMS XL SQUID magnetometer (NSF-9974899) (compound **2-1·thf**) and a Quantum Design MPMS 3 SQUID magnetometer (TAMU Vice President of Research) (dilution sample). Dc measurements were carried out over a temperature range of 1.8 to 300 K and an applied field of 1000 Oe. Ac measurements were carried out over a temperature range of 1.8 to 8 K, using a 2 to 5 Oe alternating field and applied dc fields of 0 to 2000 Oe. Data was corrected for sample holder and diamagnetic corrections were applied to the dc magnetic data of **2-1·thf**, accounting for contributions from eicosane and the core diamagnetism, with the diamagnetic contribution from the complex estimated from Pascal's constants.[87] Cole-Cole plots (χ''_M vs χ'_M) were fitted using least-squares regression to formulae describing χ''_M and χ'_M in terms of the variables constant temperature susceptibility (χ_T), adiabatic susceptibility (χ_S), relaxation time (τ) and the distribution of relaxation times (α).

2.3 Results and Discussion

2.3.1 Synthesis and structure of a Dy-isocarbonyl compound

Interestingly, $HW(CO)_3Cp$ is sufficiently acidic to undergo an amine elimination reaction with $[Dy(N(SiMe_3)_2)_3]$ to afford the highly air-sensitive dysprosium-isocarbonyl compound $(thf)_5Dy((\mu\text{-}OC)W(CO)_2Cp)_3)$ **2-1** (Figure 2.2). Large yellow, block-shaped crystals of **2-1·thf** were obtained from concentrated thf solutions at –30 °C over 24 h.

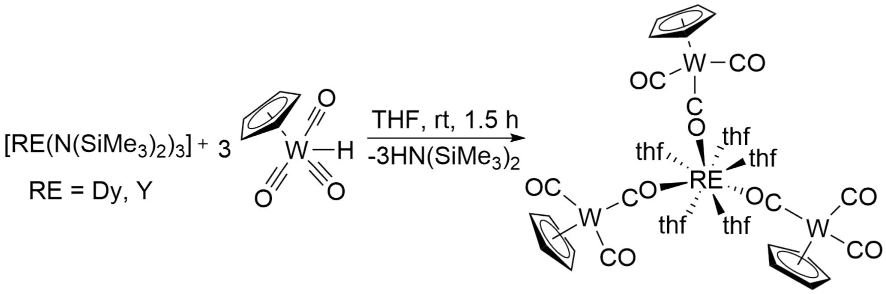

Figure 2.2: Synthesis of $[(CpW(CO)_2(\mu\text{-}CO))_3RE(thf)_5]$, RE = Dy (**2-1**) and Y (**2-2**).

Attempts to carry out the reaction and crystallizations in non-coordinating solvents were unsuccessful due to the limited solubility of $HW(CO)_3Cp$ and **2-1**. Exposure to air and moisture led to immediate decomposition and color change of the crystals from yellow to pink within seconds.

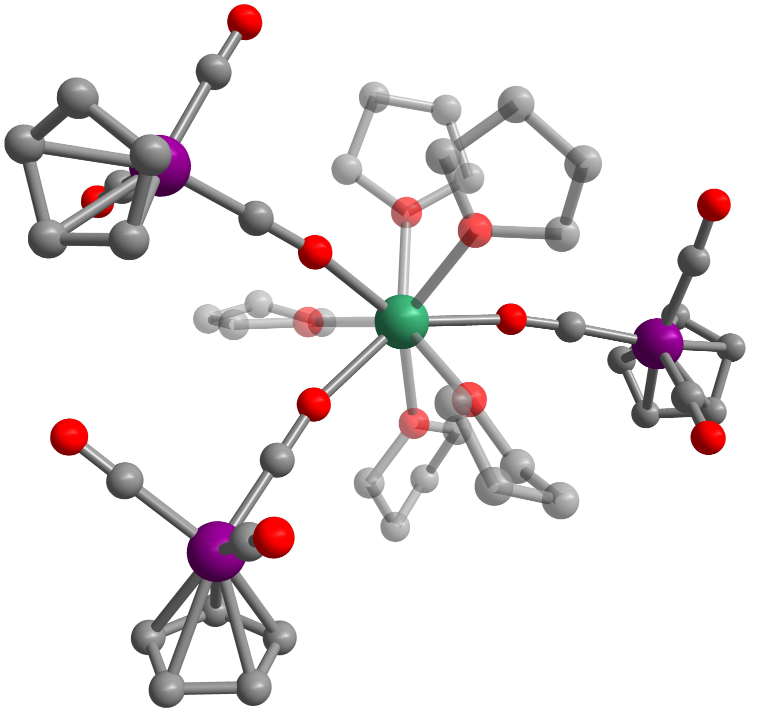

Figure 2.3: Molecular structure of **2-1** in **2-1·thf**. Green = Dy, purple = W, red = O, grey = C. Hydrogen atoms omitted for clarity.

The compound $(thf)_5Dy((\mu\text{-}OC)W(CO)_2Cp)_3\cdot thf$ (**2-1·thf**) crystallizes in the triclinic space group $P\bar{1}$ (Table 2.1). X-ray diffraction techniques revealed a distorted square antiprismatic geometry around the Dy^{3+} center (Figure 2.3). The three $[CpW(CO)_3]^-$ ligand moieties are coordinated to the Dy^{3+} center end-on through the carbonyl oxygen atom (d(Dy–O) = 2.320(5) Å, 2.270(5) Å, 2.267(5) Å) with five thf ligands ($d(\text{Dy–O}_{\text{thf}})$ = 2.384(5) - 2.462(5) Å) filling out the rest of the coordination sphere, resulting in a coordination number of 9 (Figures 2.3 and A.2). The O–Dy–O angles concerning O donors of the same distorted square are in the range of 72 °–75 °. In addition, there is one non-coordinated thf molecule per molecule of **2-1** in the crystal lattice. Intermolecular $Dy^{3+}\cdots Dy^{3+}$ distances in crystals of **2-1·thf** are in the range of 10.45 to 13.66 Å, with the shortest interaction depicted in the unit cell packing diagram in Figure A.1.

The W–C bond lengths to the bridging isocarbonyl moieties are shorter (1.875(8) –1.894(8) Å) than the terminal carbonyl W–C bonds (1.939(7)-1.955(8) Å). The C–O bond lengths of the

Compound	**2-1·thf**
Formula	$C_{48}H_{63}DyO_{15}W_3$
Crystal system	triclinic
Space group	$P\bar{1}$
a, Å	11.1292(8)
b, Å	11.2334(8)
c, Å	20.7030(16)
α, °	97.367(4)
β, °	101.318(4)
γ, °	92.721(4)
Volume, Å^3	2509.9(3)
Z	2
T, K	110(2)
ϱ_{calcd} , mg/m^3	2.109
$F(000)$	1518
$\Theta_{\min}$, $\Theta_{\max}$, °	2.2156, 25.2033
$R_1{}^{a}$, $wR_2{}^{b}$ ($I > 2\sigma(I)$)	0.0431, 0.0890
$R_1{}^{a}$, $wR_2{}^{b}$ (all data)	0.0702, 0.1027

Table 2.1: Crystallographic data for **2-1·thf**.

bridging isocarbonyl groups are longer (1.21(1)–1.22(1) Å) than those of the terminal carbonyl ligands (1.16(1)–1.18(1) Å). The W–C–O (bridging) bond angles are nearly linear, with values of 177.4(7) °, 177.7(7) °, and 177.9(6) °. The W–C (bridging) and C–O (bridging) bond distances and angles are in good agreement with those observed in a tungsten isocarbonyl complex of cerium, $[Cp''_2Ce(\mu\text{-}OC)W(CO)(Cp)(\mu\text{-}CO)]_2$,[88] and of yttrium, $[CpW(CO)_2(\mu\text{-}CO)_3Y(thf)_5]$.[77] It should be noted that similar shortening and elongation of M–C and C–O distances, respectively, has also been well established for simple contact ion pairs of alkali metal salts of transition metal carbonyl anions; the presence of the cationic charge is hereby expected to lower LUMO energies of the respective CO ligand and results in increased π-backbonding from the transition metal.[89,90]

Compound **2-1·thf** is isostructural to the yttrium analogue **2-2·thf** first prepared by Kempe et al. through an alkane elimination reaction between $Y(CH_2SiMe_3)_3(thf)_2$ and three equivalents of $HW(CO)_3Cp$.[77]

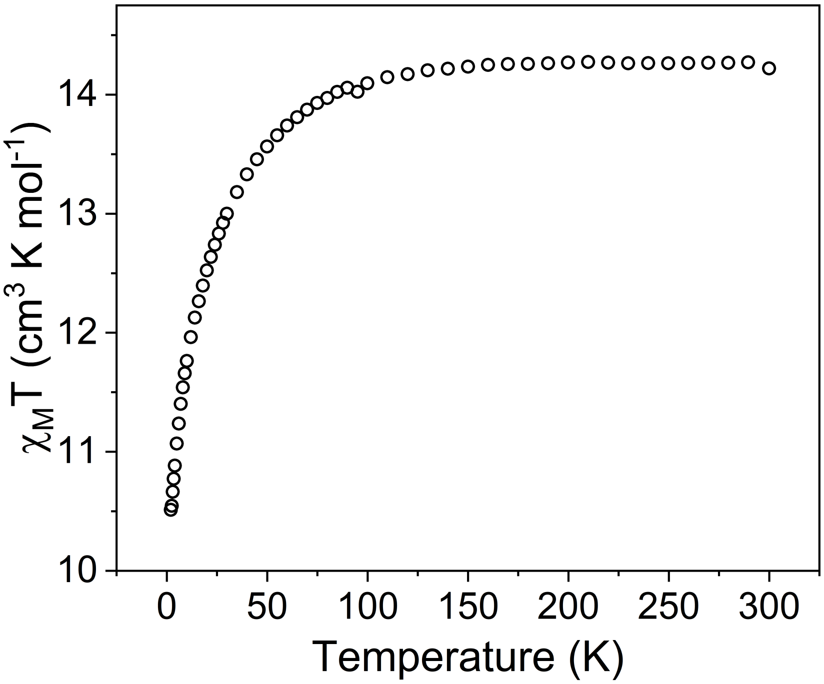

Figure 2.4: Temperature dependence of the molar magnetic susceptibility times temperature product in **2-1·thf**.

2.3.2 Magnetic properties of Dy-isocarbonyl

Dc magnetic susceptibility data were collected for **2-1·thf** over the temperature range of 2 to 300 K under an applied field of 1000 Oe (Figure 2.4). The room temperature $\chi_M T$ value of 14.22 cm^3 K mol^{-1} is in agreement with the expected value (14.17 cm^3 K mol^{-1} for one, isolated Dy^{3+} ion ($^6H_{15/2}$, $S = 5/2$, $L = 5$, $g = 4/3$). Upon cooling, a gradual decrease of $\chi_M T$ at around 100 K and a more rapid decrease below 50 K is observed, reaching a minimum value of 10.51 cm^3 K mol^{-1} at 2 K. This decrease at low temperature is attributed to thermal depopulation of the Stark sublevels (excited states) of Dy^{3+} and possible antiferromagnetic dipole-dipole interactions between Dy^{3+} centers.

The field dependence of the magnetization (M) was measured for **2-1·thf** with fields up to 70 kOe (7 T) over a temperature range of 2 –10 K (Figure 2.5). At 2 K, the magnetization increases

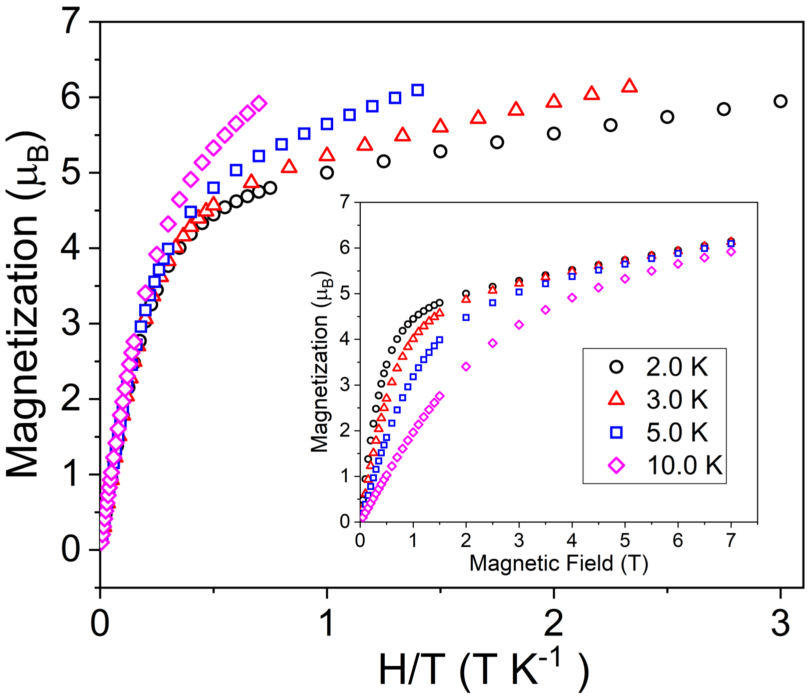

Figure 2.5: Field dependence, temperature dependence of the magnetization in **2-1·thf**. Inset: Field dependence of magnetization **2-1·thf**.

sharply until 1 T, followed by a more gradual increase, reaching an unsaturated moment of 6.14 μ_B at 7 T (Figure 2.5, inset). This is lower than the expected value of 10 μ_B for one uncorrelated Dy^{3+} ion. Magnetic moments have commonly been found to be lower than expected in Dy^{3+} complexes in the presence of ligand field effects.[91] The lack of saturation in the low temperature magnetization at 70 kOe is attributed to the existence of low lying excited states or crystal field effects (Figure 2.5; inset).[92] The non-super position in the temperature dependence (M vs HT^{-1}) suggests the presence of significant magnetic anisotropy and/or low-lying excited states (Figure 2.5).

To investigate magnetization dynamics of **2-1·thf**, variable frequency ac susceptibility measurements were carried out. In the absence of an applied dc field, no signal was observed in the out-of-phase component (χ''_M) of the ac susceptibility at frequencies up to 1000 Hz and temperatures as low as 1.8 K (Figure A.4). The absence of a signal in χ''_M is attributed to efficient quantum tunneling of magnetization (QTM) at low temperatures in **2-1·thf**, as this relaxation phenomenon is often observed in lanthanide-based SIMs (or SMMs).[13]

One commonly used technique to mitigate QTM is the application of a small dc field. The presence of the applied dc field acts to lift the degeneracy of energy levels, thereby mitigating this relaxation pathway. A signal in the χ''_M component was observed under applied dc fields of 1000 and 2000 Oe, however the maxima of the signals lie outside the frequency range of the magnetometer (1000 Hz) (Figure A.4). This out-of-phase signal could also be indicative of phonon bottleneck (PB) effect, a phenomenon that has been shown to occur at low temperatures in samples, especially under moderate dc fields.[12] PB effect can occur in crystalline samples when there is poor contact between the sample and the thermal bath.[12] In this case, the lack of phonons leads to a build up of phonons, causing thermal excitation of other spins. The sample would have to be studied at very low temperatures (0.5 K) using a microSQUID or in solution phase (better contact with thermal bath) to rule out PB effects.

A common contributor to QTM is intermolecular dipole-dipole interactions between paramagnetic metal centers. These interactions lead to mixing of the ground states, allowing a pathway for QTM to occur.[12] Dilution of a paramagnetic compound with an isostructural diamagnetic compound via co-crystallization has been shown to suppress dipole-dipole interactions and thereby mitigate QTM in Ln-based SMMs.[13,18] To investigate the effect of dipole-dipole interactions between Dy^{3+} in **2-1·thf**, a solid magnetic dilution sample was prepared. The isostructural diamagnetic Y^{3+} compound was prepared and crystals were isolated from a 1:12 thf solution of Dy:Y.

Ac susceptibility measurements on the diluted sample revealed between 1.8 K and 4 K what could be the beginning of a signal in the χ''_M component of the ac susceptibility, however the maxima lie outside of the frequency range of the magnetometer, therefore it is inconclusive (Figure 2.6). However, once again PB effect cannot be excluded.

Application of variable strength dc fields at 1.8 K revealed slow relaxation of the magnetization, an increase in magnitude and a shift in the maxima of χ''_M to lower frequencies (Figure 2.6). The largest signal in the out-of-phase component (χ''_M) was obtained by applying a 400 Oe dc field. As a result, the remainder of the ac studies were carried out under a 400 Oe dc field. A second, slower relaxation process can be seen coming in under higher fields (Figure 2.6).

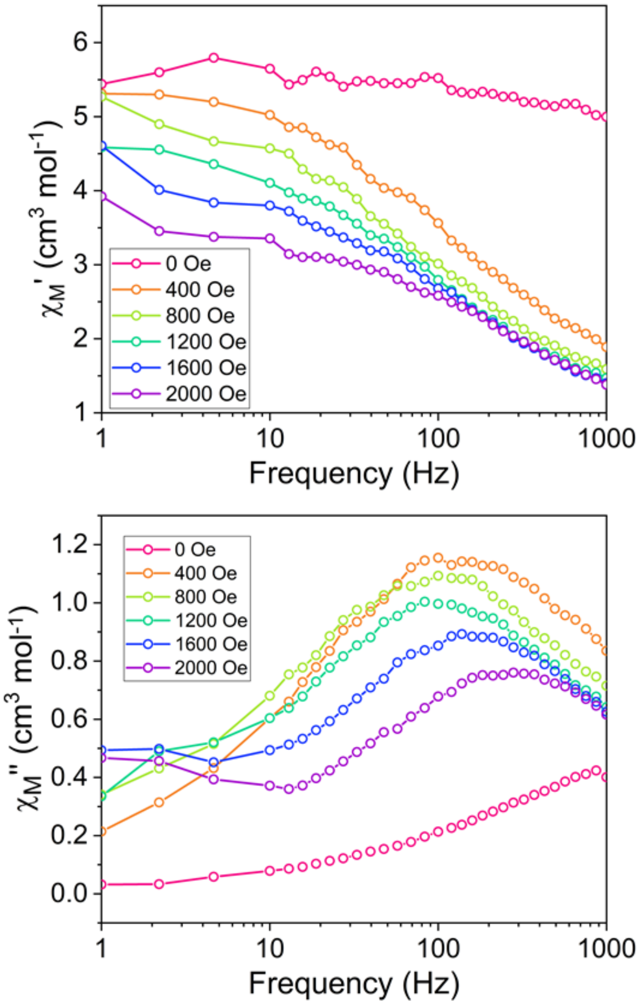

Figure 2.6: Frequency dependence of the in-phase χ'_{M} (top) and out-of-phase χ''_{M} (bottom) components of the molar ac susceptibility under various applied dc fields for the 1:12 Dy:Y dilution sample.

The temperature dependencies of χ'_{M} and χ''_{M} were investigated using a static dc field of 400 Oe up to 4 K, although by 2.4 K the maxima in χ''_{M} are beyond 1000 Hz (Figure 2.7). To extract relaxation times, τ, Cole-Cole (χ''_{M} vs χ'_{M}) plots at each temperature were fit with the generalized Debye equation (Equations 1.9 and 1.10) (Figure 2.7 - solid lines). The barrier height, U_{eff}, was determined from an Arrhenius plot of the natural logarithm of the relaxation times, ln τ vs T^{-1} (Figure 2.7). Fitting the linear portion of the plot (Orbach mechanism) to Equation 1.12 resulted in a U_{eff} value of 12.6 cm^{-1} (18.1 K) and a pre-exponential factor of $\tau_0 = 9.3 \times 10^{-8}$. It is worth noting that this barrier height is on the low end compared to other mononuclear Dy^{3+} complexes.[13,20,21,56] The deviance from linearity at temperatures below 2 K is indicative of the presence of other relaxation pathways including QTM, Raman, and direct relaxation.

The determination of the ground state magnetic anisotropic axis is useful for understanding and describing the observed magnetic properties. Chilton et al. developed MAGELLAN, based on a simple electrostatic method for predicting the magnetic anisotropy axis of Dy^{3+} compounds, even in low symmetry environments.[93] For this electrostatic method, all that is required is a molecular structure. From the structure, the ligands are assigned as point charges and the electrostatic interactions between the charged ligands and the f-electron density are minimized (energy minimization problem).

For the assignment of point charges in **2-1·thf**, two different scenarios were considered. While the anionic charge in an isolated [CpW(CO)$_3$]$^-$ anion is symmetrically delocalized, the differences in geometric parameters between bridging and end-on carbonyl ligands suggest that anionic charge is at least partially localized on the bridging carbonyl ligands in **2-1·thf**.

Assuming equivalent binding and charge localization of the three [CpW(CO)$_3$]$^-$ moieties, the orientation of the magnetic anisotropic axis is insensitive to the magnitude of this charge. Equivalent charges on all three [CpW(CO)$_3$]$^-$ ligands results in an anisotropic axis –orange, Figure 2.8. Notably, the anionic charges of the isocarbonyl-O atoms enforce the ground state electron density of the Dy^{3+} ion to be distributed perpendicular to the Dy-isocarbonyl plane. Accordingly, the easy axis is calculated to lie approximately within the plane of the Dy-isocarbonyl bonds.

However, given that the Dy–O1 bond length is roughly 0.05 Å longer than the Dy–O2 and Dy–O3 distances, the magnetic easy axis for the Dy^{3+} ion was also calculated assuming a less negative charge on O1 (–0.5) than on O2 (–1) and O3 (–1) (blue axis in Figure 2.8). Applying this uneven charge distribution results in a shift of the anisotropic axis away from the less negatively

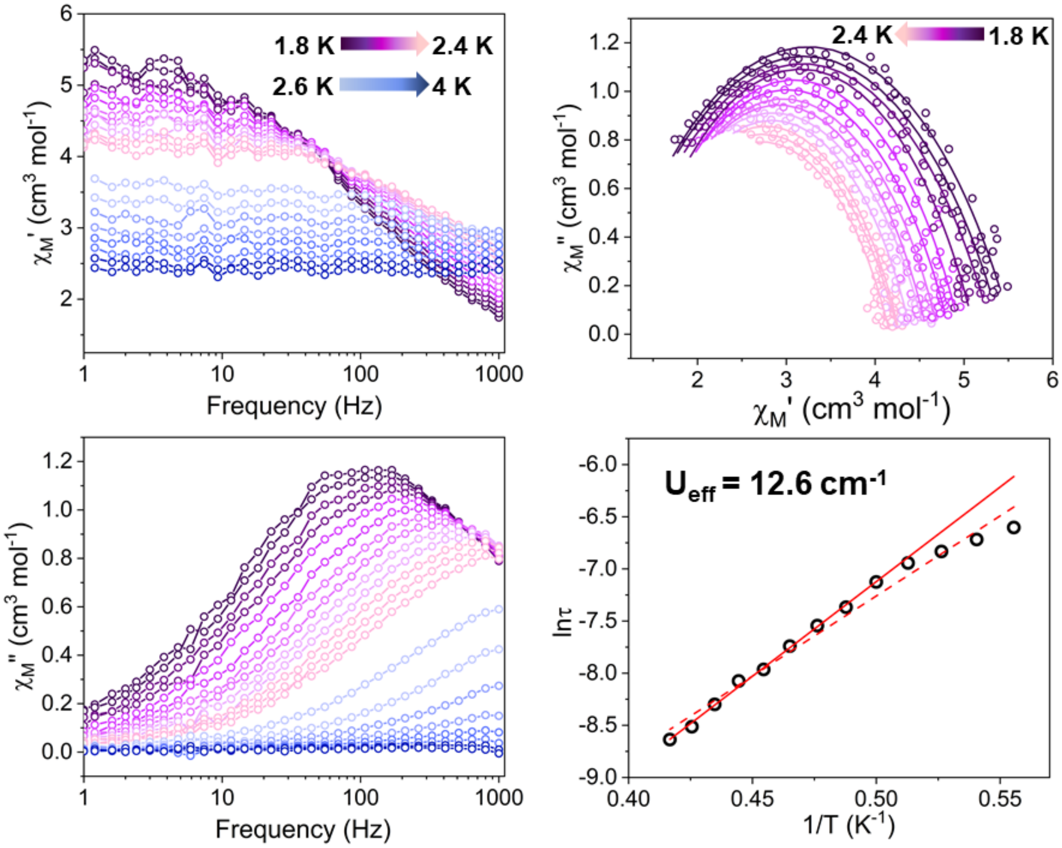

Figure 2.7: Frequency dependence as a function of the in-phase (χ_M') (top-left) and out-of-phase (χ_M") (bottom-left) components of the ac susceptibility of a 1:12 (Dy:Y) magnetic dilution of **2-1·thf** under a 400 Oe applied dc field with a 2 Oe switching field. Lines are a guide for the eye. (top-right) Cole-Cole (Argand) plots for ac susceptibility collected under an applied field of 400 Oe for the magnetic dilution of **2-1·thf**, open circles represent experimental data, solid lines represent fits. (bottom-right) Arrhenius plot of the 1:12 (Dy:Y) magnetic dilution of **2-1·thf**. Relaxation times, τ, were determined from non-linear least squares fits to the Cole-Cole plots. Open black circles correspond to experimental data, solid red line corresponds to a fit of the linear portion of the data (T = 2-2.4 K) and dashed red line to a fit of all the data (T = 1.8-2.4 K) to the Arrhenius expression $\tau = \tau_0 \exp(U_{\text{eff}}/k_B T)$, affording U_{eff} = 12.6 cm^{-1} (18.1 K) and 10.7 cm^{-1} (15.4 K), respectively.

charged ligand. This is a result of less electrostatic interaction between that ligand point charge and the f-electron density of the Dy^{3+} ion. Overall, it is preferred that a formulation of equal charge distribution for O1, O2, and O3 (orange line) is used. Although it is noted that even with unsymmetrical point charge distribution, the magnetic anisotropy axis still lies within the same plane (approximately the same plane as the ligands).

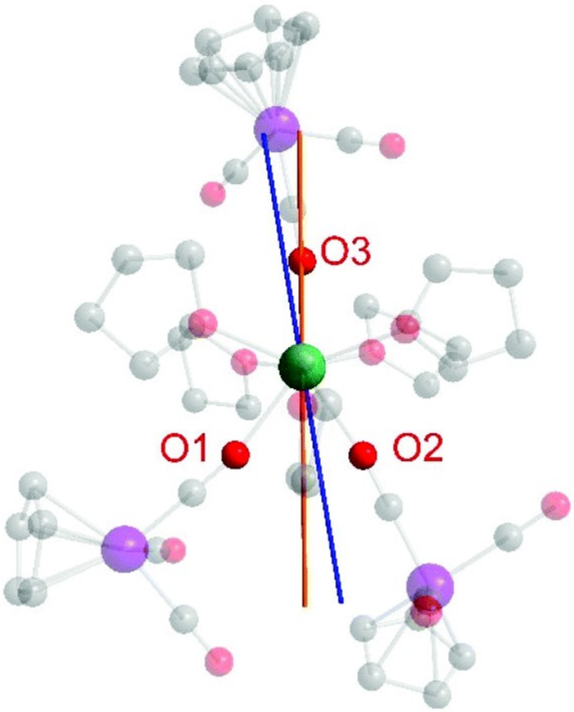

Figure 2.8: Calculated magnetic anisotropy axes in **2-1·thf** assuming equivalent negative charges on O1–O3 (orange line) and inequivalent charges for O1 (–0.5), O2 (–1), and O3 (–1) (blue line). The electrostatic calculations were carried out using MAGELLAN, developed by Chilton et al.

Electrochemical properties were investigated in attempts to produce a mixed valent compound. However, attempts to oxidize the tungsten center led to immediate decomposition of the compound, highlighting the instability of the compound and unsuitability towards redox switchable applications.

2.4 Conclusion and Outlook

The first structurally characterized dysprosium isocarbonyl complex, $[CpW(CO)_2(\mu\text{-}CO)]_3Dy(thf)_5\cdot thf$, **2-1·thf**, has been synthesized from the amine elimination reaction between $[Dy(N(SiMe_3)_2)_3]$ and $[HW(CO)_3Cp]$. Slow magnetic relaxation was observed in a magnetically dilute sample of **2-1·thf** (Dy:Y, 1:12) under a 400 Oe applied dc field, with a barrier height (U_{eff}) of 12.6 cm^{-1} (18.1 K). The utilization of lanthanide complexes stabilized by metal-carbonyl fragments may lead to new classes of heterometallic SMMs. Investigations of electrochemical properties revealed instability of the isocarbonyl compound **2-1·thf** to oxidation, resulting in rapid decomposition. Investigations of the photochemical properties of compounds are currently ongoing and may allow for the generation of species that feature lanthanide-transition metal bonds.

3. SYNTHESIS OF A BULKY TUNGSTEN HYDRIDE COMPLEX

3.1 Introduction

The dysprosium-isocarbonyl compound, $(thf)_5Dy((\mu\text{-}OC)W(CO)_2Cp)_3\cdot thf$ (**2-1**·thf), highlighted in Chapter 3, required dilution and the application of an external dc field to observe slow relaxation.[78] Even under those forcing conditions, a relatively low thermal relaxation barrier of $U_{\mathrm{eff}} = 12\ \mathrm{cm}^{-1}$ was extracted; two orders of magnitude lower than current records in the field.[7,8] The distorted square-antiprismatic geometry around the Dy^{3+} center likely contributed to the observed non-desirable magnetization dynamics, including considerable QTM at low temperatures. Removal of the five coordinating thf molecules through the generation of a three-coordinate species is expected to improve the magnetization dynamics as a result of the anticipated less distorted geometry around the paramagnetic center.

Previously, three-coordinate lanthanide complexes, especially of erbium(III), were shown to display slow relaxation under zero dc field.[34] This equatorial coordination geometry is particularly well suited for lanthanide(III) ions with prolate f-electron densities, such as Er^{3+}.[19] Furthermore, due to their oxophilic nature, lanthanide(III) ions typically have large coordination numbers and three-coordinate complexes of lanthanide ions are rare.

Attempts to synthesize and crystallize **2-1** in non-coordinating solvents, including thf and hexanes, were unsuccessful due in part to limited solubility of the tungsten hydride precursor, $HWCp(CO)_3$ and the product **2-1**. As a potential answer to the solubility issue, a new bulky tungsten hydride compound, $HWCp^{BIG}(CO)_3$ (HCp^{BIG} = $(4\text{-}n\text{-}Bu\text{-}C_6H_4)_5$-cyclopentadiene) has been prepared, featuring high solubility in non-coordinating solvents, including hexanes and toluene. Substitution of the cyclopentadiene (Cp) ligand with the bulky Cp^{BIG} derivative is expected to allow for solubility in non-coordinating solvents and encourage the formation of a three-coordinate Ln^{3+} ion. In addition to enhanced solubility in non-coordinating solvents, the bulky Cp^{BIG} ligand is anticipated to limit coordination number and prevent dimerization. Based on previous reports of an equatorial three-coordinate erbium-based SIM, it is expected that a three-coordinate Er^{3+}-isocarbonyl complex with an equatorial ligand field will have desirable magnetic properties, including slow relaxation under zero dc field.[34] Bulky, substituted cyclopentadiene derivatives, including HCp^{BIG}, may be synthesized through Heck-type coupling reactions between either cyclopentadiene or zirconocene dichloride and the desired aryl bromide.[94]

In this chapter, the synthesis of a new, bulky, tungsten hydride compound $Cp^{BIG}W(CO)_3H$ (**3-1**) is presented herein. This compound may be prepared via two different synthetic routes, either in situ through a Li^+ salt intermediate or from the isolated potassium salt, KCp^{BIG}. Attempts to prepare **3-1** from the reaction between tris(acetonitrile)tricarbonyltungsten(0) and HCp^{BIG} were unsuccessful. Preliminary results from reactions between $Cp^{BIG}W(CO)_3H$ and $Dy(N(SiMe_3)_2)_2$ are discussed herein.

3.2 Experimental

3.2.1 General considerations

Unless otherwise stated, all reactions and manipulations were carried out under anaerobic and anhydrous conditions in an argon-filled glovebox (Vigor) or using a Schlenk line under N_2. All reactions were treated as light-sensitive and exposure to light was minimized. Tetrahydrofuran (thf), toluene, and hexanes were dried and deoxygenated using a solvent purification system (JC Meyer Solvent System) and stored over molecular sieves. Anhydrous DMF and glacial acetic acid were purchased from EMD Millipore and degassed with N_2 prior to use. *n*-Butyllithium (1.6 M in hexanes) was purchased from Sigma-Aldrich and used as received. Tungsten hexacarbonyl was purchased from Acros Organics and used as received. $[Dy(N(SiMe_3)_2)_3]$ was prepared as previously described and recrystallized from toluene before use.[80] HCp^{BIG} and KCp^{BIG} were prepared as previously described.[94,95] ^1H NMR spectra were recorded on a Mercury 300 spectrometer operating at 300 MHz proton frequency.

3.2.2 Synthesis

Synthesis of HWCp^{BIG}(CO)$_3$ (3-1) from HCp^{BIG}. HCp^{BIG} (395 mg, 0.543 mmol) and thf (10 mL) were added in a Schlenk flask. A solution of *n*-butyllithium (0.6 mL, 1.6 M, 0.96 mmol) was added to the stirring Cp^{BIG}H solution at –5 °C (ice/salt bath) drop-wise by syringe. The reaction was allowed to slowly warm up to rt and was stirred for 3 h. All solvent was removed in vacuo and degassed DMF (10 mL) was added. The solution was then cannulated to a Schlenk flask containing a suspension of tungsten hexacarbonyl (229 mg, 0.651 mmol) in DMF (10 mL). The reaction was heated at 80 °C under N_2 for 24 h. After allowing to cool to rt, degassed glacial acetic acid (0.16 mL) was added via syringe and the reaction mixture was stirred overnight at rt. Solution was orange and clear. All DMF was removed in vacuo, using a KOH trap to neutralize acidic vapors. The resulting residue was extracted with hexanes. Orange block shaped single crystals were grown from a concentrated hexanes solution at –30 °C over 3 weeks. ^{1}H NMR (300 MHz, $CDCl_3$, δ): –5.26 (s, 1H, W-*H*), 0.49 (m, 15H, -C*H*$_3$), 1.32 (m, 10H, Ph-CH_2-CH_2-C*H*$_2$-CH_3), 1.95 (m, 10H, Ph-CH_2-C*H*$_2$-CH_2-CH_3), 2.93 (m, 10H, Ph-C*H*$_2$-CH_2-CH_2-CH_3), 7.30 (m, 20H, Ar H). Unit cell parameters (110 K): $P\ 2_1/c$, a = 14.1058(4) Å, b = 16.9038(4) Å, c = 20.9444(5) Å, α = 90 °, β = 98.117(2), γ = 90 °, V = 4944.0(2) Å^3.

Synthesis of Cp^{BIG}W(CO)$_3$ (3-1) from KCp^{BIG}. Tungsten hexacarbonyl (105 mg, 0.298 mmol) and anhydrous, degassed DMF (10 mL) were added in a Schlenk flask. A solution of KCp^{BIG} (226 mg, 0.311 mmol) in DMF (20 mL) was cannulated to the stirring $W(CO)_6$ solution. The reaction mixture was heated at 80 °C for 24 h. After allowing to cool to rt, degassed glacial acetic acid (0.1 mL) was added via syringe, resulting in a color change to orange. The reaction mixture was stirred for 22 h at rt (yellow in color). All solvent was removed in vacuo, using a KOH trap to neutralize any acetic acid vapors. The resulting residue was extracted with hexanes. Orange block shaped single crystals were grown from a concentrated hexanes solution at –30 °C over 24 h. Yield: 92.1 mg (31.3 %). ^{1}H NMR (300 MHz, $CDCl_3$, δ): –5.26 (s, 1H, W-*H*), 0.49 (m, 15H, -C*H*$_3$), 1.32 (m, 10H, Ph-CH_2-CH_2-C*H*$_2$-CH_3), 1.95 (m, 10H, Ph-CH_2-C*H*$_2$-CH_2-CH_3), 2.93 (m, 10H, Ph-C*H*$_2$-CH_2-CH_2-CH_3), 7.30 (m, 20H, Ar H). Unit cell parameters (110 K): $P\ 2_1/c$, a =

13.986(2) Å, $b = 16.978(3)$ Å, $c = 20.708(3)$ Å, $\alpha = 90$ °, $\beta = 98.416(8)$ °, $\gamma = 90$ °, $V = 4864.0(13)$ Å^3.

3.2.3 X-ray crystallography

Suitable crystals of Cp^{BIG}WH(CO)$_3$ were grown from concentrated cold hexane at –30 °C. A Leica MZ 75 microscope was used to select an orange block single-crystal with dimensions 0.102 x 0.084 x 0.075 mm^3. The crystal was mounted on a nylon loop and placed in a cold N_2 stream (Oxford) at 110(2) K. A BRUKER APEX 2 Duo X-ray (three-circle) diffractometer was used for unit cell determination and data collection with the detector at 6.0 cm from the crystal sample (APEX2, 512 x 512 pixel). The X-ray radiation employed was generated from a Mo sealed X-ray tube ($K_\alpha = 0.70173$ Å with a potential of 40 kV and a current of 40 mA). The data was corrected for absorption using SADABS.[82] The structure was solved using XT/XS in APEX2.[81,83–85] Elongated thermal ellipsoids C47, C48 and C3, O3 indicated disorder of these groups, which was successfully modeled between two positions each. Hydrogen atom H attached to W was located from difference Fourier maps and was set riding on the W1 atom with idealized distances. Absence of additional symmetry and voids were confirmed using PLATON (ADDSYM).[96] The structure was refined (weighted least squares refinement on F^2) to convergence using OLEX2.[86]

3.3 Results and Discussion

3.3.1 Synthesis and structural characterization

The cyclopentadienide ligand precursor, HCp^{BIG}, was prepared from the Pd(II) catalyzed Heck-type coupling reaction between the cyclopentadienide ligands of zirconocene dichloride and 1-bromo-4-*n*-butylbenzene (Figure 3.1). The bulky tungsten hydride compound, HWCp^{BIG}(CO)$_3$ (**3-1**), has been prepared via two different synthetic routes (Figure 3.1).

The first synthetic route is based on the previously reported synthesis of HW(CpBz)(CO)$_3$ by Namorado et al.[97] In the first step, HCp^{BIG} was deprotonated using *n*-butyllithium. The solvent was then removed and DMF and tungsten hexacarbonyl were added to the crude LiCp^{BIG} (without isolation) and the mixture was heated at 80 °C for 24 h to produce the intermediate [Cp^{BIG}W(CO)$_3$]$^-$.

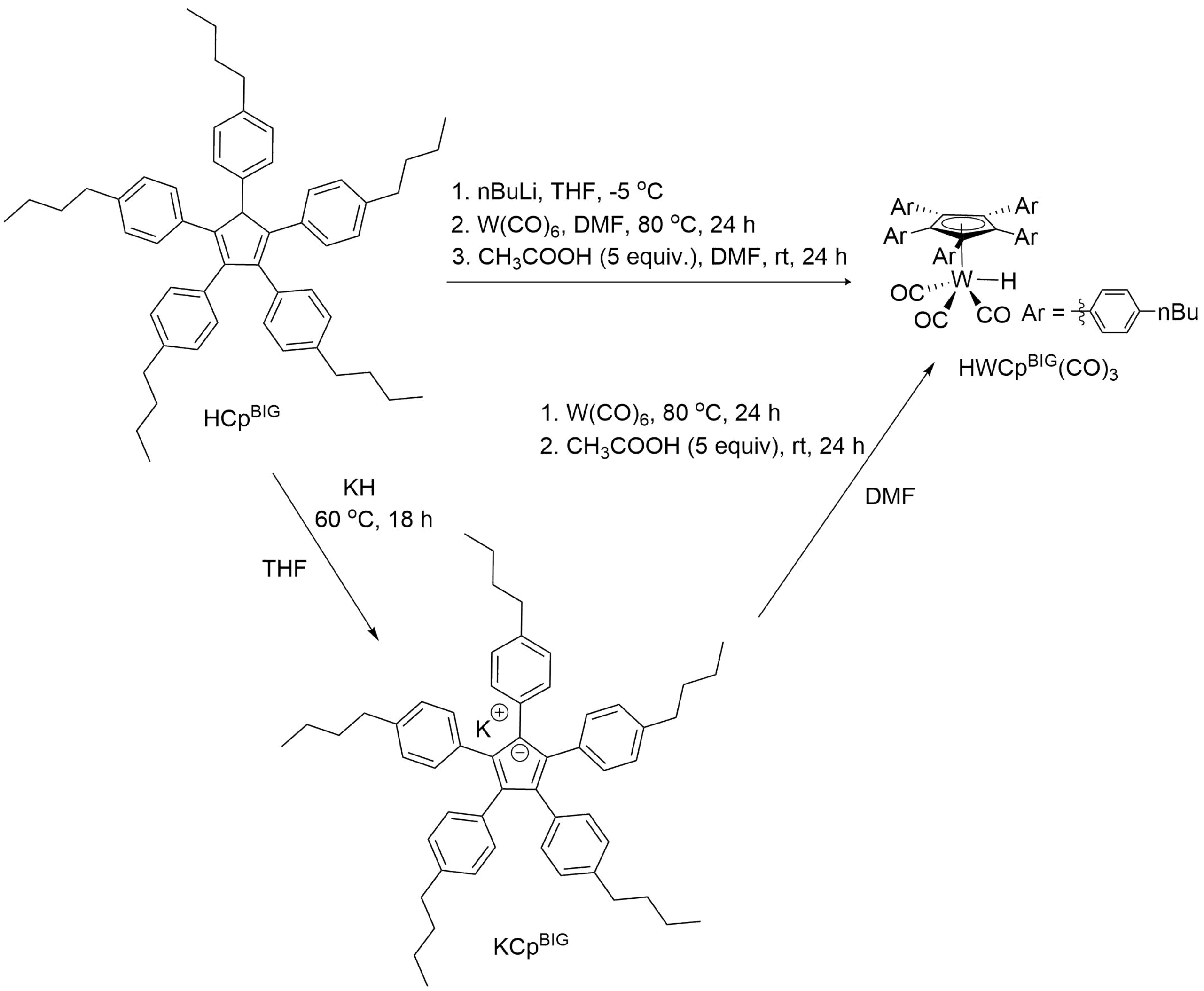

Figure 3.1: Synthesis of $HWCp^{BIG}(CO)_3$, **3-1**, via two different synthetic routes.

Glacial acetic acid was then added, affording the protonated $HWCp^{BIG}(CO)_3$ (**3-1**) (Figure 3.1). The successful synthesis of the hydride compound was confirmed by ^1H NMR spectroscopy and X-ray crystallography. The signal at –5.26 ppm in the ^1H NMR spectrum is in good agreement with other cyclopentadienyl tungsten tricarbonyl hydride compounds (Figure A.5).[97–100] In the ^1H NMR spectrum of **3-1**, coupling between ^1H and ^{183}W is observed, with $^1J_{^1H\text{-}^{183}W} = 23.7$ Hz (Figure A.6). Orange, block crystals were grown from a hexanes solution after several weeks at –30 °C. The molecular structure of **3-1** is shown in Figure 3.2.

Compound **3-1** crystallizes in the monoclinic space group *P* 21/*c* (Figure 3.1 and Table 3.1).

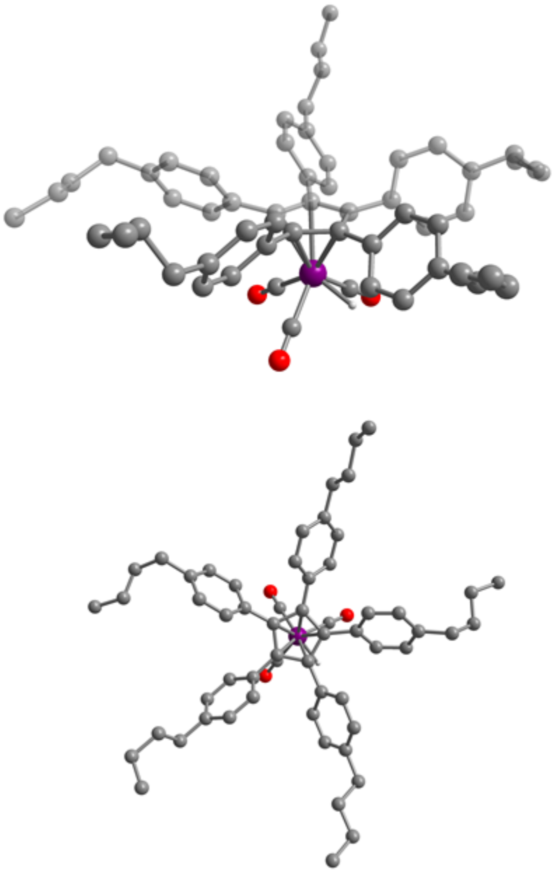

Figure 3.2: Molecular structure of **3-1**. Purple = W, red = O, grey = C, white = H.

The geometry around the W center is best described as a four-legged piano stool with three C–W–C angles of 77.6(2) °(C1–W1–C2), 81.1(3) °(C2–W1–C3), and 104.3(2) °(C1–W1–C3), comparable to other similar compounds (Figure A.7).[97,100,101] The W–CO bond distances are 1.969(5), 1.965(5), and 1.954(6) Å. These are shorter than the W–CO bond lengths found in HW(CpBz)$(CO)_3$ and HWCp$(CO)_3$ by around 0.02 Åand comparable to the W–CO bond lengths found in HW$(CpCO_2H)(CO)_3$.[97,100,101]. The W–Cp(centroid) distance in **3-1** is 2.016 Å, which is longer than in HW(CpBz)$(CO)_3$ (2.00093(11) Å), HWCp$(CO)_3$ (2.005(2) Å, and HW$(CpCO_2H)(CO)_3$ (1.998(9) Å).[97,100,101] The C–O bond distances in **3-1** are 1.157(5), 1.161(6), and 1.161(7) Å(Figure A.7). These distances are longer than the C–O bond distances reported for HWCp$(CO)_3$ and HW(CpBz)$(CO)_3$, from largest to smallest C–O bond distance **3-1** >

$HW(CpBz)(CO)_3$ > $HWCp(CO)_3$.[97,101] The three W–C–O bond angles are near 180 °, with angles of 179.2(4), 178.0(4), and 177.2(6) °, comparable to the W–C–O bond angles found in $HWCp(CO)_3$ (Figure A.7).[101] In the unit cell of **3-1**, the Cp^{BIG} ligands are directed towards one another, with the 4-*n*-butylphenyl cyclopentadienyl groups in a staggered orientation (Figure A.8).

Compound **3-1** can also be prepared via isolated KCp^{BIG}, prepared from the deprotonation of HCp^{BIG} using KH.[95] It was found that KCp^{BIG} could be metalated with tungsten hexacarbonyl in DMF at 80 °C, followed by protonation with glacial acetic acid to afford **3-1**. The product was confirmed by ^1H NMR spectroscopy and X-ray crystallography. Gratifyingly, $Cp^{BIG}W(CO)_3H$, is soluble in hexanes and toluene, which should allow for the reaction with $Ln(N(SiMe_3)_2)_3$ to proceed in non-coordinating solvents.

Compound	**3-1**
Formula	$C_{58}H_{66}O_3W$
T, K	110(2)
Crystal system	monoclinic
Space group	$P\,21/c$
a, Å	14.1058(4)
b, Å	16.9038(4)
c, Å	20.9444(5)
α, °	90
β, °	98.117(2)
γ, °	90
V, Å^3	4944.0(2)
Z	4
Density, ϱ_{calcd} , mg/m^3	1.377
Absorption coefficient, mm^{-1}	2.379
F(000)	2048
Crystal size, mm	0.102 x 0.084 x 0.075
Θ_{min} , Θ_{max} , °	1.964, 22.500
Index ranges	-15 h 15, -18 k 18, -22 l 22
Reflections collected	106087
Independent reflections	6474 [R(int) = 0.1046]
Final R indices [$(I > 2\sigma(I))$]	$R_1 = 0.0284$, $wR_2 = 0.0567$
R indices (all data)	$R_1 = 0.0407$, $wR_2 = 0.0628$

Table 3.1: Crystallographic data for **3-1**.

3.3.2 Synthetic attempts using tris(acetonitrile)tricarbonyltungsten(0)

It has been reported that reactions between tris(acetonitrile)tricarbonyltungsten(0) and cyclopentadiene derivatives may afford the corresponding tungsten hydride complex.[102–104] This synthetic route was explored using HCp^{BIG} as a potential alternative synthetic route to access $HWCp^{BIG}(CO)_3$ (**3-1**). However, attempts to prepare $HWCp^{BIG}(CO)_3$ from the reaction between $(CH_3CN)_3W(CO)_3$ and HCp^{BIG} in thf were unsuccessful. Following the reaction attempts, there was no evidence of hydride formation by ^1H NMR spectroscopy and the ^1H NMR spectrum revealed the presence of the unreacted HCp^{BIG}.

3.3.3 Reactivity with dysprosium tris(trimethylsilylamide)

Attempts were carried out to make the isocarbonyl compound from the reaction between $Dy(N(SiMe_3)_2)_3$ and $Cp^{BIG}W(CO)_3H$. Initial attempts were carried out in the non-coordinating solvent hexanes. While the solution became slightly pale yellow after stirring for 3 h, unit cell determination of crystals obtained from a concentrated cold solution in hexanes revealed the presence of $Dy(N(SiMe_3)_2)_3$ (colorless crystals) and $Cp^{BIG}W(CO)_3H$ starting materials. It is possible that the amine elimination reaction can only proceed in the presence of coordinating solvents. Therefore, the reaction was carried out in hexanes with a few drops of diethyl ether. Upon addition of diethyl ether, the solution became yellow in color. The reaction was also carried out in a 1:1 solution of hexanes/diethyl ether, similarly affording a yellow solution. Removal of the solvent in vacuo led to the isolation of a bright yellow oil. Thus far, X-ray quality crystals have been unable to be obtained from the following conditions: cold concentrated hexanes, cold concentrated hexanes/ether, or cold concentrated thf, all stored at –30 °. Any solid material obtained from the crystallization attempts were very thin plates and did not diffract. Further crystallization attempts are ongoing.

3.4 Conclusion and Outlook

The bulky tungsten hydride compound, $Cp^{BIG}W(CO)_3H$ (**3-1**) could be obtained from reaction of the deprotonated HCp^{BIG} with tungsten hexacarbonyl either in situ with *n*-butyllithium or from isolated KCp^{BIG}. On account of the five *n*-butyl groups, compound **3-1** is soluble in non-coordinating solvents, including hexanes and toluene. Up to this point, the reaction between **3-1** and $Dy(N(SiMe_3)_2)_2$ has failed to yield crystalline material. It is possible that the 15 *n*-butyl groups on the anticipated produced have thus far prevented crystallization. Observations based on color changes suggest that the reaction may only proceed in the presence of coordinating solvents, such as diethyl ether. Future reactions will explore running the reaction in thf. Additionally, salt elimination reactions between the deprotonated anionic species of **3-1**, $[WCp^{BIG}(CO)_3]^-$, and lanthanide(III) salts will be explored.

The isocarbonyl platform presented in Chapter 2 and further explored in this chapter proved to be unsuitable for redox chemistry, as electrochemical oxidation resulted in decomposition. This finding necessitated the need to investigate a new platform for redox switchability applications. The highly reversible redox properties of ferrocene, $FeCp_2$, make it an attractive moiety to include in complexes to impart redox switchability. This inspired the objective of utilizing the highly reversible redox properties of ferrocene-containing ligands to modulate the dynamic magnetic properties of a nearby lanthanide(III) ion highlighted in Chapter 4.

4. TRANSITION METAL REDOX SWITCHES FOR REVERSIBLE "ON/OFF" AND "SLOW/FAST" SINGLE-MOLECULE MAGNET BEHAVIOR

4.1 Introduction

Single-molecule magnets (SMMs) have been attracting considerable attention for potential applications in quantum computing, high-density data storage, and molecular spintronics.[1,2,10,105,106] This fascinating class of compounds is defined by a bistable magnetic ground state and an energy barrier (U_{eff}) to reorientation of their molecular spin.[3–5] The height of this barrier is determined by the magnetic anisotropy of the system and tunable via ligand field considerations. While initial efforts in the field focused on slow magnetic relaxation in multi-nuclear transition metal complexes,[6,107] complementary efforts have led to the development of lanthanide-based single-ion magnets (SIMs).[13,18] Lanthanide ions are attractive candidates for SIM applications, due to their large inherent magnetic single-ion anisotropy, leading to the development of SIMs with record barriers to spin reorientation, U_{eff}.[7,8,29,30,108]

With the ultimate-goal of utilizing SMMs in devices, the development of methodologies that will allow for the control of dynamic magnetic properties reversibly via external stimuli is an essential aspect. Possible stimuli include light, temperature, pressure, chemical, dc field, and electric potential.[35–40] Redox-active SMMs present an exciting route for the reversible modulation of magnetic properties using an electric potential.[41–44,47,49,109,110] Notably, the first reported class of lanthanide ion-based SIMs, the Tb^{3+} phthalocyanine double-decker complexes, are redox-switchable SIMs, undergoing changes in magnetization dynamics and hysteretic behavior upon electrochemical generation of an open shell π-system.[18,22,25]

There have been several reported examples of redox-switchability in multinuclear transition metal and lanthanide based SMMs. In these systems, the oxidation and/or reduction of either

---

Reproduced from Ref. 48, Dickie, C. M.; Laughlin A. L.; Wofford, J. D.; Bhuvanesh, N. S.; Nippe, M. Transition metal redox switches for reversible "on/off" and "slow/fast" single-molecule magnet behaviour in dysprosium and erbium bis-diamidoferrocene complexes. *Chem. Sci.* **2017**, *8*, 8039-8049, with permission from the Royal Society of Chemistry.

a ligand[26,27,44,45] or a metal center[41–43,111] facilitates magnetic exchange interactions; turning the SMM properties "on" or "off". In addition to these "on"/"off" examples, in some cases adding and/or removing an electron has been shown to improve SMM properties.[47,49,109,110]

Aside from the Tb^{3+} and Dy^{3+} double-decker lanthanide(III) phthalocyanine complexes,[18,22,25] to our knowledge there is only one previously reported example of proven redox controllable dynamic magnetic properties in a mononuclear lanthanide(III)-based SIM. In that example an intramolecularly attached $Ru^{2+/3+}$ redox switch was utilized to modify the magnetic relaxation dynamics of a Dy^{3+}-based SIM.[49] The oxidation of Ru^{2+} to Ru^{3+} was found to enhance slow magnetic relaxation, either through perturbations of the ligand field or the addition of another spin-carrier to the system. However, this interesting system suffered from limited thermal stability at room temperature.

The reversible redox properties of ferrocene, $FeCp_2$, make it an attractive moiety to include in complexes for redox switchability applications.[112] This inspired us to evaluate the possibility of utilizing the redox properties of ferrocene-containing ligands to modulate the dynamic magnetic properties of a nearby lanthanide(III) ion. Previously, Diaconescu et al. reported a homoleptic uranium(IV) compound stabilized by two bidentate diamidoferrocene ligands.[113,114] Notably, one-electron oxidation of the complex resulted in a mixed-valent species, indicating strong uranium-mediated electronic communication between the two iron sites. Interestingly, there have been no similar studies reported with lanthanide(III) bis-diamidoferrocene compounds.

Herein, we present the first class of Ln^{3+} ion-based redox switchable SMMs using the redox chemistry of ferrocene/ferrocenium in the ligand scaffold.[115–120] We show how the reversible one-electron oxidation of Fe^{2+} to Fe^{3+} in Dy^{3+} (oblate electron density) and Er^{3+} (prolate electron density) bis(1,1’-diamidoferrocene) compounds modulates dynamic magnetic properties. Depending on the experimental conditions, these materials can exhibit switchability of their slow magnetic relaxation either between "on" and "off" or between "slow" and "fast". Remarkably, this is the first example of redox switchable SMM properties observed in an Er^{3+} compound. Additionally, this is the first magnetic investigation of homoleptic, four-coordinate Dy^{3+} and Er^{3+} complexes. This set of compounds has been characterized using X-ray crystallography, dc/ac magnetometry, ^{57}Fe Mössbauer spectroscopy, UV-vis-NIR spectroscopy, and cyclic voltammetry.

Notably, this is the first example of using the redox chemistry of a transition metal to alter the magnetization dynamics of a lanthanide ion, while maintaining thermal stability of all redox partners. This molecular level study is intended to provide design guidelines for future switchable solid materials.

4.2 Experimental

4.2.1 General considerations

All reactions and manipulations were carried out under anaerobic and anhydrous conditions in an argon filled glovebox (Vigor). All syntheses and manipulations were carried out using disposable plastic spatulas. Tetrahydrofuran (thf), hexanes, toluene and diethyl ether were dried and deoxygenated using a solvent purification system (JC Meyer Solvent Systems) and were stored over molecular sieves in an argon-filled glovebox. Anhydrous dysprosium(III) iodide and iodine were purchased from Alfa Aesar. Eicosane was purchased from Acros Organics. Sublimed anhydrous erbium(III) iodide was generously donated by Prof. Tim Hughbanks' group (Texas A& M). fc[HNSi(t-Bu)Me_2]$_2$ was prepared as previously described.[113] Benzyl potassium was prepared via the deprotonation of toluene by *n*-BuLi/KO*t*-Bu as described previously.[121] UV-vis-NIR spectra were recorded using a Shimadzu SolidSpec-3700 spectrophotometer over a range of 300 nm to 2000 nm and matched screw-capped quartz cuvettes. Elemental analyses were carried out by Midwest Microlab (Indianapolis, IN).

4.2.2 Experimental procedures

Preparation of [K_2(OEt_2)]fc[NSi(*t*-Bu)Me_2]$_2$. Performed via a modification of a previous procedure.[113] fc[HNSi(*t*-Bu)Me_2]$_2$ (314.9 mg, 0.7083 mmol) was dissolved in diethyl ether (8 mL) and cooled in a freezer (–30 °C) for 30 min. Solid benzyl potassium (186.2 mg, 1.430 mmol) was added to the cold stirring solution of fc[HNSi(*t*-Bu)Me_2]$_2$ in diethyl ether. The reaction mixture was allowed to warm up to rt and stirred for 2 h. All solvent was removed in vacuo. The remaining orange solid was washed with hexanes and collected on a medium frit. Solid was dried in vacuo and used without further purification (369.4 mg, 88 %).

Preparation of K(thf)$_5$[Dy(fc[NSi(*t*-Bu)Me$_2$]$_2$)$_2$] [4-1]$^-$. [K$_2$(OEt$_2$)]fc[NSi(*t*-Bu)Me$_2$]$_2$ (127 mg, 0.213 mmol) was dissolved in 3 mL of tetrahydrofuran and cooled in the freezer (–30 °C) for 30 min. To a separate vial, dysprosium(III) iodide (58.0 mg, 0.107 mmol) and thf (3 mL) were added and the solution was cooled in the freezer (–30 °C) for 30 min. The [K$_2$(OEt$_2$)]fc[NSi(*t*-Bu)Me$_2$]$_2$ solution was added drop-wise to the stirring DyI_3 suspension while cold. The reaction mixture was stirred for 1.5 h at rt. All volatiles were removed in vacuo and the solid was washed with hexanes and dried. A minimal amount of thf was added and the solution was filtered through Celite. Removal of the thf in vacuo yielded a yellow-orange solid. Air sensitive yellow-orange plate crystals were obtained from a concentrated thf solution layered with hexanes at –30 °C for 24 h (117 mg, 76 %). Unit cell parameters (110 K): a = 16.500(2) Å, b = 19.510(3) Å, c = 12.286(2) Å, α = 90 °, β = 90 °, γ = 90 °, V = 3955 Å^3. Anal. calcd for $C_{64}H_{116}N_4DyFe_2KSi_4O_5$ (**[4-1]**$^-$): C, 53.11; H, 8.08; N, 3.87. Found: C, 52.62; H, 7.77; N, 3.59.

Preparation of K(thf)$_5$[Er(fc[NSi(*t*-Bu)Me$_2$]$_2$)$_2$] [4-2]$^-$. Same procedure as in the synthesis of **[4-1]**$^-$, with [K$_2$(OEt$_2$)]fc[NSi(*t*-Bu)Me$_2$]$_2$ (135 mg, 0.227 mmol), erbium(III) iodide (62.2 mg, 0.113 mmol) and 8 mL of tetrahydrofuran. Single crystals were obtained from a concentrated thf solution layered with hexanes in the freezer (–30 °C) for 24 h yielded 117 mg (71 %) of very air-sensitive yellow-orange plate crystals. Unit cell parameters (110 K): a = 16.443(3) Å, b = 18.088(4) Å, c = 12.828(3) Å, α = 90 °, β = 90 °, γ = 90 °, V = 3815 Å^3. Anal. calcd for $C_{56}H_{100}N_4ErFe_2KSi_4O_3$ (**[4-2]**$^-$ – 2 thf): C, 51.4; H, 7.71; N, 4.28. Found: C, 51.32; H, 7.50; N, 3.86.

Preparation of Dy(fc[NSi(*t*-Bu)Me$_2$]$_2$)$_2$ (4-1). K(thf)$_5$[Dy(fc[NSi(*t*-Bu)Me$_2$]$_2$)$_2$] (75.6 mg, 0.0522 mmol) and diethyl ether (5 mL) were added to a vial and placed in the freezer (–30 °C) for 30 min. To a separate vial, iodine (6.8 mg, 0.027 mmol) and diethyl ether (5 mL) were added and placed in the freezer (–30 °C) for 30 min. The iodine solution was added to the stirring K(thf)$_5$[Dy(fc[NSi(*t*-Bu)Me$_2$]$_2$)$_2$] solution while cold, resulting in immediate color change to dark red. The reaction mixture was stirred for 40 min at rt. All volatiles were removed in vacuo. The resulting dark solid was extracted into hexanes and filtered through Celite. The volatiles were removed in vacuo, yielding a dark purple solid. X-ray quality dark red-purple block crystals were grown from a concentrated hexanes solution after 24 h at –30 °C (27.7 mg, 51 %). Unit cell parameters (110 K): *Pbca*, $a = 20.025(4)$ Å, $b = 19.663(4)$ Å, $c = 24.499(5)$ Å, $\alpha = 90$ °, $\beta = 90$ °, $\gamma = 90$ °, $V = 9646$ Å^3. Anal. calcd for $C_{44}H_{76}N_4DyFe_2Si_4$ (**4-1**): C, 50.44; H, 7.31; N, 5.35 %. Found: C, 50.17; H, 6.88; N, 5.30 %.

Preparation of Er(fc[NSi(*t*-Bu)Me$_2$]$_2$)$_2$ (4-2). The same procedure as for **4-1** was followed using K(thf)$_5$[Er(fc[NSi(*t*-Bu)Me$_2$]$_2$)$_2$] (101.8 mg, 0.07011 mmol), iodine (8.5 mg, 0.034 mmol) and diethyl ether (10 ml). X-ray quality air sensitive dark red-orange block crystals were grown from a concentrated hexanes solution after 24 h at –30 °C (39.6 mg, 55 %). Unit cell parameters (110 K): *Pbca*, $a = 19.794(2)$ Å, $b = 19.822(2)$ Å, $c = 24.603(2)$ Å, $\alpha = 90$ °, $\beta = 90$ °, $\gamma = 90$ °, $V = 9653$ Å^3: Anal. calcd for $C_{44}H_{76}N_4ErFe_2Si_4$ (**4-2**): C, 50.22; H, 7.28; N, 5.32 %. Found: C, 49.99; H, 7.24; N, 5.20 %.

4.2.3 X-ray structure determination

Crystals suitable for X-ray diffraction were mounted on a nylon loop and placed in a cold N_2 stream (Oxford) maintained at 110 K. A BRUKER APEX 2 Duo X-ray (three-circle) diffractometer was used for crystal screening, unit cell determination, and data collection. The X-ray radiation employed was generated from a Mo sealed X-ray tube ($K_\alpha = 0.70173$ Å, with a potential of 40 kV and a current of 40 mA). Bruker AXS APEX II software was used for data collection and reduction. Absorption corrections were applied using the program SADABS.[82] A solution was obtained using XT/XS in APEX2.[81,83–85] Hydrogen atoms were placed in idealized positions and were set riding on the respective parent atoms. All non-hydrogen atoms were refined with anisotropic thermal parameters. Absence of additional symmetry and voids were confirmed using PLATON (ADDSYM).[96,122] The structure was refined (weighted least squares refinement on F^2) to convergence.[85,86] For **4-1**, the Si4(C39–C44) group was found disordered between two positions and was modeled successfully with an occupancy ratio of 0.55:0.45.

4.2.4 Magnetic measurements

A representative procedure for the preparation of the samples for magnetic characterization is as follows. Crystalline sample was crushed up into a fine powder before loading into a high purity 7 mm NMR tube (Norell). A layer of eicosane was added to the tube, covering the sample. The tube was then flame sealed under vacuum. To restrain the sample, the sealed tube was placed in a water bath (39 °C) until the eicosane melted and was evenly distributed throughout the sample. The sample was loaded into a straw affixed to the end of the sample rod. Magnetic measurements were carried out using a Quantum Design MPMS 3 SQUID magnetometer (TAMU Vice President of Research). Dc susceptibility measurements were carried out over a temperature range of 1.8 to 300 K. Ac measurements were carried out using a 2 Oe switching field. Data was corrected for diamagnetic contributions from the straw, sample tube, eicosane, and core diamagnetism using Pascal's constants.[87] Cole-Cole plots were fitted to the generalized Debye equation using least-squares regression (Equations 1.9 and 1.10). Arrhenius plots and τ vs. H plots were fit using least squares regression.

4.2.5 ^{57}Fe Mössbauer spectroscopy

Crystalline samples were loaded into a Teflon cup inside a glovebox and covered with a layer of paraffin oil. The cup was brought out of the glovebox and immediately stored frozen in liquid nitrogen until measured. Mössbauer spectra were collected on a model MS4 WRC low-field, variable temperature spectrometer (See Co., Edina, MN). Zero magnetic field spectra were obtained by removing the 500 G magnets from the exterior of the instrument. Temperatures were varied using a temperature controller on the heating coil on the sample holder. The instrument was calibrated using an α-Fe foil at room temperature. Obtained spectra were fitted using WMOSS software (See Co.).

4.2.6 Electrochemistry

Cyclic voltammograms were measured in an argon filled glovebox (Vigor). Data were collected using a Gamry Instruments Reference 600 potentiostat with Gamry Framework software. Glassy carbon working electrode, 1 mm diameter Pt wire counter electrode, and silver-wire pseudo-reference electrode were used. Scan rates of 100 mV s^{-1} to 250 mV s^{-1} were used. Ferrocene was added at the end of each data collection and the ferrocene/ferrocenium couple was used as an internal standard.

4.3 Results and Discussion

4.3.1 Synthesis and structural characterization

The reaction between LnI_3 (Ln = Dy or Er) and two equivalents of $[K_2(OEt_2)]fc[NSi(\textit{t}\text{-}Bu)Me_2]_2$ in thf yielded the anionic lanthanide(III) species $K(thf)_5[Ln(fc[NSi(\textit{t}\text{-}Bu)Me_2]_2)_2]$ (Dy = **[4-1]**$^-$, Er = **[4-2]**$^-$) (Figure 4.1). Yellow plate crystals were grown from a concentrated thf solution layered with hexanes at –30 °C over 24 hours. One-electron oxidation of $K(thf)_5[Ln(fc[NSi(\textit{t}\text{-}Bu)Me_2]_2)_2]$ with half an equivalent of iodine afforded the neutral mixed valent Fe^{3+}/Fe^{2+} compounds $Dy(fc[NSi(\textit{t}\text{-}Bu)Me_2]_2)_2$ (**4-1**) and $Er(fc[NSi(\textit{t}\text{-}Bu)Me_2]_2)_2$ (**4-2**) (Figure 4.2). Dark purple (**4-1**) and dark red-brown (**4-2**) block crystals were grown from concentrated hexanes solutions at –30 °C over 24 h.

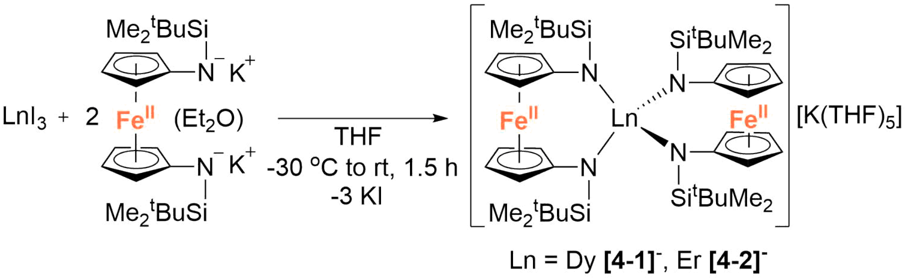

Figure 4.1: Synthesis of $K(thf)_5[Ln(fc(NSi(\textit{t}\text{-}Bu)Me_2)_2)_2]$ (Ln = Dy **[4-1]**$^-$, Er **[4-2]**$^-$).

Although **[4-1]**$^-$ and **[4-2]**$^-$ readily crystallize under the experimental conditions, single crystal X-ray diffraction data indicated severe disorder. However, the connectivity of **[4-1]**$^-$ and **[4-2]**$^-$ could be established and equivalent distances between the Ln^{3+} ion and the two Fe^{2+} ions were found. The neutral, mixed-valent compounds **4-1** and **4-2** are isostructural to each other and crys-

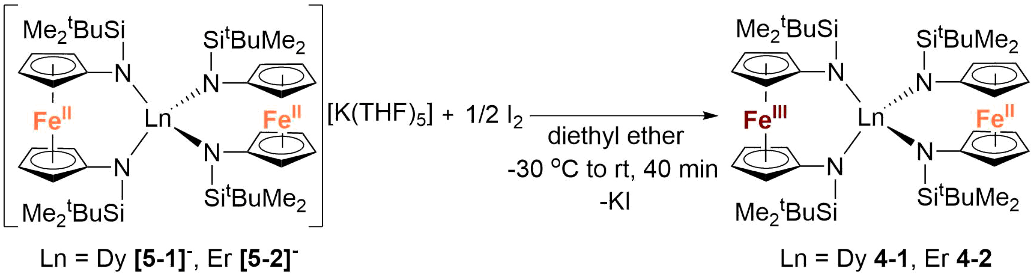

Figure 4.2: Synthesis of Ln(fc[NSi(*t*-Bu)Me$_2$]$_2$)$_2$ (Ln = Dy **4-1**, Er **4-2**).

tallize in the orthorhombic space group *Pbca* (Figure 4.3, Tables B.1 and B.2). The central Ln^{3+} ion is four-coordinate, ligated through the nitrogen atoms of the amide moieties of two bidentate diamidoferrocene ligands. Notably, the one-electron oxidized complexes feature lower symmetry around the Ln^{3+} ion. The coordination geometry around the Ln^{3+} ion is distorted tetrahedral, with N–Ln–N angles varying from 100.3(2) ° to 131.9(2) ° and 102.2(6) ° to 126.7(6) ° for **4-1** and **4-2**, respectively. The differences in Fe–C bond lengths of the two crystallographically independent Fe sites indicate valence localization in the solid state at this temperature (110 K). The two Ln···Fe distances in **4-1** and **4-2** are inequivalent, with long Ln···Fe distances of 3.792(2) Å and 3.819(5) Å and short Ln···Fe distances of 3.368(2) Å and 3.498(4) Å (Figure B.3). The Ln–N distances in **4-1** and **4-2** are also inequivalent with longer Ln–N distances (2.370(4), 2.338(4) Å and 2.29(1), 2.27(2) Å) and shorter distances (2.262(4), 2.252(4) Å and 2.22(2), 2.21(2) Å). In the solid state, the closest Fe···Fe distances are intermolecular with separations of 6.464(2) Å and 6.478(5) Å, while the intramolecular Fe···Fe distances are 7.098(2) Å and 7.267(5) Å for **4-1** and **4-2**, respectively (Figures 4.4 and B.4).

4.3.2 Static-field magnetic properties

To investigate static magnetic properties, direct current (dc) magnetic measurements were carried out using crushed polycrystalline samples under an applied field of 1000 Oe from 300 K to 2 K (Figure 4.5). The room temperature $\chi_M T$ value of 14.22 cm^3 K mol^{-1} for **[4-1]$^-$** is in agreement with the expected value of 14.17 cm^3 K mol^{-1} for one isolated Dy^{3+} ion ($^6H_{15/2}$, $S = 5/2$, $L = 5$, $g = 4/3$). Upon cooling, the $\chi_M T$ decreases gradually, then more rapidly below 130 K to reach a

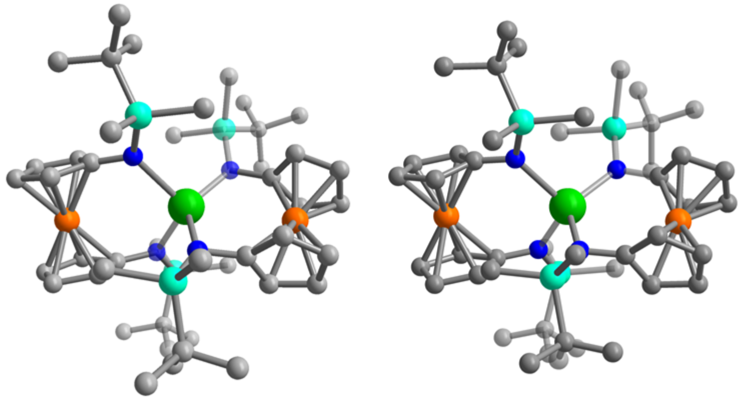

4-1 **4-2**

Figure 4.3: Molecular structure of Dy(fc[NSi(*t*-Bu)Me_2]$_2$)$_2$ (**4-1**) (left) and Er(fc[NSi(*t*-Bu)Me_2]$_2$)$_2$ (**4-2**) (right). Green = Ln, orange = Fe, cyan = Si, blue = N, grey = C. Hydrogen atoms omitted for clarity.

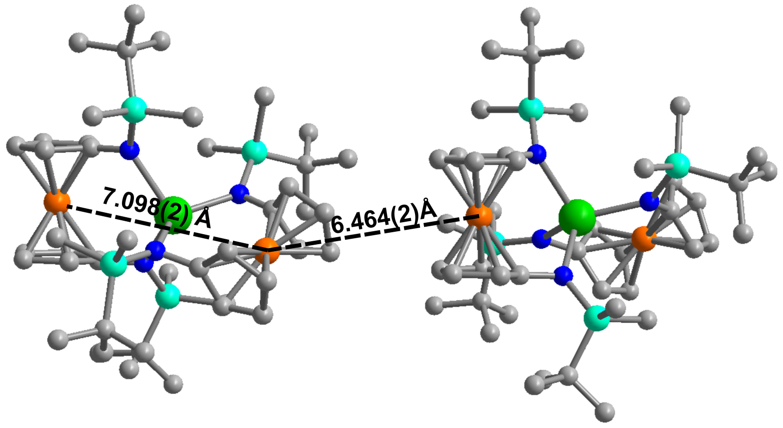

Figure 4.4: Solid state intra- and intermolecular Fe···Fe distances in **4-1** at 110 K. Hydrogen atoms omitted for clarity.

minimum of 12.55 cm^3 K mol^{-1} at 2 K. This decrease is mainly attributed to the thermal depopulation of excited states. After one-electron oxidation of **[4-1]**$^-$ to form **4-1**, an increase in the room temperature $\chi_M T$ value to 14.36 cm^3 K mol^{-1} is observed. This increase is in accordance with the presence of a single Dy^{3+} ion and an additional non-interacting $S = 1/2$ site (low-spin Fe^{3+}, 0.375 cm^3 K mol^{-1} expected for $g = 2$, but actual g-value likely different). Upon decreasing the temperature, the $\chi_M T$ value of **4-1** decreases more rapidly than **[4-1]**$^-$ below 60 K, reaching a minimum of

10.13 cm^3 K mol^{-1} at 2 K. The more rapid decrease could be indicative of thermal depopulation of Stark sublevels or the presence of intra- and/or inter-molecular antiferromagnetic interactions.[92]

For the Er^{3+} analogues, the room temperature $\chi_M T$ value for **[4-2]$^-$** is 10.82 cm^3 K mol^{-1}. This value is only slightly lower than the expected value of 11.28 cm^3 K mol^{-1} for a single isolated Er^{3+} ion ($^4I_{15/2}$, $S = 3/2$, $L = 6$, $g = 6/5$). After one-electron oxidation to **4-2**, the room temperature $\chi_M T$ value increases to 11.43 cm^3 K mol^{-1}, corresponding to one Er^{3+} ion and one non-interacting Fe^{3+} ion. As observed in the analogous Dy^{3+} compounds, there is a more rapid decrease in the $\chi_M T$ of the oxidized mixed-valent compound **4-2** at low temperatures.

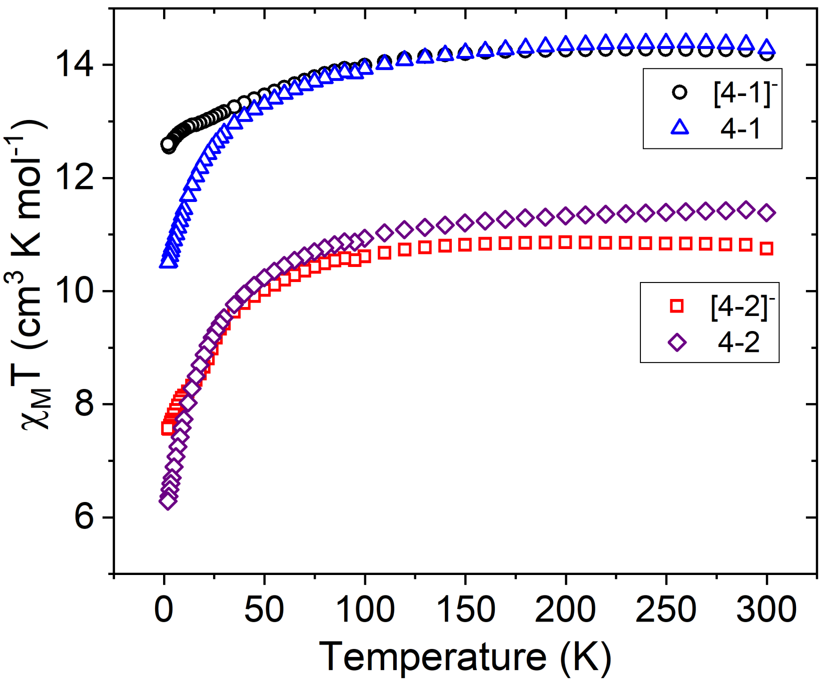

Figure 4.5: Temperature dependence of the molar magnetic susceptibility times temperature product ($\chi_M T$) for compounds **[4-1]$^-$** (black circles), **4-1** (blue triangles), **[4-2]$^-$** (red squares), and **4-2** (purple diamonds) under a 1000 Oe dc field.

The field dependence of the magnetization (M) was measured for each compound with fields up to 70 kOe (7 T) over a temperature range of 2–8 K (Figure B.5–B.12). In the Dy^{3+} compound **[4-1]$^-$**

at 2 K, the magnetization increases sharply until 1 T, followed by a more gradual increase, reaching a saturated moment of 5.34 μ_B at 7 T (Figure B.5). This is near to the expected value of 5.23 μ_B for one uncorrelated Dy^{3+} ion in the presence of ligand field effects.[91] The non-superposition in the temperature dependence (*M* vs. *H/T*) suggests the presence of significant magnetic anisotropy in **[4-1]**$^-$ (Figure B.6). In **4-1** at 2 K, the magnetization increases sharply until 1 T and then gradually increases, reaching an unsaturated moment of 5.07 μ_B at 7 T (Figure B.7). The lack of obvious saturation along with the non-superposition in the *M* vs. *H/T* data suggests the presence of low-lying excited states and/or significant anisotropy (Figure B.8).[92] The Er^{3+} compounds **[4-2]**$^-$ and **4-2** reach unsaturated moments at 7 T of 4.97 μ_B and 4.86 μ_B, respectively (Figures B.9 and B.11). These unsaturated moments are in accordance with previously characterized mononuclear Er^{3+} complexes.[123–125] The lack of clear saturation in the *M* vs. *H* data along with the non-superposition of *M* vs. *H/T* (Figures B.10 and B.12), implies low-lying excited states and/or magnetic anisotropy.

4.3.3 Dynamic magnetic properties and redox switchability

Dynamic magnetic properties were investigated using alternating-current (ac) measurements. In **[4-1]**$^-$, a signal in the out-of-phase component (χ") of the ac susceptibility was observed under zero applied dc field, indicative of slow magnetic relaxation (Figure 4.6b). Cole-Cole (semi-circle) plots of the in-phase (χ') vs out-of-phase (χ") components of the ac susceptibility were fit to a generalized Debye model to extract relaxation times, τ (Figure 4.6c).[107,126] The natural logarithm of τ was plotted vs the inverse temperature to construct the corresponding Arrhenius plot (Figure 4.6d). The large temperature independent region observed at low temperatures in the χ" and Arrhenius plots of **[4-1]**$^-$ implies prevalent quantum tunnelling of the magnetization (QTM), a relaxation process that proceeds without the input of thermal energy.

The Arrhenius plot of **[4-1]**$^-$ (Figure 4.6d) was fit using least squares regression to a model that accounted for multiple relaxation processes, including, QTM, Raman, and Orbach processes (Equation 4.6).

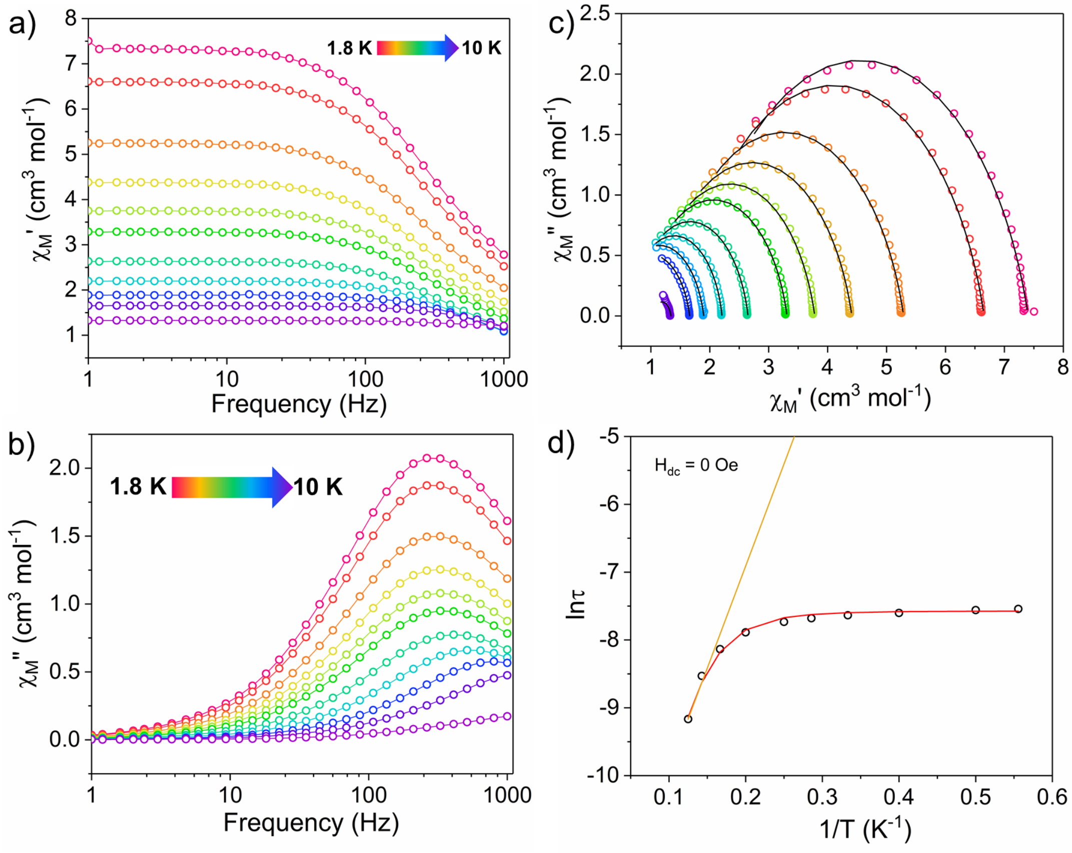

Figure 4.6: Ac susceptibility measurements for **[4-1]**$^-$ under zero dc field. Frequency dependence of the (a) in-phase, χ', and (b) out-of-phase, χ'', components of the ac susceptibility. (c) Cole-Cole plots, open circles are experimental data and black lines are fits to the generalized Debye equation. (d) Arrhenius plot, open circles are experimental data points. The orange line represents fit of the linear region, using the three highest temperature points, to the equation using the expression $\tau^{-1} = \tau_0{}^{-1}\exp(-U_{\text{eff}}/k_BT)$; with U_{eff} = 20.9 cm^{-1} and τ_0 = 2.43 x 10^{-6} s. The red curve represents the fit to Equation 4.1, with U_{eff} = 27.3(8) cm^{-1} and τ_0 = 1.63(2) x 10^{-6} s.

$$\tau^{-1} = \tau_{\text{QTM}}^{-1} + CT^{n_2} + \tau_0^{-1}\exp\left(\frac{-U_{\text{eff}}}{k_BT}\right) \tag{4.1}$$

The parameters τ_{QTM}, C (Raman coefficient), τ_0 (pre-exponential factor), and U_{eff} (thermal barrier for Orbach relaxation) were treated as free-fit parameters. For Kramers ions, parameter n_2 in the Raman pathway is expected to be 9; although allowing n_2 to be a free-fit parameter resulted in a value of n_2 = 5. A value lower than 9 may be expected in systems with low-lying excited states if optical phonons are taken into consideration.[12,127] Only the Orbach process, the "over the barrier" pathway, appears linear on the plot of ln τ vs T^{-1}.

Due to the predominance of quantum tunnelling of magnetization (QTM) at low temperatures, few temperature dependent points were obtained. However, a barrier height, $U_{\mathrm{eff}} = 27.3(8)\ \mathrm{cm}^{-1}$ ($\tau_0 = 1.63(2) \times 10^{-6}$ s), for the thermally activated Orbach process was calculated for **[4-1]⁻** under $H_{\mathrm{dc}} = 0$ Oe using equation 4.1. All parameters of the fit are listed in Figure B.13.

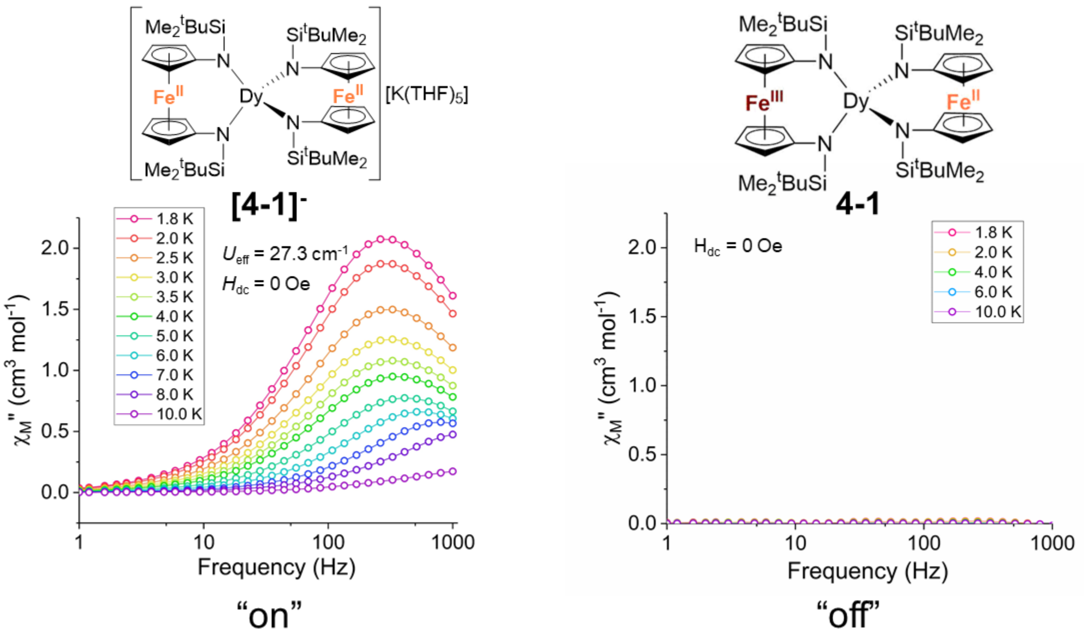

Figure 4.7: The one-electron oxidation of **[4-1]⁻** to **4-1** with half an equivalent of iodine results in redox switching of slow relaxation between "on" (**[4-1]⁻**, left) and "off" (**4-1**, right) modes under zero applied dc field. Lines are a guide for the eye.

Notably, the one-electron oxidation product **4-1** shows no evidence of slow relaxation under zero applied dc field at ac frequencies up to 1000 Hz (Figures B.15 and B.16). This is likely due to faster QTM in the oxidized species **4-1** than in the non-oxidized species **[4-1]⁻**. This could be attributed to both the lower symmetry around the Dy^{3+} ion in the mixed-valent compound and/or the introduction of an $S = 1/2$ site nearby the magnetically anisotropic Dy^{3+} ion. In detail, changes in ligand field and dipole-dipole interactions have been shown to facilitate mixing of magnetic states through which QTM can be introduced. Structural changes (and potentially packing effects) likely make the largest contribution to the change in magnetization dynamics. The appreciable loss of symmetry upon oxidation and change in ligand field would undoubtedly influence the orientation of the magnetic anisotropy axis and therefore the magnetization dynamics. In the absence of applied dc fields, the changes in magnetization dynamics upon reversible one-electron oxidation of **[4-1]**$^-$ to **4-1** can be thought of as "on"/"off" switching of the slow magnetic relaxation (frequencies up to 1000 Hz) (Figure 4.7).

For both Er^{3+} compounds, **[4-2]**$^-$ and **4-2**, no signal was observed in the out-of-phase component (χ") of the ac susceptibility under zero dc field at ac frequencies up to 1000 Hz (Figures B.18 and B.20); likely a result of efficient ground state QTM processes for these species.

QTM between orthogonal Kramers ground states is typically caused by a perturbation Hamiltonian that allows for mixing of energetically close lying states. Examples of such perturbations include the presence of transverse anisotropy and dipole-dipole interactions between paramagnetic metal centers.[9] To mitigate QTM in this series of compounds, various dc fields were applied during ac susceptibility measurements. Application of the static dc field lifts the degeneracy of the Kramers states, thereby reducing QTM. In the presence of a dc field, compounds **[4-1]**$^-$, **4-1**, and **[4-2]**$^-$ show clear evidence of slow relaxation of the magnetization, with a signal in the out-of-phase component (χ") observed within the ac frequency range of 1 to 1000 Hz (Figures B.22, B.26, and B.30). Notably, the oxidized mixed-valent Er^{3+} compound **4-2** displayed no evidence of slow relaxation at any investigated temperature or field (Figure B.34).

In the variable field ac measurements for **[4-1]**$^-$ at 5 K, a transition from a faster relaxation process to a slower relaxation process is observed around 300 Oe (Figure B.22). An optimal static field of 1000 Oe was determined from the maximum (slowest relaxation) in the plot of the field dependence of τ (Figures 4.9; inset and B.24). Therefore, variable temperature ac susceptibility measurements for **[4-1]**$^-$ were collected with a dc field of 1000 Oe (Figure 4.8a). At 1000 Oe, the maxima of the out-of-phase signals (χ") are shifted to lower frequencies relative to the zero field

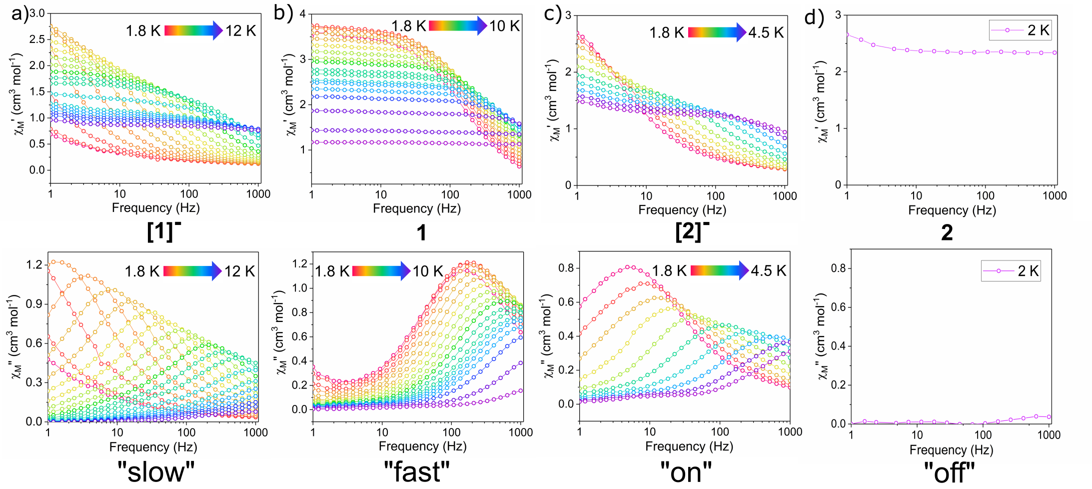

Figure 4.8: Frequency dependences of the in-phase, χ', (top) and out-of-phase, χ", (bottom) components of the ac susceptibility for (a) **[4-1]⁻** with a 1000 Oe dc field (b) **4-1** with a 1000 Oe dc field (c) **[4-2]⁻** with a 500 Oe dc field (d) **4-2** with a 500 Oe dc field. Lines are guide for the eye.

measurements, as the reduction of QTM results in slower magnetic relaxation. Furthermore, with the application of the 1000 Oe dc field, the Arrhenius plot displays temperature dependence over the entire temperature regime (Figure 4.9).

Arrhenius plots (ln τ vs T^{-1}) for the applied field measurements were fit using least squares regression to a model that accounted for multiple relaxation pathways, including direct, QTM, Raman, and Orbach (Equation 4.2).

$$\tau^{-1} = AH^{n_1}T + \tau_{\mathrm{QTM}}^{-1} + CT^{n_2} + \tau_0^{-1}\mathrm{exp}\left(\frac{-U_{\mathrm{eff}}}{k_{\mathrm{B}}T}\right) \tag{4.2}$$

$$\tau^{-1} = AH^{n_1}T + \frac{B_1}{1 + B_2H^2} + D \tag{4.3}$$

To avoid over-parameterization during fitting, the field dependence of τ was initially fit for the two field dependent processes, direct and QTM, to obtain the direct relaxation parameter A and the QTM parameters B_1 and B_2, according to equation 4.3.[127] Typically, n_1 = 4 for Kramers ions in the absence of hyperfine interactions.[12] Parameter D was added to account for the field

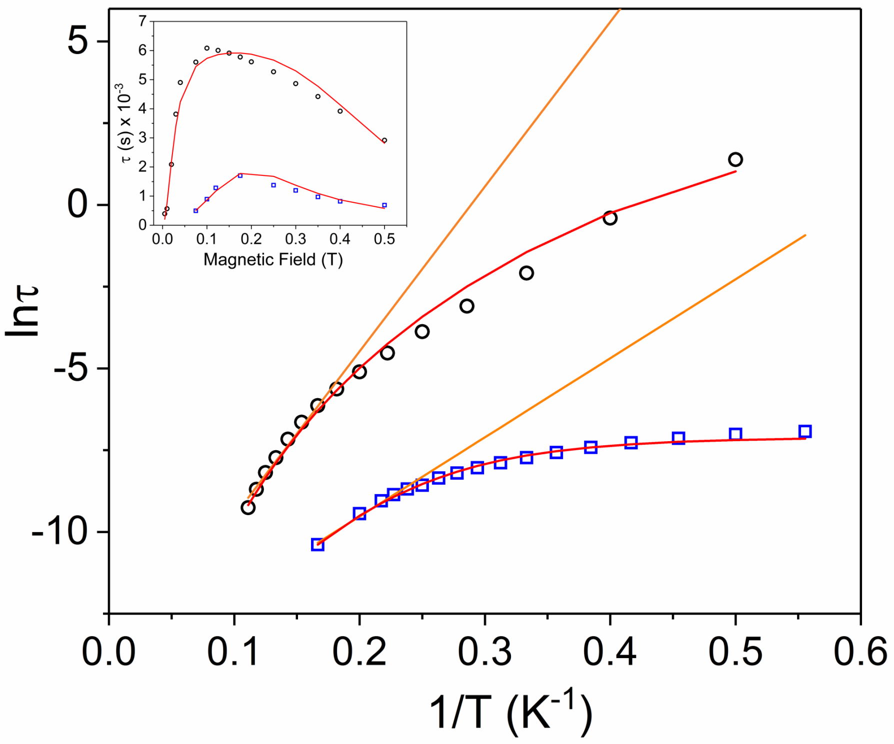

Figure 4.9: Arrhenius plots for Dy^{3+} complexes **[4-1]**⁻ (black circles) and **4-1** (blue squares) under 1000 Oe applied dc field. The orange lines represent fits of the linear regions to the expression $\tau^{-1} = \tau_0^{-1}\exp(-U_{eff}/k_BT)$ (Orbach only); resulting in U_{eff} values of 35.0 cm^{-1} (τ_0 = 4.79 x 10^{-7} s) for **[4-1]**⁻ and 16.8 cm^{-1} (τ_0 = 5.79 x 10^{-7} s) for **4-1**. Red lines represent fits of the entire temperature region to Equation 4.2, giving U_{eff} values of 46(2) cm^{-1} (τ_0 = 7.3(7) x 10^{-7} s) for **[4-1]**⁻ and 27.2(5) cm^{-1} (τ_0 = 5.0(4) x 10^{-7} s) for **4-1**. Inset: field dependence of the relaxation times (τ) for **[4-1]**⁻ (black circles) and **4-1** (blue squares), red lines are fits to Equation 4.3. See Figure B.13 for all fitting parameters.

independent contributions from Raman and Orbach relaxation processes.[127] Parameters A, B_1, B_2, and D were treated as free fit parameters. All fitting parameters are listed in Figures B.13 and B.14. For **[4-1]**⁻ at 5 K, the very gradual decrease in τ values at fields above 1000 Oe suggests minimal contributions of single phonon direction relaxation mechanisms (Figures 4.9; inset and B.24).[127] At fields below 1000 Oe, the increase in τ with increasing field was modeled successfully by the QTM term.

The parameters obtained from Equation 4.3 were held fixed while fitting the temperature dependent Arrhenius plots (ln τ vs T^{-1}), according to Equation 4.2. For **[4-1]**$^-$, the temperature dependence of τ was fit to direct, Raman, and Orbach relaxation processes (Figure 4.9). Allowing the Raman exponent n_2 to be a free fit parameter resulted in a value of n_2 = 7. For Kramers ions, an n_2 value of 9 is expected; however, lower n_2 values may be anticipated if optical phonons are taken into consideration.[127] A barrier height of U_{eff} = 46(2) cm^{-1} (τ_0 = 7.3(7) x 10^{-7} s) was obtained; 18.7 cm^{-1} larger than the barrier calculated under zero dc field.

Variable field ac measurements for **4-1** at 2 K are displayed in Figures B.25 –B.27 . The field dependence of τ was fit for both direct and QTM processes according to Equation 4.3 (Figures 4.9 (inset) and B.28). A value of n_1 = 2 was used to obtain a fit, corresponding to a Kramers ion in a hyperfine field.[12,128] The maximum τ value (slowest relaxation) occurs at a field of 1750 Oe at 2 K. However, to maintain consistency with the ac measurements for **[4-1]**$^-$, variable temperature ac measurements for **4-1** were carried out using a 1000 Oe dc field (Figure 4.8b). The maxima of χ'' for the mixed-valent compound **4-1** are shifted to higher frequencies relative to **[4-1]**$^-$, implying faster magnetic relaxation for a given temperature of the mixed-valent compound **4-1** (Figure 4.8b). The Arrhenius plot was fit using Equation 4.2, accounting for direct, Raman, QTM and, Orbach processes, to give U_{eff} = 27.2(5) cm^{-1} (τ_0 = 5.0(4) x 10^{-7} s) (Figure 4.9). Notably, the U_{eff} for the mixed-valent species **4-1** is 18.8 cm^{-1} lower than the non-oxidized species **[4-1]**$^-$. All fitting parameters for **4-1** are listed in Figure B.13.

Redox switchability of the dynamic magnetic properties is best illustrated by comparing the relaxation times in the Arrhenius plot of **[4-1]**$^-$ and **4-1** (Figure 4.9): the one-electron oxidation of **[4-1]**$^-$ to **1** results in faster relaxation times at a given temperature and a lower U_{eff} value.

Using the above described methodology, variable-field ac measurements were collected for the Er^{3+} compound **[4-2]**$^-$ at 2 K (Figures B.29 –B.31). The field dependence of τ was successfully fit using Equation 4.3 (Figures 4.10 (inset), B.32, and B.14). Variable temperature ac susceptibility data were collected using an applied field of 500 Oe (Figure 4.8c). The corresponding relaxation times were fit over the entire temperature region of the Arrhenius plot (Figure 4.10), according to Equation 4.2, resulting in an extracted value of U_{eff} = 29(2) cm^{-1} (τ_0 = 4(1) x 10^{-7} s). The

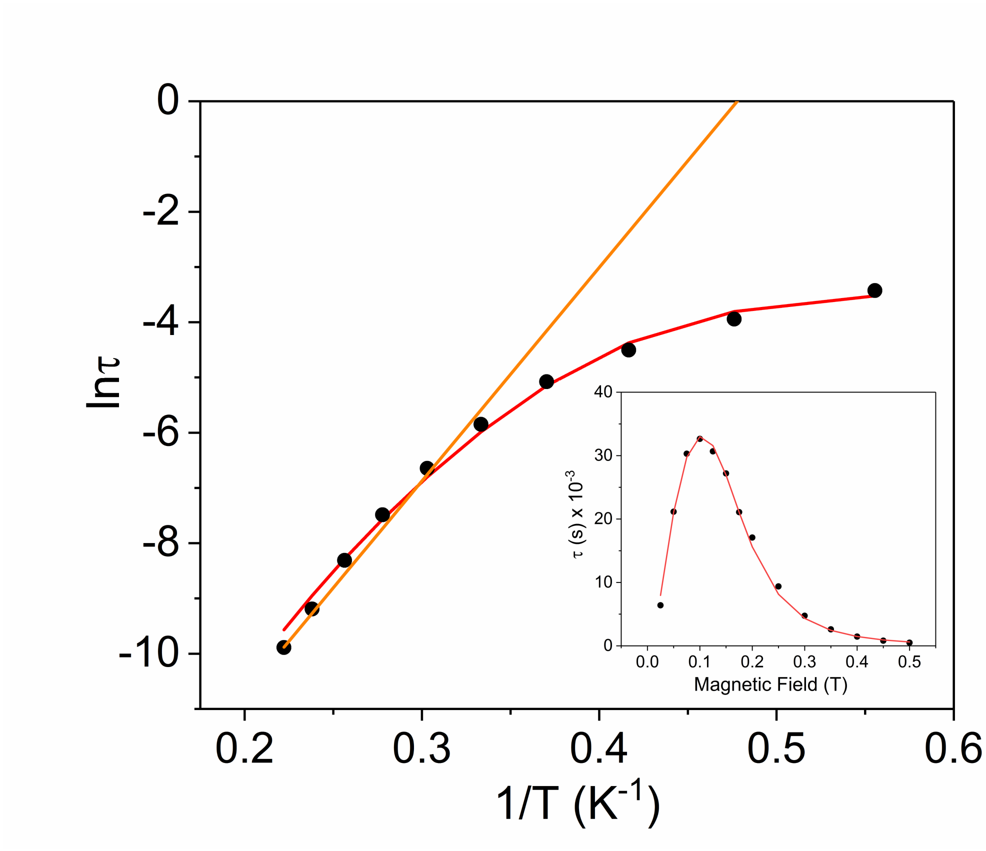

Figure 4.10: Arrhenius plot for the Er^{3+} complex **[4-2]⁻** (black circles) under a 500 Oe applied dc field. The orange line represents the fit of the linear region (six highest temperature points) to the expression $\tau^{-1} = \tau_0^{-1}\exp(-U_{\mathrm{eff}}/k_B T)$ (Orbach only); resulting in a U_{eff} value of 26.9 cm^{-1} ($\tau_0 = 9.52 \times 10^{-9}$ s). The red line represents fit of the entire temperature region to 4.2, giving a U_{eff} value of 29(2) cm^{-1} ($\tau_0 = 4(1) \times 10^{-7}$ s). Inset: field dependence of the relaxation times (τ) for **[4-2]⁻** (black circles), red line is fit to Equation 4.3. See Figure B.14 for all fitting parameters.

one-electron oxidized species, **4-2**, did not display any signs of slow magnetic relaxation under dc fields as high as 1500 Oe in ac experiments (Figure B.34).

In summarizing the magnetic results, we find that the prolate Er^{3+} ion in the **[4-2]⁻/4-2** system allows solely for reversible "on"/"off" switching of the slow magnetic relaxation (in the presence of a small dc field) (Figures 4.8c and d), while the oblate Dy^{3+} ion in the **[4-1]⁻/4-1** redox system enables bi-functional redox switchability of magnetic properties: "on"/"off" (no dc field) (Figure 4.7) and "slow"/"fast" (with dc field) (Figures 4.8a–b, and 4.9).

The distinct shapes of f-electron density of Dy^{3+} (oblate) and Er^{3+} (prolate) result in very different magnetic anisotropy axes and therefore different magnetization dynamics under the same ligand field and molecular symmetry conditions. Previously, isostructural Dy^{3+} and Er^{3+} complexes have been shown to exhibit different magnetization dynamics.[129–131] In the four-coordinate, trigonal pyramidal series of compounds $[Li(thf)_4][Ln(N(SiMe_3)_2)_3Cl]\cdot 2thf$, the Er^{3+} analogue displayed SMM behavior under zero dc field, whereas the Dy^{3+} analogue exhibited only field induced SMM behavior.[129] This difference was mainly attributed to the local symmetry and orientation of the magnetic anisotropic axis. The trigonal pyramidal geometry was found to not be ideal for either oblate or prolate ions but was relatively more favourable for prolate type ions, such as Er^{3+}.[131]

The coordination geometry of the bis(diamido)ferrocene complexes presented here was found to be relatively more favourable for the oblate Dy^{3+} ion than for the prolate Er^{3+} ion. The differences in behavior between the Dy^{3+} and Er^{3+} complexes are attributed to the orientation of the anisotropy axis under the same ligand field conditions due to the difference in f-electron density. We believe the largest contributor to the change in magnetization dynamics upon oxidation to be the change in ligand field and lowering of local symmetry. In detail, the oxidation of one of the diamidoferrocene ligands (in going from **[4-1]**$^-$ and **[4-2]**$^-$ to **4-1** and **4-2**) results in inequivalent binding of the two ligands to the central lanthanide ion. Additionally, packing effects and the presence or absence of counter ions may contribute to the structural changes.

The magnetic anisotropy axis of **4-1** was determined utilizing a quantitative electrostatic model for the prediction of the orientation of the ground state anisotropy axis in Dy^{3+} compounds described by Chilton et al. (MAGELLAN).[93] Considering charged ligands as point charges, the method minimizes electrostatic repulsion between the point charges and f-electron density. Using the molecular structure of **4-1**, the anisotropy axis was determined under three different scenarios: (1) assigning both Fe centers as neutral, (2) assigning a +1 charge to the Fe center closer to the Dy^{3+} ion, and (3) assigning a +1 charge to the Fe center further from the Dy^{3+} ion (Figure B.39). The addition and location of the +1 point charge did not lead to considerable differences in the orientation of the anisotropic axis (Figure B.39). The location of the negative point charges (amide ligands) was found to be the largest contributor, with the magnetic anisotropy axis aligned in the same plane as the shorter Dy–N bonds.

4.3.4 Cyclic voltammetry for **[4-1]**$^-$/4-1 and [4-2]$^-$/4-2

The separation in electrochemical potentials between individual redox couples of multi-redox systems can provide a useful initial estimate for the presence of electronic communication in mixed-valent species. The cyclic voltammogram of a solution of **[4-1]**$^-$ in thf, displays two quasi-reversible redox processes centered at $E_{1/2}$ = –1.00 and –0.540 V vs $[Cp_2Fe]^{0/1+}$ (Figure 4.11, top/blue). These processes correspond to the $Fe^{2+/3+}$ redox couples of the two individual ferrocene diamide ligands. The cyclic voltammogram of the free ligand exhibits one reversible redox process at –0.60 V vs $[Cp_2Fe]^{0/1+}$.[113] The potential separation of the two processes in **[4-1]**$^-$ is $\Delta E_{1/2}$ = 0.460 V, corresponding to a comproportionation constant of $K_c = 5.96 \times 10^7$. The cyclic voltammogram of a solution of **[4-2]**$^-$ in thf displays two reversible redox processes centered at $E_{1/2}$ = –0.930 and –0.410 V vs $[Cp_2Fe]^{0/1+}$ (Figure 4.11, bottom/red), corresponding to $K_c = 6.16 \times 10^8$. The large K_c values in **[4-1]**$^-$ and **[4-2]**$^-$ suggest considerable electronic interaction between the two iron sites in solution and is consistent with a Robin and Day Class II classification.[132] These values are significantly large but smaller than the values observed for the U^{4+} analogue reported by Monreal et al. ($\Delta E_{1/2}$ = 1.25 V, $K_c = 1.55 \times 10^{21}$).[113] Importantly, these observations are consistent with the formulation that the central f-block element is indeed critically involved in the electronic communication between the mixed-valent iron ions, resulting in larger electronic coupling for the actinide ion (U^{4+}) than for the trivalent lanthanide ions (Dy^{3+}, Er^{3+}), featuring the more contracted frontier orbitals.

4.3.5 ^{57}Fe Mössbauer spectroscopy and UV-vis-NIR spectroscopy

We utilized ^{57}Fe Mössbauer spectroscopy to establish the presence of electronic communication of the mixed-valent iron ions in **4-1** in the solid state. In the ^{57}Fe Mössbauer spectrum of the all ferrous species **[4-1]**$^-$ in zero field, a single characteristic doublet was observed, corresponding to the spectroscopically identical low-spin Fe^{2+} ions in **[4-1]**$^-$, with an isomer shift (δ) of 0.54 mm s^{-1} and quadrupole splitting (ΔE_Q) of 2.34 mm s^{-1} (Figure B.40). The ^{57}Fe Mössbauer spectrum

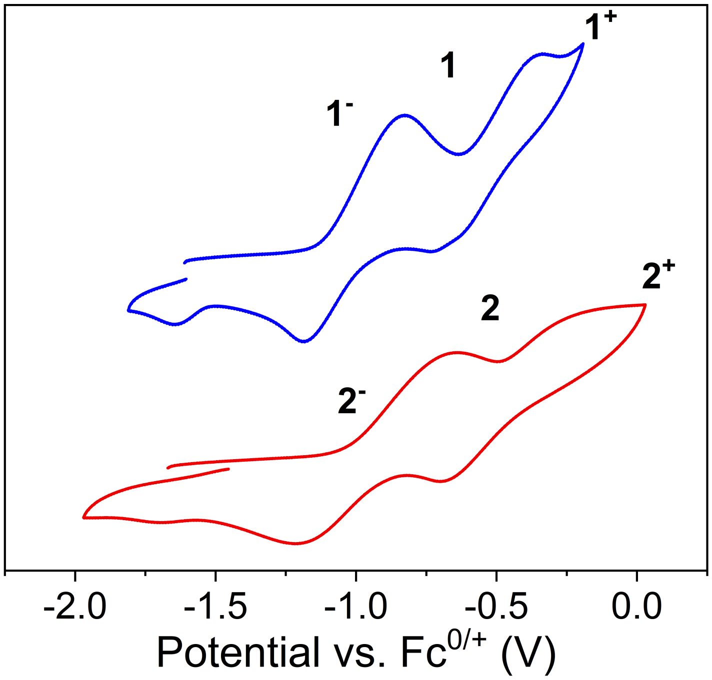

Figure 4.11: Cyclic voltammograms of **[4-1]**$^-$ (top) and **[4-2]**$^-$ (bottom) at 200 mV s^{-1} in thf with 0.1 M Bu_4NPF_6 as electrolyte. Referenced vs $Cp_2Fe^{0/+}$.

of the mixed-valent compound **4-1** exhibited two doublets (Figure 4.12). The spectrum could in principle be fit using both a two-site (Figure 4.12) model (two doublets) or a three-site model (Figure B.41) (one doublet, two singlets). Given the chemical nature of **4-1**, we believe that only the two-site model is appropriate here. As such, we fit the data using one doublet corresponding to the Fe^{2+} ion (δ = 0.528 mm s^{-1};ΔE_Q = 2.238 mm s^{-1}) and an equally contributing second doublet corresponding to the Fe^{3+} ion (δ = 0.506 mm s^{-1}; ΔE_Q = 0.490 mm s^{-1}). The Mössbauer spectrum is consistent with a trapped valent system over the temperature range studied (5 K to 150 K; Figure B.42), in which electron transfer is slower than the time scale of Mössbauer spectroscopy ($\sim 10^{-7}$ s^{-1}). However, electronic communication between Fe^{2+} and Fe^{3+} is clearly present, as the signal corresponding to the ferric site is quadrupole split. In the absence of electronic communication this signal would be expected to occur as a singlet.[115] Furthermore, the smaller ΔE_Q observed for the ferrous site in **4-1** as compared to **[4-1]**$^-$ is also consistent with the formulation of Fe$^{2+}\cdots$Fe^{3+} electronic communication. Similar spectroscopic signatures in mixed-valent dinuclear iron complexes have previously been reported for [Cp$^\star{}_2$Fe$_2$(as-indacene)]$^{\cdot+}$.[133]

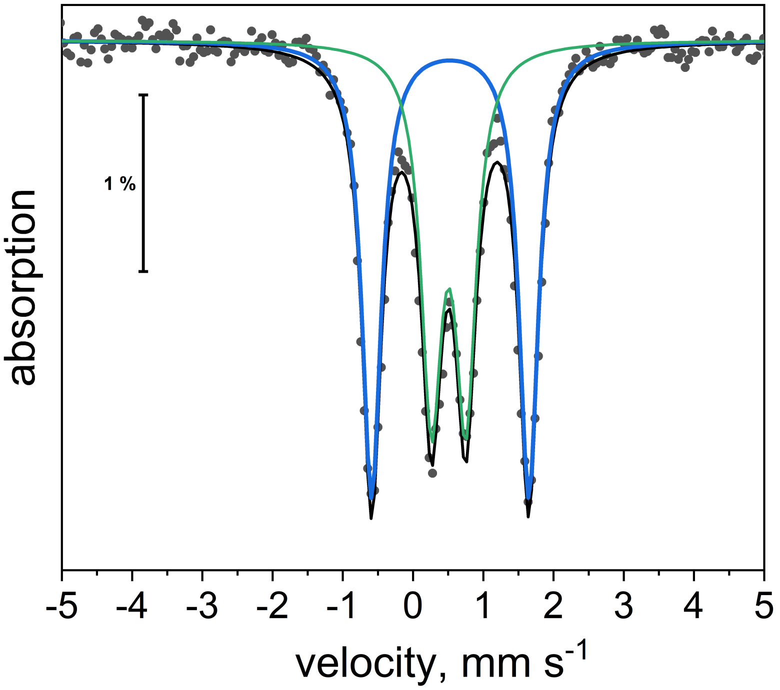

Figure 4.12: ^{57}Fe Mössbauer spectrum of **4-1** at 5 K. Black dots are experimental points. Black line is overall two-site fit. Blue and green lines are the individual sub-spectra for the two-site fit.

We utilized UV-vis-NIR absorption spectroscopy to probe the degree of electronic communication in solution. A broad band associated with an intervalence charge transfer (IVCT) transition was observed in the near-IR region of dilute thf solutions of the mixed-valent compounds **4-1** and **4-2** at λ_{max} = 1056 nm and 1043 nm, respectively (Figure B.44 and B.46). This broad, low-energy IVCT band is indicative of electronic communication in solution and is consistent with a Class II system,[134] supporting the observations from CV and ^{57}Fe Mössbauer spectroscopy. Moreover, in solution, intermolecular communication is assumed to be negligible, indicating the presence of intramolecular electronic communication in these mixed valent systems. The UV-vis-NIR absorption spectra of **[4-1]**$^-$ and **[4-2]**$^-$ in thf displayed no bands in the NIR region (Figure B.43 and B.45).

4.4 Conclusion and Outlook

Our studies highlight the utility of diamidoferrocene ligands in the construction of redox switchable SMMs. The high chemical reversibility of the $Fe^{2+/3+}$ redox couples can be exploited to alter magnetization dynamics of Dy^{3+} and Er^{3+} based SMMs. The mixed valent Fe ions in complexes **4-1** and **4-2** feature electronic communication with each other. Importantly, redox-switchable "on"/"off" and "slow"/"fast" SMM behavior can be obtained depending on the experimental conditions and the nature of the four-coordinate lanthanide ion. The combined results of this comprehensive molecular level study are important contributions towards the development of rational molecular design guidelines for future switchable magnetic molecules and materials.

5. MAGNETIC PROPERTIES OF CHROMIUM(II) HALF-SANDWICH COMPLEXES

5.1 Introduction

The field of single-molecule magnetism began with the development of large, multinuclear transition-metal compounds with high total spin.[6] More recent efforts have been focused on the development of mononuclear transition metal- and lanthanide-based compounds for single molecule magnet applications.[13,135] There are now many examples of mononuclear compounds of Co(II), Fe(II), Mn(III) that exhibit either zero field or field-induced slow relaxation.[135,136]

There are numerous examples of mononuclear Mn(III) complexes that display field-induced slow magnetic relaxation.[137] Despite being isoelectronic with Mn(III), there are only three examples of Cr(II)-based compounds that display field induced Cr(II)-based slow relaxation, with only two of those examples being mononuclear Cr(II) compounds.[138,139] The scarcity of Cr(II) compounds in molecular magnetism (and in general) could be due to its tendency to oxidize, requiring very rigorously air free conditions. The first reported Cr(II)-based compound to show field-induced slow magnetic relaxation was reported in 2014 by Cornia et al.[138] The pentachromium(II) extended metal atom chain (EMAC), $[Cr_5(tpda)_4Cl_2]$, showed field-induced slow relaxation of magnetization, resulting in a U_{eff} of 6.4 cm^{-1} under an applied dc field of 2500 Oe. In 2015, the first mononuclear Cr(II) complexes to show field-induced slow relaxation were reported by Deng et al.[139] The two square planar Cr(II) complexes, *trans*-$Cr(N(SiMe_3)_2)_2(py)_2$ and *trans*-$Cr(N(SiMe_3)_2)_2(thf)_2$, exhibited field-induced slow relaxation of magnetization with U_{eff} of 6.3(4) cm^{-1} (1500 Oe dc field) and 8.2(5) cm^{-1} (2500 Oe dc field), respectively. The synthesis and structure of the square planar compound $Cr(N(SiMe_3)_2)_2(thf)_2$ were first reported in 1972 by Bradley et al.,[140] however the magnetic properties were not investigated at that time.

Chromocene is an extremely reactive electron deficient compound, with 16 d-electrons. It is very air and moisture sensitive; rapidly oxidizing to Cr(III). Unlike the metallocenes of group 8 (Fe, Ru, Os), electrophilic aromatic substitution does not occur in chromocene. In chromocene, substitution of the Cp ligand by strong nucleophiles is very facile, as has been shown in other other electron deficient metallocenes.[141] For example, the cyclopentadienide ligands in manganocene have been shown to be very labile, with one or both Cp ligands being displaced by nucleophiles.[141–143] Chromocene is an electron deficient 16-electron complex and it can undergo Cp ligand substution with retention of the +2 oxidation state.[141] This Cp ligand substitution is most frequently observed with organo-alkali metal and lithium amide and phosphide reagents.[141,144] Depending on the reagents and reaction conditions (solvent, temperature etc.) either one or both of the Cp ligands may be substituted.[141] There are also examples of Cp ligand substitution at chromocene accompanied by oxidation of the Cr center from the +2 to +3 oxidation state. This is most commonly observed in reactions of chromocene with halogenated solvents or with redox-active ligands that can accept an electron.[145,146]

In 2013, Scheuermayer et al. reported the reactions of a series of pnictogen nucleophiles, $LiE(SiMe_3)_2$ (E = N, P, As), with chromocene, showing that the pnictogen nucleophile could substitute a Cp ligand on chromocene, with elimination of LiCp, to generate a series of pnictogen-bridged Cr(II) half-sandwich compounds.[144] The nitrogen compound was found to be a polymeric chain, with Li coordinated μ:η^2-Cp. The other pnictogen compounds (E = P, As) were found to be homometallic dimers, with $E(SiMe_3)_2$ units bridging between CpCr units. The static magnetic properties of these compounds were reported, revealing coupling between the Cr(II) centers in the homometallic dimers (E = P, As), however no magnetization dynamics (or slow relaxation) were reported.

We became interested in Cr(II) half-sandwich compounds as possible precursors to combined d- and f-block complexes. Herein, the synthesis and characterization of the Cr(II) half-sandwich polymer, $[CpCr(\mu\text{-}N(SiMe_3)_2)_2K]_\infty$ (**5-1**), and the mononuclear Cr(II) half-sandwich cryptand complex, $[K(\text{crypt-222})][(CpCr(N(SiMe_3)_2)_2]$ (**5-2**), are reported. Interestingly, the polymer can be converted to the mononuclear compound through addition of cryptand-222. Notably the cryptand complex is the first non-square planar mononuclear Cr(II) compound to show field-induced slow relaxation and is currently the record holder for largest U_{eff} in a Cr(II)-based complex (U_{eff} = 9.8(6) cm^{-1}).

5.2 Experimental

5.2.1 General considerations

All reactions and manipulations were carried out in anaerobic and anhydrous conditions in an argon-filled glovebox (Vigor). Toluene, tetrahydrofuran (thf), diethyl ether, and hexanes were dried and deoxygenated using a solvent purification system (JC Meyer Solvent Systems). Chromocene (Cp_2Cr) was purchased from Alfa Aesar and used as received. $K(N(SiMe_3)_2)$ was purchased from Sigma-Aldrich and used as received. Cryptand-222 was purchased from Sigma-Aldrich and dried under vacuum before use. Eicosane was purchased from Acros Organics and dried under vacuum before use. Elemental analyses were carried out by Midwest Microlab (Indianapolis, IN).

Synthesis of $[CpCr(N(SiMe_3)_2)_2K]_\infty$ (5-1). To a solution of Cp_2Cr (47.5 mg, 0.261 mmol) in toluene (2 mL), layered a solution of $K(N(SiMe_3)_2)$ (208.5 mg, 1.045 mmol) in toluene (8 mL) on top and let stand undisturbed at rt. After 48 h, X-ray quality blue plate crystals had formed. The crystals were washed with toluene (10 mL) and diethyl ether (10 mL) for purification. Yield 50 % (54.4 mg, 0.130 mmol). Unit cell parameters (110 K): $C2/c$, a = 19.2845(8) Å, b = 8.5126(4) Å, c = 15.6920(7) Å, α = 90 °, β = 94.010(2) °, γ = 90 °, V = 2569.7(2) Å^3. Anal. calcd for $C_{17}H_{41}CrKN_2Si_4$: C, 42.81; H, 8.66; N, 5.87 %. Found: C, 41.98; H, 8.22; N, 5.58 %.

Synthesis of $[K(crypt\text{-}222)][CpCr(N(SiMe_3)_2)_2]$ (5-2) in situ from chromocene. To a stirring solution of Cp_2Cr (17.5 mg, 0.0961 mmol) in thf (2 mL) added a solution of $K(N(SiMe_3)_2)$ (19.2 mg, 0.0960 mmol) in thf (4 mL). A solution of cryptand-222 (43.4 mg, 0.115 mmol) in thf (2 mL) was immediately added to the stirring solution. Immediate color change to blue. Let reaction stir for 1 h at rt. The reaction mixture was concentrated in vacuo (3 mL) and filtered through a Celite pipet. The blue filtrate was further concentrated, layered with hexanes and stored at –30 °C for 48 h to yield blue crystals and a white precipitate. Diethyl ether (5 mL) was added to the resulting solid and the blue solution was filtered through Celite. All diethyl ether was removed in vacuo. X-ray quality single crystals were grown from a concentrated thf solution layered with hexanes at –30 °C for 72 h. Yield 56 % (45.9 mg, 0.0537 mmol). Unit cell parameters (110 K): $P2_1/c$, $a = 10.7319(12)$ Å, $b = 21.949(2)$ Å, $c = 21.170(2)$ Å, $\alpha = 90$ °, $\beta = 104.226(3)$ °, $\gamma = 90$ °, $V = 4833.7(9)$ Å^3. Anal. calcd for $C_{35}H_{77}CrKN_4O_6Si_4$: C, 42.81; H, 8.66; N, 5.87 %. Found: C, 41.98; H, 8.22; N, 5.58 %.

Synthesis of [K(crypt-222)][CpCr(N(SiMe$_3$)$_2$)$_2$)] (5-2) from polymer 5-1. To a stirring solution of **5-1** (13.7 mg, 0.0287 mmol) in thf (2 mL), added a solution of cryptand-222 (13.5 mg, 0.0359 mmol) in thf (3 mL). Let stir for 2 hours at rt. All solvent was removed in vacuo to give a blue solid and a white solid. The remaining solid was extracted with diethyl ether (5 mL) to give a blue solution and a white precipitate. The solution was filtered through Celite and all ether was removed in vacuo. The blue solid was dissolved in a minimal amount of thf, layered with hexanes. After 48 h at –30 °C, blue crystals had formed, which were confirmed by unit cell to be **5-2**. The synthesis could also be carried out in diethyl ether with a reaction time of 48 h at rt. Unit cell parameters (110 K): $a = 10.83$ Å, $b = 22.11$ Å, $c = 21.36$ Å, $\alpha = 90$ °, $\beta = 104.91$ °, $\gamma = 90$ °, $V = 4938$ Å^3.

Synthesis of Cr(N(SiMe$_3$)$_2$)$_2$(thf)$_2$. To a stirring solution of Dy(OTf)$_3$ (18.9 mg, 0.0310 mmol) in thf (2 mL) added a solution of **5-1** (14.8 mg, 0.0310 mmol) in thf (3 mL). Immediate color change to pink. After stirring at rt for 15 min, all solvent was removed in vacuo. The solid was extracted into toluene and crystallized from a concentrated toluene at –30 °C over 48 h. Unit cell parameters (110 K): $a = 10.77$ Å, $b = 11.38$ Å, $c = 13.10$ Å, $\alpha = 69.38$ °, $\beta = 78.90$ °, $\gamma = 85.32$ °, $V = 1478$ Å^3.

5.2.2 X-ray structure determination

Single crystals suitable for X-ray diffraction were mounted on a MiTiGen loop and placed in a cold N_2 stream at 110 K. A Bruker APEX 2 Duo X-ray (three-circle) diffractometer was used for unit cell determination and data collection for **5-1** and a Bruker D8 Quest X-ray diffractometer was used for unit cell determination and data collection for **5-2**. The X-ray radiation was generated from a Mo sealed X-ray tube (Kα= 0.70173 Å, with a potential of 40 kV and a current of 40 mA). Bruker AXS APEX II (**5-1**) and APEX3 (**5-2**) software was used for data collection.

Data analysis: BRUKER AXS APEX II software was used for integration and data reduction. Absorption corrections were applied using the program SADABS.[82] A solution was obtained using XT/XS in OLEX2.[81,83–85] Hydrogen atoms were placed in idealized positions and were set riding on the respective parent atoms. All non-hydrogen atoms were refined with anisotropic thermal parameters. The structure was refined (weighted least squares refinement on F^2) to convergence using OLEX2.[85,86]

5.2.3 Magnetic measurements

A representative procedure for the preparation of the samples for magnetic characterization is as follows. Crystalline sample was crushed up into a fine powder before loading into a high purity 7 mm NMR tube (Norell). A layer of eicosane was added to the tube, covering the sample. The tube was then flame sealed under vacuum. To restrain the sample, the sealed tube was placed in a water bath (39 °C) until the eicosane melted and was evenly distributed throughout the sample. The sample was loaded into a straw affixed to the end of the sample rod. Magnetic measurements were carried out using a Quantum Design MPMS 3 SQUID magnetometer (TAMU Vice President of Research). Dc susceptibility measurements were carried out over a temperature range of 2 K to 300 K. Ac susceptibility measurements were carried out using a 2 Oe switching field. Data was corrected for diamagnetic contributions from the straw, sample tube, eicosane, and core diamagnetism using Pascal's constants.[87] The calculated diamagnetic corrections are as follows: -5.26×10^{-8} emu (**5-1**) and -3.4×10^{-8} emu (**5-2**). Cole-Cole plots were fitted to the generalized Debye equation using least-squares regression (Equations 1.9 and 1.10). Arrhenius plots and τ vs. H plots were fit using least squares regression.

5.3 Results and Discussion

5.3.1 Synthesis and structural characterization

The reaction between chromocene (Cp_2Cr) and $K(N(SiMe_3)_2)$ in the absence and presence of cryptand-222 was investigated. Layering a toluene solution of four equivalents of $K(N(SiMe_3)_2)$ on a solution of chromocene in toluene and allowing the reaction mixture stand undisturbed at rt for

48 h afforded X-ray quality blue plate crystals of the polymeric species $[CpCr(\mu\text{-}N(SiMe_3)_2)_2K]_\infty$ (**5-1**) in 50 % yield (Figure 5.1). The Cr^{2+} center is highly electron deficient with a formal electron count of 14. The polymeric species **5-1** crystallizes in the monoclinic space group *C2/c*, with half of the repeating unit comprising the asymmetric unit (Table 5.1, Figures 5.2 and C.1). The extended polymer chain is linear, with η^5-coordination of the Cp ligand to both the Cr center and the K center (Figure 5.2). The Cr^{2+} and K^+ centers are bridged by two trimethylsilyl amide groups. The two Cr–N bonds are equivalent by symmetry with a length of 2.082(3) Å and a N–Cr–N bond angle of 107.43(14) °(Figure C.1). This angle is considerably larger than the N–Cr–N bond angles of 96.28(7) ° and 96.22(7) ° in the Li^+ polymer, $[(\mu{:}\eta^2{:}\eta^5\text{-}Cp)Cr(\mu\text{-}N(SiMe_3)_2)_2)Li]$, reported by Scheuermayer et al.[144]

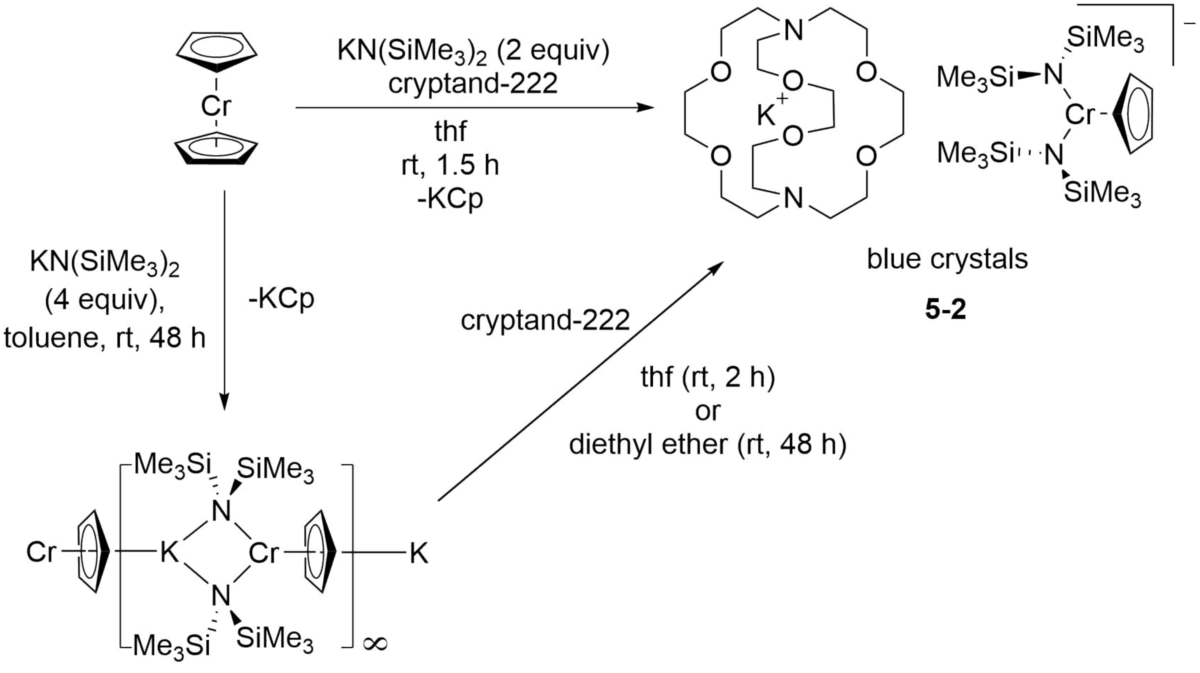

Figure 5.1: Synthesis of the polymeric compound **5-1** and the mononuclear cryptand compound **5-2**.

There is pronounced rotational disorder of the Cp ligand around the Cr-Cp(centroid) axis in

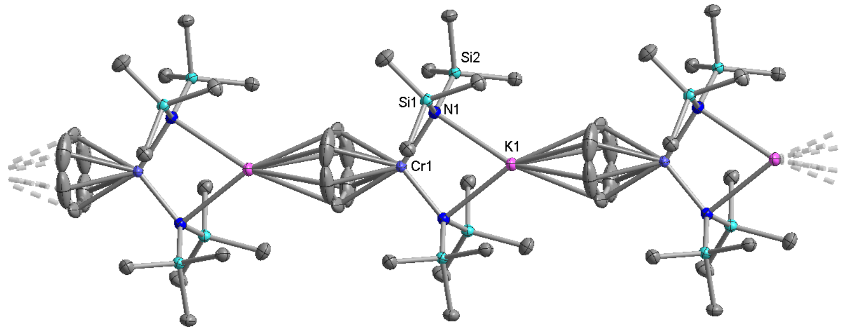

Figure 5.2: Molecular structure of **5-1**. Violet = Cr, pink = K, teal = Si, red = O, blue = N, grey = C. Hydrogen atoms omitted for clarity. Thermal ellipsoids are set at the 50 % probability level.

Compound	**5-1**	**5-2**
Formula	$C_{20}H_{20}CrKN_2Si_2$	$C_{35}H_{77}CrKN_4Si_4O_6Si_4$
Crystal system	monoclinic	monoclinic
Space group	$C2/c$	$P2_1/c$
a, Å	19.2845(8)	10.7319(12)
b, Å	8.5126(4)	21.949(2)
c, Å	15.6920	21.170(2)
α , °	90	90
β , °	94.010(2)	104.226(3)
γ , °	90	90
Volume, Å^3	2569.7(2)	4833.7(9)
Z	8	4
T, K	110(2)	110(2)
Density ϱ_{calcd} , mg/m^3	2.252	1.402
$F(000)$	1800	2029
Θ_{min} , Θ_{max}, °	2.60, 22.86	2.42, 28.75
Index ranges	-24 h 24, -10 k 10, -19 l 19	-15 h 15, -31 k 31, -30 l 30
Reflections collected	52818	339879
Independent reflections	2655 [R(int) = 0.0907]	14956 [R(int) = 0.1430]
Final R indices [$(I > 2\sigma(I))$]	$R_1 = 0.0508$, $wR_2 = 0.1273$	$R_1 = 0.0712$, $wR_2 = 0.1164$
R indices (all data)	$R_1 = 0.0634$, $wR_2 = 0.1334$	$R_1 = 0.1239$, $wR_2 = 0.1334$

Table 5.1: Crystallographic data for **5-1** and **5-2**

5-1. The Cr–Cp(centroid) distance is 2.065 Å(Figure C.1). The K–N bond distances are equivalent with a length of 2.887(3) Å. The N–K–N bond angle is 71.07(10) °. The Cr···K distance in **5-1** is 3.5813(12) Å. Compared to the zig-zag structure of the Li^+ polymer reported by Scheuermayer et al. with Li^+ coordinated to Cp in μ:n^2-Cp (inequivalent Cp-Li distances), the K^+ polymer **5-1** is a linear chain, with the K^+ ion coordinated to Cp in n^5-Cp.[144] This is likely due to the larger size of K^+ relative to Li^+. The Cr···Cr distance within the polymeric chain in **5-1** is 8.513 Å.

The reaction of chromocene with two equivalents of $K(N(SiMe_3)_2)$ in thf in the presence of a slight excess of cryptand-222 proceeded smoothly in 1.5 h to afford the mononuclear Cr(II) compound, [K(crypt-222)][(CpCr$(N(SiMe_3)_2)_2$] (**5-2**) (Figure 5.1). The mixture of chromocene and $K(N(SiMe_3)_2)$ in thf is red-orange, however upon addition of cryptand-222 there was an immediate color change to blue. X-ray quality blue crystals were grown from a concentrated thf solution layered with hexanes at –30 °C over 72 h in a 56 % crystalline yield.

The cryptand compound, [K(crypt-222)][CpCr$(N(SiMe_3)_2)_2$] (**5-2**) crystallizes in the monoclinic space group $P2_1/c$ (Figures 5.3 and C.2, Table 5.1). The asymmetric unit contains one $[CpCr(N(SiMe_3)_2)_2]^-$ and one $[K(crypt\text{-}222)]^+$ moiety. Four of these asymmetric units make up the unit cell. If the Cp ligand is considered as occupying three coordination sites, the Cr(II) center is five-coordinate, coordinated by one Cp ligand and two trimethylsilylamide ligands. This is an electron deficient compound, with a formal electron count of 14.

The Cp ligand is bound to the Cr(II) center in n^5 fashion, with C–Cr bond distances in the range of 2.358(3) to 2.436(3) Å, with an average C–Cr bond length of 2.391[3] Å. The distance from the centroid of the Cp to the Cr(II) center is 2.071 Å(Figure C.3). The two Cr–N bond distances are inequivalent, with bond lengths of 2.053(2) and 2.069(2) Å(Figure C.3). The N–Cr–N angle is 107.66(8) °(Figure C.3). This N–Cr–N angle is only slightly larger than the N–Cr–N angle found in the polymer **5-1**, which has an angle of 107.43(14) °. It is considerably larger than the N–Cr–N bond angles reported by Schuermayer et al. in the Li polymer (96.28(7)/96.22(7) °) and in the homometallic dimers (99.98(3)/99.43(3) ° and 94.41(2)/93.79(2) ° for E = P and As, respectively).[144] In **5-2**, the two Cr–N bond lie in the same plane. The closest Cr···Cr distance in **5-2** is 14.173(1) Å; considerably larger then the closest Cr···Cr contact in the polymer **5-1**. The K^+ cation is chelated by the cryptand, in eight-coordinate fashion. The K^+ cation is non-interacting/coordinating to the Cr(II) center. The distance between the Cr(II) center and the K^+ cation is 9.5070(9) Å.

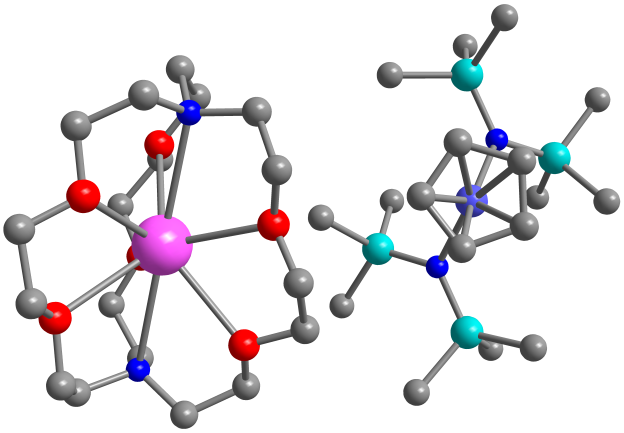

Figure 5.3: Molecular structure of **5-2**. Violet = Cr, pink = K, teal = Si, red = O, blue = N, grey = C. Hydrogen atoms omitted for clarity

The mononuclear cryptand complex could also be prepared from the polymeric species through dissolving the polymer in thf in the presence of cryptand-222, stirring for 2 h, and recrystallizing under the same conditions as above (concentrated thf solution layered with hexanes at –30 °C). The polymeric compound is fully soluble in thf to give a dark blue, clear solution. However, it is currently unknown whether or not it remains polymeric in solution. Interestingly, the cryptand compound **5-2** could also be prepared through addition of cryptand-222 to a suspension of the polymer **5-1** in diethyl ether, albeit over a longer time period of 48 h. This is notable because the polymer **5-1** is insoluble in diethyl ether, forming a suspension when diethyl ether is added.

The progress of the reaction could be monitored through the disappearance of blue solid and color change of the solution to dark blue. After 48 h, the solution was blue with only a white precipitate present (KCp). Following filtration, recrystallization from a concentrated thf solution layered with hexanes at –30 °over 48 h afforded blue crystals. Unit cell determination by X-ray diffraction revealed the crystals to be **5-2**. The solubility of the cryptand compound **5-2** in diethyl ether provides an effective purification method, as the polymer **5-1** is insoluble in diethyl ether.

Dissolving the polymeric **5-1** in thf, layering with hexanes and storing at –30 ° for 4 d led to the isolation of the polymeric species **5-3** (Figure 5.4). Notably, there is an extra equivalent of KCp in **5-3** relative to the starting material **5-1**. This could either be from a decomposition reaction that also produces $Cr(N(SiMe_3)_2)_2$ or a KCp impurity in **5-1**. To determine the exact cause, further investigation is required.

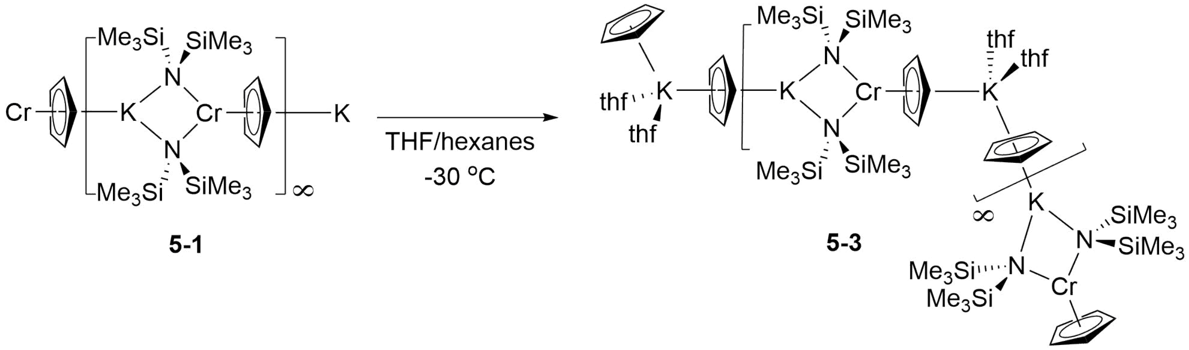

Figure 5.4: Recrystallization of **5-1** in thf layered with hexanes.

5.3.2 Reactivity

Interestingly, in our hands the reaction between Cp_2Cr and $Li(N(SiMe_{32})$ as described by Scheuermayer et al. could not be reproduced.[144] Reactivity studies between chromocene and $Dy(N(SiMe_3)_2)_3$ in toluene and thf have thus far been unsuccessful. Only starting materials have been isolated following the reactions, suggesting that no reaction has occurred.

The reaction between **5-1** and one equivalent of $Dy(OTf)_3$ in thf resulted in a color change to

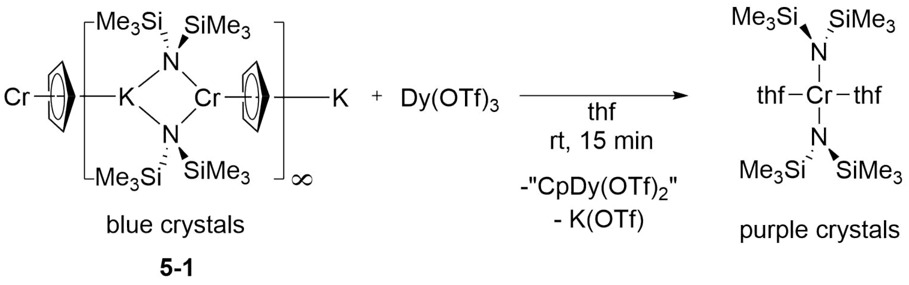

Figure 5.5: Reactivity of the Cr(II) polymer, **5-1**

purple. Recrystallization from a concentrated cold toluene yielded highly-air sensitive purple block crystals that were identified by X-ray diffraction to be the square planar Cr(II) compound, *trans*-$Cr(N(SiMe_3)_2)_2(thf)_2$ (Figure 5.5). Notably this compound has been previously prepared from the reaction of Cr(II) chloride with 2 equivalents of $Li(N(SiMe_3)_2)$ in thf.[140] Its magnetic properties were investigated by Deng et al. in 2015.[139] The reaction of **5-1** with $Fe(OTf)_2$ also yielded purple crystals of $Cr(N(SiMe_3)_2)_2(thf)_2$. In these reactions, **5-1** acts as a Cp transfer agent.

5.3.3 Static magnetic properties

The static and dynamic magnetic properties of **5-1** and **5-2** were investigated. The static magnetic properties were investigated under a 1000 Oe (0.1 T) dc field over a temperature range of 300 K to 2 K. The measured room temperature $\chi_M T$ for **5-1** of 2.70 cm^3 K mol^{-1} is lower than the expected value of 2.88 cm^3 K mol^{-1} for one, non-interacting Cr^{2+} center (Cr(II), S = 2, g = 1.96), consistent with $g < 2.00$ for high-spin Cr(II) (Figure 5.6, black circles).[138,147] The $\chi_M T$ value is nearly independent of temperature from 300 K down to 90 K, where the it begins to decrease, followed by a very rapid decrease below 16 K, reaching a minimum value of 1.51 cm^3 K mol^{-1} at 2 K (Figure 5.6, black circles).

The measured room temperature $\chi_M T$ for **5-2** of 2.96 cm^3 K mol^{-1} is very close to the expected value of 2.88 cm^3 K mol^{-1} for one, non-interacting Cr^{+2} center (Cr(II), S = 2, g = 1.96) (Figure, 5.6, blue triangles). The $\chi_M T$ value is essentially temperature independent down to 10 K, where it decreases sharply to reach a minimum value of 2.33 cm^3 K mol^{-1} (Figure 5.6, blue triangles).

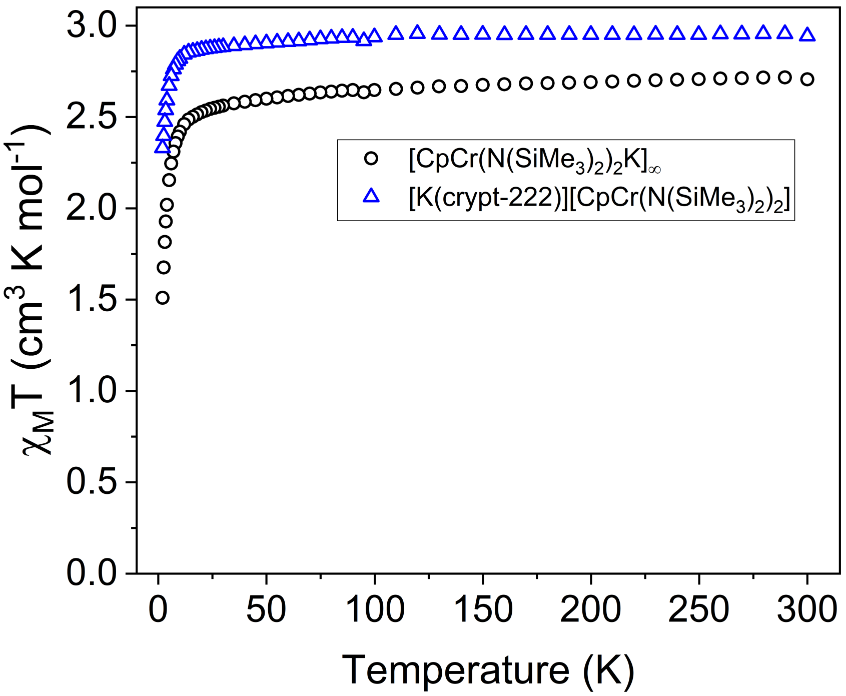

Figure 5.6: Temperature dependence of the molar magnetic susceptibility times temperature product ($\chi_M T$) for compounds **5-1** (black circles) and **5-2** (blue triangles) under a 1000 Oe dc field.

The field dependence of the magnetization (M) in **5-1** and **5-2** was measured at fields up to 70 kOe (7 T) over a temperature range of 2 –10 K. In the polymeric compound, **5-1**, no saturation of magnetization was observed up to 7 T (Figure C.6). At 2 K, the magnetization increases sharply until 1.5 T where it then increased more gradually to reach an unsaturated moment of 3.14 μ_B at 7 T (Figure C.6). This is lower than the expected value however it is in agreement with the value found for square planar Cr(II) complexes *trans*-$Cr(N(SiMe_3)_2)_2(py)_2$ and *trans*-$Cr(N(SiMe_3)_2)_2(thf)_2$.[139] In the reduced magnetization (M vs H/T) of **5-1**, the lack of superposition indicates low-lying excited states or anisotropy (Figure C.7).

Similarly, in the mononuclear compound **5-2**, no saturation of magnetization was observed up to 7 T (Figure C.8). At 2 K, the magnetization increases sharply until 1 T, where it then increases more gradually to reach an unsaturated moment of 3.51 μ_B (Figure C.8). This is in agreement with four unpaired electrons at the Cr(II) center.[144] In the reduced magnetization (*M* vs *H/T*) of **5-2**, the lack of superposition indicates low-lying excited states or anisotropy (Figure C.9).

5.3.4 Dynamic magnetic properties

The polymeric compound **5-1** displayed no evidence of slow relaxation, even at very low temperatures (1.8 K) under applied dc fields (500 –2000 Oe) (Figure C.5). Interestingly, field-induced slow relaxation was observed in the mononuclear compound **5-2** at low temperature (Figure 5.7). The field dependence of the relaxation times, τ, could not be fit to Equation 1.13 on account of the non-smooth trend.

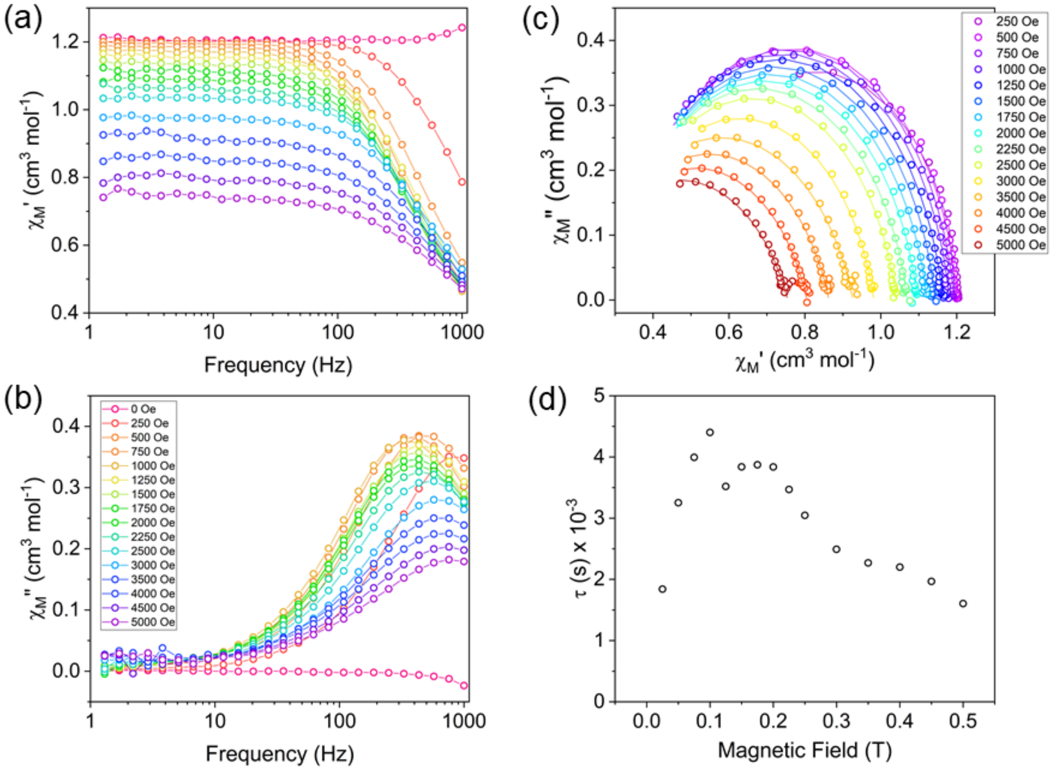

Figure 5.7: (a) In-phase, χ', and (b) for out-of-phase, χ", components of the ac susceptibility for **5-2** at 2 K with variable fields. Lines are a guide for the eye. (c) Cole-Cole plots for **5-2** at 2 K. Open circles represent experimental data and solid lines are fits to the generalized Debye equation. (d) Field dependence of the relaxation time (τ) in **5-2** at 2 K.

From the field dependence of τ, an optimal dc field of 1000 Oe was selected for the temperature dependent measurements. Under a 1000 Oe dc field, slow relaxation was observed from 1.8 K up to 2.8 K, when the signal shifts outside of the high frequency limit (1000 Hz) (Figure 5.8, bottom left). The Cole-Cole (χ" vs χ') plot was fit to the generalized Debye equation to extract relaxation times (τ), which were then plotted vs temperature in the Arrhenius plot (Figure 5.8, right). Interestingly, the relaxation times showed temperature dependence through the entire temperate range measured (no evidence of QTM). As a result, the Arrhenius plot was fit to the linear equation (Equation 5.1), considering Orbach relaxation processes only. From this fit, a U_{eff} value of 9.8(6) cm^{-1} (τ_0 of 3.60 x 10^{-7}) was extracted. It is not anticipated that Cr(II) in this geometry would have large anisotropy. Notably, it has been reported for the isoelectronic Mn(III) that slow relaxation may be observed, even in the absence of large anisotropy.[136] Notably, this is only the fourth report of a compound showing Cr(II)-based field-induced slow relaxation and of those previously reported compounds, **5-2** possesses the highest U_{eff} value.

$$\tau = \tau_0 \exp(U_{\text{eff}}/k_{\text{B}}T) \tag{5.1}$$

The difference in magnetization dynamics between the polymeric compound **5-1** and the cryptand compound **5-2** is considerable. Despite containing the same bound atoms in the primary coordination sphere, 5-2 displays field-induced slow relaxation, where as **5-1** does not. This difference could be attributed to the subtle changes in ligand field upon going from the polymer **5-1** to the mononuclear compound **5-2**. Interestingly, the N–Cr–N bond angles of the two compounds are very similar, with angles of 107.43 °in **5-1** and 107.65 °in **5-2**. The Cr–N bond distance in **5-1** is 2.082(3) Å, which is longer than the Cr–N1 and Cr–N2 bond lengths of 2.053(3) Å and 2.069(2) Å in **5-2**. The Cr-Cp(centroid) distances are comparable between the two compounds with distances of 2.065 Å and 2.071 in **5-1** and **5-2**, respectively. Notably, the Cp ligand in **5-1** suffers from considerable rotational disorder, whereas the Cp ligand in **5-2** does not. Interactions between the Cr(II) centers may also contribute to the observed difference in magnetization dynamics. The Cr···Cr distance in the polymer **5-1** is 8.513 Å; whereas in

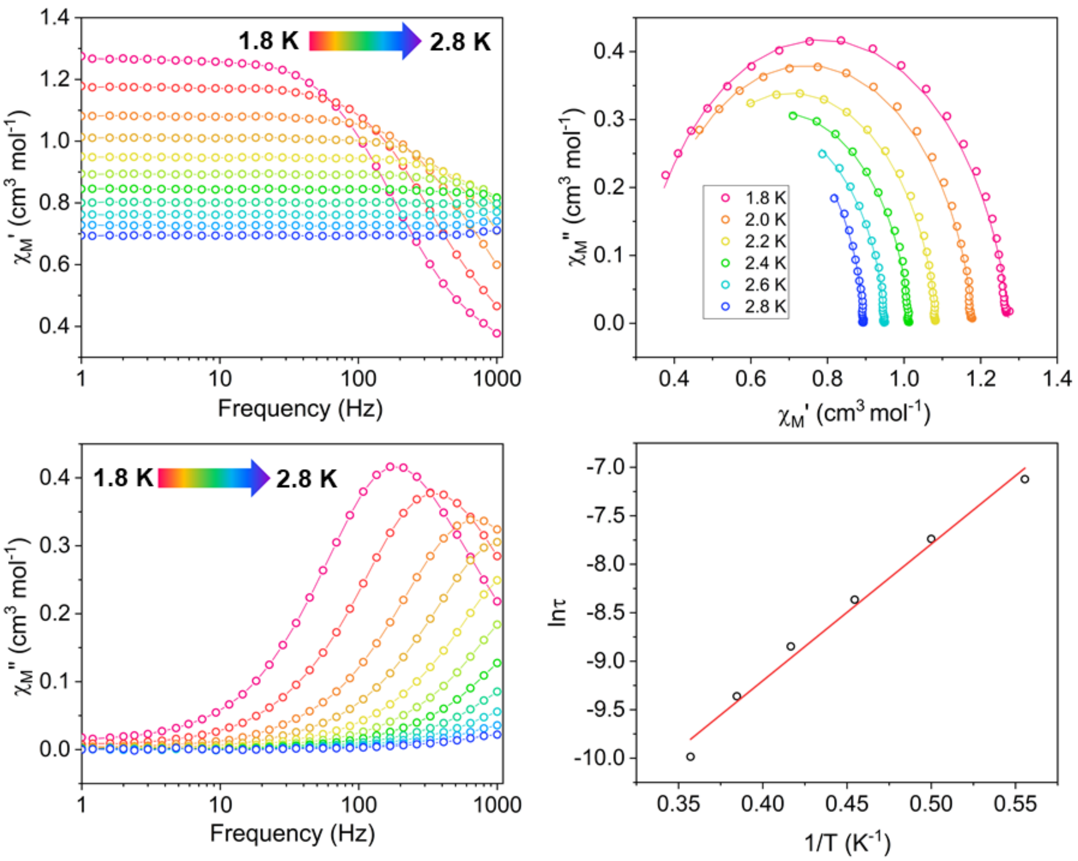

Figure 5.8: In-phase χ’ (top-left) and out-f-phase, χ" (bottom-left) components of the ac susceptibility for **5-2** under a 1000 Oe applied dc field over a temperature range of 1.8 - 2.8 K. Lines are a guide for the eye. Cole-Cole plots (top-right) for **5-2** under 1000 Oe dc field. Open circles are experimental data points, lines represent fits to the generalized Debye equation. Arrhenius plot (bottom-right) for **5-2** under a 1000 Oe dc field. Open black circles represent experimental data. Red line is a fit of the data to Equation 5.1 to give U_{eff} = 9.8(6) cm^{-1} and τ_0 = 3.60 x 10^{-7}.

the crpytand compound **5-2** the closest Cr···Cr contact is much longer at 14.173(14) Å. It is possible that the closer Cr···Cr contact in the polymeric compound **5-1** leads to increased Cr–Cr interactions, thereby inhibiting field-induced slow relaxation. However, the exact contributions of ligand field and Cr–Cr interactions to the observed difference in magnetization dynamics remains undetermined at this time. Future computational studies intend to elucidate the relationship of the ligand field and Cr–Cr interactions with the observed magnetization dynamics in the polymeric compound **5-1** and the cryptand compound **5-2**.

5.4 Conclusion and Outlook

The polymeric Cr(II) species, **5-1**, could be formed from the reaction of chromocene and $K(N(SiMe_3)_2)$ in toluene. In the presence of cryptand-222 the mononuclear Cr(II) species **5-2** could be formed, either in situ or through adding cryptand-222 to a solution of **5-1** in thf. The cryptand compound, **5-2**, displayed field induced slow relaxation with $U_{\mathrm{eff}} = 9.8(6)$ cm^{-1} (H_{dc} = 1000 Oe). Notably, this is only the third reported mononuclear Cr(II) compound to display field-induced slow relaxation and is the first example that is not square planar in geometry.

6. DYSPROSIUM-161 AND TIN-119 SYNCHROTRON MÖSSBAUER SPECTROSCOPY FOR THE INVESTIGATION OF MAGNETIZATION DYNAMICS

6.1 Introduction

The development of new characterization methods is essential for continued advancement in the field of molecular magnetism. An important metric used in the evaluation of SMMs is the barrier height, U_{eff}, for Orbach (thermal) relaxation (Chapter 1, Section 1.1.2). U_{eff} is typically calculated from the slope (U_{eff}/k_B) of an Arrhenius plot of relaxation time ($\ln \tau$) vs temperature (T^{-1}). However, considerable deviations from linearity may occur due to the presence of competing relaxation pathways.

Mössbauer spectroscopy may be used as an alternative and/or complementary technique to study relaxation dynamics. An advantage of utilizing Mössbauer spectroscopy is the lifetime of the measurement (10^{-8} to 10^{-9} s) is 5-6 orders of magnitude faster than SQUID magnetometry (10^{-3} to 10^{-4} s), allowing for the determination of relaxation times at higher temperatures than can currently be measured through magnetometry methods.[148–150] Mössbauer spectroscopy is especially useful for studying compounds in which QTM is the dominant relaxation pathway at low temperature. In this case, the Arrhenius plot will feature a large temperature independent region, with only a few temperature dependent points at higher temperatures to fit, before the relaxation times become too fast to be measured (out of frequency range). Mössbauer spectroscopy is also useful for compounds featuring fast relaxation, where even at the low temperature limit of the SQUID (1.8 K), the relaxation is faster than the frequency limit (maximum 1000-10000 Hz).

The objective of this research project is to investigate magnetization dynamics utilizing synchrotron Mössbauer spectroscopy. Notably, this is the first time magnetization dynamics of SMMs have been studied using ^{119}Sn and ^{161}Dy synchrotron Mössbauer spectroscopy.

6.1.1 Introduction to Mössbauer spectroscopy

The basics of Mössbauer spectroscopy will be covered briefly here and a thorough introduction to Mössbauer spectroscopy can be found in Appendix D. Mössbauer spectroscopy is a technique used to study nuclear transitions through the resonant absorption and emission of γ-rays.[151] This technique relies on the Mössbauer effect; the nearly recoil-free resonant absorption and emission in nuclei in a solid crystalline lattice. The Mössbauer effect is limited to isotopes with very low-lying and long-lived excited states. Two of the most ubiquitous nuclei in Mössbauer spectroscopy include ^{57}Fe and ^{119}Sn; both fit the above mentioned criteria. The narrow linewidth of γ-rays makes Mössbauer spectroscopy highly sensitive to small perturbations in energy levels in the absorbing nuclei caused by modifications in the surrounding environment. Parameters that are sensitive to the environment include: isomer shift (δ), quadrupole splitting (ΔE_{Q}) and magnetic (hyperfine) splitting (ΔE_{M}).

The isomer shift, δ, is a shift of the entire spectrum dependent on the local environment surrounding the nuclei. The isomer sift arises from interactions between the nucleus and the inner electrons (s-electrons) and provides information about oxidation state, spin state, and bonding. The isomer shift cannot be measured absolutely, it must be measured relative to a reference (ie α-Fe for ^{57}Fe Mössbauer spectroscopy). Quadrupole splitting, ΔE_{Q}, occurs in nuclei with non-spherical charge distributions ($I > \frac{1}{2}$). Interaction of the nuclei with the asymmetric electric field gradient (efg) splits the nuclear energy levels, providing information about oxidation state and spin state. Magnetic (Zeeman) hyperfine splitting arises from the interaction of the nuclear spin moment with a surrounding magnetic field. The magnetic field splits the nucleus with spin I into ($2I$ + 1) sub-levels. The source of the magnetic field may be inherent to the compound or external, $B_{\mathrm{eff}} = (B_{\mathrm{contact}} + B_{\mathrm{orbital}} + B_{\mathrm{dipolar}}) + B_{\mathrm{applied}}$. The selection rule for allowed nuclear transitions is $\Delta m_{\mathrm{I}} = 0$ or 1.

6.1.2 Investigating magnetization dynamics with Mössbauer spectroscopy

Dynamical magnetic data are typically collected through ac magnetometry using a SQUID magnetometer (Chapter 1, Section 1.1.1). The frequency limit of the magnetometer, a maximum of 1000 to 10,000 Hz depending on the instrument, limits the temperature range over which relaxation times may be studied. At a certain point, relaxation times will become too fast to be measured by magnetometry. Based on this, only a small snapshot of the magnetic relaxation dynamics can be observed using this method (Figure 6.1).

Mössbauer spectroscopy has been used to obtain information about the magnetization dynamics of magnetic materials, including exchange coupling[152–154] and magnetic anisotropy.[153–157] Long and coworkers have shown ^{57}Fe Mössbauer spectroscopy to be a complementary and viable alternative technique to ac magnetometry for the determination of U_{eff} in linear Fe(I) and Fe(II) SIMs.[148–150] Mössbauer spectroscopy is advantageous for the investigation of slow relaxation in SMMs because the lifetime of the measurement is 5-6 orders of magnitude faster than ac magnetometry, thereby allowing for the study of magnetization dynamics at higher temperatures (faster relaxation times) than available using SQUID magnetometry (Figure).

Mössbauer spectroscopy has been utilized to calculate U_{eff} for complexes where it is not possible to determine relaxation times using zero-field ac magnetometry. For example, in the series of trigonal pyramidal iron(II) pyrrolide complex [M(solv)$_n$][(tpa^R)Fe] developed by Harman et al., no signal was observed in the out-of-phase component, χ", under zero dc field at frequencies up to 1500 Hz, the frequency limit of the SQUID magnetometer.[148] This fast relaxation is likely the result of efficient QTM at low temperatures under zero field. Through fitting the temperature dependence of the ^{57}Fe Mössbauer spectra with the Dattagupta and Blume formalism,[158] a zero-field U_{eff} value was calculated from the temperature-dependent region above 10 K.

Mössbauer spectroscopy may also be used as a complementary technique with ac magnetometry to generate an Arrhenius plot over a wider temperature range than possible with ac magnetometry alone. Zadrozny et al. used both ac magnetometry and ^{57}Fe Mössbauer spectroscopy to study the magnetization dynamics of two-coordinate, linear Fe(I) and Fe(II) SIMs.[149,150] Re-

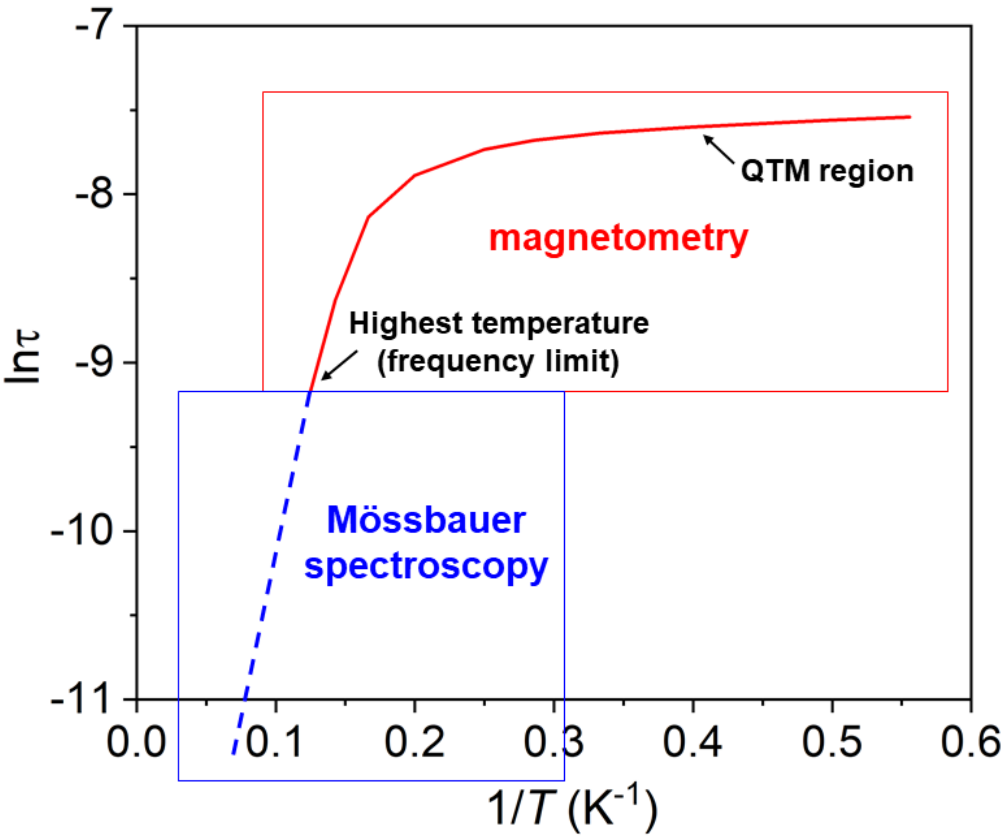

Figure 6.1: Arrhenius plot of a Dy^{3+} compound with prominent QTM at low temperatures. The red line is the temperature region accessible using ac magnetometry. Utilizing Mössbauer spectroscopy, the dashed blue line region would hypothetically be accessible, allowing for the investigation of magnetization dynamics at higher temperatures than achievable through ac magnetometry.

laxation times of the iron(I) complex, [K(crypt-222)][$Fe(C(SiMe_3)_3)_2$], and the iron(II) complex, $Fe(C(SiMe_3)_3)_2$, were calculated by fitting the spectral line broadening as temperature was increased from 5 K up to 295 K. For [K(crypt-222)][$Fe(C(SiMe_3)_3)_2$], plotting the relaxation times obtained from 30 K to 295 K using Mössbauer spectroscopy and below 30 K using ac magnetometry, revealed two Orbach relaxation processes occurring in different temperature regimes, with U_{eff} values of 246 cm^{-1} and 420 cm^{-1}. Notably, the 420 cm^{-1} relaxation process above 40 K could not be observed by ac magnetometry.

Not only has ^{57}Fe Mössbauer spectroscopy been used to study the magnetic properties of iron centers in iron-based single-ion magnets, there have also been examples using an ^{57}Fe nuclei to

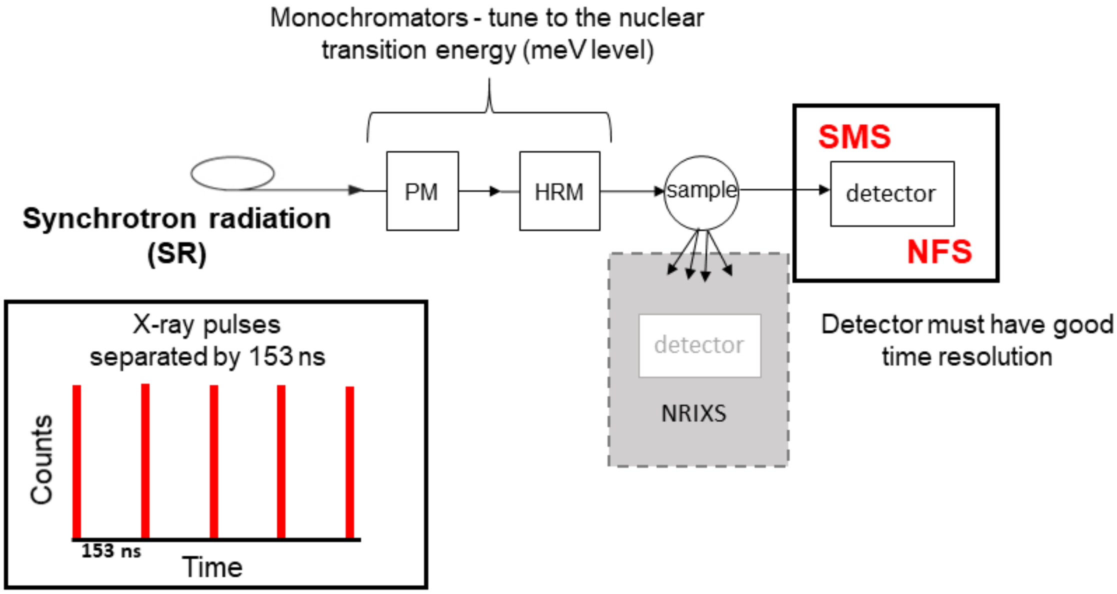

Figure 6.2: Schematic of the experimental setup for SMS at the Advanced Photon Source at Argonne National Lab. PM = premonochromator, HRM = high-resolution monochromator.

investigate the static magnetic properties and relaxation dynamics of nearby paramagnetic metal ions in the crystal lattice. In these examples, typically the Fe center is part of the magnetic system and therefore contributes to the observed magnetic properties.[153–157,159] However, there is precedence for utilizing ferrocenium as a probe for observing the magnetization dynamics in Mn_{12}Ac, in which the Fe center is simply a spectator.[160]

While Mössbauer spectroscopy has been used to calculate U_{eff} in compounds where the Mössbauer active nucleus (^{57}Fe) is also the center of the single-ion magnet, this method has never been extended to include using a Mössbauer active nuclei to determine U_{eff} for a nearby, slowly relaxing paramagnetic ion. This proposed technique would significantly expand the scope of utilizing Mössbauer spectroscopy to obtain information about magnetization dynamics to include any SMM amenable to the addition of Mössbauer active nuclei in the ligand framework or crystalline lattice.

6.1.3 Synchrotron Mössbauer spectroscopy

Synchrotron Mössbauer spectroscopy (SMS) uses highly brilliant synchrotron radiation (SR) tuned to a Mössbauer resonance; producing Mössbauer spectra in the time domain.[161–165] In SMS, an X-ray source tuned to the nuclear transition energy of interest is applied and the nuclear forward scattering (NFS) over time is measured. A schematic of the SMS experimental set-up at the Advanced Photon Source (APS) at Argonne National Laboratory is depicted in Figure 6.2. The X-ray source is the electrons in the synchrotron storage ring. The X-rays pass through an undulator, generating short, high-energy, X-ray pulses in regular time intervals. The time structure at APS is 23 "bunch mode" with a bunch separation time of 153 ns. A series of two monochromators is used to tune the X-ray energy to the nuclear transition energy of interest. The premonochromator (PM) reduces the bandwidth of the incoming electrons to 1 eV, reducing the power of the X-ray beam and protecting the temperature sensitive high-resolution monochromator (HRM). The HRM then tunes the energy to the nuclear transition energy and reduces the bandwidth to a narrow 1 meV. A time-discrimination technique is used to filter out the highly intense electronic scattering. Electronic scattering occurs within femtoseconds of excitation; nearly instantaneous when compared to the delayed nuclear resonant scattering (NRS).[161] Therefore, data collected immediately following the synchrotron radiation pulse is disregarded. After the initial period, all scattering is expected to be nuclear in origin. The placement of the detector allows for either nuclear resonant inelastic scattering (NRIXS) or nuclear forward scattering (NFS) experiments to be performed (Figure 6.2). SMS uses NFS, with the detector placed in line with the incident radiation.

For SMS, the nuclear isotope of interest must possess resonances below 30 keV. At energies higher than 30 keV, the intensity of the SR source decreases and the X-ray optics and detectors become less efficient.[161] A list of possible Mössbauer active isotopes that can be used for SMS is in Table 6.1. Notably, both ^{119}Sn and ^{161}Dy Mössbauer spectroscopy may be performed using synchrotron radiation.[166]

Interpretation of the time spectra generated by SMS requires an understanding of the nuclear forward scattering process. Nuclear transitions of slightly different energies produce phase dif-

Isotope	E_0 (keV)	lifetime (τ) (ns)
^{181}Ta	6.214	8730
^{169}Tm	8.410	5.8
^{83}Kr	9.404	212
^{73}Ge	13.263	4260
^{57}Fe	14.4125	141
^{151}Eu	21.541	14
^{149}Sm	22.496	10.2
^{119}Sn	**23.88**	**25.7**
^{161}Dy	**25.651**	**40.5**
^{40}K	29.83	6.1

Table 6.1: Available Mössbauer active isotopes for SMS.

ferences in the scattered radiation originating from the regions of constructive and destructive interference. This interference creates an oscillation pattern of dynamical and quantum beats that corresponds to the energy differences of the nuclear transitions and the nuclear level splitting. Thickness effects accelerate nuclear decay and lead to asymmetric dynamical beats with no constant frequency, described by Equation 6.1, where I is the intensity of the delayed radiation and t_{eff} is the effective thickness.[167] The effective thickness, t_{eff} of a sample is defined in equation 6.2, where d is the geometric thickness of the sample, n is the number of Mössbauer nuclei per unit volume, σ_0 is the nuclear absorption cross section, and f_{LM} is the Lamb-Mössbauer factor. The Lamb-Mössbauer factor is the fraction of the number of recoil-free transitions of the total number of transitions. Overall, t_{eff} is a measure of the number of nuclei that take part in the coherent scattering.

$$I(t_{\text{eff}}, t) \sim e^{-1/\tau} t_{\text{eff}}^2 \left(\frac{J_1 \sqrt{t_{\text{eff}} t/\tau}}{\sqrt{t_{\text{eff}} t/\tau}} \right)^2 \tag{6.1}$$

$$t_{\text{eff}} = d n f_{\text{LM}} \sigma_0 \tag{6.2}$$

The presence of an electric field gradient (efg) (nuclei with $I > \frac{1}{2}$) results in a spectra featuring quantum beats (QBs) with a regular oscillation frequency corresponding to the quadrupole splitting (ΔE_{Q} according to Equation 6.3; relating the intensity (I) of the delayed radiation over time, t.[167] Both the dynamical (thickness effects) and quantum beat structure (efg) are temperature-dependent. Additionally, magnetic hyperfine interactions also cause a regular beat pattern, further convoluting the time spectra.

$$I(t) \sim e^{-1/\tau}\cos^2\left(\frac{\Delta E_{\mathrm{Q}} \cdot t}{2\hbar}\right) \tag{6.3}$$

6.1.4 Synchrotron Mössbauer spectroscopy vs conventional Mössbauer spectroscopy

In conventional Mössbauer spectroscopy, the radioactive γ-ray source is moved with a tunable velocity (mm s^{-1}), generating an energy spectrum with velocity (mm s^{-1}) on the x-axis. Comparatively, SMS produces spectra in the time domain, with the x-axis in units of time (ns). An inherent disadvantage of SMS is the time-domain spectra are less intuitive to interpret and often require an extensive fitting process.

Some advantages of SMS over conventional Mössbauer spectroscopy include higher intensity and collimation of synchrotron radiation. Additionally, in SMS, polarization of the radiation can be controlled. SMS is especially ideal for Mössbauer nuclei in which the conventional γ-ray source has a short half life. Finally, SMS allows for microfocusing which is ideal for small samples and samples where directionality matters (ie. thin films).[55] A variety of high pressure and high temperature measurements that cannot be done using conventionl Mössbauer spectroscopy can be performed with SMS.[161] However, there are a couple of drawbacks of SMS, including less intuitive spectra and the availability of sychrotron beamtime.

A comparison between spectra in the energy and time domain is shown in Figure 6.3. An SMS spectrum with isomer shift (δ) only is linear, only dependent on the nuclear decay. Quadrupole splitting (ΔE_{Q}) produces oscillations at a constant frequency, called quantum beats (QBs) (Figure 6.3). Thickness effects, which result in line broadening in conventional Mössbauer spectroscopy, cause dynamical beats in an irregular frequency in SMS (Figure 6.3). Finally, hyperfine interac-

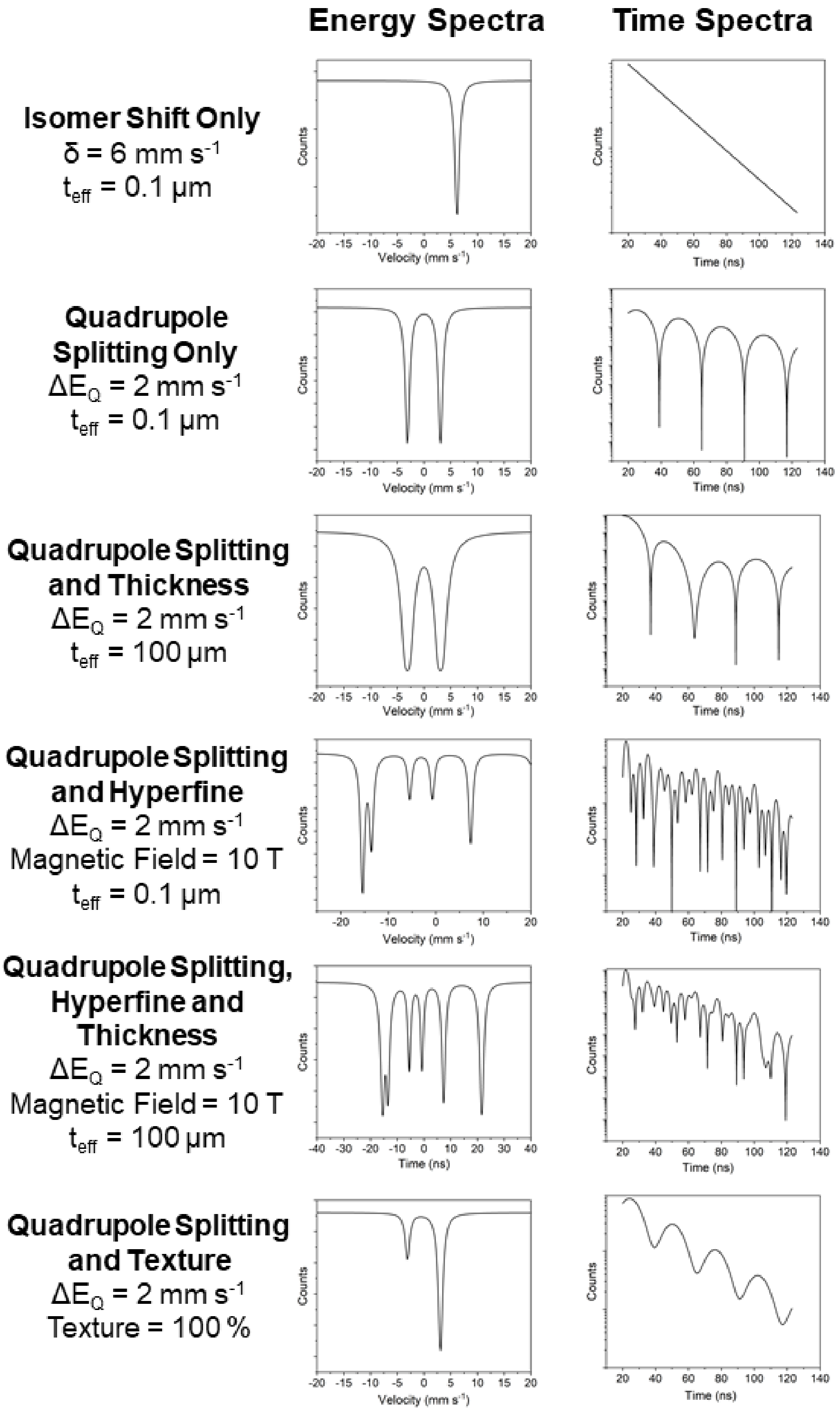

Figure 6.3: Comparison of energy (left) vs time (right) domain ^{119}Sn Mössbauer spectra for the same conditions. Simulations generated using CONUSS.

tions further complicate the spectra by adding additional beats (Figure 6.3). From this, it can be easily observed how the interpretation of SMS spectra may become non-intuitive if several parameters are considered.

All of the ^{119}Sn and ^{161}Dy SMS spectra in this Chapter have been fit using the software CONUSS developed by Sturhahn.[168]

6.1.5 ^{119}Sn and ^{161}Dy Mössbauer spectroscopy

The γ-ray transition used for ^{119}Sn Mössbauer is the 23.88 keV decay from the first excited state. The source used in conventional Mössbauer spectroscopy is metastable ^{119m}Sn ($t_{1/2}$ = 250 d). Using synchrotron radiation, the X-ray energy is tuned to the 23.88 keV transition using a series of monochrometers. ^{119}Sn Mössbauer spectroscopy has some similarities to the more familiar ^{57}Fe Mössbauer spectroscopy. For example, the I = 3/2 to 1/2 transition is a magnetic dipole transition, resulting in similar hyperfine parameters to ^{57}Fe. Additionally, the probability of a recoilless event is similar to ^{57}Fe.[151]

Magnetic hyperfine splitting of the ^{119}Sn resonance is only observed in the presence of a polarizing field external to the Sn atom. The polarizing field could either be a large internal magnetic field generated by a nearby paramagnetic ion or an external applied magnetic field. The magnetic hyperfine field causes polarization of the otherwise spin-paired molecular orbitals (covalent bonds) in Sn. In the first of its kind study presented in this Chapter, we were interested to investigate whether a Sn atom would exhibit magnetic hyperfine effects in the presence of a nearby, slowly relaxation paramagnetic Dy^{3+} ion.

A distinct advantage of using ^{119}Sn Mössbauer spectroscopy over ^{57}Fe Mössbauer spectroscopy for investigating magnetization dynamics is the ease of modifying previously reported compounds to install a Sn atom in the ligand periphery without considerably altering the magnetic properties; provided the symmetry and ligand field aren't significantly altered through the addition of the organostannane moiety. The use of^{119}Sn Mössbauer spectroscopy is advantageous, as the Sn site is diamagnetic and therefore will not contribute to observed magnetic properties; it will simply be spectator.

Dysprosium has six known Mössbauer active resonances, shown in Table 6.2. However, out of the six resonances, the 25.651 keV resonance of the ^{161}Dy isotope is the only one that has been extensively studied, due to the large recoil-free fraction and narrow linewidth (0.37 mm s^{-1}).[151] The 25.65 keV resonance corresponds to the transition between I_e = 5/2 and I_g = 5/2. The ^{161}Dy isotope is 18.889 % abundant, usually negating the need to isotopically enrich samples. Additionally, the ^{161}Dy resonance is the only one that can be measured using synchrotron Mössbauer spectroscopy because it is the only transition that occurs below 30 keV.

Isotope	Natural Abundance (%)	Mössbauer Resonance (keV)
^{160}Dy	2.329	86.79
^{161}Dy	18.889	**25.651**, 43.81, 74.57
^{162}Dy	25.475	80.7
^{164}Dy	28.260	73.392

Table 6.2: Mössbauer active isotopes of dysprosium: their natural abundances and resonant energies.

The source used in conventional ^{161}Dy Mössbauer spectroscopy is typically ^{161}Tb ($t_{1/2}$ = 7 d) produced from the β-decay of ^{161}Gd ($t_{1/2}$ = 3.7 min).[151] The short half lives of the conventional sources is problematic and is a possible reason for the under utilization of ^{161}Dy Mössbauer spectroscopy. An advantage of using SMS for ^{161}Dy Mössbauer spectroscopy is the ability to tune the synchrotron radiation to match the 25.651 keV resonance. Interestingly, ^{161}Dy Mössbauer spectroscopy has never been used to investigate the relaxation dynamics at a Dy^{3+} center of an SMM. This would be analogous to the previously reported examples using ^{57}Fe Mössbauer spectroscopy for investigating relaxation dynamics of Fe-based SIMs.

The objectives for using SMS in this Chapter are two-fold: (1) to use ^{119}Sn synchrotron Mössbauer spectroscopy in a first of its kind study to probe the magnetization dynamics at a nearby Dy^{3+} (paramagnetic) center and (2) to utilize ^{161}Dy synchrotron Mössbauer to investigate relaxation dynamics in a series of Dy^{3+} complexes. Notably, this is the first time SMMs have been investigated by ^{161}Dy or ^{119}Sn Mössbauer spectroscopy. To achieve these objectives, a series of compounds are required that in the ideal case: (a) display slow relaxation under zero dc field by ac magnetometry, (b) are air and moisture stable, and (c) can be easily functionalized to to install organotin groups.

We have chosen to investigate a series of Dy^{3+} tris(hexafluoroacetylacetonate) complexes with either 2,2'-bipyridine (bpy) or 1,10-phenanthroline (phen) capping ligands. There have been many reported examples of tris(b-diketonate)complexes of Dy^{3+} featuring bpy or phen capping ligands that display slow relaxation under zero dc field.[169–172] Additionally, these compounds are air and moisture stable, greatly simplifying the sample preparation and measurements at the synchrotron. Furthermore, organotin moieties, SnR_3 (R = Me, Bu) can be easily installed on the bpy ligand.

In this chapter, a series of tris(hexafluoroacetylacetonate) compounds of Dy^{3+} and Y^{3+} with bpy and phen capping ligands are prepared and characterized. All of the Dy^{3+} compounds have been fully magnetically characterized by ac- and dc- magnetometry. The compounds containing the organotin moeties have been studied by variable temperature ^{119}Sn synchrotron Mössbauer spectroscopy. The Dy^{3+}-based compounds have been characterized by ^{161}Dy Mössbauer spectroscopy. Notably, this is the first time Dy-based SMMs have been investigated using ^{161}Dy Mössbauer spectroscopy.

6.2 Experimental

6.2.1 General considerations

5-Bromo-2,2'-bipyridine was synthesized according to a published procedure.[173] 5-Tri(*n*-butyl)tin-2,2'-bipyridine was prepared as previously reported.[174] Dy(hfac)$_3$(bpy) was prepared according to a previously published procedure.[171] Trimethyltin chloride was purchased from Strem and used as received in air and moisture free conditions. Hexafluoroacetylacetone (Hhfac) was purchased from Strem and used as received. 1,10-Phenanthroline was purchased from Alfa Aesar and used as received. ^{1}H NMR spectra were recorded on an INOVA 500 spectrometer. Elemental analyses were carried out by Midwest Microlab (Indianapolis, IN).

6.2.2 Synthesis

Synthesis of 5-trimethyltin-2,2'-bipyridine, (bpy^{SnMe3}). Prepared via a similar procedure to 5-tri(*n*-butyl)tin-2,2'-bipyridine.[174] To a stirring solution of 5-bromo-2,2'-bipyridine (0.4156 g, 1.768 mmol) in anhydrous, degassed diethyl ether (30 mL) at –78 °C under N_2 a solution of *n*-butyllithium (1.6 M in hexanes, 1.2 mL, 1.9 mmol) was added, resulting in an immediate color change to dark red. The solution was stirred at –78 °C for 3 h under N_2 and then trimethyltin chloride (0.4310 g, 2.163 mmol) in anhydrous, degassed diethyl ether (30 mL) was added by cannula at –78 °C, resulting in an immediate color change to orange and formation of a white precipitate. The solution was stirred at –78 °C for 30 min and then was slowly warmed up to rt and stirred overnight under N_2. After stirring overnight at rt, deionized water (30 mL) was added and the organic layer was collected. The organic layer was washed with 3 x 30 mL of deionized water, 30 mL of sat. aqueous NaCl solution, and dried with $MgSO_4$. All solvent was removed in vacuo, yielding a dark yellow/orange oil. The crude product was purified by column chromatography using neutral alumina and 98:2 to 95:5 petroleum ether to ethyl acetate eluent, yielding a colorless oil (0.238 g, 42 %). Product was confirmed by ^{1}H NMR. ^{1}H NMR (500 MHz, $CDCl_3$, δ): 0.38 (s, 9H, Me), 7.33 (m, 1H, Ar-H), 7.84 (m, 1H, Ar-H), 7.97 (m, 1H, Ar-H), 8.37 (m, 1H, Ar-H), 8.46 (m, 1H, Ar-H), 8.70 (m, 2H, Ar-H).

Synthesis of Dy(hfac)$_3$(H$_2$O)$_2$ and Y(hfac)$_3$(H$_2$O)$_2$. Prepared based on a modified literature procedure.[175,176] Hexaflouroacetylacetone (2.04 g, 9.80 mmol) was dissolved in 125 mL of DI water. Sodium carbonate was added until the pH was approximately 7. Additional water was added as needed to keep everything in solution, resulting in a clear, slightly yellow solution. Dysprosium(III) chloride hexahydrate (1.21 g, 3.21 mmol) was added resulting in immediate formation of a white precipitate. Diethyl ether (100 mL) was layered on top and the solution was stirred for 2 h at rt. The ether layer was decanted off. The aqueous layer was washed with 2 x 25 mL of diethyl ether. The organic (ether) layers were combined and washed with saturated aqueous KCl solution and dried with $MgSO_4$. All volatiles were removed in vacuo. The resulting yellow oil was extracted with hot hexanes. X-ray quality colorless, block crystals (0.560 g, 21.3 %) were formed by cooling and slow evaporation of the concentrated hexanes solutions. Product confirmed by unit cell determination. Unit cell parameters (110 K): a = 9.97 Å, b = 11.56 Å, c = 12.46 Å, α = 67.77 °, β = 73.91 °, γ = 76.01 °, V = 1263 Å^3. For Y(hfac)$_3$(H$_2$O)$_2$: Yield = 48.5 % , unit cell parameters (110 K): a = 9.97 Å, b = 11.54 Å, c = 12.41 Å, α = 67.80 °, β = 73.86 °, γ = 75.76 °, V = 1249.7 Å^3.

Synthesis of Dy(hfac)$_3$(5-trimethylstannyl-2,2'-bipyridine), 6-1. To a solution of Dy(hfac)$_3$(H$_2$O)$_2$ (68.8 mg, 0.0839 mmol) in methanol (4 mL) added a solution of 5-trimethylstannyl-2,2'-bipyridine (48.0 mg, 0.150 mmol) in methanol (3 mL). Stirred for 18 h at rt. All methanol was removed in vacuo, yielding a colorless oil. The oil was extracted with hexanes and the hexanes solution was placed in the freezer (–30 °C). After 48 h at –30 °C, large, X-ray quality colorless crystals formed (64.5 mg, 70 %). Unit cell parameters (110 K): *Cc*, a = 18.2847(9) Å, b = 13.7173(6) Å, c = 15.1827 Å, α = 90 °, β = 105.757(2) °, γ = 90 °, V = 3665.0(3) Å^3. Anal. calcd for $C_{28}H_{19}F_{18}N_2O_6Sn_1Dy_1$: C, 30.50; H, 1.74; N, 2.54 %. Found: C, 30.82; H, 1.81; N, 2.53 %.

Synthesis of Y(hfac)$_3$(5-trimethylstannyl-2,2'-bipyridine), 6-2. Prepared analogously to the Dy^{3+} compound using 5-trimethylstannyl-2,2'-bipyridine (22.2 mg, 0.0696 mmol) and Y(hfac)$_3$(H$_2$O)$_2$ (35.0 mg, 0.0469 mmol). Yield 41.0 mg (85 %). Unit cell parameters (100 K): *Cc*, a = 18.2231(12) Å, b = 13.7012 Å, c = 15.1623 Å, α = 90 °, β = 105.6915(14) °, γ = 90 °, V = 3644.6(4) Å^3. Anal. calcd for $C_{28}H_{19}F_{18}N_2O_6Sn_1Y_1$: C, 32.68; H, 1.86; N, 2.72 %. Found: C, 33.17; H, 1.94; N, 2.71 %.

Synthesis of [Dy(hfac)$_2$(5-tributylstannyl-2,2'-bipyridine)(μ-OMe)]$_2$, 6-3. To a stirring solution of Dy(hfac)$_3$(H$_2$O)$_2$ (50.2 mg, 0.0612 mmol) in methanol (4 mL), added a solution of 5-tributylstannyl-2,2'-bipyridine (52.3 mg, 0.117 mmol) with triethylamine (3 drops) in methanol (2 mL). Immediate formation of a white precipitate. Let stir for 18 h at rt. Decanted off methanol, dried white solid. Recrystallized from a concentrated dichloromethane solution layered with methanol over 48 h. Crystalline yield: 34.0 mg (52.7 %). Unit cell parameters (110 K): $P\bar{1}$, a = 10.4125(5) Å, b = 13.2764(6) Å, c = 15.3756(8) Å, α = 107.122(3) °, β = 102.371(3) °, γ =

102.371(3) °, V = 1950.93(17) Å^3. Anal. calcd for $C_{66}H_{78}F_{24}N_4O_{10}Sn_2Dy_2$: C, 37.65; H, 3.73; N, 2.66 %. Found: C, 37.52; H, 3.94; N, 2.66 %.

Synthesis of [Y(hfac)$_2$(5-tributylstannyl-2,2'-bipyridine)(μ-OMe)]$_2$, 6-4. Prepared analogously to the Dy^{3+} compound with Y(hfac)$_3$(H$_2$O)$_2$ (45.6 mg, 0.0611 mmol) and 5-tributylstannyl-2,2'-bipyridine (46.7 mg, 0.105 mmol). Crystalline yield: 33.6 mg (56.1 %). Unit cell parameters (110 K): P$\bar{1}$, a = 10.565(2) Å, b = 13.224(3) Å, c = 15.376(3) Å, α = 106.91(3) °, β = 102.74(3) °, γ = 96.01(3) °, V = 1971.6(8) Å^3. Anal. calcd for $C_{66}H_{78}F_{24}N_4O_{10}Sn_2Y_2$: C, 40.47; H, 4.01; N, 2.86 %. Found: C, 40.53; H, 4.11; N, 2.83 %.

Synthesis of [Dy(hfac)$_2$(5-tributylstannyl-2,2'-bipyridine)(μ-OH)]$_2$, 6-5. To a stirring solution of Dy(hfac)$_3$(H$_2$O)$_2$ (84.4 mg, 0.103 mmol) in methanol (5 mL), added a solution of 5-tributylstannyl-2,2'-bipyridine (85.2 mg, 0.192 mmol) and triethylamine in methanol (2 mL). Immediate formation of a white precipitate. Let stir for 18 h at rt. Decanted off methanol, dried white solid. Yield: 42.1 % (42.1 mg). Crystallized from slow evaporation of a DCM solution. Unit cell parameters (110 K): a = 9.90 Å, b = 17.33 Å, c = 22.25 Å, α = 90 °, β = 94.96 °,γ = 90 °, V = 3805 Å^3. ^{1}H NMR (500 MHz, CDCl$_3$, δ): -26.01 (s, Ar-H), -17.10 (s, Ar-H), -10.46 (s, Ar-H), -4.70 (s, Ar-H), -0.99 (m, alkyl-H).

Synthesis of [Y(hfac)$_2$(5-tributylstannyl-2,2'-bipyridine)(μ-OH)]$_2$, 6-6. Prepared analogously to the Dy^{3+} compound with Y(hfac)$_3$(H$_2$O)$_2$ (58.0 mg, 0.0777 mmol) and 5-tributylstannyl-2,2'-bipyridine (64.4 mg, 0.145 mmol).

Synthesis of Dy(hfac)$_3$(phen), 6-7. Prepared via similar procedure for Dy(hfac)$_3$(bpy).[171] Dy(hfac)$_3$(H$_2$O)$_2$ (82.0 mg, 0.100 mmol) was refluxed in anhydrous *n*-heptane (40 mL) for 2 h. Let cool below 40 °C, then added 1,10-phenanthroline (19.9 mg, 0.110 mmol) in dichloromethane (10 mL). Refluxed for 1 h and filtered through Celite while still warm. Colorless crystals (20 mg, 20.8 %) were grown from storing the filtrate at –30 °C for 24 h. Unit cell parameters (110 K): a = 21.65 Å, b = 9.39 Å, c = 16.20 Å, α = 90 °, β = 110 °, γ = 90 °, V = 3076 Å^3.

6.2.3 X-ray Crystallography

For compounds **6-2 –6-7**, single crystals suitable for X-ray diffraction were mounted on a MiTiGen loop and placed in a cold N_2 stream at 110 K. A BRUKER APEX 2 Duo X-ray (three-circle) diffractometer was used for unit cell determination and data collection. The X-ray radiation was generated from a Mo sealed X-ray tube (K_α = 0.70173 Å, with a potential of 40 kV and a current of 40 mA). Bruker AXS APEX II software was used for data collection.

For compound **6-1**, a single crystal suitable for X-ray diffraction was mounted on a MiTiGen loop and placed in a cold N_2 stream kept at 100 K. A BRUKER D8 Venture diffractometer was used for unit cell determination and data collection. The X-ray radiation was generated from a Cu sealed X-ray tube (K_α = 1.54178 Å, with a potential of 40 kV and a current of 40 mA). Bruker AXS APEX 3 software was used for data collection.

Data analysis: BRUKER AXS APEX II software was used for data reduction. Absorption corrections were applied using SADABS.[82] A solution was obtained using XT/XS in OLEX2.[81,83–85] Hydrogen atoms were placed in idealized positions and were set riding on the respective parent atoms. All non-hydrogen atoms were refined with anisotropic thermal parameters. The structure was refined (weighted least squares refinement on F^2) to convergence using OLEX2.[85,86]

6.2.4 Magnetic Measurements

Representative procedure for preparation of samples of compounds **6-1**, **6-5**, and **6-7** for magnetic characterization is as follows. Crystalline sample was crushed up into a fine powder and loaded into a high purity 7 mm NMR tube (Norell). A layer of eicosane was added to the tube, covering the sample. The tube was then flame sealed under vacuum. The sealed tube was then placed in a 39 °C water bath until the eicosane was melted and evenly distributed, restraining the sample. The sample was loaded into a straw affixed to the end of the sample rod. For compound **6-3**, crystalline sample was loaded into a plastic bag and crushed into a fine powder. The bag was tightly rolled up and loaded into a straw affixed to the sample rod.

Magnetic measurements were carried out using a Quantum Design MPMS 3 (SQUID) magnetometer (TAMU Vice President of Research). Dc susceptibility measurements were carried out over a temperature range of 2 K to 300 K. Ac susceptibility measurements were carried out using a 2 Oe switching field. Data was corrected for diamagnetic contributions from the straw, sample tube (or bag), eicosane, and core diamagnetism using Pascal's constants.[87] The calculated diamagnetic corrections are as follows: –2.97 x 10^{-8} emu (**6-1**), –6.33 x 10^{-9} emu (**6-3**, –1.09 x 10^{-8} (**6-5**), and –3.77 x 10^{-8} emu (**6-7**).

6.2.5 Synchrotron Mössbauer spectroscopy

^{119}Sn synchrotron Mössbauer spectroscopy experiments were carried out at Sector 3-ID (**6-1**, **6-5**) and Sector 30-ID (**6-2**, **6-6**) at the Advanced Photon Source (APS) at Argonne National Laboratory in collaboration wiht Dr. Ercan Alp, Dr. Wenli Bi, Dr. Ayman Said, and Dr. Michael Hu. Crushed, crystalline sample was loaded into holes (diameter = 1 mm, length = 3.2 mm) on a copper rod. The monochromator was tuned to the transition energy of 23.88 keV. All spectra were collected under zero external field.

^{161}Dy Mössbauer spectroscopy experiments were carried out at Sector 3-ID at the APS at Argonne National Laboratory in collaboration wiht Dr. Ercan Alp, Dr. Wenli Bi, and Dr. Michael Hu. Crushed crystalline sample was loaded into a copper sample holder with holes drilled through it. The back of the holes were covered with Kapton tape. The samples were firmly pressed into the holes and then the holes were covered with Kapton tape. The monochromator was tuned to the transition energy of 25.651 keV. All spectra were collected under zero external field.

All Mössbauer spectra were fit using least-squares regression with the software pacakage CONUSS developed by Sturhahn.[168] All of the samples measured were crushed, polycrystalline powders. To account for the inhomogeneity in the powders, a symmetric gaussian thickness distribution was used in the fits. All errors on fitted parameters are given to the 68 % confidence interval (one standard deviation). Simulation of the energy spectra were generated using CONUSS. The ^{161}Dy Mössbauer spectra were fit by Dr. Wenli Bi (Argonne National Laboratory)

6.3 Results and Discussion

6.3.1 Synthesis and structural characterization

The organotin substituted bpy ligands, 5-trimethylstannyl-2,2'-bipyridine (**bpy$^{\mathbf{SnMe3}}$**) and 5-tributylstannyl-2,2'-bipyridine (**bpy$^{\mathbf{SnBu3}}$**) were prepared from a two-step synthesis. In the first step, 5-bromo-2,2'-bipyridine was prepared from a Stille Coupling between 2,5-dibromopyridine and 2-tributylstannylpyridine, according to a published procedure (Figure 6.4).[173] 5-Bromo-2,2'-bipyridine was then stannylated via a halide substitution with *n*-butyllithium followed by the addition of either trimethyltin chloride or tributyltin chloride at low temperature (–78 °C) to afford the organotin substituted bpy compound in yields of 42 % and 47 %, respectively (Figure 6.4). This procedure was adapted from the reported synthesis of 5-tributylstannyl-2,2'bipyridine.[174]

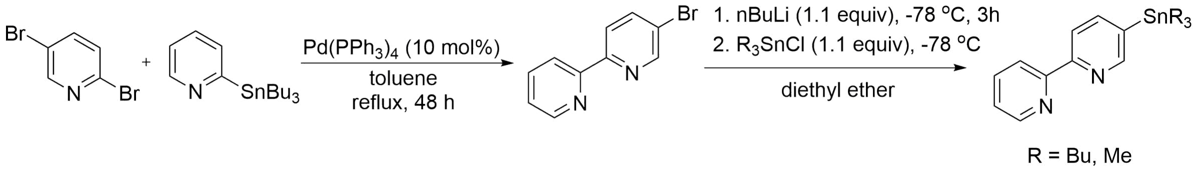

Figure 6.4: Synthesis of the stannylated bpy ligands, 5-trimethylstannyl-2,2'-bipyridine (**bpy$^{\mathbf{SnMe3}}$**) and 5-tributylstannyl-2,2'-bipyridine (**bpy$^{\mathbf{SnBu3}}$**).

The reaction between 5-trimethylstannyl-2,2'-bipyridine (**bpy$^{\mathbf{SnMe3}}$**) and either Dy(hfac)$_3$(H$_2$O)$_2$ or Y(hfac)$_3$(H$_2$O)$_2$ proceeded smoothly at rt to afford the mononuclear compound RE(hfac)$_3$(bpy$^{\mathrm{SnMe3}}$) (RE = Dy (**6-1**), Y (**6-2**)) (Figure 6.5). X-ray quality single plate crystals were grown from concentrated hexanes solutions stored at –30 °C over 24 h in 70 % and 85 % crystalline yields for **6-1** and **6-2**, respectively.

The Dy^{3+} and Y^{3+} compounds **6-1** and **6-2** are isostructural, crystallizing in the monoclinic space group *Cc* (Figure 6.6, Table 6.3). The central RE^{3+} ion is eight-coordinate, with six O donors from the three bidentate hfac ligands and two donors from the one bidentate bipyridine ligand. The geometry around the RE^{3+} center is approximately square antiprismatic, with some distortion. The

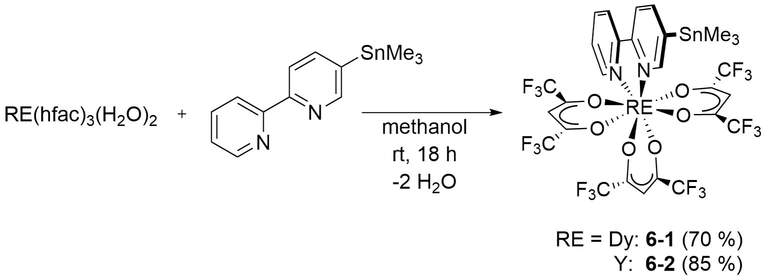

Figure 6.5: Synthesis of the mononuclear compounds RE(hfac)$_3$(bpy^{SnMe3}), RE = Dy^{3+} (**6-1**) and Y^{3+} (**6-2**).

unit cell contains one crystallographically independent RE(hfac)$_3$(bpy^{SnMe3}) moiety, comprising the asymmetric unit. Four RE(hfac)$_3$(bpy^{SnMe3}) moeities make up the unit cell (Z = 4).

Since the Dy^{3+} and Y^{3+} compounds are isostructural, only the Dy^{3+} compound **6-1** will be discussed in detail here. The Dy–O bond lengths range from 2.315(15) to 2.344(14) Å, with an average length of 2.330[14] Å. The two Dy-N bond lengths are 2.49(2) and 2.51(23) Å. It is of note for the following Mössbauer spectroscopy studies that the distance between the Dy^{3+} center and the intramolecular Sn center is 6.370(2) Å and the closest intermolecular Dy···Sn contacts are 7.182 and 7.645 Å. The closest Dy···Dy contact is interplanar, with a distance of 8.043(2) Å. The Dy···Dy contact within the same plane is 11.429(2) Å.

In the previously published structure Dy(hfac)$_3$(bpy, weak π-π stacking was observed between bpy moieties of neighbouring molecules.[171] However, no π-stacking is observed in **6-1** or **6-2**. This may be attributed to the SnMe$_3$ groups preventing π-stacking interactions, likely due to steric considerations.

The dinuclear compounds [RE(hfac)$_2$(bpy^{SnBu3})(μ-OMe)]$_2$ (RE = Dy (**6-3**) and Y (**6-4**)) with bridging methoxide groups, were prepared via the reaction between RE(hfac)$_3$(H$_2$O)$_2$ and 5-tributylstannyl-2,2'-bipyridine (**bpy^{SnBu3}**) in the presence of a small amount of triethylamine (TEA) in methanol at rt (Figure 6.7). The product is insoluble in methanol, resulting in the immediate precipitation of **6-3** and **6-4** out of the solution. X-ray quality large needle crystals were grown from concentrated dichloromethane solutions layered with methanol at rt over 24 h in

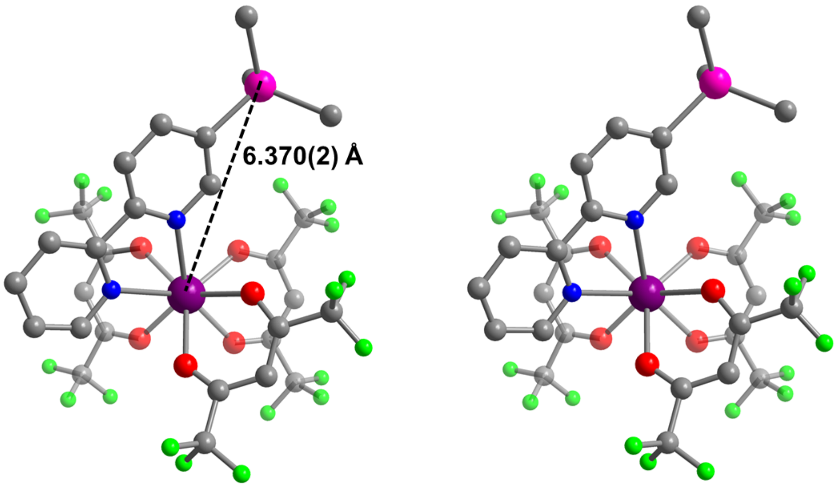

6-1 **6-2**

Figure 6.6: Molecular structures of the isostructural compounds Dy(hfac)$_3$(bpy$^{\mathrm{SnMe3}}$) (**6-1**) (left) and Y(hfac)$_3$(bpy$^{\mathrm{SnMe3}}$) (**6-2**) (right). The intramolecular Dy···Sn distance is shown in **6-1** (6.370(2) Å). Purple = RE, pink = Sn, green = F, red = O, blue = N, grey = C. Hydrogen atoms omitted for clarity.

Compound	**6-1**	**6-2**	**6-3**	**6-4**
Crystal system	monoclinic	monoclinic	triclinic	triclinic
Space group	*Cc*	*Cc*	$P\bar{1}$	$P\bar{1}$
a, Å	18.2847(9)	18.2231(12)	10.4125(5)	10.565(2)
b, Å	13.7173(6)	13.7012(9)	13.2764(6)	13.224(3)
c, Å	15.1827(7)	15.1623(10)	15.3756(8)	15.376(3)
α, °	90	90	107.122(3)	106.91(3)
β, °	105.757(2)	105.6915(14)	102.371(3)	102.74(3)
γ, °	90	90	96.146(3)	96.01(3)
Volume, Å^3	3665.0(3)	3644.6(4)	1950.93(17)	1971.6(8)
Z	4	4	1	1
T, K	100	110	110	110
Density ϱ_{calcd} , mg/m^3	2.225	2.104	1.330	1.584
F(000)	2321	2213	732	899
Radiation type	CuK	Mo	Mo	Mo
Θ_{min} , Θ_{max} , °	4.086, 68.859	1.886, 25.297	2.37, 24.04	1.637, 33.926
Absorption correction	SADABS	SADABS	SADABS	SADABS
Reflections collected	29409	29905	110877	159357
Independent reflections	5824	5907	18778	15729
Final R indices [(I 2σ(I))], wR_2, wR_2	0.0712, 0.1164	0.0320, 0.0582	0.0738, 0.1593	0.0371, 0.0874
R indices (all data), R_1, wR_2	0.1239, 0.1334	0.0450, 0.0615	0.1735, 0.2112	0.0657, 0.1004

Table 6.3: Crystallographic data for **6-1** to **6-4**.

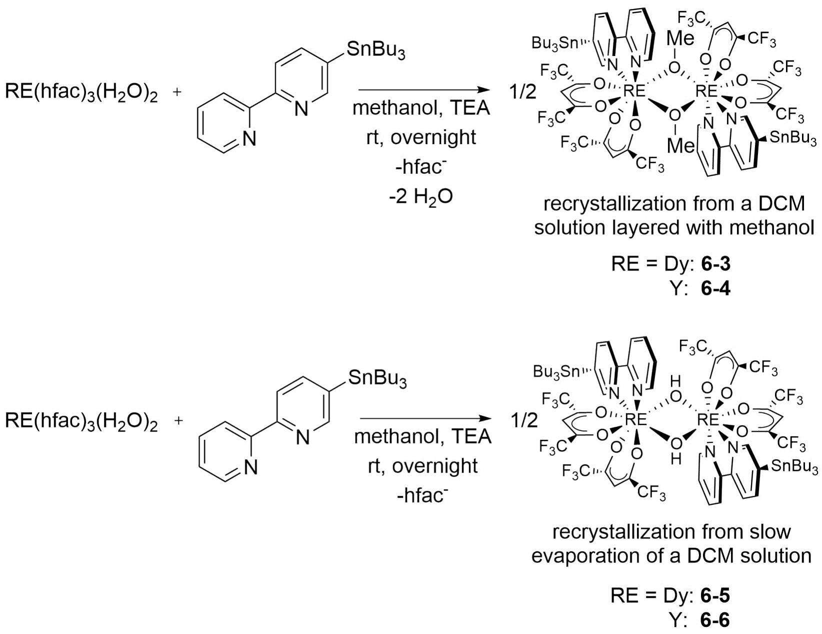

Figure 6.7: Synthesis of the dinuclear methoxide bridged compounds [RE(hfac)$_2$(bpy$^{\mathrm{SnBu3}}$)(μ-OMe)]$_2$, RE = Dy (**6-3**), Y (**6-4**) and hydroxide bridged compounds [RE(hfac)$_2$ (bpy$^{\mathrm{SnBu3}}$)(μ-OH)]$_2$, RE = Dy (**6-5**), Y (**6-6**).

52.7 % and 56.1 % crystalline yields for RE = Dy (**6-3**) and Y (**6-4**), respectively.

The influence of TEA on this reaction was discovered serendipitously. In the purification of 5-tributylstannyl-2,2'-bipyridine by column chromotography, 70:30 hexanes–diethyl ether with 2 % TEA was used as the eluent. After failed attempts at repeating the initial synthesis, it was discovered via ^{1}H NMR spectroscopy that trace amounts of TEA were present in the 5-tributylstannyl-2,2'-bipyridine starting material (sticky oil) that was used in the initial reaction. Through the purposeful addition of TEA to the 5-tributyltin-2,2'-bipyridine solution prior to reacting with RE(hfac)$_3$(H$_2$O)$_2$, the synthesis of **6-3** and **6-4** could be reliably repeated in good yields, with the desired product consistently crashing out as a precipitate from methanol. It should be noted that carrying out the reaction between RE(hfac)$_3$(H$_2$O)$_2$ and **bpy$^{\mathbf{SnBu3}}$** in methanol in the absence of TEA did not result in the formation of a precipitate and no crystalline product could be isolated, despite many crystallization conditions attempted.

Presumably, TEA (weak base) is necessary for the deprotonation of methanol to form the bridging methoxide groups. Notably, one hfac ligand per RE center is lost during the reaction and is replaced by the bridging methoxide moieties. It is unusual for hfac$^-$ ligand loss to occur in these complexes, as the hfac ligands are typically thought of as not labile. On account of insolubility in methanol, the dinuclear compound with two hfac ligands, one **bpy**$^{\mathbf{SnBu3}}$ ligand and bridging methoxide or hydroxide groups precipitates out of the solution immediately. This product is possibly an intermediate or a kinetic product that is trapped as it forms due to insolubility in methanol.

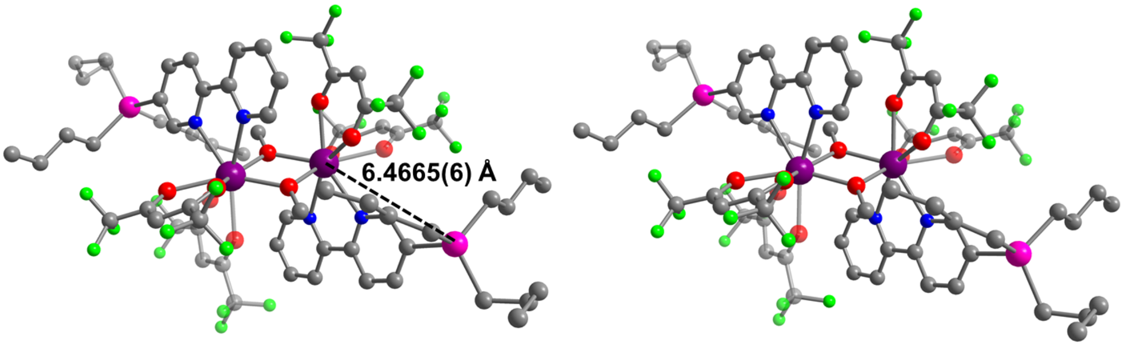

6-3 **6-4**

Figure 6.8: Molecular structure of [Dy(hfac)$_2$(bpy^{SnBu3})(μ-OMe)]$_2$ (left) and [Y(hfac)$_2$(bpy^{SnBu3})(μ-OMe)]$_2$ (right). The intramolecular Dy···Sn distance is shown in **6-3** (6.4665(6) Å). Purple = RE, pink = Sn, green = F, red = O, blue = N, grey = C. Hydrogen atoms omitted for clarity.

The dinuclear compounds **6-3** and **6-4** are isostructural, crystallizing in the triclinic space group $P\bar{1}$ (Figure 6.7, Table 6.3). The asymmetric unit contains one-half of the dinuclear molecule; resulting in only one unique RE center and one unique Sn center. The unit cell contains only one molecule of the dinuclear compound (Z = 1) (Figure 6.8). The RE^{3+} center is eight-coordinate and the geometry around the RE^{3+} center is approximately square antiprismatic (distorted). The RE^{3+} center has six O donors, four from the two bidentate hfac ligands and two from the bridging methoxide groups. In addition, there are two N donors from the **bpy**$^{\mathbf{SnBu3}}$ ligand.

Since **6-3** and **6-4** are isostructural, only the structure of the Dy^{3+} complex **6-3** is discussed in detail here. The Dy–O$_{(hfac)}$ bond lengths range between 2.365(4) and 2.422(4) Å, with an average

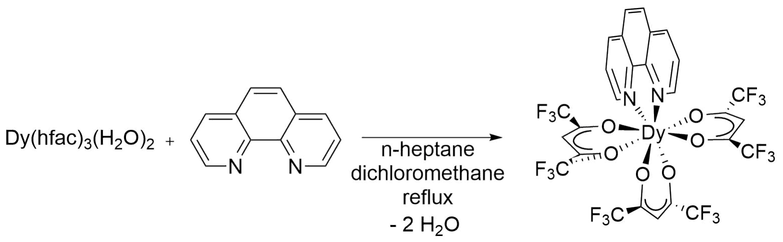

Figure 6.9: Synthesis of Dy(hfac)$_3$(phen) (**6-7**).

bond length of 2.388[4] Å. The Dy–O bonds to the bridging methoxides are comparably shorter, with bond lengths of 2.250(4) and 2.266(4) Å. The Dy–N bond lengths are 2.533(5) and 2.549(5) Å. The Dy···Dy distance is 3.6930(6) Å, which is outside of the sum of the ionic radii of 2.54 Å (eight-coordinate Dy^{3+} ionic radius = 1.027 Å).

The distance between the Dy^{3+} center and the intramolecular Sn center is 6.4665(6) Å. This is longer than the Dy···Sn distance in **6-1** by nearly 0.1 Å. The closest intermolecular Dy···Sn distance in **6-3** is 8.837(7) Å. In the crystal packing, the RE^{3+} ions are aligned in approximately in the same plane, with the tributyltin groups occupying the interplanar region between the planes of the RE centers. The powder X-ray diffraction pattern of **6-3** indicated the presence of only the bridging methoxide complex (no hydroxide-bridged complex).

Crystallization of the reaction between Dy(hfac)$_3$(H$_2$O)$_2$ and 5-tributyltin-2,2'-bipyridine (bpy^{SnBu3}) from the slow evaporation of a DCM solution yielded the dinuclear hydroxide bridged compound, [Dy(hfac)$_2$(bpy^{SnBu3})(μ-OH)]$_2$ (**6-5**) (Figure 6.7). The isostructural Y^{3+} compound could also be prepared via the same route (**6-6**). Interestingly, with the change in crystallization conditions the identity of the bridging group also changes, either a bridging methoxide (methanol layered on DCM) or hydroxide (slow evaporation of DCM). The crystals grown from the slow evaporation of DCM were of poor quality, however connectivity could be established, indicating the hydroxide bridge species; with a different unit cell than that obtained for the methoxide bridged species.

The compound Dy(hfac)$_3$(phen) (**6-7**) could be prepared analogously to Dy(hfac)$_3$(bpy) as described by Wang et al. (Figure 6.9).[171] The compound was crystallized from *n*-heptane at –30 °C in an 20.8 % crystalline yield. The crystals obtained were high-quality, however the molecule suffers from entire molecule disorder. Despite the disorder, the connectivity can be established without refining. Work to solve the whole molecule disorder is ongoing at this time.

6.3.2 Static magnetic properties

The static magnetic properties of the Dy^{3+} complexes **6-1**,**6-3**, **6-5**, and **6-7** were investigated under a 1000 Oe (0.1 T) dc field over a temperature range of 300 –2 K. The measured room temperature $\chi_M T$ value in **6-1** of 14.23 cm^3 K mol^{-1} is consistent with the expected value of 14.17 cm^3 K mol^{-1} for one, non-interacting Dy^{3+} center ($^6H_{15/2}$, S = 5/2, L = 5, g = 4/3) (Figure 6.10). Upon cooling, there is a gradual decrease down to 90 K, where the $\chi_M T$ value begins to decreases more drastically. There is an additional change in slope below 15 K, where the $\chi_M T$ value decreases rapidly to reach a minimum value of 11.25 cm^3 K mol^{-1} at 2 K. The room temperature $\chi_M T$ value of 13.50 cm^3 K mol^{-1} for the complex **6-7** is lower than the expected value for one, non-interacting Dy^{3+} center ($^6H_{15/2}$, S = 5/2, L = 5, g = 4/3) (Figure 6.10). However, lower than expected $\chi_M T$ values have been reported for Dy^{3+} complexes. While the inflection points suggest a phase change, similar types of compounds have been investigated using low temperature X-ray crystallography and structural thermal effects were determined to be negligible.[177]

The room temperature $\chi_M T$ value for the dinuclear complex **6-3** of 27.25 cm^3 K mol^{-1} is lower than the expected value for two, non-interacting Dy^{3+} centers of 28.24 cm^3 K mol^{-1}. Notably, no ferromagnetic coupling is seen at low temperatures between the Dy^{3+} centers. Interestingly, ferromagnetic coupling is observed in the $\chi_M T$ of the hydroxide bridged complex **6-5** at low temperatures (below 15 K). However the room temperature $\chi_M T$ value for **6-5** is 22.80 cm^3 K mol^{-1}, much lower than the expected value of 28.24 cm^3 K mol^{-1}. This is attributed to mass error, as only 5.2 mg of sample was used in the measurement.

6.3.3 Magnetization dynamics

The magnetization dynamics of the Dy^{3+} complexes **6-1**, **6-3**, **6-5**, and **6-7** were investigated using alternating current (ac) susceptibility measurements. In the mononuclear compound **6-1**,

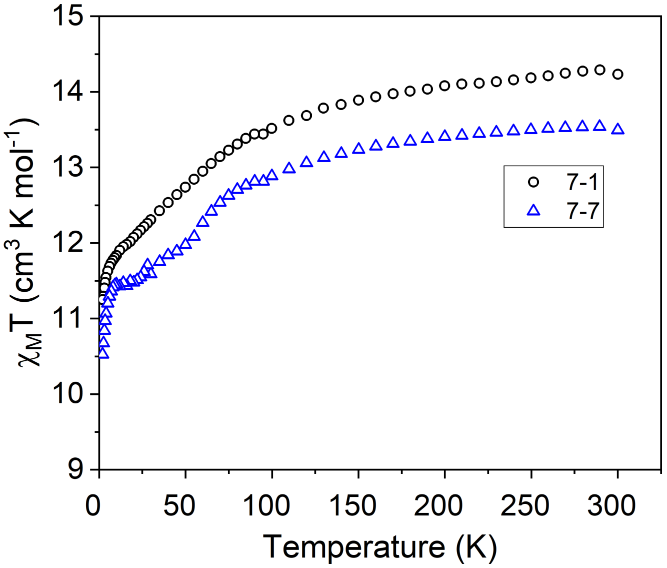

Figure 6.10: Temperature dependence of the molar magnetic susceptibility times temperature product ($\chi_\mathrm{M}T$) in **6-1** (black circles) and **6-7** (blue triangles).

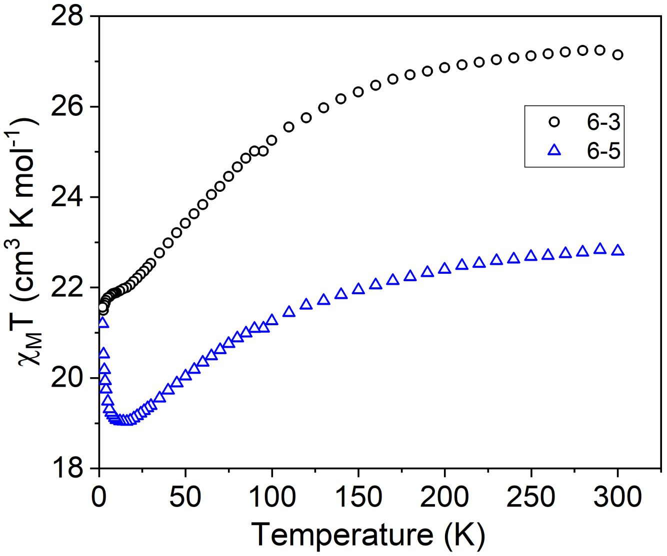

Figure 6.11: Temperature dependence of the molar magnetic susceptibility times temperature product ($\chi_\mathrm{M}T$) in the dinuclear complexes **6-3** (black circles) and **6-5** (blue triangles).

slow relaxation was observed in the out-of-phase component (χ") of the ac susceptibility at low temperatures under zero dc field (Figure 6.12). However, the maxima of the out-of-phase, χ", signal at 1.8 K is at 800 Hz, nearly outside the frequency limit of the magnetometer (1000 Hz). There is considerable QTM at low temperatures, as can be observed in the temperature independence of the χ" peak maxima and the temperature independent region of the Arrhenius plot (Figure 6.12). The lack of temperature dependence of the relaxation times (τ) precluded the calculation of U_{eff} from the zero field ac susceptibility data.

Notably, a similar compound, Dy(hfac)$_3$(bpy), has been reported to display slow relaxation under zero dc field with U_{eff} = 26.7 cm^{-1}, albeit this barrier height was determined through fitting only three temperature dependent data points.[171] The slight changes in the coordination geometry and packing with the addition of the SnMe$_3$ moiety to the 2,2'-bipyridine ligand influence have a considerable influence on the magnetization dynamics.

Due to the predominance of QTM in **6-1**, the ac susceptibility was measured under the presence of dc fields of varying strength at 5 K (Figure 6.13). At small dc fields of 250–600 Oe, a transition to a slower relaxation process is observed. At dc fields above 700 Oe, only the slower process is observed. This can be attributed to the mitigation of QTM through the application of the dc field. The field-dependence of τ was fit to Equation 6.4, accounting for the field-dependent direct and QTM relaxation pathways. From the field-dependence of τ, an optimal field of 1000 Oe (slowest relaxation) was selected for temperature dependent ac measurements.

$$\tau^{-1} = AH^{n_1}T + \frac{B_1}{1 + B_2H^2} + D \qquad (6.4)$$

At an applied dc field of 1000 Oe, the maxima of the out-of-phase signals (χ") are shifted to lower frequencies relative to the zero field measurements, as the mitigation of QTM results in slower relaxation (Figure 6.14). For comparison, at 2 K under a 1000 Oe dc field, the maximum in the out-of-phase signal is less than 1 Hz (out of the low frequency range), whereas under zero dc field the maximum occurs at 800 Hz. Furthermore, with an applied 1000 Oe dc field, temperature dependence is observed over the entire temperature range investigated (2 K to 8 K) (Figure 6.14).

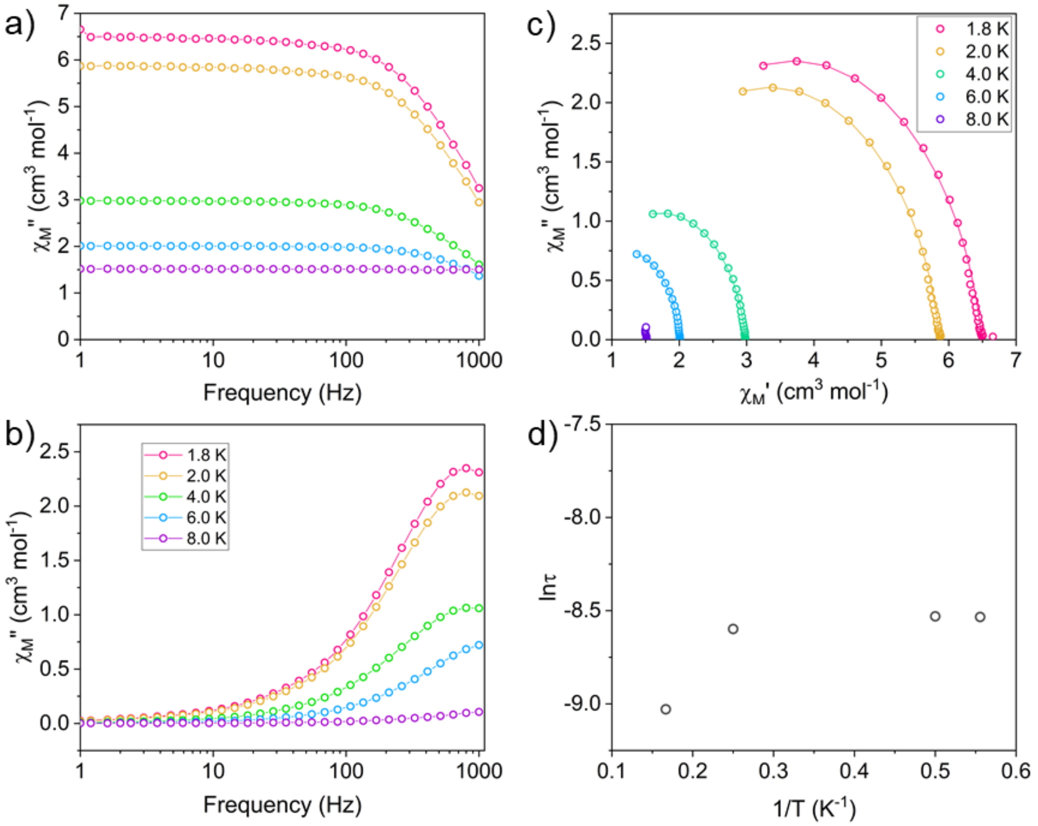

Figure 6.12: Ac susceptibility measurements for **6-1** under zero dc field. (Left) Frequency dependence of the (a) in-phase (χ') and (b) out-of-phase (χ'') components of the ac susceptibility. (c) Cole-Cole plots, open circles are experimental data and lines are fits to the generalized Debye equation. (d) Arrhenius plot.

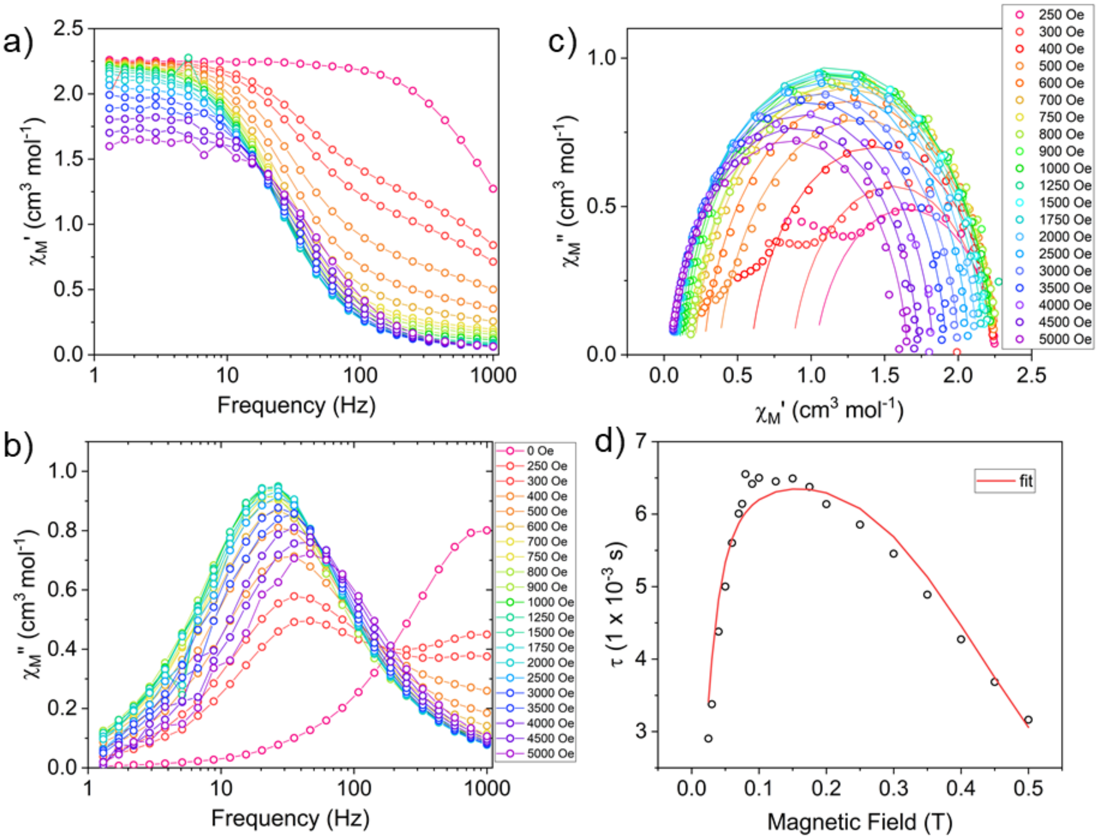

Figure 6.13: Ac susceptibility measurements for **6-1** at 5 K under various dc fields. (left) Frequency dependence of the (a) in-phase (χ') and (b) out-of-phase (χ'') components of the ac susceptibility. (c) Cole-Cole plots, open circles are experimental data and lines are fits to the generalized Debye equation. (d) Field-dependence of the relaxation time, τ. Open circles are experimental data points. Red line is fit to the Equation 6.4.

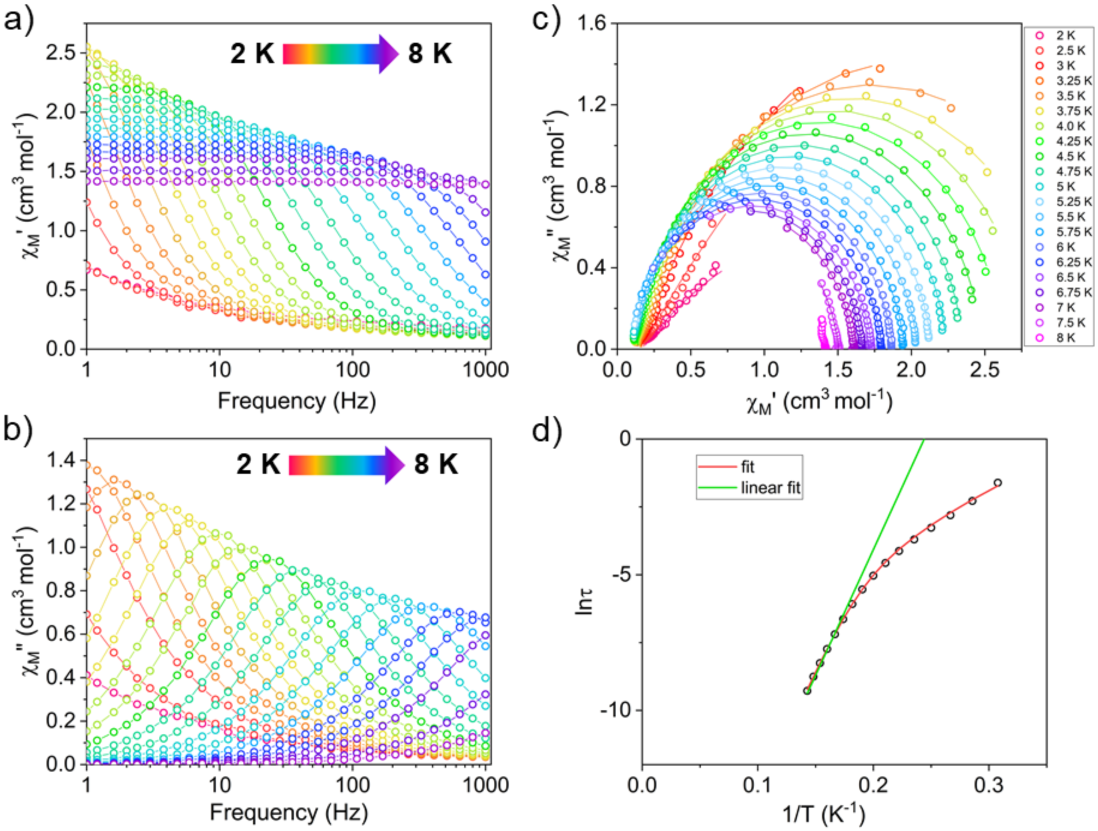

Figure 6.14: Ac susceptibility measurements for **6-1** under a 1000 Oe dc field from 2 K to 8 K. (left) Frequency dependence of the (a) in-phase (χ') and (b) out-of-phase (χ'') components of the ac susceptibility. (c) Cole-Cole plots, open circles are experimental data and lines are fits the generalized Debye equation. (d) Arrhenius plot, black circles represent experimental data. The green line represents fits of the linear region to Equation 6.6. The red line represents fits of the entire temperature region to Equation 6.5.

The Arrhenius plot (lnτ vs T^{-1}) for the 1000 Oe applied field measurements was fit using least squares regression to a model that accounted for multiple relaxation pathways, including direct, QTM, Raman, and Orbach (Equation 6.5). To avoid overparameterization during fitting, the direct relaxation parameter, A, was obtained through fitting the field dependence of τ (Figure 6.13), according to eqn 6.4. Typically, n_1 = 4 for Kramers ions in the absence of hyperfine interactions.[12] For Kramers ions, parameter n_2 of the Raman pathway term is expected to be 9, although allowing n_2 to be a free-fit parameter resulted in a value of n_2 = 7. It has been previously noted that lower n_2 values may be expected in systems with low-lying excited states if optical phonons are taken into consideration.[12,127] The parameters C (Raman coefficient), τ_0 (pre-exponential factor), U_{eff} (thermal barrier for Orbach relaxation) and τ_{QTM} were treated as free-fit parameters. A barrier height of U_{eff} = 66.0 cm^{-1} (τ_0 = 7.04 x 10^{-10} s) was obtained for **6-1**. A linear approximation fit to equation 6.6 was also applied, yielding a U_{eff} value of 64.4 cm^{-1} (τ_0 = 1.52 x 10^{-10} s). This is larger than the U_{eff} determined for Dy(hfac)$_3$(bpy) under zero dc field. However, applied field ac measurements have not been carried out on Dy(hfac)$_3$(bpy), therefore no direct comparison can be made at this time.

$$\tau^{-1} = AH^{n_1}T + \tau_{\text{QTM}}^{-1} + CT^{n_2} + \tau_0^{-1}\exp\left(\frac{-U_{\text{eff}}}{k_{\text{B}}T}\right) \tag{6.5}$$

$$\tau^{-1} = \tau_0^{-1}\exp\left(\frac{-U_{\text{eff}}}{k_{\text{B}}T}\right) \tag{6.6}$$

The dinuclear compound, **6-3**, displays no evidence of slow relaxation under zero dc field, at temperatures as low as 2 K and frequencies up to 1000 Hz. However, field-induced slow relaxation was observed, even with the application of only a very small dc field of 250 Oe (Figure 6.15). Likely the absence of a signal in the out-of-phase component of the ac susceptibility under zero dc field is a result of efficient QTM, which is suppressed with the application of even slight dc fields. The ac susceptibility was measured at 5 K under various dc fields from 250 Oe up to 5000 Oe (Figure 6.15). The relaxation times slow (χ''_{max} to lower frequencies) until a dc field of 1250

Oe, a result of decreasing QTM, and then remain nearly constant from 1250 to 2250 Oe. Above 2250 Oe, relaxation times decrease due the prevalence of direct processes. The field dependence of τ was fit with Equation 6.4. A dc field of 1500 Oe was selected for the temperature-dependent ac measurements.

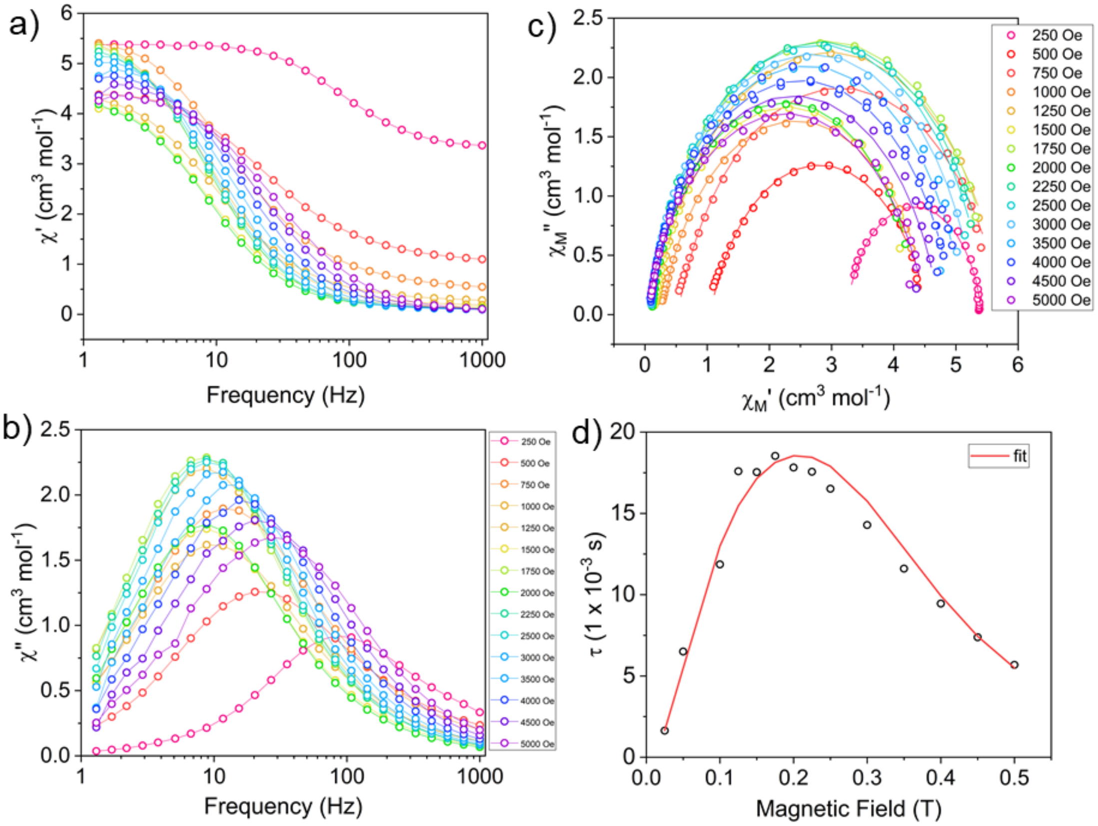

Figure 6.15: Ac susceptibility measurements for **6-3** at 5 K under varying dc field strengths. (left) Frequency dependence of the (a) in-phase (χ') and (b) out-of-phase (χ") components of the ac susceptibility. (c) Cole-Cole plots, open circles are experimental data and lines are fits to the generalized Debye equation. (d) Field-dependence of the relaxation time, τ. Open circles are experimental data points. Red line is fit to the Equation 6.4.

Variable temperature ac susceptibility measurements for **6-3** were collected with a static dc field of 1500 Oe. The relaxation times show temperature dependence across the entire temperature range investigated (2 –14 K). The Arrhenius plot was fit with Equation 6.5 to account for direct,

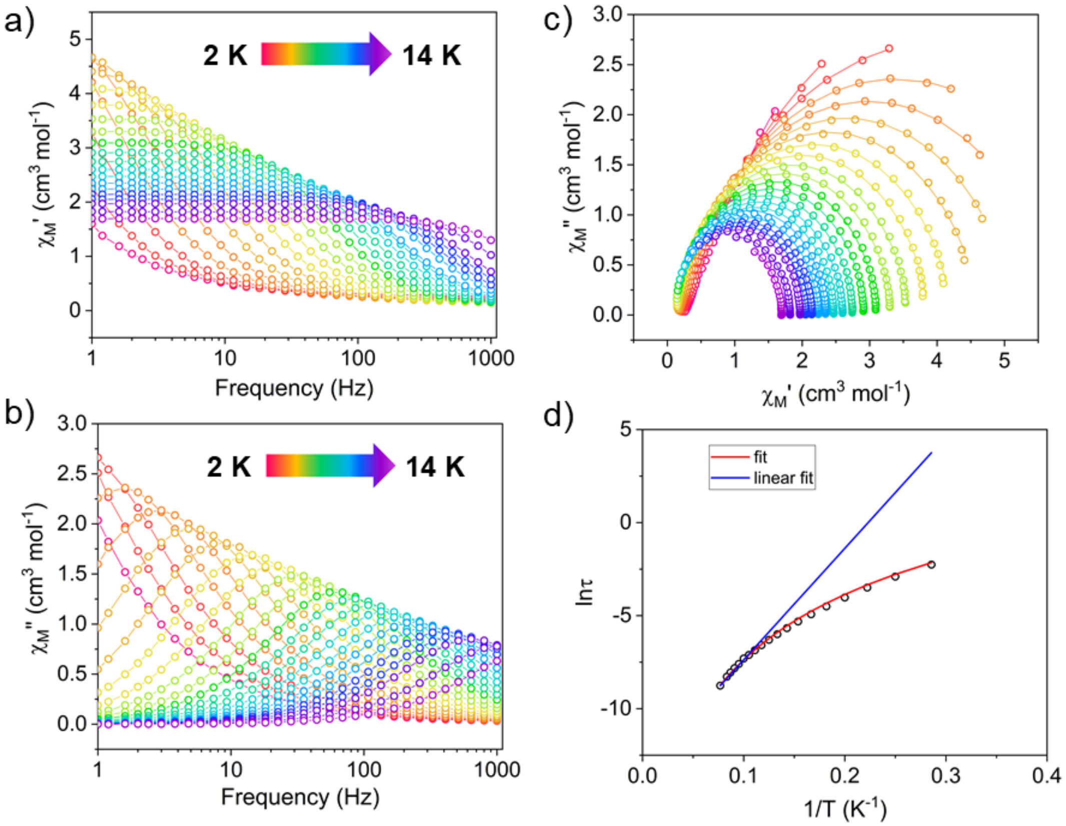

Figure 6.16: Ac susceptibility measurements for **6-3** under a 1500 Oe applied dc field. (left) Frequency dependence of the (a) in-phase (χ') and (b) out-of-phase (χ") components of the ac susceptibility. (c) Cole-Cole plots, open circles are experimental data and lines are fits the generalized Debye equation. (d) Arrhenius plot, black circles represent experimental data. The blue line represents fits of the linear region to Equation 6.6. The red line represents fits of the entire temperature region to Equation 6.5.

Raman and Orbach relaxation. The direct relaxation parameter, A, was determined from the field-dependence of τ and was held constant during the fitting of the Arrhenius plot. Parameters C, U_{eff}, and τ_0 were treated as free fit parameters. For **6-3** under a 1500 Oe dc field, a U_{eff} value of 51.8 cm^{-1} (τ_0 = 5.03 x 10^{-6} s) was determined from fitting with Equation 6.5. For comparison, a linear approximation afforded U_{eff} = 41.7 cm^{-1} (τ_0 = 1.56 x 10^{-6} s).

In contrast to the methoxide bridged complex **6-3**, the hydroxide bridged complex **6-5** displays slow relaxation under zero dc field (Figure 6.17). A prominent QTM region is apparent at lower temperatures, however temperature dependence is observed above 3 K. From the temperature de-

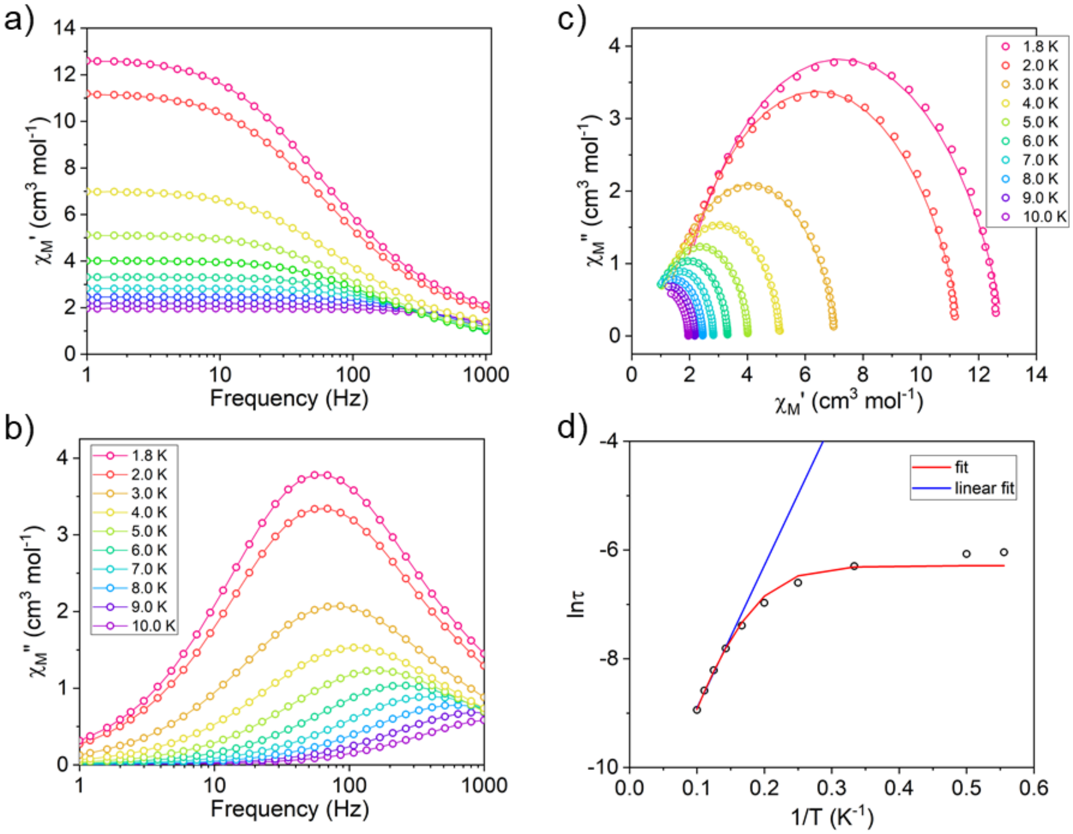

Figure 6.17: Ac susceptibility measurements for **6-5** under zero dc field. (left) Frequency dependence of the (a) in-phase (χ') and (b) out-of-phase (χ") components of the ac susceptibility. (c) Cole-Cole plots, open circles are experimental data and lines are fits the generalized Debye equation. (d) Arrhenius plot, black circles represent experimental data. The blue line represents fits of the linear region to Equation 6.6. The red line represents fits of the entire temperature region to Equation 6.5.

pendence of the τ, a barrier height U_{eff} = 18.6 cm^{-1} (τ_0 = 1.43 x 10^{-5} s) was determined through fitting to Equation 6.5. The parameters U_{eff}, τ_0, τ_{QTM}, and C were treated as free-fit parameters and an n_2 value of 5 was used, corresponding to low-lying exited states. Note the direct process term in Equation 6.5 disappears under zero field. A fit of the linear region of the Arrhenius plot gave a value of U_{eff} = 18.2 cm^{-1} (τ_0 = 9.86 x 10^{-6} s). The field dependence of the relaxation time for **6-5** still needs to be determined.

In **6-7**, slow relaxation was observed in the form of a signal in the out-of-phase component (χ") of the ac susceptibility under zero dc field. There is a prominent QTM region at low temperatures, however from the temperature dependent region a barrier height of U_{eff} = 48.5 cm^{-1} (τ_0 = 6.01 x 10^{-6} s) was calculated using Equation 6.5 and treating U_{eff}, τ_0, τ_{QTM}, and C as free-fit parameters and an n_2 value of 5, corresponding to a Kramers ion with low-lying excited states. A linear approximation using Equation 6.6 gave U_{eff} = 23.6 cm^{-1} (τ_0 = 6.01 x 10^{-6} s). The ac susceptibility in **6-7** was investigated under various dc fields at 8 K (Figure 6.19). A transition from a faster to a slower relaxation process is observed at applied fields from 250 to 500 Oe. Relaxation times decrease only slightly after reaching a maximum at 1800 Oe dc field, attributed to very small contributions from the direct relaxation pathway.

Variable temperature ac susceptibility measurements for **6-7** were carried out under an applied dc field of 1000 Oe (Figure 6.20). Under a 1000 Oe dc field, temperature dependence is observed over the entire temperature range studied from 4 K to 12 K. Below 4 K, the maxima in χ" are less than 1 Hz and above 12 K the maxima in χ" are greater than 1000 Hz (high frequency limit). The temperature dependence of τ with equation 6.5 treating U_{eff}, τ_0, τ_{QTM}, and C as free fit parameters. A value of n_2 = 5 was used, same as in the zero-field data, accounting for low-lying excited states. The direct relaxation parameter, A determined from fitting the field dependence was held constant at 466.25 s^{-1} T$^{-n_1}$ K^{-1}. The fit resulted in U_{eff} = 77.6 cm^{-1} (τ_0 = 1.72 x 10^{-8} s). A linear approximation gave U_{eff} = 58.4 cm^{-1} (τ_0 = 1.25 x 10^{-7} s).

6.3.4 ^{119}Sn synchrotron Mössbauer spectroscopy

Using synchrotron Mössbauer spectroscopy (SMS), the ^{119}Sn Mössbauer spectra of compounds **6-1**, **6-2**, **6-5**, and **6-6** were collected. The synchrotron X-ray radiation was tuned to the ^{119}Sn transition energy of 23.88 keV. The ^{119}Sn Mössbauer spectra were collected with zero external field. All of the ^{119}Sn Mössbauer spectra were fit using the program CONUSS, developed by Sturhahn.[168] The fits are discussed in detail below.

In compound **6-5**, ^{119}Sn Mössbauer spectra were collected from 7.5 K up to 90 K (Figure 6.21). At 90 K, the count rate dropped drastically, greatly lengthening data collection times. The spectra display two asymmetric beats that shift to longer times (ns) with increasing temperature. The time dependence of the beat structure is dependent on the effective thickness (t_{eff}), quadrupole

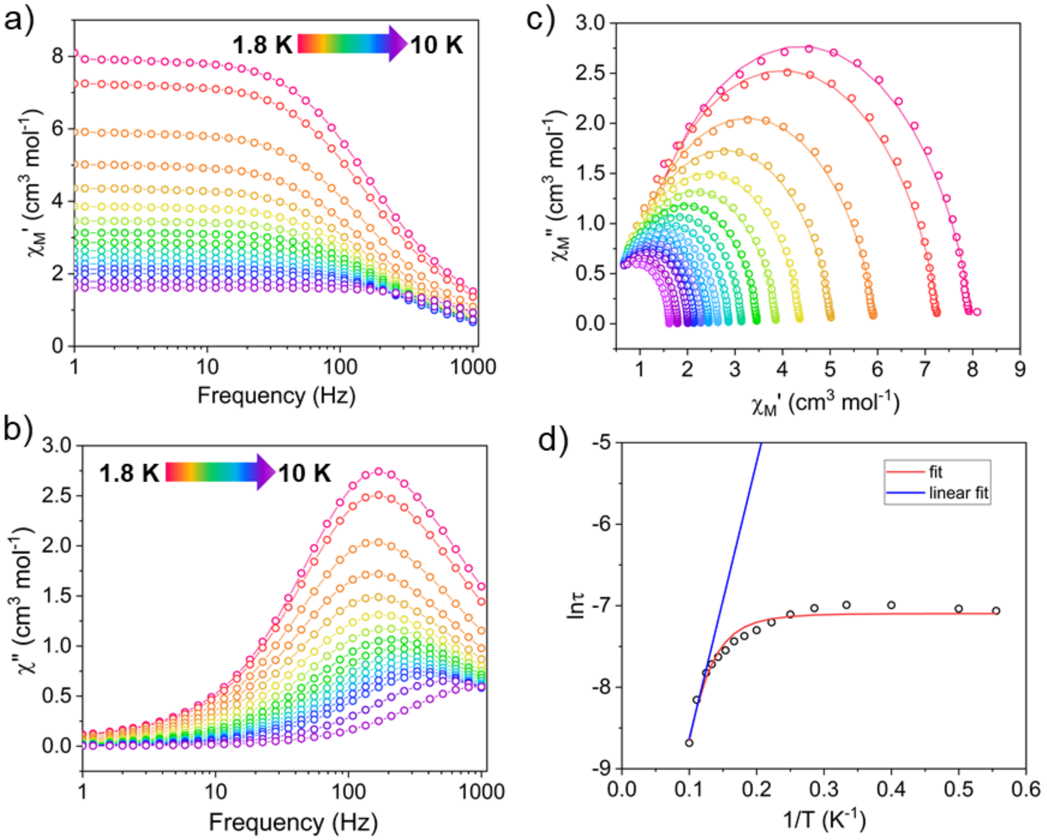

Figure 6.18: Ac susceptibility measurements for **6-7** under a zero field. (left) Frequency dependence of the (a) in-phase (χ') and (b) out-of-phase (χ") components of the ac susceptibility. (c) Cole-Cole plots, open circles are experimental data and lines are fits the generalized Debye equation. (d) Arrhenius plot, black circles represent experimental data. The blue line represents fits of the linear region to Equation 6.6. The red line represents fits of the entire temperature region to Equation 6.5.

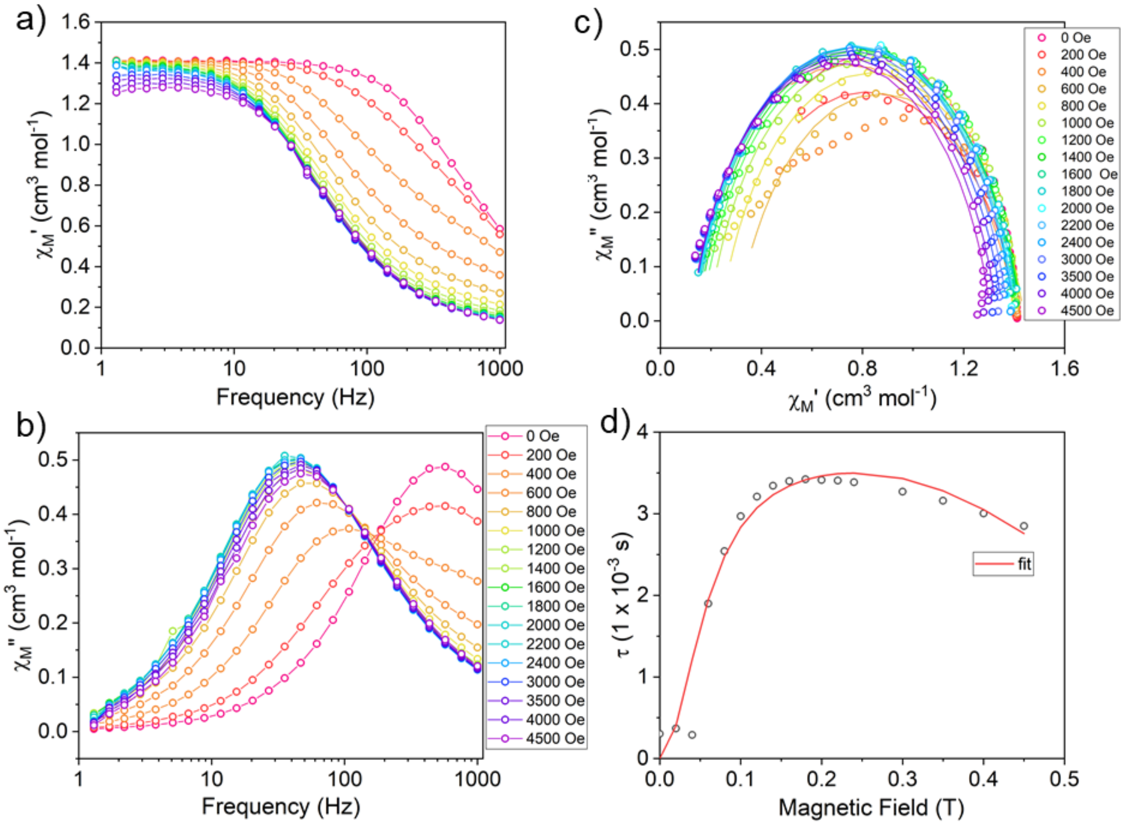

Figure 6.19: Ac susceptibility measurements for **6-7** at 8 K under various dc fields. (left) Frequency dependence of the (a) in-phase (χ') and (b) out-of-phase (χ") components of the ac susceptibility. (c) Cole-Cole plots, open circles are experimental data and lines are fits to the generalized Debye equation. (d) Field-dependence of the relaxation time, τ. Open circles are experimental data points. Red line is fit to the Equation 6.4.

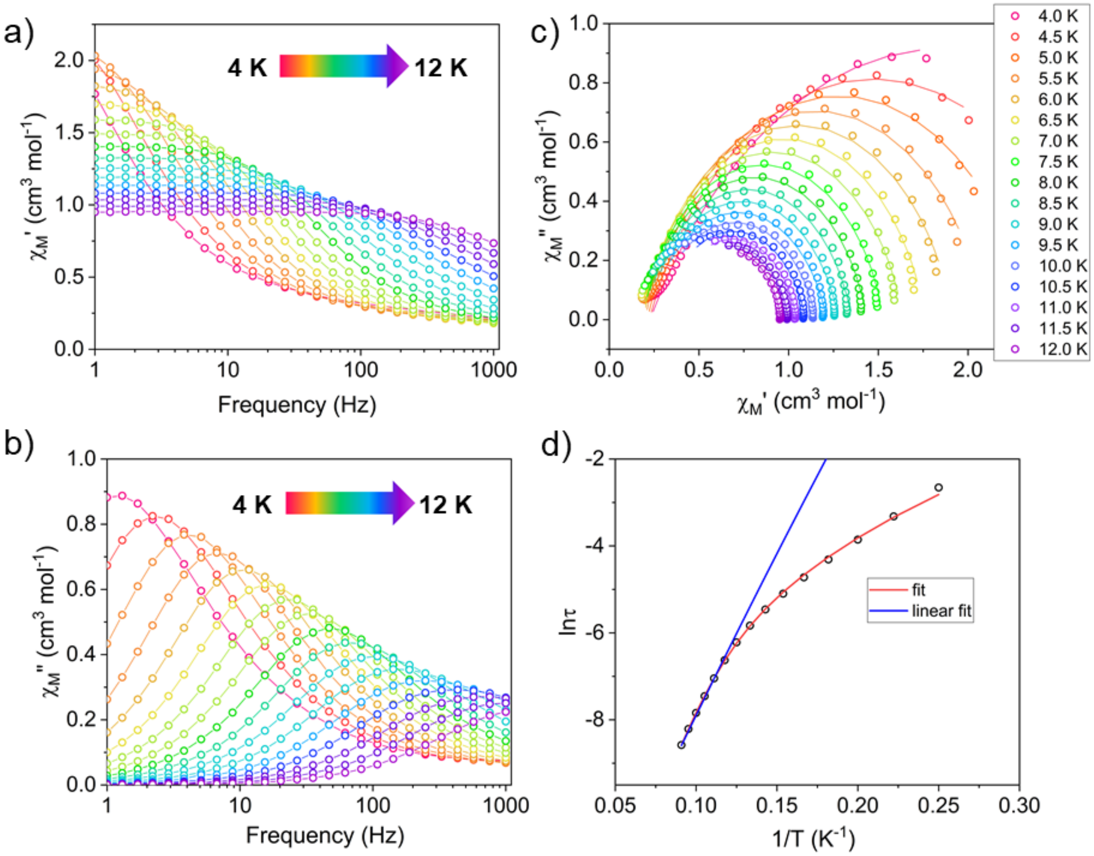

Figure 6.20: Ac susceptibility measurements for **6-7** under a 1000 Oe dc field. (left) Frequency dependence of the (a) in-phase (χ') and (b) out-of-phase (χ'') components of the ac susceptibility. (c) Cole-Cole plots, open circles are experimental data and lines are fits the generalized Debye equation. (d) Arrhenius plot, black circles represent experimental data. The blue line represents fits of the linear region to Equation 6.6. The red line represents fits of the entire temperature region to Equation 6.5.

splitting (ΔE_Q), sample texture (randomness of orientation), and magnetic hyperfine interactions. Quadrupole splitting generates a symmetrical quantum beat pattern (Equation 6.3) and the asymmetric dynamical beats in the spectra can be attributed to thickness effects (Equation 6.1). The absence of additional beats suggests the absence of a measurable magnetic hyperfine field at the Sn center. From this, it can be concluded that the diamagnetic Sn center does not experience any measurable effects from the paramagnetic Dy^{3+} center. Most likely, the Dy^{3+} center is too far away from the Sn center. Therefore, the ^{119}Sn Mössbauer spectra for **6-5** were fit using least-squares regression in CONUSS with the following as free-fit parameters: effective thickness (t_{eff}), quadrupole splitting (ΔE_Q) and texture coefficient (%). Notably, the entire temperature range could be fit with the magnetic hyperfine field set to 0 T.

Fitting the 90 K spectra afforded a quadrupole splitting value of ΔE_Q = 0.813(3) mm s^{-1}. As characterization of organnostannes by ^{119}Sn Mössbauer spectroscopy is quite rare, the most similar example found in the literature was 4-trimethylstannylpyridine; found to have ΔE_Q = 0.61 mm s^{-1} at 78 K using conventional Mössbauer spectroscopy.[178] The quadrupole splitting in **6-5** shows a temperature dependence, increasing with decreasing temperature to reach a value of 0.826(1) mm s^{-1} at 7.5 K (Figure 6.22). This trend of increasing quadrupole splitting with decreasing temperature has been reported in conventional ^{119}Sn and ^{57}Fe Mössbauer spectroscopy and in ^{57}Fe SMS with a powder sample.[167,179] Previously this effect has been attributed to dynamic distribution causing a time and temperature dependent electric field gradient (efg).[167]

The effective thickness (t_{eff}) at 90 K was determined to be 13(1) μm. The effective thickness increased linearly with decreasing temperature (R^2 = 0.9559), reaching a value of 41.1(3) μm at 7.5 K (Figure 6.22). An increase in t_{eff} with decreasing temperature has been reported previously in synchrotron Mössbauer spectroscopy.[167,179] Effective thickness is a measure of the number of ^{119}Sn nuclei that take part in the coherent resonant scattering. Stochastic fluctuation of the efg tensor reduces coherence between excited nuclei, lowering the number of nuclei that can take part in the excitation and thereby lowering forward scattering intensity.[167] At lower temperatures, there is less dynamic distribution/fluctuation, corresponding to a higher effect thickness, t_{eff}.

Finally, a texture coefficient parameter was added to the fit. The texture coefficient is a measure of the orientation of the sample, with 0 % being completely random and 100 % being completely ordered. The orientations of the sample relative to the efg influence the time spectra. The texture coefficients in **6-5** were between 10 % and 25 % and fluctuated with temperature (Figure 6.22).

The isostructural, diamagnetic Y^{3+} complex **6-6** was measured as a reference compound for comparison purposes. As observed in **6-5** at 90 K, a pattern of two asymmetric beats was observed, corresponding to an efg (quadrupole splitting, ΔE_Q) and thickness effects (Figure 6.23). The spectra for **6-6** were fit using the same free fit parameters as in the the Dy^{3+} compound **6-5**: effective thickness (t_{eff}), quadrupole splitting (ΔE_Q) and texture coefficient.

Notably, below 30 K in the Y^{3+} compound **6-6**, the second beat begins to split (Figure 6.23). The splitting can be modeled through increasing thickness effects (t_{eff}). When t_{eff} is larger than approximately 100 µm, thickness effects become so prominent that the beat splits. Compared to **6-5**, t_{eff} is much higher throughout the entire temperature range for **6-6**. At 90 K in **6-6** the t_{eff} is 24.1(2) µm, compared to a t_{eff} = 13(1) µm in **6-5** of at the same temperature (Figure 6.24). It is reasonable to expect that differences in sample loading could have resulted in **6-5** and **6-6** possessing different geometric thicknesses, with the Y^{3+} compound **6-6** having a larger geometric thickness. The effect is even more pronounced at low temperatures, with t_{eff} = 140.2(3) µm in **6-6** at 7.2 K and t_{eff} = 41.1(3) µm in **6-5** at 7.5 K. The t_{eff} in **6-6** increases linearly with decreasing temperature (R^2 = 0.97764).

At 90 K, the quadrupole splitting in **6-6** is 8.150(1) mm s^{-1}. This ΔE_Q value is comparable to the value found for the isostructural **6-5** at 90 K of 0.813(3) mm s^{-1}. Similar ΔE_Q values are expected, as the environment around the Sn center should be similar in both compounds. With decreasing temperature, ΔE_Q in **6-6** follows no particular trend, reaching a maximum value of 0.829(4) mm s^{-1} at 30 K (Figure 6.24). The texture coefficient in **6-6** was found to be below 10 % throughout the entire temperature range (7.2 K to 90 K) (Figure 6.24). This is lower than the texture coefficient in **6-5** and is indicative of a less ordered (more random) orientation in **6-6**.

The mononuclear isostructural compounds, **6-1** and **6-2** were studied by ^{119}Sn sychrotron

Mössbauer spectroscopy. The ^{119}Sn Mössbauer spectra for the Dy^{3+} compound **6-1** from 7.7 K to 80 K are shown in Figure 6.25. As with the dinuclear compounds described above, the spectra were fit with the following parameters: ΔE_Q, t_{eff}, and texture coefficient. The 7.7 K and 30 K spectra could not be fit effectively with only these parameters. The temperature dependence of the parameters are in Figure 6.26. The ΔE_Q of around 0.81 mm s^{-1} from 40 K to 80 K is near the value found for the tributyltin compounds, **6-5** and **6-6**. There is a large increase in the ΔE_Q from 0.81(1) mm s^{-1} at 40 K to 0.89(1) mm s^{-1} at 20 K. As anticipated, t_{eff} increases with decreasing temperature.

The ^{119}Sn Mössbauer spectra and fits for the mononuclear Y^{3+} compound **6-2** are plotted in Figure 6.27. The spectra were fit with the following parameters: ΔE_Q, t_{eff}, and texture coefficient. The ΔE_Q is 0.817(1) mm s^{-1} at 90 K and it increases drastically below 30 K to a maximum of 0.866(6) mm s^{-1} at 10 K (Figure 6.28). A drastic increase in ΔE_Q is also observed in the isostructural Dy^{3+} compound **6-1**. Once again, t_{eff} increases with decreasing temperature (Figure 6.27). The thickness effects from the large t_{eff} values become especially prominent below 30 K, when the beat starts to split as t_{eff} approaches 100 μm (Figure 6.27).

In summary, the ^{119}Sn Mössbauer spectra of the organotin-containing compounds studied, **6-1**, **6-2**,**6-5**, and **6-6**, could be fit over the temperature range from 7 K to 90 K using the free-fit parameters: quadrupole splitting (ΔE_Q), effective thickness (t_{eff}), and texture coefficient. No magnetic hyperfine splitting or magnetic hyperfine field was detected at the Sn center in any of the compounds investigated here, including the Dy^{3+} compounds **6-1** and **6-5**. Presumably, the Sn center is too far away from the paramagnetic Dy^{3+} center to experience any measurable effects from the magnetic hyperfine field generated from the Dy^{3+} ion.

The quadrupole splittings for all compounds were in the range of 0.81 mm s^{-1} to 0.89 mm s^{-1}, with an average of 0.824 mm s^{-1}. These quadrupole splittings are larger than the reported value of 0.61 mm s^{-1} for 4-trimethyltinpyridine at 78 K, determined using conventional Mössbauer spectroscopy.[178] In all of the compounds, t_{eff} increased with decreasing temperature. This was anticipated, as effective thickness is a measure of the number of ^{119}Sn nuclei that take part in the coherent resonant scattering.

6.3.5 ^{161}Dy Synchrotron Mössbauer spectroscopy

The ^{161}Dy Mössbauer spectra for compounds **6-1**, **6-5**, **6-7**, Dy(hfac)$_3$(bpy), and Dy(hfac)$_3$(H$_2$O)$_2$ were collected using synchrotron Mössbauer spectroscopy with the incident X-ray energy tuned to the resonance at 25.651 keV. All compounds were measured starting at 4 K (liquid He) up to a certain maximum temperature where the count rates dropped drastically. The maximum temperature varied depending on the compound. The drop in count rate likely corresponds to an intermediate relaxation regime.[167] The spectra were fit with the following parameters: thickness (t_{eff}), texture, magnetic hyperfine field, and magnetic hyperfine field angles (ϑ and φ). All ^{161}Dy Mössbauer measurements were carried out with no external field, therefore any magnetic hyperfine field is expected to be generated from the paramagnetic Dy^{3+} center.

The mononuclear compound **6-1** was measured from 4 K up to 20 K, where the count rate dropped drastically (Figure 6.29). The magnetic hyperfine field at 20 K was found to be 565 T, whereas the magnetic hyperfine field at 4 K was 579.3(4) T. In **6-1**, the magnitude of the magnetic hyperfine field increased linearly with decreasing temperature (Figure 6.30). Interestingly, the t_{eff} increased exponentially from 128.0(5) µm at 4 K to 820(20) µm at 20 K. Since t_{eff} is a measure of the number of nuclei taking place in the resonant absorption and emission, it is expected to decreases with increasing temperature as dynamic processes become more prominent. Therefore, the cause of the increase observed in **6-1** is unknown at this time and requires further investigation. Notably, the same increase in t_{eff} with increasing temperature is observed for the other Dy^{3+} compounds investigated herein. Also notable is the larger temperature dependence of t_{eff} in the ^{161}Dy Mössbauer spectra relative to the ^{119}Sn Mössbauer spectra. In the ^{161}Dy spectra of **6-1**, $\Delta t_{\text{eff}} = 692$ µm from 4 K to 20 K (Figure 6.30), whereas in the ^{119}Sn Mössbauer spectra of **6-1** $\Delta t_{\text{eff}} = 75.3$ µm from 90 K to 20 K (Figure 6.26). This may be at least partially attributed to the larger Lamb-Mössbauer factor (f_{LM}) for ^{161}Dy ($f_{\text{LM}} = 0.75$) than for ^{119}Sn ($f_{\text{LM}} = 0.3$) (Equation 6.2). There is also an observed change in slope, increasing steepness with increasing temperature, however we cannot attribute this to a physical property at this time. A hyperfine magnetic field value of around

500 T was determined in **6-1** from fitting the ^{161}Dy Mössbauer spectra.

^{161}Dy Mössbauer spectra were collected for Dy(hfac)$_3$(bpy) from 4 K until the count rate dropped drastically at 20 K (Figure 6.31). Dy(hfac)$_3$(bpy) is similar to **6-1**, however it displays temperature dependent and slow relaxation (U_{eff} = 26.74 cm^{-1}) under zero dc field by ac magnetometry. Interestingly, the count rate for both compounds both dropped off at a maximum temperature of 20 K. The temperature dependence of the magnetic hyperfine field displays the opposite trend in Dy(hfac)$_3$(bpy) than in **6-1**, in that the magnetic hyperfine field actually decreases with decreasing temperature, from 577.5(7) T at 20 K to 553 T at 4 K (Figure 6.32). Despite the opposing temperature dependencies, the magnetic hyperfine fields at 10 K are comparable with H = 572.8(3) T in Dy(hfac)$_3$(bpy) and H = 571.9(2) T in **6-1**. As observed in **6-1**, t_{eff} increases with increasing temperature from 10 K to 20 K in Dy(hfac)$_3$(bpy). However, the largest t_{eff} is at 4 K, t_{eff} = 1.0(1) x 10^3 μm.

The ^{161}Dy Mössbauer spectra from 4 K to 29 K for **6-7** are displayed in Figure 6.33. Spectra were collected until the count rate dropped off above 29 K. By ac magnetometry studies, zero field slow relaxation was observed with U_{eff} = 48.5 cm^{-1} and field-dependent slow relaxation was observed with U_{eff} = 77.6 cm^{-1}. The ^{161}Dy Mössbauer spectra still need to be fit.

Compound **6-5** was the only dinuclear compound studied by ^{161}Dy Mössbauer spectroscopy. Compound **6-5** is unique in that it is the only dinuclear compound studied herein and ferromagnetic coupling was observed by ac magnetometry at low T. Interestingly, of the compounds investigated herein, **6-5** recorded the highest temperature (T = 32 K) before the count rate dropped. The beats in the ^{161}Dy spectra of **6-5** display a much more regular repeating pattern, however we cannot explain this observation at this time. From the magnetometry studies, **6-5** showed slow relaxation under zero dc field with U_{eff} = 18.1 cm^{-1} and ferromagnetic coupling below 15 K (Figure 6.11 and 6.17). The t_{eff} value increased exponentially with increasing temperature between 15 K and 32 K in **6-5**, from 204(4) μm at 15 K to 470(9) μm at 32 K. Despite the dinuclear nature and relative close proximity of the Dy^{3+} centers, the magnetic hyperfine field in **6-5** is comparable to the fields in **6-1** and Dy(hfac)$_3$(bpy). The magnetic hyperfine field in **6-5** increases from 568.44(7) T at 4 K to a maximum of 572.8(0.1) T at 30 K.

Finally, the ^{161}Dy Mössbauer spectrum of Dy(hfac)$_3$(H$_2$O)$_2$ at 4 K was collected (Figure 6.36). Notably, Dy(hfac)$_3$(H$_2$O)$_2$ does not display zero-field or field-induced slow relaxation by ac magnetometry and the count rate was lost after 4 K, the lowest temperature of any of the compounds measured herein.

The exact relationship between slow relaxation/U_{eff} and the synchrotron Mössbauer spectroscopy parameters still needs to be determined. It also remains to be seen whether or not relaxation times, τ, and therefore U_{eff}, may be determined from ^{161}Dy Mössbauer spectroscopy as has been demonstrated with ^{57}Fe Mössbauer spectroscopy. From the preliminary results of the ^{161}Dy Mössbauer studies discussed herein, a possible relationship exists between the highest temperature above which the count rate is lost and slow relaxation under zero dc field as observed by ac magnetometry. However, this possible relationship must be further investigated. At the moment, we cannot explain the observed increase in t_{eff} with increasing temperature or the relationship between the measured magnetic hyperfine field and slow magnetic relaxation. There is also a discrepancy in the temperature dependence of the magnetic hyperfine field. In Dy(hfac)$_3$(bpy) and **6-5** the magnitude of the magnetic hyperfine field increased with increasing temperature and in **6-1** the magnitude of the hyperfine field decreases with increasing temperature. In collaboration with Argonne National Laboratory, data analysis and further studies in this area are ongoing.

6.4 Conclusion and Outlook

A series of tris(hexafluoroacetlyacteonante) complexes of Dy^{3+} and Y^{3+} with bpy-based and phen capping ligands were isolated and investigated by magnetometry and synchrotron Mössbauer spectroscopy. The trimethyltin substituted bpy ligand (**bpy$^{\mathbf{SnMe3}}$**) formed a mononuclear compound with RE^{3+}, whereas the tributyltin substituted bpy ligand (**bpy$^{\mathbf{SnBu3}}$**) formed a dinuclear compound with either bridging methoxide or hydroxide groups, depending on the crystallization conditions. Ac magnetometry studied revealed zero field slow relaxation in **6-1**, **6-5**, and **6-7** and field-induced slow relaxation in **6-3**.

Through zero-field ^{119}Sn synchrotron Mössbauer spectroscopy studies, no measurable magnetic hyperfine fields were detected at the diamagnetic Sn center, even for the Dy^{3+}-based compounds **6-1** and **6-5**. Presumably the Dy^{3+} center is too far away from the Sn center (6.370(2) Å in **6-1**). Future studies will involve utilizing an external field to induce hyperfine splitting at the Sn center and measuring the field generated from Dy^{3+} as a perturbation on the applied field. Additionally, new systems with slower relaxation and Sn centers closer to the Dy^{3+} centers will be investigated.

The Dy^{3+}-based complexes were studied by ^{161}Dy synchrotron Mössbauer spectroscopy, representing the first time Dy-based SMMs have been studied using zero-field ^{161}Dy Mössbauer spectroscopy. From the variable temperature spectra collected here, a relationship may exist between the loss of count rate (intermediate relaxation regime) and relaxation times/U_{eff} determined from magnetometry studies, however this relationship (if it exists) requires further investigation. It also remains to be seen whether this technique could be utilized to calculate $\mathrm{U_{eff}}$ in Dy-based SMMs. Future work involving ^{161}Dy Mössbauer spectroscopy includes collecting spectra at higher temperatures to investigate whether or not the count rates recover once past the intermediate relaxation regime and collecting spectra in the presence of external fields.

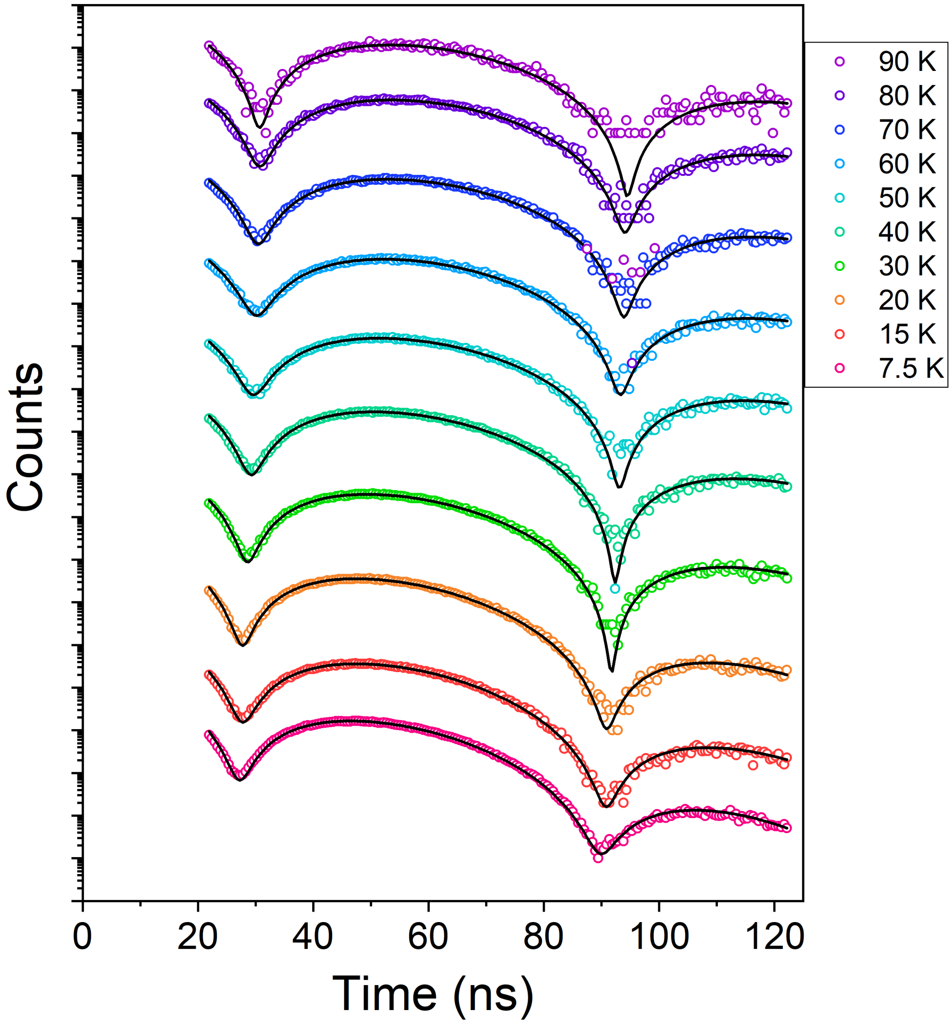

Figure 6.21: ^{119}Sn synchrotron Mössbauer spectra of **6-5** at temperatures from 7.5 K to 90 K with zero external field. Open colored circles are experimental data, black lines represent fits. Time (in ns) is after synchrotron pulse.

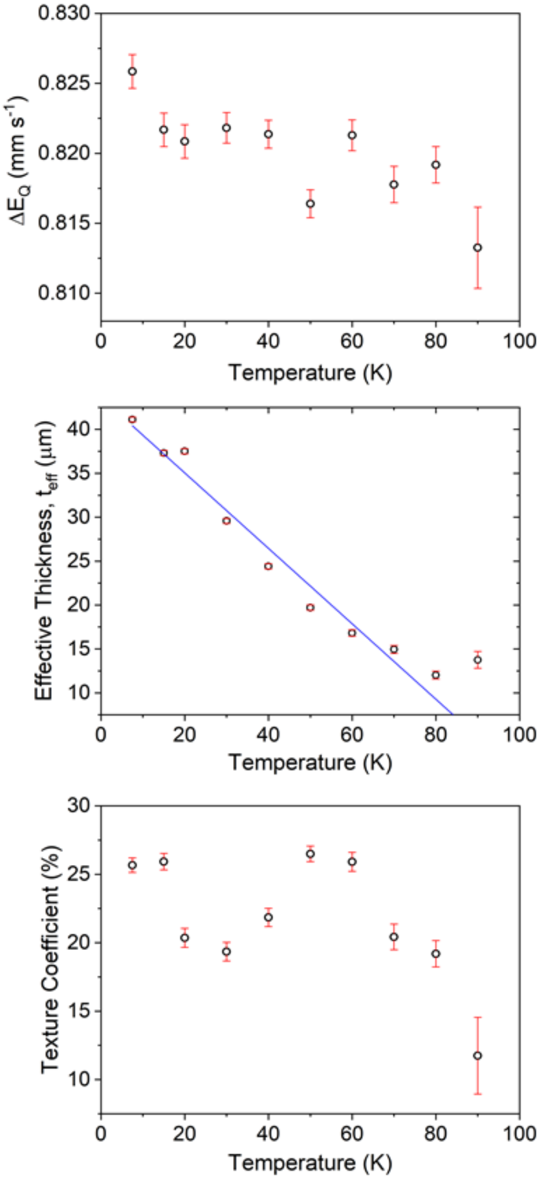

Figure 6.22: Temperature dependence of the fit parameters for the ^{119}Sn spectra of **6-5**. Temperature dependence of the quadrupole splitting (ΔE_Q) (top) , temperature dependence of the effective thickness (t_{eff}) (middle), and temperature dependence of the texture coefficient (bottom). All errors are given to the 68 % confidence interval.

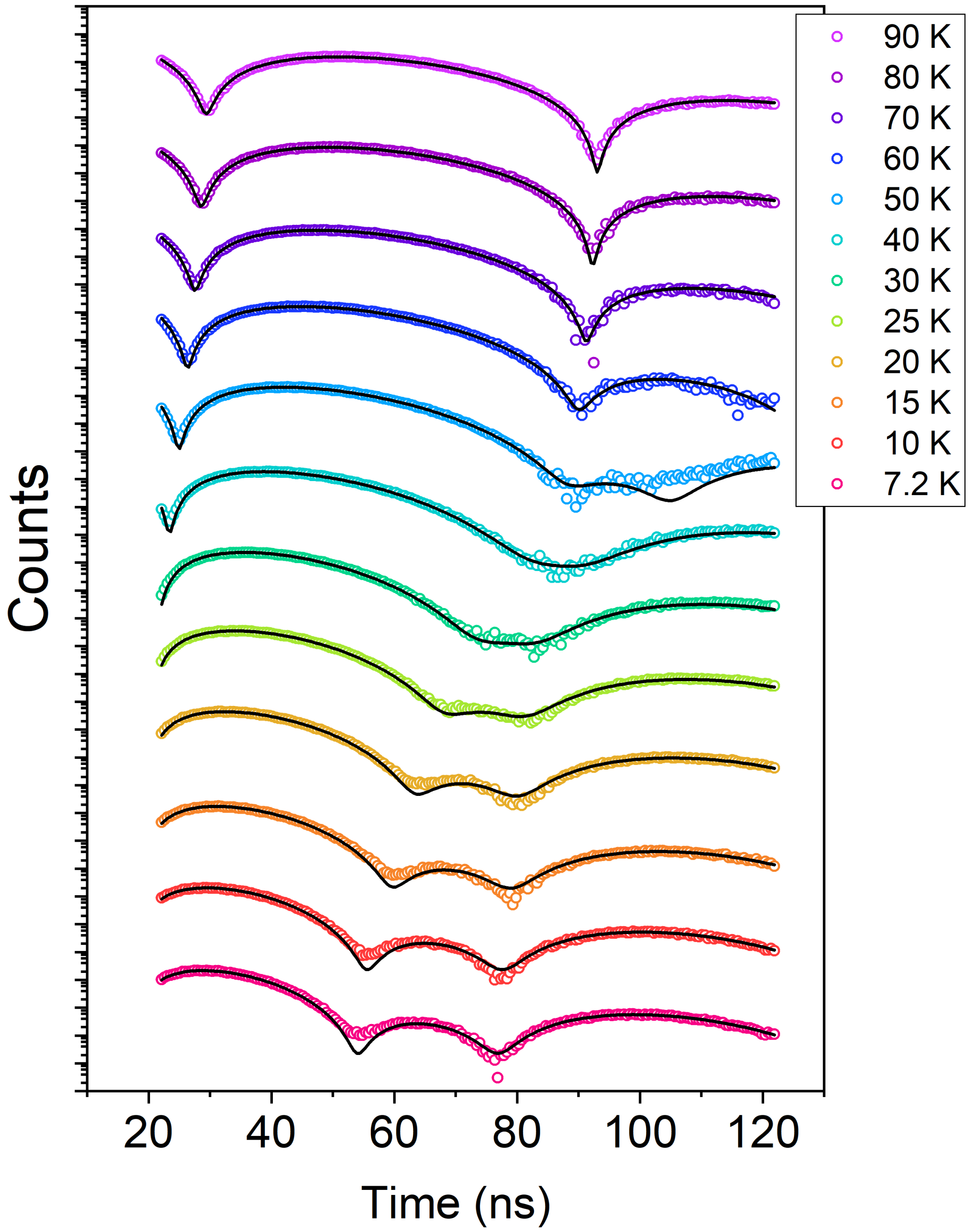

Figure 6.23: ^{119}Sn Mössbauer spectra for **6-6** at temperatures from 7.2 K to 90 K with zero external field. Open colored circles are experimental data, black lines represent fits. Time (in ns) is after synchrotron pulse.

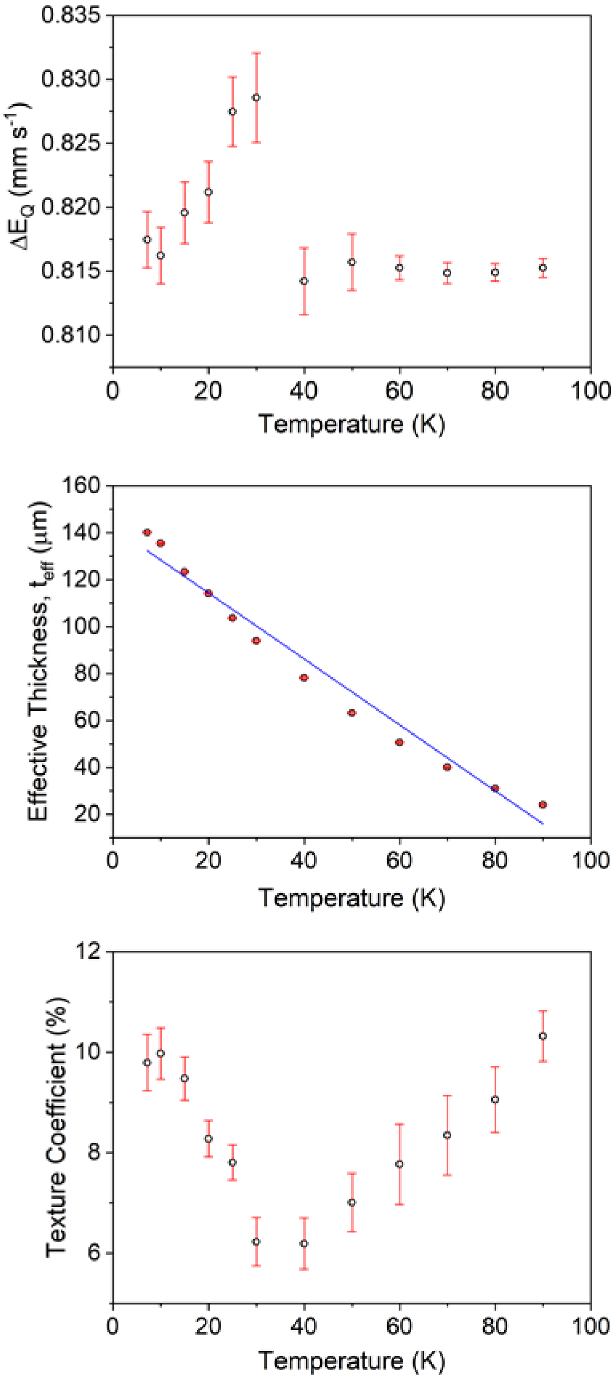

Figure 6.24: Temperature Dependence of the fit parameters for **6-6** (^{119}Sn Mössbauer spectroscopy). All errors are given to the 68 % confidence level.

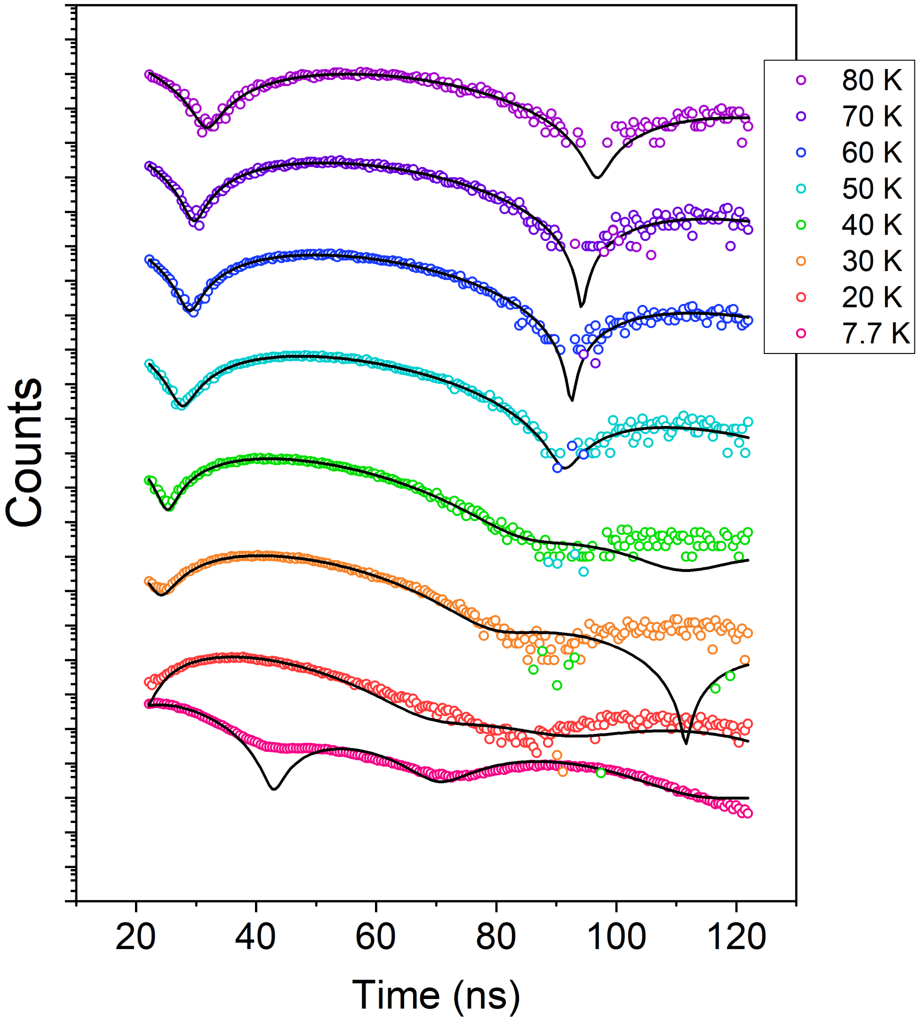

Figure 6.25: ^{119}Sn Mössbauer spectra for **6-1** from 7.7 K to 80 K. Open colored circles are experimental data, black lines represent fits. Time (in ns) is after X-ray pulse.

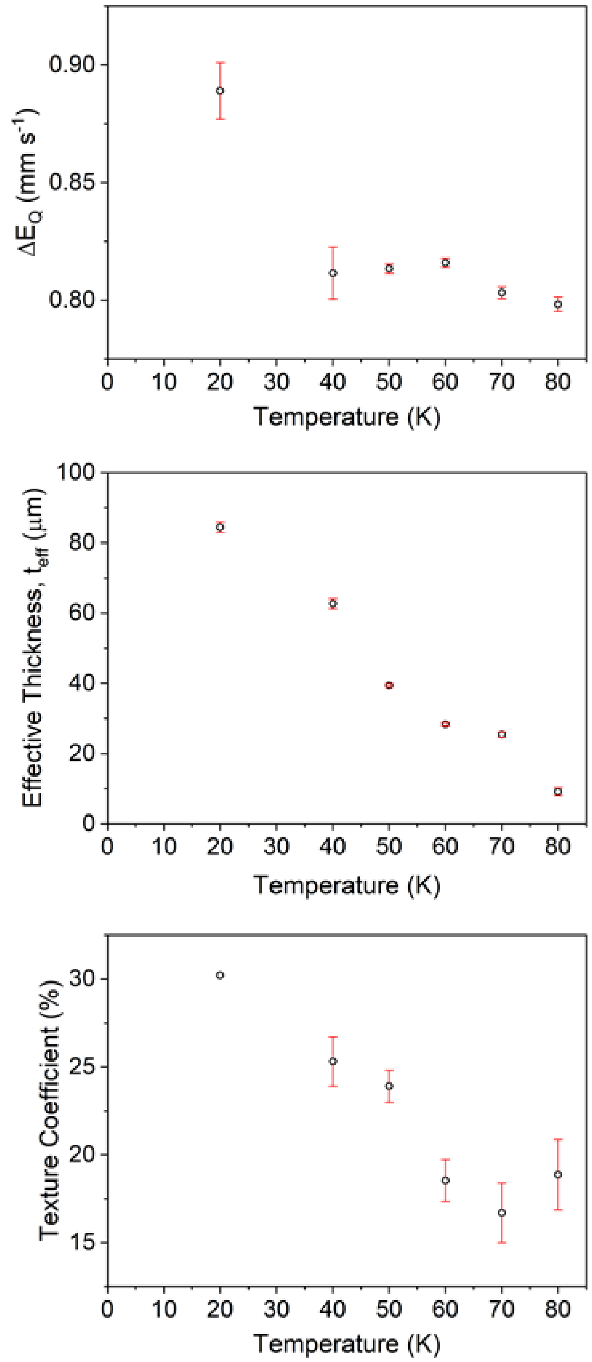

Figure 6.26: Temperature Dependence of the fit parameters in **6-1** (^{119}Sn Mössbauer spectroscopy). All errors are given to the 68 % confidence interval.

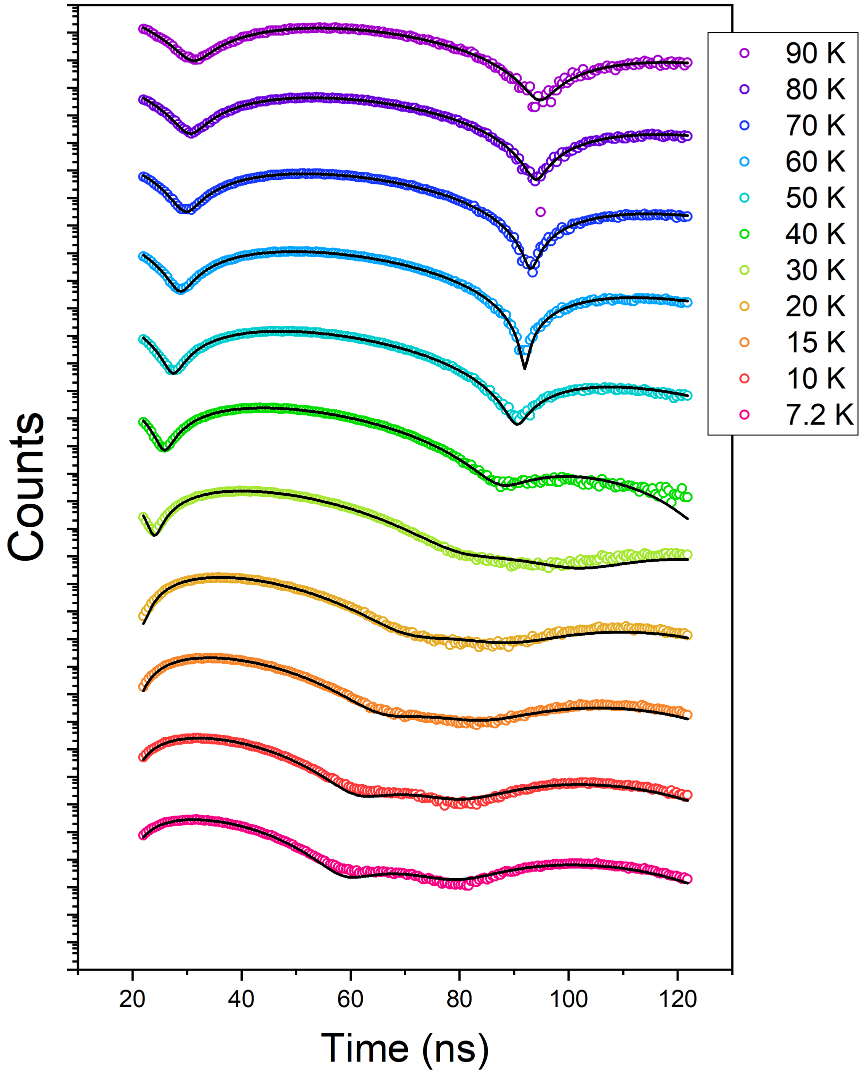

Figure 6.27: ^{119}Sn Mössbauer spectra temperature for **6-2**. Open colored circles are experimental data, black lines represent fits. Time (in ns) is after synchrotron pulse.

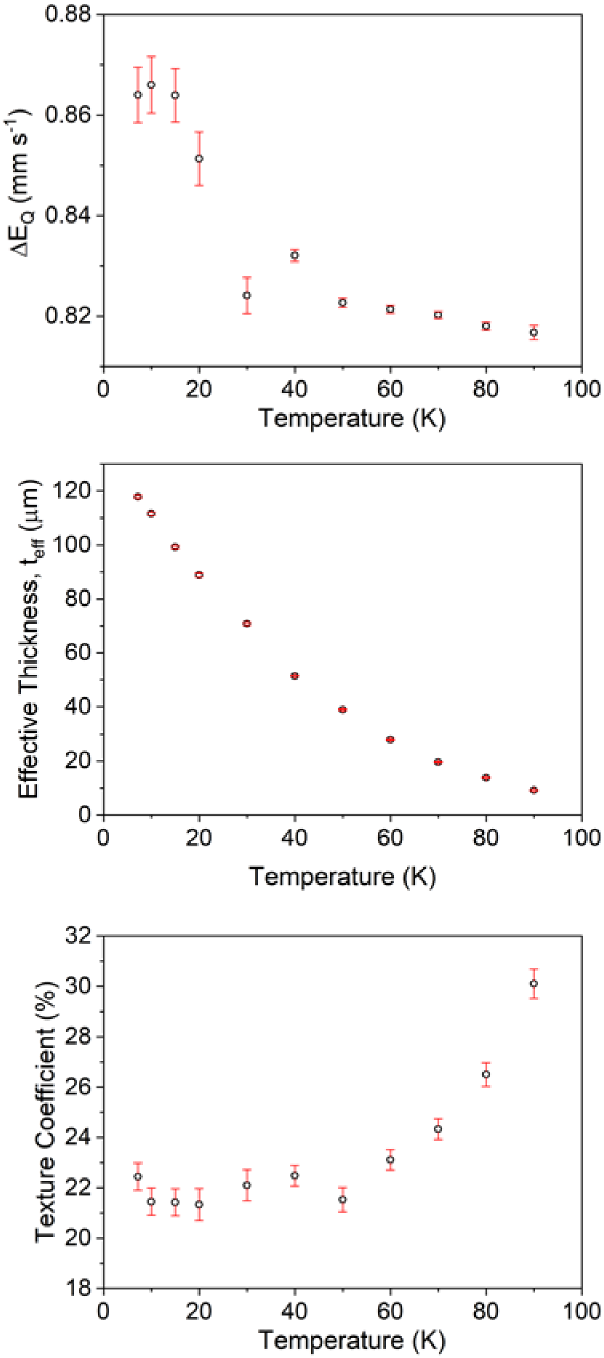

Figure 6.28: Temperature Dependence of parameters in **6-2** (^{119}Sn Mössbauer spectroscopy). All errors are given to the 68 % confidence interval.

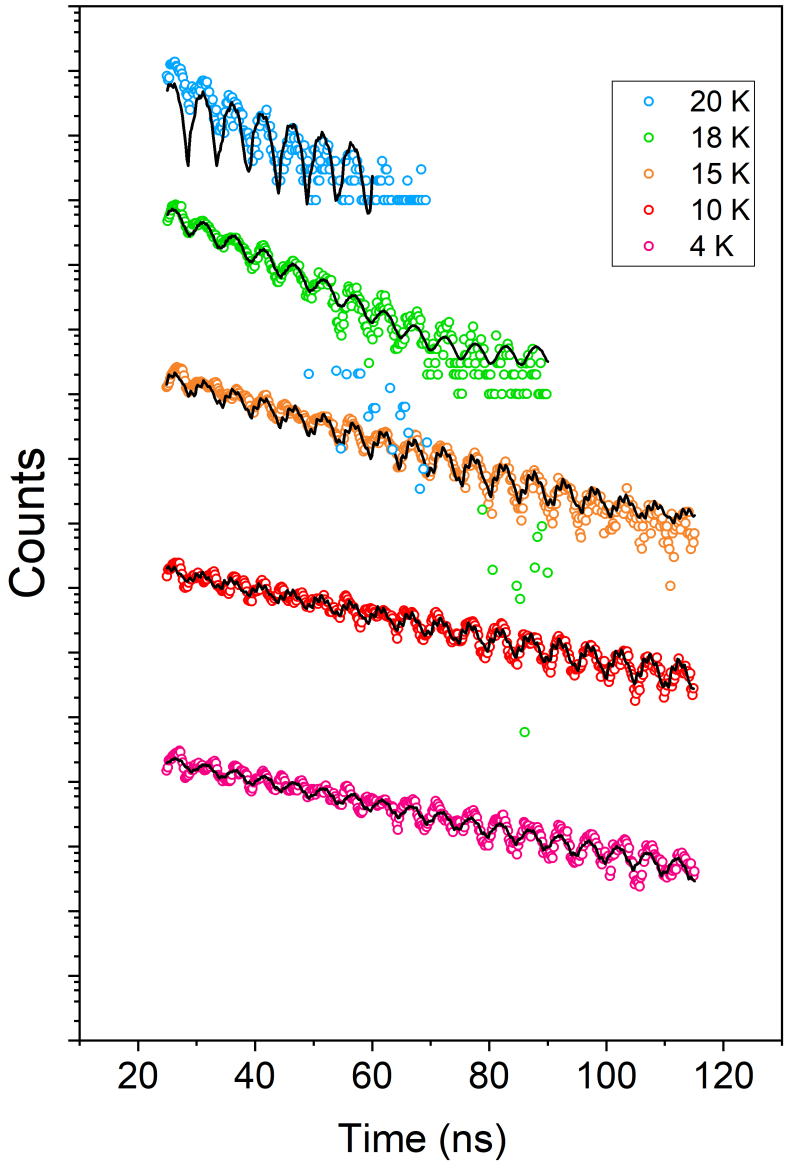

Figure 6.29: ^{161}Dy Mössbauer spectra and fits for **6-1**. Open circles are experimental data points and lines are fits generated using CONUSS. Count rate was lost above 20 K.

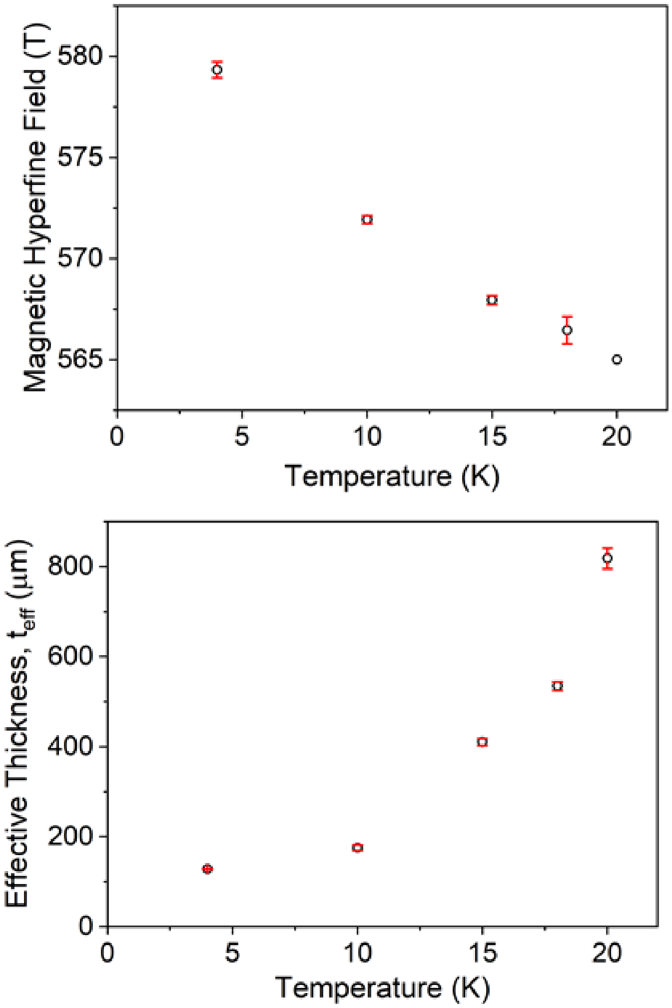

Figure 6.30: Temperature dependence of the fit parameters for **6-1** (^{161}Dy Mössbauer spectroscopy). All errors are given to the 68 % confidence interval.

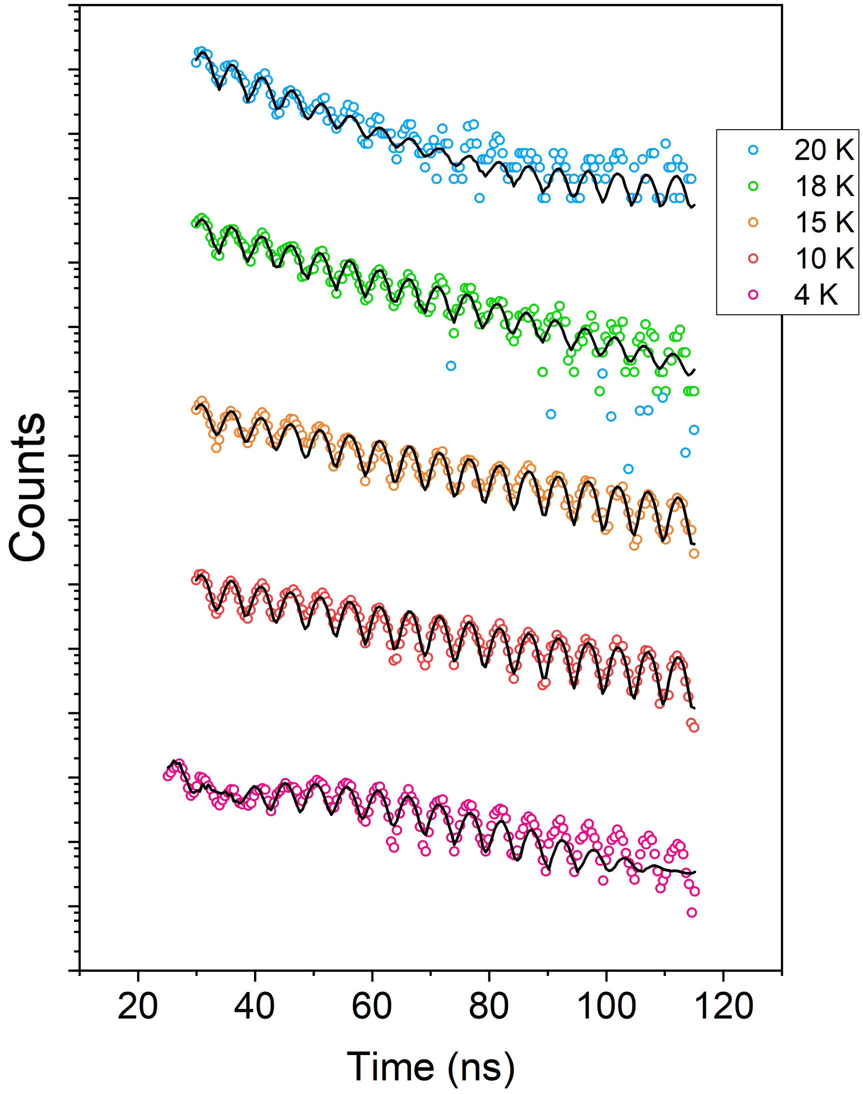

Figure 6.31: ^{161}Dy Mössbauer spectra (colored circles) and fits (black lines) for Dy(hfac)$_3$(bpy). Count rate lost above 20 K.

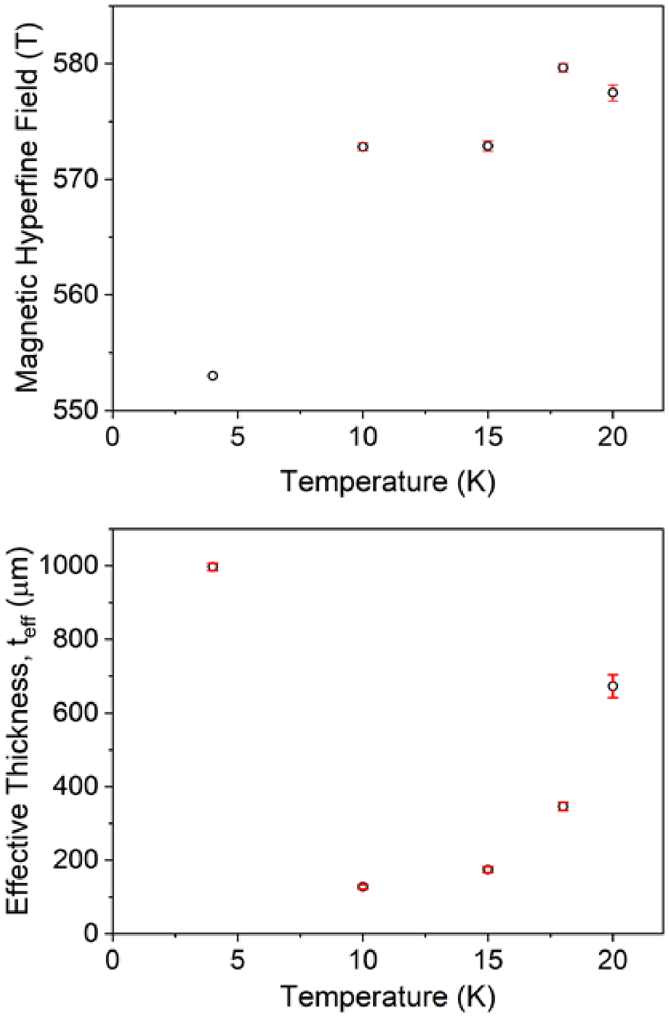

Figure 6.32: Temperature Dependence of parameters for Dy(hfac)$_3$(bpy) (^{161}Dy Mössbauer spectroscopy). All errors are given to the 68 % confidence interval.

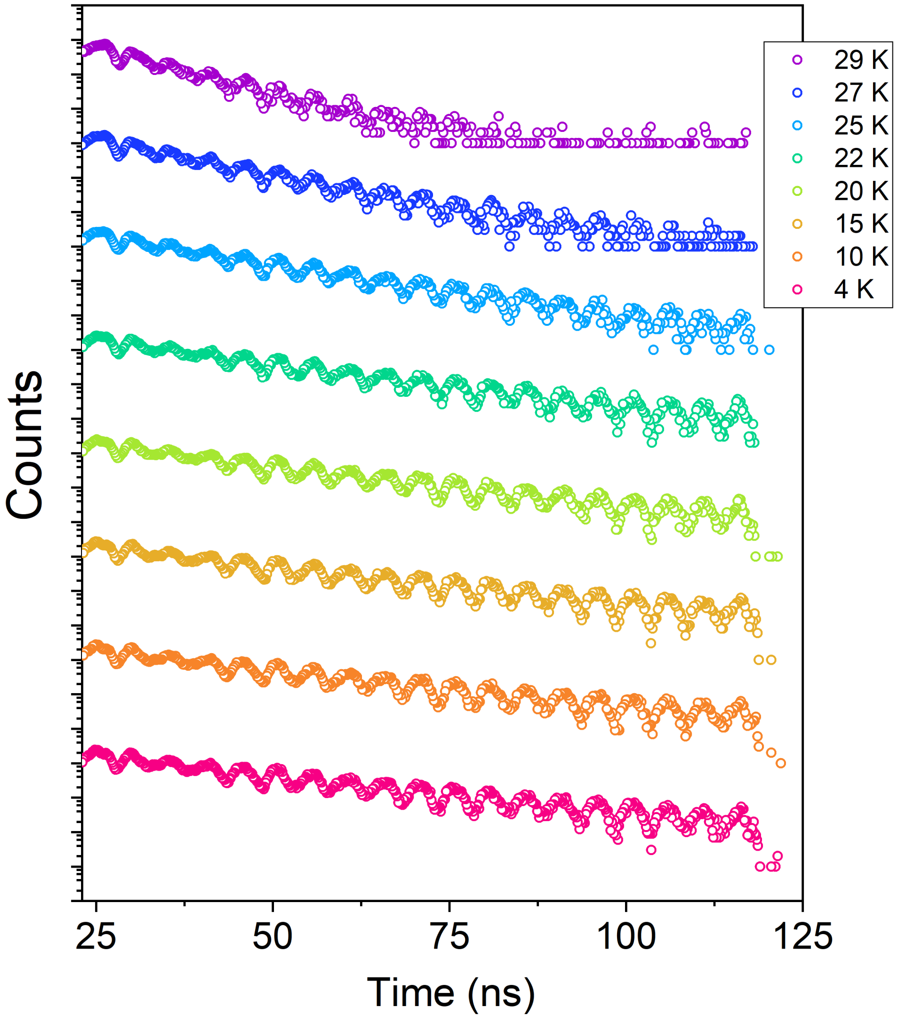

Figure 6.33: ^{161}Dy Mössbauer spectra for **6-7**, without fits. Count rate lost above 29 K.

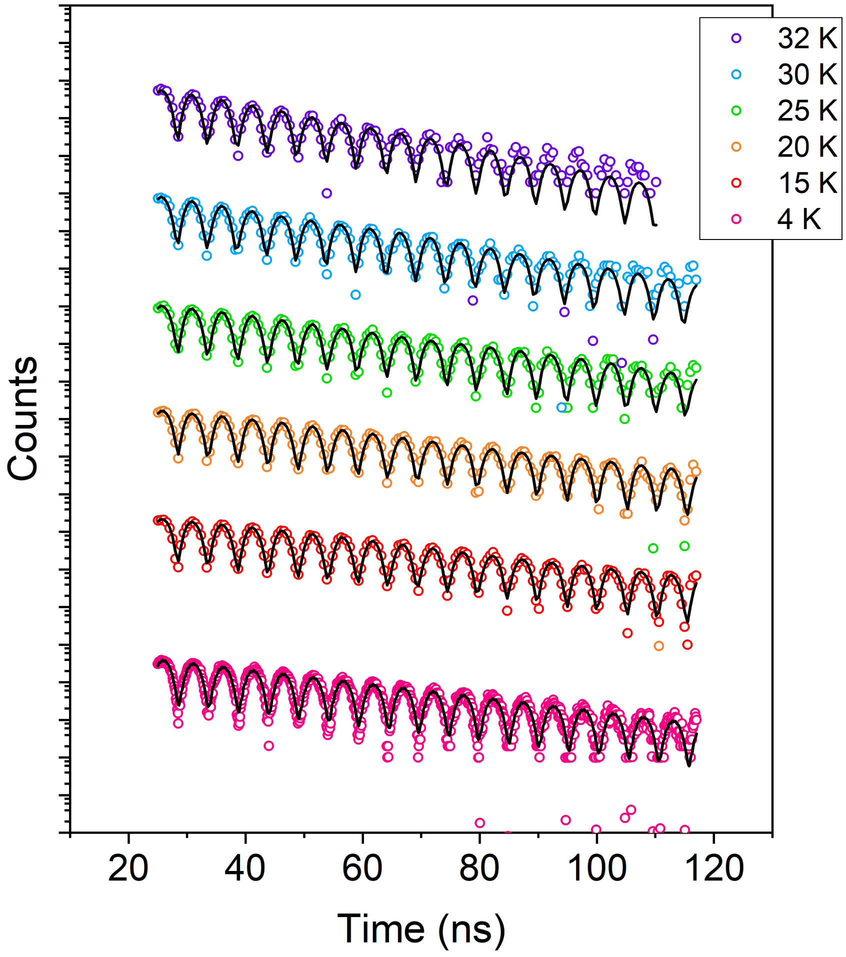

Figure 6.34: ^{161}Dy Mössbauer spectra (colored circles) and fits (black lines) for **6-5**.

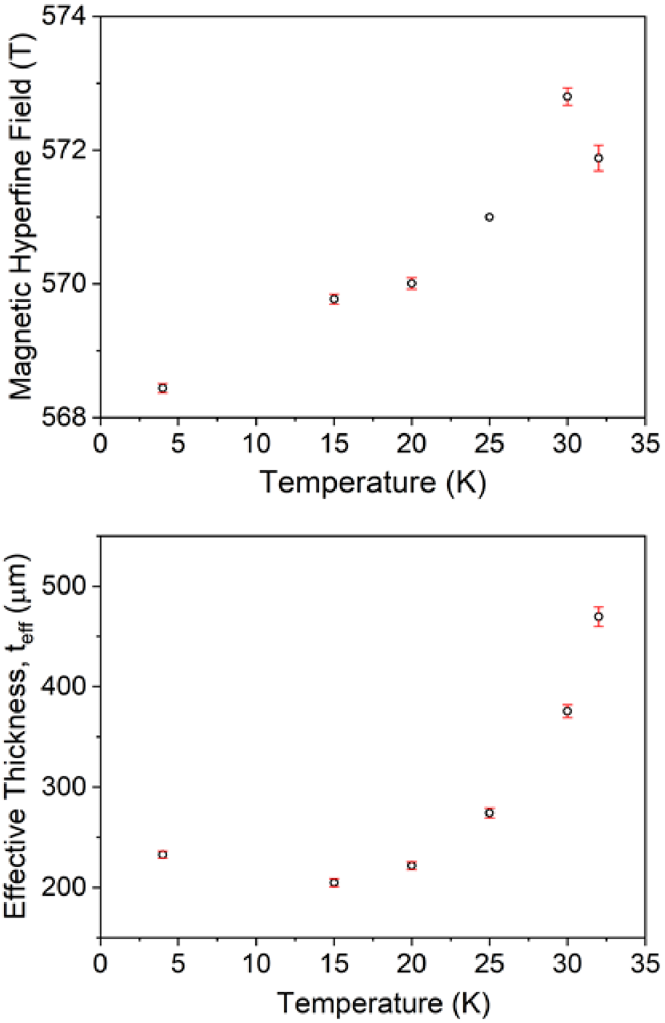

Figure 6.35: Temperature dependence of the fit parameters in **6-5** (^{161}Dy Mössbauer spectroscopy. All errors are given to the 68 % confidence interval.

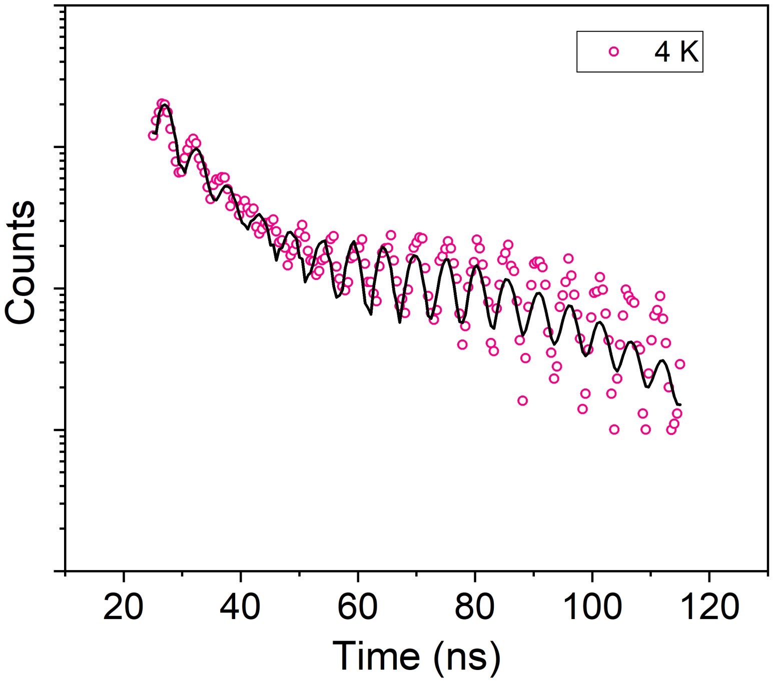

Figure 6.36: ^{161}Dy Mössbauer spectrum and fit (black line) for Dy(hfac)$_3$(H$_2$O)$_2$ at 4 K.

7. CONCLUSION

7.1 Redox-switchable magnetization dynamics

Towards the utilization of SMMs in devices, the development of compounds featuring reversible redox-switchability of magnetization dynamics was targeted. In particular, compounds containing both d-block and f-block metal centers were targeted in an effort to combine the intrinsic high single-ion anisotropy of lanthanide(III) ions with the desirable redox properties of transition metals. Initial efforts in the area led to the isolation of the first structurally characterized dysprosium isocarbonyl complex, $[CpW(CO)_2(\mu\text{-}CO)]_3Dy(thf)_5]$, from the amine elimination reaction between $[Dy(N(SiMe_3)_2)_3]$ and $[HW(CO)_3Cp]$. Field-induced slow magnetic relaxation was observed in a magnetically dilute sample (Y:Dy, 12:1) under a 400 Oe applied dc field, with a barrier height (U_{eff}) of 12.6 cm^{-1}. Electrochemical oxidization of the tungsten center led to immediate decomposition of the compound, highlighting the unsuitability of these isocarbonyl compounds towards redox switchability applications, therefore necessitating the investigation of new platforms.

The reversible redox properties of ferrocene/ferrocenium, $[FeCp_2]^{0/+}$, make it an attractive moiety to include in complexes for redox switchability applications. This inspired the objective of utilizing ferrocene-containing ligands to modulate the magnetization dynamics at a nearby lanthanide center. The utility of diamidoferrocene ligands in the construction of redox switchable SMMs has been highlighted in Chapter 5. The highly reversible Fe^{2+}/Fe^{3+} redox couple was utilized to modulate the magnetization dynamics of Dy^{3+} and Er^{3+} based SMMs. Notably, the Dy^{3+} compound exhibited either "on/off" or "slow/fast" switching in the presence or absence of a dc field, respectively, whereas the Er^{3+} compound exhibited "on/off" functionality in the presence of a dc field. The Fe ions in the mixed-valent complexes were shown by UV-Vis-NIR spectroscopy, cyclic voltammetry, and ^{57}Fe Mössbauer spectroscopy to feature electronic communication in both solution and solid state. The results of this study contribute towards the development of rational design principles for the generation of future switchable magnetic materials.

Half-sandwich complexes of Cr(II) are potentially interesting building blocks for mixed metal d-block/f-block compounds. The polymeric Cr(II) species, $[\text{CpCr}(\text{N}(\text{SiMe}_3)_2)_2\text{K}]_\infty$, could be formed from the reaction of chromocene and $\text{K}(\text{N}(\text{SiMe}_3)_2)$ in toluene with the elimination of KCp. In the presence of cryptand-222 the mononuclear Cr(II) species $[\text{K}(\text{crypt-222})][\text{CpCr}(\text{N}(\text{SiMe}_3)_2)_2]$ was be isolated, either in situ or through adding cryptand-222 to a solution of the polymeric species in thf. The mononuclear Cr(II) cryptand compound, $[\text{K}(\text{crypt-222})][\text{CpCr}(\text{N}(\text{SiMe}_3)_2)_2]$, displayed field induced slow relaxation with U_{eff} = 9.8(6) cm^{-1} (H_{dc} = 1000 Oe). Notably, this is only the third reported mononuclear Cr(II) compound to display field-induced slow relaxation and is the only example that is not square planar. Further reactivity studies involving these half-sandwich Cr(II) compounds are on-going.

7.2 Towards utilizing synchrotron Mössbauer spectroscopy for magnetic relaxation measurements

The development of new methods for the characterization of SMMs is essential to the advancement of the field. This study represents the first time ^{119}Sn and ^{161}Dy Mössbauer spectroscopy have been utilized to investigate magnetization dynamics. Towards this goal, a series of tris(hexafluoroacetylacetonate) complexes of Dy^{3+} and Y^{3+} with bpy-based and phen capping ligands were isolated. The trimethyltin substituted bpy ligand ($\text{bpy}^{\text{SnMe3}}$) was found to form a mononuclear compound with RE^{3+}, whereas the tributyltin substituted bpy ligand ($\text{bpy}^{\text{SnBu3}}$) formed dinuclear compounds. Interestingly, no measureable magnetic hyperfine fields were detected at the diamagnetic Sn center in the ^{119}Sn synchrotron Mössbauer spectra, even for the Dy^{3+} compounds. Presumably in these compounds the Sn center is too far away from the paramagnetic the Dy^{3+} center to feel the effects.

The Dy^{3+}-based complexes were studied by ^{161}Dy synchrotron Mössbauer spectroscopy, representing the first time Dy-based SMMs have been studied using ^{161}Dy Mössbauer spectroscopy. From the variable temperature spectra collected here, a relationship may exist between the loss of count rate (intermediate relaxation regime) and relaxation times/U_{eff} as determined from ac magnetometry studies. However, further investigations are required in order to draw a conclusion. It also remains to be seen whether or not this technique could be utilized to calculate U_{eff} values in Dy-based SMMs. Further work in this area is ongoing.

REFERENCES

[1] Troiani, F.; Affronte, M. Molecular spins for quantum information technologies. *Chem. Soc. Rev.* **2011**, *40*, 3119–3129.

[2] Bogani, L.; Wernsdorfer, W. Molecular spintronics using single-molecule magnets. *Nat. Mater.* **2008**, *7*, 179–186.

[3] Gatteschi, D.; Sessoli, R.; Villain, J. *Molecular Nanomagnets*; Oxford University Press, 2006.

[4] Benelli, C.; Gatteschi, D. *Introduction to Molecular Magnetism: From Transition Metals to Lanthanides*, 1st ed.; John Wiley & Sons, Inc., 2015.

[5] Layfield, R. A.; Murugesu, M. *Lanthanides and Actinides in Molecular Magnetism*, 1st ed.; Wiley, 2015.

[6] Sessoli, R.; Gatteschi, D.; Caneschi, A.; Novak, M. A. Magnetic bistability in a metal-ion cluster. *Nature* **1993**, *365*, 141–143.

[7] Goodwin, C. A. P.; Ortu, F.; Reta, D.; Chilton, N. F.; Mills, D. P. Molecular magnetic hysteresis at 60 kelvin in dysprosocenium. *Nature* **2017**, *548*, 439–442.

[8] Guo, F.-S.; Day, B. M.; Chen, Y.-C.; Tong, M.-L.; Mansikkamäki, A.; Layfield, R. A. A Dysprosium Metallocene Single-Molecule Magnet Functioning at the Axial Limit. *Angew. Chem. Int. Ed.* **2017**, *56*, 11445–11449.

[9] Gatteschi, D.; Sessoli, R. Quantum Tunneling of Magnetization and Related Phenomena in Molecular Materials. *Angew. Chem. Int. Ed.* **2003**, *42*, 268–297.

[10] Affronte, M. Molecular nanomagnets for information technologies. *J. Mater. Chem.* **2009**, *19*, 1731–1737.

[11] Pedersen, K. S.; Bendix, J.; Clérac, R. Single-molecule magnet engineering: building-block approaches. *Chem. Commun.* **2014**, *50*, 4396–4415.

[12] Liddle, S. T.; van Slageren, J. Improving f-element single molecule magnets. *Chem. Soc. Rev.* **2015**, *44*, 6655–6669.

[13] Woodruff, D. N.; Winpenny, R. E. P.; Layfield, R. A. Lanthanide Single-Molecule Magnets. *Chem. Rev.* **2013**, *113*, 5110–5148.

[14] Milios, C. J.; Vinslava, A.; Wernsdorfer, W.; Moggach, S.; Parsons, S.; Perlepes, S. P.; Christou, G.; Brechin, E. K. A Record Anisotropy Barrier for a Single-Molecule Magnet. *J. Am. Chem. Soc.* **2007**, *129*, 2754–2755.

[15] Ako, A. M.; Hewitt, I. J.; Mereacre, V.; Clérac, R.; Wernsdorfer, W.; Anson, C. E.; Powell, A. K. A Ferromagnetically Coupled Mn19 Aggregate with a Record S=83/2 Ground Spin State. *Angew. Chem. Int. Ed.* **2006**, *45*, 4926–4929.

[16] Neese, F.; Pantazis, D. A. What is not required to make a single molecule magnet. *Faraday Discuss.* **2010**, *148*, 229–238.

[17] Yao, X.-N.; Du, J.-Z.; Zhang, Y.-Q.; Leng, X.-B.; Yang, M.-W.; Jiang, S.-D.; Wang, Z.-X.; Ouyang, Z.-W.; Deng, L.; Wang, B.-W.; Gao, S. Two-Coordinate Co(II) Imido Complexes as Outstanding Single-Molecule Magnets. *J. Am. Chem. Soc.* **2017**, *139*, 373–380.

[18] Ishikawa, N.; Sugita, M.; Ishikawa, T.; Koshihara, S.-y.; Kaizu, Y. Lanthanide Double-Decker Complexes Functioning as Magnets at the Single-Molecular Level. *J. Am. Chem. Soc.* **2003**, *125*, 8694–8695.

[19] Rinehart, J. D.; Long, J. R. Exploiting single-ion anisotropy in the design of f-element single-molecule magnets. *Chem. Sci.* **2011**, *2*, 2078–2085.

[20] Feng, M.; Tong, M.-L. Single Ion Magnets from 3d to 5f: Developments and Strategies. *Chem. Eur. J.* **2018**, *24*, 7574–7594.

[21] Zhang, P.; Guo, Y.-N.; Tang, J. Recent advances in dysprosium-based single molecule magnets: Structural overview and synthetic strategies. *Coord. Chem. Rev.* **2013**, *257*, 1728–1763.

[22] Ishikawa, N.; Sugita, M.; Tanaka, N.; Ishikawa, T.; Koshihara, S.-y.; Kaizu, Y. Upward Temperature Shift of the Intrinsic Phase Lag of the Magnetization of Bis(phthalocyaninato)terbium by Ligand Oxidation Creating an S = 1/2 Spin. *Inorg. Chem.* **2004**, *43*, 5498–5500.

[23] Latendresse, T. P.; Vieru, V.; Wilkins, B. O.; Bhuvanesh, N. S.; Chibotaru, L. F.; Nippe, M. Magnetic Properties of a Terbium-[1]Ferrocenophane Complex: Analogies Between Lanthanide-Ferrocenophane and Lanthanide-Bis-phthalocyanine Complexes. *Angew. Chem. Int. Ed.* **2018**, *0*.

[24] Sievers, J. Asphericity of 4f-shells in their Hund's rule ground states. *Z. Phys. B Con. Mat.* **1982**, *45*, 289–296.

[25] Gonidec, M.; Davies, E. S.; McMaster, J.; Amabilino, D. B.; Veciana, J. Probing the Magnetic Properties of Three Interconvertible Redox States of a Single-Molecule Magnet with Magnetic Circular Dichroism Spectroscopy. *J. Am. Chem. Soc.* **2010**, *132*, 1756–1757.

[26] Rinehart, J. D.; Fang, M.; Evans, W. J.; Long, J. R. Strong exchange and magnetic blocking in N23-radical-bridged lanthanide complexes. *Nat. Chem.* **2011**, *3*, 538–542.

[27] Rinehart, J. D.; Fang, M.; Evans, W. J.; Long, J. R. A N23- Radical-Bridged Terbium Complex Exhibiting Magnetic Hysteresis at 14 K. *J. Am. Chem. Soc.* **2011**, *133*, 14236–14239.

[28] Chen, Y.-C.; Liu, J.-L.; Ungur, L.; Liu, J.; Li, Q.-W.; Wang, L.-F.; Ni, Z.-P.; Chibotaru, L. F.; Chen, X.-M.; Tong, M.-L. Symmetry-Supported Magnetic Blocking at 20 K in Pentagonal Bipyramidal Dy(III) Single-Ion Magnets. *J. Am. Chem. Soc.* **2016**, *138*, 2829–2837.

[29] Liu, J.; Chen, Y.-C.; Liu, J.-L.; Vieru, V.; Ungur, L.; Jia, J.-H.; Chibotaru, L. F.; Lan, Y.; Wernsdorfer, W.; Gao, S.; Chen, X.-M.; Tong, M.-L. A Stable Pentagonal Bipyramidal Dy(III) Single-Ion Magnet with a Record Magnetization Reversal Barrier over 1000 K. *J. Am. Chem. Soc.* **2016**, *138*, 5441–5450.

[30] Ding, Y.-S.; Chilton, N. F.; Winpenny, R. E. P.; Zheng, Y.-Z. On Approaching the Limit of Molecular Magnetic Anisotropy: A Near-Perfect Pentagonal Bipyramidal Dysprosium(III) Single-Molecule Magnet. *Angew. Chem. Int. Ed.* **2016**, *55*, 16071–16074.

[31] Chilton, N. F. Design Criteria for High-Temperature Single-Molecule Magnets. *Inorg. Chem.* **2015**, *54*, 2097–2099.

[32] Chilton, N. F.; Goodwin, C. A. P.; Mills, D. P.; Winpenny, R. E. P. The first near-linear bis(amide) f-block complex: a blueprint for a high temperature single molecule magnet.

Chem. Commun. **2015**, *51*, 101–103.

[33] Meihaus, K. R.; Long, J. R. Magnetic Blocking at 10 K and a Dipolar-Mediated Avalanche in Salts of the Bis(η8-cyclooctatetraenide) Complex [Er(COT)2]-. *J. Am. Chem. Soc.* **2013**, *135*, 17952–17957.

[34] Zhang, P.; Zhang, L.; Wang, C.; Xue, S.; Lin, S.-Y.; Tang, J. Equatorially Coordinated Lanthanide Single Ion Magnets. *J. Am. Chem. Soc.* **2014**, *136*, 4484–4487.

[35] Suzuki, K.; Sato, R.; Mizuno, N. Reversible switching of single-molecule magnet behaviors by transformation of dinuclear dysprosium cores in polyoxometalates. *Chem. Sci.* **2013**, *4*, 596–600.

[36] Sato, O. Dynamic molecular crystals with switchable physical properties. *Nat. Chem.* **2016**, *8*, 644–656.

[37] Liu, T.; Zheng, H.; Kang, S.; Shiota, Y.; Hayami, S.; Mito, M.; Sato, O.; Yoshizawa, K.; Kanegawa, S.; Duan, C. A light-induced spin crossover actuated single-chain magnet. *Nat. Commun.* **2013**, *4*, 2826.

[38] Nihei, M.; Okamoto, Y.; Sekine, Y.; Hoshino, N.; Shiga, T.; Liu, I. P.-C.; Oshio, H. A Light-Induced Phase Exhibiting Slow Magnetic Relaxation in a Cyanide-Bridged [Fe4Co2] Complex. *Angew. Chem. Int. Ed.* **2012**, *51*, 6361–6364.

[39] Fatila, E. M.; Rouzières, M.; Jennings, M. C.; Lough, A. J.; Clérac, R.; Preuss, K. E. Fine-Tuning the Single-Molecule Magnet Properties of a [Dy(III)-Radical]2 Pair. *J. Am. Chem. Soc.* **2013**, *135*, 9596–9599.

[40] Pinkowicz, D.; Southerland, H. I.; Avendaño, C.; Prosvirin, A.; Sanders, C.; Wernsdorfer, W.; Pedersen, K. S.; Dreiser, J.; Clérac, R.; Nehrkorn, J.; Simeoni, G. G.; Schnegg, A.; Holldack, K.; Dunbar, K. R. Cyanide Single-Molecule Magnets Exhibiting Solvent Dependent Reversible "On" and "Off" Exchange Bias Behavior. *J. Am. Chem. Soc.* **2015**, *137*, 14406–14422.

[41] Freedman, D. E.; Jenkins, D. M.; Iavarone, A. T.; Long, J. R. A Redox-Switchable Single-Molecule Magnet Incorporating [Re(CN)7]3-. *J. Am. Chem. Soc.* **2008**, *130*, 2884–2885.

[42] Tong, J.; Demeshko, S.; John, M.; Dechert, S.; Meyer, F. Redox-Induced Single-Molecule Magnetism in Mixed-Valent [2 x 2] Co4 Grid Complexes. *Inorg. Chem.* **2016**, *55*, 4362–4372.

[43] Zhu, X.; Su, S.; Cao, W.; Wen, Y.; Hu, S.; Wu, X.; Sheng, T. Redox effects of low-spin Ru(II/III) on slow magnetic relaxation of Ru-Mn(III) 1D cyanide-bridged complexes. *Dalton Trans.* **2017**, *46*, 7267–7272.

[44] Fortier, S.; Le Roy, J. J.; Chen, C.-H.; Vieru, V.; Murugesu, M.; Chibotaru, L. F.; Mindiola, D. J.; Caulton, K. G. A Dinuclear Cobalt Complex Featuring Unprecedented Anodic and Cathodic Redox Switches for Single-Molecule Magnet Activity. *J. Am. Chem. Soc.* **2013**, *135*, 14670–14678.

[45] Jeon, I.-R.; Park, J. G.; Xiao, D. J.; Harris, T. D. An Azophenine Radical-Bridged Fe2 Single-Molecule Magnet with Record Magnetic Exchange Coupling. *J. Am. Chem. Soc.* **2013**, *135*, 16845–16848.

[46] Ma, X.; Suturina, E. A.; De, S.; Négrier, P.; Rouzières, M.; Clérac, R.; Dechambenoit, P. Redox-active bridging ligand as a tool to promote spin delocalization, high spin complexes and magnetic multi-switchability. *Angew. Chem. Int. Ed.* **2018**,

[47] Newton, G. N.; Yamashita, S.; Hasumi, K.; Matsuno, J.; Yoshida, N.; Nihei, M.; Shiga, T.; Nakano, M.; Nojiri, H.; Wernsdorfer, W.; Oshio, H. Redox-Controlled Magnetic Mn13 Keggin Systems. *Angew. Chem. Int. Ed.* **2011**, *50*, 5716–5720.

[48] Dickie, C. M.; Laughlin, A. L.; Wofford, J. D.; Bhuvanesh, N. S.; Nippe, M. Transition metal redox switches for reversible "on/off" and "slow/fast" single-molecule magnet behaviour in dysprosium and erbium bis-diamidoferrocene complexes. *Chem. Sci.* **2017**, *8*, 8039–8049.

[49] Norel, L.; Feng, M.; Bernot, K.; Roisnel, T.; Guizouarn, T.; Costuas, K.; Rigaut, S. Redox Modulation of Magnetic Slow Relaxation in a 4f-Based Single-Molecule Magnet with a 4d Carbon-Rich Ligand. *Inorg. Chem.* **2014**, *53*, 2361–2363.

[50] Mannini, M.; Bertani, F.; Tudisco, C.; Malavolti, L.; Poggini, L.; Misztal, K.; Menozzi, D.; Motta, A.; Otero, E.; Ohresser, P.; Sainctavit, P.; Condorelli, G. G.; Dalcanale, E.; Sessoli, R.

Magnetic behaviour of TbPc2 single-molecule magnets chemically grafted on silicon surface. *Nat. Commun.* **2014**, *5*, 4582.

[51] Gonidec, M.; Biagi, R.; Corradini, V.; Moro, F.; De Renzi, V.; del Pennino, U.; Summa, D.; Muccioli, L.; Zannoni, C.; Amabilino, D. B.; Veciana, J. Surface Supramolecular Organization of a Terbium(III) Double-Decker Complex on Graphite and its Single Molecule Magnet Behavior. *J. Am. Chem. Soc.* **2011**, *133*, 6603–6612.

[52] Mannini, M.; Bonacchi, D.; Zobbi, L.; Piras, F. M.; Speets, E. A.; Caneschi, A.; Cornia, A.; Magnani, A.; Ravoo, B. J.; Reinhoudt, D. N.; Sessoli, R.; Gatteschi, D. Advances in Single-Molecule Magnet Surface Patterning through Microcontact Printing. *Nano Lett.* **2005**, *5*, 1435–1438.

[53] Cornia, A.; Fabretti, A. C.; Pacchioni, M.; Zobbi, L.; Bonacchi, D.; Caneschi, A.; Gatteschi, D.; Biagi, R.; Pennino, U. D.; Renzi, V. D.; Gurevich, L.; Zant, V. d. H. S. J. Direct Observation of Single-Molecule Magnets Organized on Gold Surfaces. *Angew. Chem. Int. Ed.* **2003**, *42*, 1645–1648.

[54] Mannini, M.; Pineider, F.; Sainctavit, P.; Danieli, C.; Otero, E.; Sciancalepore, C.; Talarico, A. M.; Arrio, M.-A.; Cornia, A.; Gatteschi, D.; Sessoli, R. Magnetic memory of a single-molecule quantum magnet wired to a gold surface. *Nat. Mater.* **2009**, *8*, 194–197.

[55] Cini, A.; Mannini, M.; Totti, F.; Fittipaldi, M.; Spina, G.; Chumakov, A.; Rüffer, R.; Cornia, A.; Sessoli, R. Mössbauer spectroscopy of a monolayer of single molecule magnets. *Nat. Commun.* **2018**, *9*, 480.

[56] Feltham, H. L. C.; Brooker, S. Review of purely 4f and mixed-metal nd-4f single-molecule magnets containing only one lanthanide ion. *Coord. Chem. Rev.* **2014**, *276*, 1–33.

[57] Liu, K.; Shi, W.; Cheng, P. Toward heterometallic single-molecule magnets: Synthetic strategy, structures and properties of 3d-4f discrete complexes. *Coord. Chem. Rev.* **2015**, *289-290*, 74–122.

[58] Andruh, M.; Costes, J.-P.; Diaz, C.; Gao, S. 3d-4f Combined Chemistry: Synthetic Strategies and Magnetic Properties. *Inorg. Chem.* **2009**, *48*, 3342–3359.

[59] Benelli, C.; Gatteschi, D. Magnetism of Lanthanides in Molecular Materials with Transition-Metal Ions and Organic Radicals. *Chem. Rev.* **2002**, *102*, 2369–2388.

[60] Piquer, L. R.; Sañudo, E. C. Heterometallic 3d-4f single-molecule magnets. *Dalton Trans.* **2015**, *44*, 8771–8780.

[61] Li, J.; Wei, R.-M.; Pu, T.-C.; Cao, F.; Yang, L.; Han, Y.; Zhang, Y.-Q.; Zuo, J.-L.; Song, Y. Tuning quantum tunnelling of magnetization through 3d-4f magnetic interactions: an alternative approach for manipulating single-molecule magnetism. *Inorg. Chem. Front.* **2017**, *4*, 114–122.

[62] Demir, S.; Jeon, I.-R.; Long, J. R.; Harris, T. D. Radical ligand-containing single-molecule magnets. *Coord. Chem. Rev.* **2015**, *289-290*, 149–176.

[63] Mondal, K. C.; Sundt, A.; Lan, Y.; Kostakis, G. E.; Waldmann, O.; Ungur, L.; Chibotaru, L. F.; Anson, C. E.; Powell, A. K. Coexistence of Distinct Single-Ion and Exchange-Based Mechanisms for Blocking of Magnetization in a CoII2DyIII2 Single-Molecule Magnet. *Angew. Chem. Int. Ed.* **2012**, *51*, 7550–7554.

[64] Li, X.-L.; Min, F.-Y.; Wang, C.; Lin, S.-Y.; Liu, Z.; Tang, J. Utilizing 3d-4f Magnetic Interaction to Slow the Magnetic Relaxation of Heterometallic Complexes. *Inorg. Chem.* **2015**, *54*, 4337–4344.

[65] Zhang, W.-Y.; Tian, Y.-M.; Li, H.-F.; Chen, P.; Zhang, Y.-Q.; Yan, P.-F.; Sun, W.-B. Strictly linear trinuclear Dy-Ca/Mg-Dy single-molecule magnets: the impact of long-range f-f ferromagnetic interactions on suppressing quantum tunnelling of magnetization leading to slow magnetic relaxation. *Dalton Trans.* **2017**, *46*, 8259–8268.

[66] Zhang, L.; Zhang, Y.-Q.; Zhang, P.; Zhao, L.; Guo, M.; Tang, J. Single-Molecule Magnet Behavior Enhanced by Synergic Effect of Single-Ion Anisotropy and Magnetic Interactions. *Inorg. Chem.* **2017**, *56*, 7882–7889.

[67] Ward, A. L.; Lukens, W. W.; Lu, C. C.; Arnold, J. Photochemical Route to Actinide-Transition Metal Bonds: Synthesis, Characterization and Reactivity of a Series of Thorium and Uranium Heterobimetallic Complexes. *J. Am. Chem. Soc.* **2014**, *136*, 3647–3654.

[68] Crease, A. E.; Legzdins, P. The Lewis acidity of organolanthanides. The interaction of cyclopenta-dienyl-lanthanides with some carbonyl and nitrosyl complexes. *J. Chem. Soc., Dalton Trans.* **1973**, 1501–1507.

[69] Suleimanov, G. Z.; Beletskaya, I. P. Reaction of cobalt carbonyl and its derivatives with lanthanide chlorides. *Dokl. Akad. Nauk SSSR* **1981**, *261*, 381–383.

[70] Suleimanov, G. Z.; Rybakova, L. F.; Sigalov, A. B.; Nuriev, Y. A.; Kochetkova, N. S.; Beletskaya, I. P. Synthesis and study of some properties of bimetallic cobaltocarbonyl derivatives of lanthanides. *Zh. Org. Khim.* **1982**, *18*, 2482–2485.

[71] Wang, X.; Zhou, X.; Wang, Y. Far-infrared spectra of some organometallic complexes containing rare earth-to-metal bond. *Guangpuxue Yu Guangpu Fenxi* **1987**, *7*, 28–30.

[72] Wang, X.; Zhou, X.; Zhang, J.; Xia, Y.; Liu, R.; Wang, S. The synthesis and structural investigation of some binuclear organometallic complexes with iron-to-rare earth bond. *Kexue Tongbao (Foreign Lang. Ed.)* **1985**, *30*, 351–355.

[73] Li, S.; Yang, X.; Sun, Y.; Li, P.; Wang, X.; Zhou, X. Analysis of organometallic compounds (XV). Relation between the Rf values of thin layer chromatography and infrared spectral absorption of some rare earth-metal binuclear organometallic compounds. *Gaodeng Xuexiao Huaxue Xuebao* **1988**, *9*, 1242–1245.

[74] Yan, P.-F.; Gao, J.-S.; Le, Z.-Y.; Mao, G.-J. Formation and reactivity of (Na[Fe(CO)2C5H5]2)n. *Gaodeng Xuexiao Huaxue Xuebao* **1998**, *19*, 21–23.

[75] Beletskaya, I. P.; Voskoboynikov, A. Z.; Chuklanova, E. B.; Kirillova, N. I.; Shestakova, A. K.; Parshina, I. N.; Gusev, A. I.; Magomedov, G. K. I. Bimetallic lanthanide complexes with lanthanide-transition metal bonds. Molecular structure of (C4H8O)(C5H5)2LuRu(CO)2(C5H5). The use of 139La NMR spectroscopy. *J. Am. Chem. Soc.* **1993**, *115*, 3156–3166.

[76] Pasynskii, A. A.; Eremenko, I. L.; Suleimanov, G. Z.; Nuriev, Y. A.; Beletskaya, I. P.; Shklover, V. E.; Struchkov, Y. T. Synthesis and molecular structure of lanthanum tris[cyclopentadienylmolybdenotricarbonylate] tetrahydrofuranate,

(THF)5La[CpMo(CO)3]3 THF. *J. Organomet. Chem.* **1984**, *266*, 45–52.

[77] Sobaczynski, A. P.; Obenauf, J.; Kempe, R. Alkane Elimination Reactions between Yttrium Alkyls and Tungsten Hydrides. *Eur. J. Inorg. Chem.* **2014**, *2014*, 1211–1217.

[78] Dickie, C. M.; Nippe, M. Magnetization dynamics of a heterometallic Dy-isocarbonyl complex. *Inorg. Chem. Front.* **2016**, *3*, 97–103.

[79] Pugh, T.; Chilton, N. F.; Layfield, R. A. A Low-Symmetry Dysprosium Metallocene Single-Molecule Magnet with a High Anisotropy Barrier. *Angew. Chem. Int. Ed.* **2016**, *55*, 11082–11085.

[80] Bradley, D. C.; Ghotra, J. S.; Hart, F. A. Low coordination numbers in lanthanide and actinide compounds. I. Preparation and characterization of tris[bis(trimethylsilyl)amido]lanthanides. *J. Chem. Soc., Dalton Trans.* **1973**, 1021–3.

[81] APEX2 Program for Data Collection on Area Detectors.

[82] Sheldrick, G. SADABS Program for Absorption Correction of Area Detector Frame. 2000.

[83] Sheldrick, G. M. A short history of SHELX. *Acta Crystallogr. Sect. A* **2008**, *64*, 112–122.

[84] Sheldrick, G. M. Crystal structure refinement with SHELXL. *Acta Crystallogr. Sect. C* **2015**, *71*, 3–8.

[85] XT, XS.

[86] Dolomanov, O. V.; Bourhis, L. J.; Gildea, R. J.; Howard, J. A. K.; Puschmann, H. OLEX2: a complete structure solution, refinement and analysis program. *J. Appl. Crystallogr.* **2009**, *42*, 339–341.

[87] Bain, G. A.; Berry, J. F. Diamagnetic Corrections and Pascal's Constants. *J. Chem. Educ.* **2008**, *85*, 532–536.

[88] Hazin, P. N.; Huffman, J. C.; Bruno, J. W. Preparation, luminescence studies, and solution behavior of a cerium-tungsten heterobimetallic compound. *J. Chem. Soc., Chem. Commun.* **1988**, 1473–1474.

[89] Darensbourg, M. Y.; Barros, H. L. C. Cation interaction with transition metal carbonylates

and cyanocarbonylates. *Inorg. Chem.* **1979**, *18*, 3286–3288.

[90] Darensbourg, M. Y.; Hanckel, J. M. Site-specific ion pairing of monosubstituted vanadium carbonylates, LV(CO)5-. *Organometallics* **1982**, *1*, 82–87.

[91] Layfield, R.; McDouall, J. J.; Sulway, S.; Tuna, F.; Collison, D.; Winpenny, R. E. Influence of the N-Bridging Ligand on Magnetic Relaxation in an Organometallic Dysprosium Single-Molecule Magnet. *Chem. Eur. J.* **2010**, *16*, 4442–4446.

[92] Jiang, S.-D.; Wang, B.-W.; Su, G.; Wang, Z.-M.; Gao, S. A Mononuclear Dysprosium Complex Featuring Single-Molecule-Magnet Behavior. *Angew. Chem. Int. Ed.* **2010**, *49*, 7448–7451.

[93] Chilton, N. F.; Collison, D.; McInnes, E. J. L.; Winpenny, R. E. P.; Soncini, A. An electrostatic model for the determination of magnetic anisotropy in dysprosium complexes. *Nat. Commun.* **2013**, *4*, 2551.

[94] Dyker, G.; Heiermann, J.; Miura, M.; Inoh, J.-I.; Pivsa-Art, S.; Satoh, T.; Nomura, M. Palladium-Catalyzed Arylation of Cyclopentadienes. *Chem. Eur. J.* **2000**, *6*, 3426–3433.

[95] Harder, S.; Ruspic, C. Insight in cyclopentadienyl metal complexes with superbulky ligands: The crystal structure of [CpBIGK]. *J. Organomet. Chem.* **2009**, *694*, 1180–1184.

[96] Spek, A. L. PLATON. 2008.

[97] Namorado, S.; Cui, J.; de Azevedo, C. G.; Lemos, M. A.; Duarte, M. T.; Ascenso, J. R.; Dias, A. R.; Martins, A. M. (Pentabenzylcyclopentadienyl)molybdenum Complexes: Synthesis, Structures and Redox Properties. *Eur. J. Inorg. Chem.* **2007**, 1103–1113.

[98] Chierotti, M. R.; Rossin, A.; Gobetto, R.; Peruzzini, M. Interaction between a Transition-Metal Fluoride and a Transition-Metal Hydride: Water-Mediated Hydrofluoric Acid Evolution Following Fluoride Solvation. *Inorg. Chem.* **2013**, *52*, 12616–12623.

[99] Mahmoud, K. A.; Rest, A. J.; Alt, H. G. Photochemistry of tricarbonyl(n5-cyclopentadienyl)hydrido complexes of molybdenum and tungsten and of dicarbonyl(n5-cyclopentadienyl)-(ethylene)hydridotungsten in solution and in frozen gas matrices at 12 K. *J. Chem. Soc., Dalton Trans.* **1984**, *0*, 187–197.

[100] Shafiq, F.; Szalda, D. J.; Creutz, C.; Bullock, R. M. Water-Soluble Tungsten Hydrides: Synthesis, Structures, and Reactions of (C5H4CO2H)(CO)3WH and Related Complexes. *Organometallics* **2000**, *19*, 824–833.

[101] Burchell, R. P. L.; Sirsch, P.; Decken, A.; McGrady, G. S. A structural study of [CpM(CO)3H] (M = Cr, Mo and W) by single-crystal X-ray diffraction and DFT calculations: sterically crowded yet surprisingly flexible molecules. *Dalton Trans.* **2009**, *0*, 5851–5857.

[102] Royo, E.; Acebrón, S.; Mosquera, M. E. G.; Royo, P. Allyl Isomerization Mediated by Cyclopentadienyl Group 6 Metal Compounds. *Organometallics* **2007**, *26*, 3831–3839.

[103] Hoffman, N. W. Single-flask synthesis of (C5H5)W(CO)3Cl from W(CO)6. *Inorg. Chim. Acta* **1984**, *88*, 59–61.

[104] Javier de la Mata, F.; Giner, P.; Royo, P. Synthesis and reactivity of new silyl-substituted monocyclopentadienyl molybdenum and tungsten complexes. *J. of Organomet. Chem.* **1999**, *572*, 155–161.

[105] Mannini, M.; Pineider, F.; Danieli, C.; Totti, F.; Sorace, L.; Sainctavit, P.; Arrio, M.-A.; Otero, E.; Joly, L.; Cezar, J. C.; Cornia, A.; Sessoli, R. Quantum tunnelling of the magnetization in a monolayer of oriented single-molecule magnets. *Nature* **2010**, *468*, 417–421.

[106] Vincent, R.; Klyatskaya, S.; Ruben, M.; Wernsdorfer, W.; Balestro, F. Electronic read-out of a single nuclear spin using a molecular spin transistor. *Nature* **2012**, *488*, 357–360.

[107] Bagai, R.; Christou, G. The Drosophila of single-molecule magnetism: [Mn12O12(O2CR)16(H2O)4]. *Chem. Soc. Rev.* **2009**, *38*, 1011–1026.

[108] Harriman, K. L. M.; Brosmer, J. L.; Ungur, L.; Diaconescu, P. L.; Murugesu, M. Pursuit of Record Breaking Energy Barriers: A Study of Magnetic Axiality in Diamide Ligated DyIII Single-Molecule Magnets. *J. Am. Chem. Soc.* **2017**, *139*, 1420–1423.

[109] Nava, A.; Rigamonti, L.; Zangrando, E.; Sessoli, R.; Wernsdorfer, W.; Cornia, A. Redox-Controlled Exchange Bias in a Supramolecular Chain of Fe4 Single-Molecule Magnets. *Angew. Chem. Int. Ed.* **2015**, *54*, 8777–8782.

[110] Dolinar, B. S.; Gómez-Coca, S.; Alexandropoulos, D. I.; Dunbar, K. R. An air stable radical-bridged dysprosium single molecule magnet and its neutral counterpart: redox switching of magnetic relaxation dynamics. *Chem. Commun.* **2017**, *53*, 2283–2286.

[111] Gaudette, A. I.; Jeon, I.-R.; Anderson, J. S.; Grandjean, F.; Long, G. J.; Harris, T. D. Electron Hopping through Double-Exchange Coupling in a Mixed-Valence Diiminobenzoquinone-Bridged Fe2 Complex. *J. Am. Chem. Soc.* **2015**, *137*, 12617–12626.

[112] Ringenberg, M. R.; Wittkamp, F.; Apfel, U.-P.; Kaim, W. Redox Induced Configurational Isomerization of Bisphosphine-Tricarbonyliron(I) Complexes and the Difference a Ferrocene Makes. *Inorg. Chem.* **2017**, *56*, 7501–7511.

[113] Monreal, M. J.; Carver, C. T.; Diaconescu, P. L. Redox Processes in a Uranium Bis(1,1'-diamidoferrocene) Complex. *Inorg. Chem.* **2007**, *46*, 7226–7228.

[114] Duhović, S.; Oria, J. V.; Odoh, S. O.; Schreckenbach, G.; Batista, E. R.; Diaconescu, P. L. Investigation of the Electronic Structure of Mono(1,1'-Diamidoferrocene) Uranium(IV) Complexes. *Organometallics* **2013**, *32*, 6012–6021.

[115] Broderick, E. M.; Guo, N.; Vogel, C. S.; Xu, C.; Sutter, J.; Miller, J. T.; Meyer, K.; Mehrkhodavandi, P.; Diaconescu, P. L. Redox Control of a Ring-Opening Polymerization Catalyst. *J. Am. Chem. Soc.* **2011**, *133*, 9278–9281.

[116] Wang, X.; Thevenon, A.; Brosmer, J. L.; Yu, I.; Khan, S. I.; Mehrkhodavandi, P.; Diaconescu, P. L. Redox Control of Group 4 Metal Ring-Opening Polymerization Activity toward l-Lactide and ε-Caprolactone. *J. Am. Chem. Soc.* **2014**, *136*, 11264–11267.

[117] Quan, S. M.; Wang, X.; Zhang, R.; Diaconescu, P. L. Redox Switchable Copolymerization of Cyclic Esters and Epoxides by a Zirconium Complex. *Macromolecules* **2016**, *49*, 6768–6778.

[118] Abubekerov, M.; Shepard, S. M.; Diaconescu, P. L. Switchable Polymerization of Norbornene Derivatives by a Ferrocene-Palladium(II) Heteroscorpionate Complex. *Eur. J. Inorg. Chem.* **2016**, 2634–2640.

[119] Huang, W.; Diaconescu, P. L. Reactivity and Properties of Metal Complexes Enabled by

Flexible and Redox-Active Ligands with a Ferrocene Backbone. *Inorg. Chem.* **2016**, *55*, 10013–10023.

[120] Shepard, S. M.; Diaconescu, P. L. Redox-Switchable Hydroelementation of a Cobalt Complex Supported by a Ferrocene-Based Ligand. *Organometallics* **2016**, *35*, 2446–2453.

[121] Bailey, P. J.; Coxall, R. A.; Dick, C. M.; Fabre, S.; Henderson, L. C.; Herber, C.; Liddle, S. T.; Loroño González, D.; Parkin, A.; Parsons, S. The First Structural Characterisation of a Group 2 Metal Alkylperoxide Complex: Comments on the Cleavage of Dioxygen by Magnesium Alkyl Complexes. *Chem. Eur. J.* **2003**, *9*, 4820–4828.

[122] Spek, A. L. Single-crystal structure validation with the program PLATON. *J. Appl. Crystallogr.* **2003**, *36*, 7–13.

[123] Han, T.; Ding, Y.-S.; Leng, J.-D.; Zheng, Z.; Zheng, Y.-Z. Polymeric Perturbation to the Magnetic Relaxations of the C2v-Symmetric [Er(Cp)2(OBu)2]- Anion. *Inorg. Chem.* **2015**, *54*, 4588–4590.

[124] Das, C.; Upadhyay, A.; Vaidya, S.; Singh, S. K.; Rajaraman, G.; Shanmugam, M. Origin of SMM behaviour in an asymmetric Er(III) Schiff base complex: a combined experimental and theoretical study. *Chem. Commun.* **2015**, *51*, 6137–6140.

[125] Rechkemmer, Y.; Fischer, J. E.; Marx, R.; Dörfel, M.; Neugebauer, P.; Horvath, S.; Gysler, M.; Brock-Nannestad, T.; Frey, W.; Reid, M. F.; van Slageren, J. Comprehensive Spectroscopic Determination of the Crystal Field Splitting in an Erbium Single-Ion Magnet. *J. Am. Chem. Soc.* **2015**, *137*, 13114–13120.

[126] Aubin, S. M. J.; Sun, Z.; Pardi, L.; Krzystek, J.; Folting, K.; Brunel, L.-C.; Rheingold, A. L.; Christou, G.; Hendrickson, D. N. Reduced Anionic Mn12 Molecules with Half-Integer Ground States as Single-Molecule Magnets. *Inorg. Chem.* **1999**, *38*, 5329–5340.

[127] Novikov, V. V.; Pavlov, A. A.; Nelyubina, Y. V.; Boulon, M.-E.; Varzatskii, O. A.; Voloshin, Y. Z.; Winpenny, R. E. A Trigonal Prismatic Mononuclear Cobalt(II) Complex Showing Single-Molecule Magnet Behavior. *J. Am. Chem. Soc.* **2015**, *137*, 9792–9795.

[128] Lucaccini, E.; Sorace, L.; Perfetti, M.; Costes, J.-P.; Sessoli, R. Beyond the anisotropy

barrier: slow relaxation of the magnetization in both easy-axis and easy-plane Ln(trensal) complexes. *Chem. Commun.* **2014**, *50*, 1648–1651.

[129] Brown, A. J.; Pinkowicz, D.; Saber, M. R.; Dunbar, K. R. A Trigonal-Pyramidal Erbium(III) Single-Molecule Magnet. *Angew. Chem. Int. Ed.* **2015**, *54*, 5864–5868.

[130] Zhang, P.; Jung, J.; Zhang, L.; Tang, J.; Le Guennic, B. Elucidating the Magnetic Anisotropy and Relaxation Dynamics of Low-Coordinate Lanthanide Compounds. *Inorg. Chem.* **2016**, *55*, 1905–1911.

[131] Singh, S. K.; Pandey, B.; Velmurugan, G.; Rajaraman, G. Key role of higher order symmetry and electrostatic ligand field design in the magnetic relaxation of low-coordinate Er(III) complexes. *Dalton Trans.* **2017**, *46*, 11913–11924.

[132] Brunschwig, B. S.; Creutz, C.; Sutin, N. Optical transitions of symmetrical mixed-valence systems in the Class II-III transition regime. *Chem. Soc. Rev.* **2002**, *31*, 168–184.

[133] Manriquez, J. M.; Ward, M. D.; Reiff, W. M.; Calabrese, J. C.; Jones, N. L.; Carroll, P. J.; Bunel, E. E.; Miller, J. S. Structural and Physical Properties of Delocalized Mixed-Valent [CpstarM(pentalene)M'Cpstar]n+ and [CpstarM(indacene)M'Cpstar]n+ (M, M' = Fe, Co, Ni; n = 0, 1, 2) Complexes. *J. Am. Chem. Soc.* **1995**, *117*, 6182–6193.

[134] Patra, S.; Miller, T. A.; Sarkar, B.; Niemeyer, M.; Ward, M. D.; Lahiri, G. K. An Unusual Dinuclear Ruthenium(III) Complex with a Conjugated Bridging Ligand Derived from Cleavage of a 1,4-Dihydro-1,2,4,5-Tetrazine Ring. Synthesis, Structure, and UV-Vis-NIR Spectroelectrochemical Characterization of a Five-Membered Redox Chain Incorporating Two Mixed-Valence States. *Inorg. Chem.* **2003**, *42*, 4707–4713.

[135] Craig, G. A.; Murrie, M. 3d single-ion magnets. *Chem. Soc. Rev.* **2015**, *44*, 2135–2147.

[136] Gomez-Coca, S.; Aravena, D.; Morales, R.; Ruiz, E. Large magnetic anisotropy in mononuclear metal complexes. *Coord. Chem. Rev.* **2015**, *289-290*, 379–392.

[137] Vallejo, J.; Pascual-Álvarez, A.; Cano, J.; Castro, I.; Julve, M.; Lloret, F.; Krzystek, J.; De Munno, G.; Armentano, D.; Wernsdorfer, W.; Ruiz-García, R.; Pardo, E. Field-Induced Hysteresis and Quantum Tunneling of the Magnetization in a Mononuclear Manganese(III)

Complex. *Angew. Chem. Int. Ed.* **2013**, *52*, 14075–14079.

[138] Cornia, A.; Rigamonti, L.; Boccedi, S.; Clérac, R.; Rouzières, M.; Sorace, L. Magnetic blocking in extended metal atom chains: a pentachromium(II) complex behaving as a single-molecule magnet. *Chem. Commun.* **2014**, *50*, 15191–15194.

[139] Deng, Y.-F.; Han, T.; Wang, Z.; Ouyang, Z.; Yin, B.; Zheng, Z.; Krzystek, J.; Zheng, Y.-Z. Uniaxial magnetic anisotropy of square-planar chromium(II) complexes revealed by magnetic and HF-EPR studies. *Chem. Commun.* **2015**, *51*, 17688–17691.

[140] Bradley, D. C.; Hursthouse, M. B.; Newing, C. W.; Welch, A. J. Square planar and tetrahedral chromium(II) complexes; crystal structure determinations. *J. Chem. Soc., Chem. Commun.* **1972**, 567–568.

[141] Jonas, K. Reactive Organometallic Compounds Obtained from Metallocenes and Related Compounds and Their Synthetic Applications. *Angew. Chem. Int. Ed.* **1985**, *24*, 295–311.

[142] A. Layfield, R. Manganese(ii): the black sheep of the organometallic family. *Chem. Soc. Rev.* **2008**, *37*, 1098–1107.

[143] Abernethy, C. D.; Clyburne, J. A. C.; Cowley, A. H.; Jones, R. A. Reactions of Transition-Metal Metallocenes with Stable Carbenes. *J. Am. Chem. Soc.* **1999**, *121*, 2329–2330.

[144] Scheuermayer, S.; Tuna, F.; Pineda, E. M.; Bodensteiner, M.; Scheer, M.; Layfield, R. A. Transmetalation of Chromocene by Lithium-Amide, -Phosphide, and -Arsenide Nucleophiles. *Inorg. Chem.* **2013**, *52*, 3878–3883.

[145] Koehler, F. H.; Ackermann, K.; Sedlmair, J. Dichloro(eta5-cyclopentadienyl)chlromium Dimer. *Z. Naturforsch. B.* **1983**, *38b*, 1406–1411.

[146] Zhou, W.; Desnoyer, A. N.; Bailey, J. A.; Patrick, B. O.; Smith, K. M. Direct Synthesis of Ligand-Based Radicals by the Addition of Bipyridine to Chromium(II) Compounds. *Inorg. Chem.* **2013**, *52*, 2271–2273.

[147] Telser, J.; Pardi, L. A.; Krzystek, J.; Brunel, L.-C. EPR Spectra from "EPR-Silent" Species: High-Field EPR Spectroscopy of Aqueous Chromium(II). *Inorg. Chem.* **1998**, *37*, 5769–5775.

[148] Harman, W. H.; Harris, T. D.; Freedman, D. E.; Fong, H.; Chang, A.; Rinehart, J. D.; Ozarowski, A.; Sougrati, M. T.; Grandjean, F.; Long, G. J.; Long, J. R.; Chang, C. J. Slow Magnetic Relaxation in a Family of Trigonal Pyramidal Iron(II) Pyrrolide Complexes. *J. Am. Chem. Soc.* **2010**, *132*, 18115–18126.

[149] Zadrozny, J. M.; Xiao, D. J.; Long, J. R.; Atanasov, M.; Neese, F.; Grandjean, F.; Long, G. J. Mössbauer Spectroscopy as a Probe of Magnetization Dynamics in the Linear Iron (I) and Iron(II) Complexes [Fe(C(SiMe3)3)2]1-/0. *Inorg. Chem.* **2013**, *52*, 13123–13131.

[150] Zadrozny, J. M.; Xiao, D. J.; Atanasov, M.; Long, G. J.; Grandjean, F.; Neese, F.; Long, J. R. Magnetic blocking in a linear iron(I) complex. *Nat. Chem.* **2013**, *5*, 577–581.

[151] Greenwood, N. N.; Gibb, T. *Mössbauer Spectroscopy*; Chapman and Hall (London), 1971.

[152] Abbas, G.; Lan, Y.; Mereacre, V.; Wernsdorfer, W.; Clérac, R.; Buth, G.; Sougrati, M. T.; Grandjean, F.; Long, G. J.; Anson, C. E.; Powell, A. K. Magnetic and 57Fe Mössbauer Study of the Single Molecule Magnet Behavior of a Dy3Fe7 Coordination Cluster. *Inorg. Chem.* **2009**, *48*, 9345–9355.

[153] Mereacre, V.; Prodius, D.; Lan, Y.; Turta, C.; Anson, C. E.; Powell, A. K. Antiferromagnetically Coupled Iron Ions in a Polynuclear FeIII-Dy Complex: Confirmation by Variable-Field 57Fe Mössbauer Spectroscopy. *Chem. Eur. J.* **2011**, *17*, 123–128.

[154] Chen, S.; Mereacre, V.; Prodius, D.; Kostakis, G. E.; Powell, A. K. Developing a "Highway Code" To Steer the Structural and Electronic Properties of FeIII/DyIII Coordination Clusters. *Inorg. Chem.* **2015**, *54*, 3218–3227.

[155] Baniodeh, A.; Mereacre, V.; Magnani, N.; Lan, Y.; Wolny, J. A.; Schünemann, V.; Anson, C. E.; Powell, A. K. Para versus meta ligand substituents as a means of directing magnetic anisotropy in FeDy2 coordination clusters. *Chem. Commun.* **2013**, *49*, 9666–9668.

[156] Mereacre, V.; Baniodeh, A.; Anson, C. E.; Powell, A. K. Effect of Ligand Substitution on the Interaction Between Anisotropic Dy(III) Ions and 57Fe Nuclei in Fe2Dy2 Coordination Clusters. *J. Am. Chem. Soc.* **2011**, *133*, 15335–15337.

[157] Mereacre, V.; Klöwer, F.; Lan, Y.; Clérac, R.; Wolny, J. A.; Schünemann, V.; Anson, C. E.;

Powell, A. K. Spin relaxation in antiferromagnetic Fe-Fe dimers slowed down by anisotropic Dy(III) ions. *Beilstein J. Nanotech.* **2013**, *4*, 807–814.

[158] Dattagupta, S.; Blume, M. Stochastic theory of line shape. I. Nonsecular effects in the strong-collision model. *Phys. Rev. B* **1974**, *10*, 4540–4550.

[159] Bag, P.; Goura, J.; Mereacre, V.; Novitchi, G.; Powell, A. K.; Chandrasekhar, V. Synthesis, magnetism and Mössbauer studies of tetranuclear heterometallic FeIII2Ln2(Ln = Gd, Dy, Tb) complexes: evidence of slow relaxation of magnetization in the terbium analogue. *Dalton Trans.* **2014**, *43*, 16366–16376.

[160] Kuroda-Sowa, T.; Lam, M.; Rheingold, A. L.; Frommen, C.; Reiff, W. M.; Nakano, M.; Yoo, J.; Maniero, A. L.; Brunel, L.-C.; Christou, G.; Hendrickson, D. N. Effects of Paramagnetic Ferrocenium Cations on the Magnetic Properties of the Anionic Single-Molecule Magnet [Mn12O12(O2CC6F5)16(H2O)4]-. *Inorg. Chem.* **2001**, *40*, 6469–6480.

[161] Sturhahn, W. Nuclear resonant spectroscopy. *J. Phys.: Condens. Matter* **2004**, *16*, S497.

[162] Smirnov, G. V. General properties of nuclear resonant scattering. *Hyperfine Interact.* **1999**, *123-124*, 31–77.

[163] Smirnov, G. V. Synchrotron Mössbauer 57Fe radiation. *Hyperfine Interact.* **2000**, *125*, 91–112.

[164] Chen, Y.-L.; Yan, D.-P. *Mössbauer Effects in Lattice Dynamics*; Wiley (Weinham), 2007.

[165] Fultz, B. *Mössbauer Spectrometry in Characterization of Materials*; Wiley, 2012.

[166] Alp, E. E.; Mooney, T. M.; Toellner, T.; Sturhahn, W.; Witthoff, E.; Röhlsberger, R.; Gerdau, E.; Homma, H.; Kentjana, M. Time resolved nuclear resonant scattering from 119Sn nuclei using synchrotron radiation. *Phys. Rev. Lett.* **1993**, *70*, 3351–3354.

[167] Trautwein, A. X.; Winkler, H.; Schwendy, S.; Grünsteudel, H.; Meyer-Klaucke, W.; Leupold, O.; Rüter, H. D.; Gerdau, E.; Haas, M.; Realo, E.; Mandon, D.; Weiss, R. Iron porphyrins reinvistigated by new method: Mössbauer spectroscopy using synchrotron radiation. *Pure Appl. Chem.* **1998**, *70*, 917–924.

[168] Sturhahn, W. CONUSS and PHOENIX: Evaluation of nuclear resonant scattering data. *Hy-*

perfine Interact. **2000**, *125*, 149–172.

[169] Bi, Y.; Guo, Y.-N.; Zhao, L.; Guo, Y.; Lin, S.-Y.; Jiang, S.-D.; Tang, J.; Wang, B.-W.; Gao, S. Capping Ligand Perturbed Slow Magnetic Relaxation in Dysprosium Single-Ion Magnets. *Chem. Eur. J.* **2011**, *17*, 12476–12481.

[170] Zhu, J.; Wang, C.; Luan, F.; Liu, T.; Yan, P.; Li, G. Local Coordination Geometry Perturbed β-Diketone Dysprosium Single-Ion Magnets. *Inorg. Chem.* **2014**, *53*, 8895–8901.

[171] Wang, Y.-L.; Ma, Y.; Yang, X.; Tang, J.; Cheng, P.; Wang, Q.-L.; Li, L.-C.; Liao, D.-Z. Syntheses, Structures and Magnetic and Luminescence Properties of a New DyIII-Based Single-Ion Magnet. *Inorg. Chem.* **2013**, *52*, 7380–7386.

[172] Tong, Y.-Z.; Gao, C.; Wang, Q.-L.; Wang, B.-W.; Gao, S.; Cheng, P.; Liao, D.-Z. Two mononuclear single molecule magnets derived from dysprosium(III) and tmphen (tmphen = 3,4,7,8-tetramethyl-1,10-phenanthroline). **2015**, *44*, 9020–9026.

[173] Boulay, A.; Deraeve, C.; Vander Elst, L.; Leygue, N.; Maury, O.; Laurent, S.; Muller, R. N.; Mestre-Voegtlé, B.; Picard, C. Terpyridine-Based Heteroditopic Ligand for RuIILn3III Metallostar Architectures (Ln = Gd, Eu, Nd, Yb) with MRI/Optical or Dual-Optical Responses. *Inorg. Chem.* **2015**, *54*, 1414–1425.

[174] Chen, J.; Kuss-Petermann, M.; Wenger, O. S. Distance Dependence of Bidirectional Concerted Proton-Electron Transfer in Phenol-Ru(2,2'-bipyridine) Dyads. *Chem. Eur. J.* **2014**, *20*, 4098–4104.

[175] Fatila, E. M.; Hetherington, E. E.; Jennings, M.; Lough, A. J.; Preuss, K. E. Syntheses and crystal structures of anhydrous Ln(hfac)3(monoglyme). Ln = La, Ce, Pr, Sm, Eu, Gd, Tb, Dy, Er, Tm. *Dalton Trans.* **2012**, *41*, 1352–1362.

[176] Eisentraut, K. J.; Sievers, R. E. Thermogravimetric studies of metal β-diketonates. *J. Inorg. Nucl. Chem.* **1967**, *29*, 1931–1936.

[177] Qian, K.; Baldoví, J. J.; Jiang, S.-D.; Gaita-Ariño, A.; Zhang, Y.-Q.; Overgaard, J.; Wang, B.-W.; Coronado, E.; Gao, S. Does the thermal evolution of molecular structures critically affect the magnetic anisotropy? *Chem. Sci.* **2015**, *6*, 4587–4593.

[178] Phillips, J. E.; Herber, R. H. Bonding in triorganotin pyridines. *J. Organomet. Chem.* **1984**, *268*, 39–47.

[179] Paulsen, H.; Schünemann, V.; Trautwein, A. X.; Winkler, H. Mössbauer studies of coordination compounds using synchrotron radiation. *Coord. Chem. Rev.* **2005**, *249*, 255–272.

APPENDIX A

FIRST APPENDIX

Text for the Appendix follows.

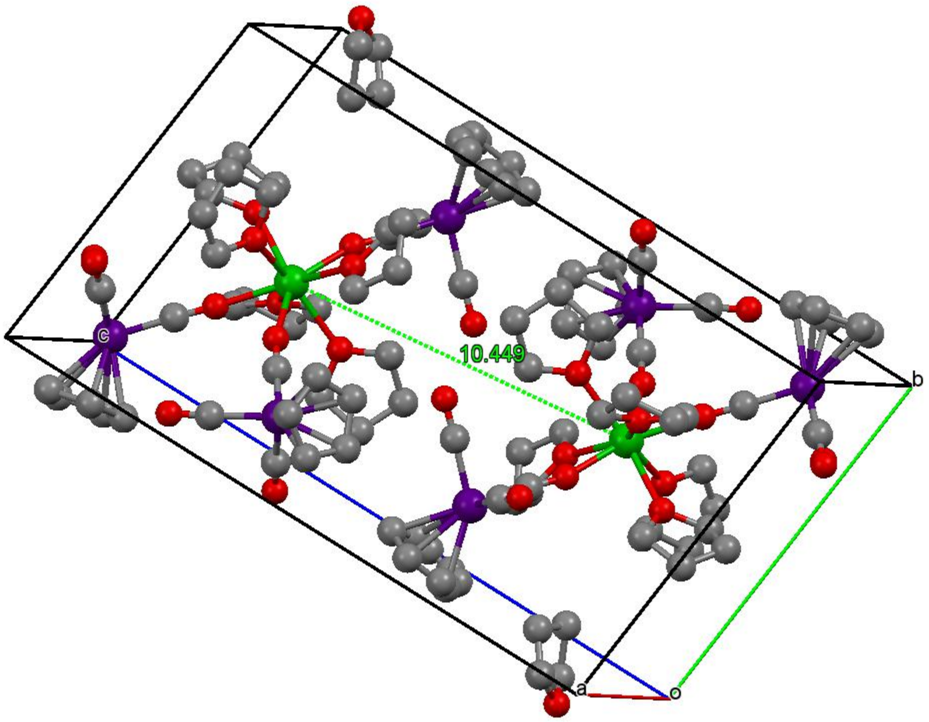

Figure A.1: Unit cell packing diagram of **2-1·thf** depicting the closest $Dy^{3+}\cdots Dy^{3+}$ contact of 10.45 Å

Dy - O1, Å	2.320(5)
Dy - O2, Å	2.267(5)
Dy - O3, Å	2.270(5)
Dy - O4, Å	2.428(5)
Dy - O5, Å	2.384(5)
Dy - O6, Å	2.462(5)
Dy - O7, Å	2.385(5)
Dy - O8, Å	2.432(5)
O1 – Dy – O2, °	71.8(2)
O2 – Dy – O6, °	72.4(2)
O6 – Dy – O5, °	72.3(2)
O5 – Dy – O1, °	73.3(2)
O3 – Dy – O4, °	72.6(2)
O4 – Dy – O7, °	73.8(2)
O7 – Dy – O8, °	73.5(2)
O8 – Dy – O3, °	75.4(2)

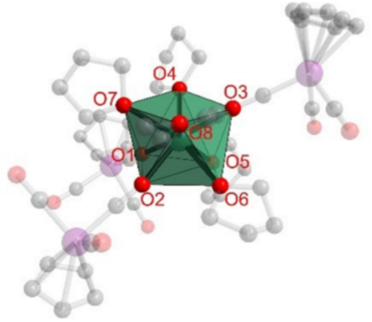

Figure A.2: Selected geometric parameters in **2-1·thf**

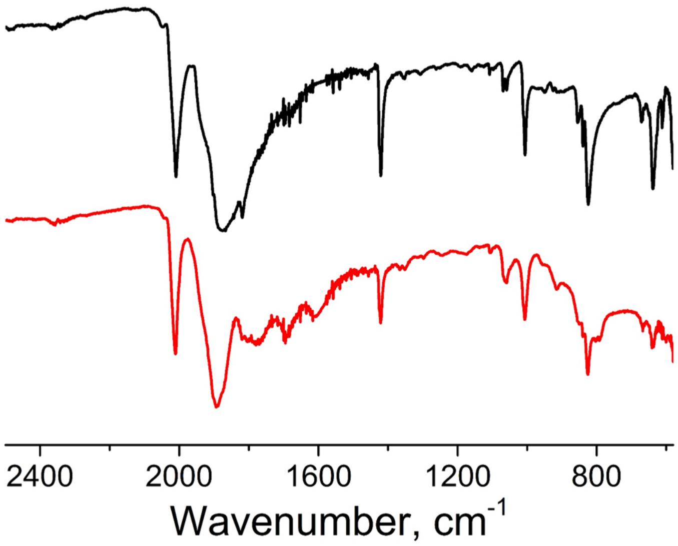

Figure A.3: IR spectra of $HW(CO)_3Cp$ (black) and **2-1·thf** (red)

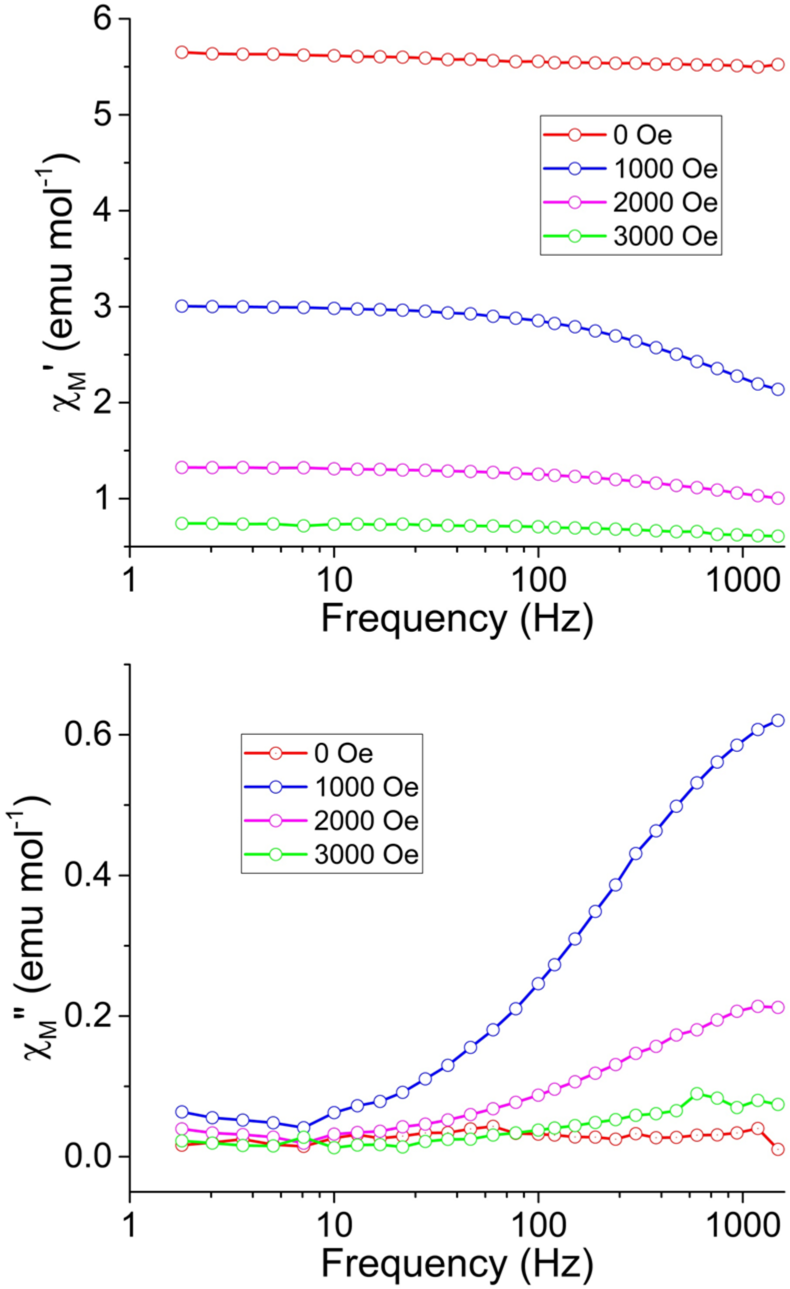

Figure A.4: Frequency dependence of the in-phase (top) and out-of-phase (bottom) components of the ac magnetic susceptibility for **2-1·thf** under variable applied dc fields of 0 to 3000 Oe at 1.8 K and with a 5 Oe switching field. Lines are a guide for the eye.

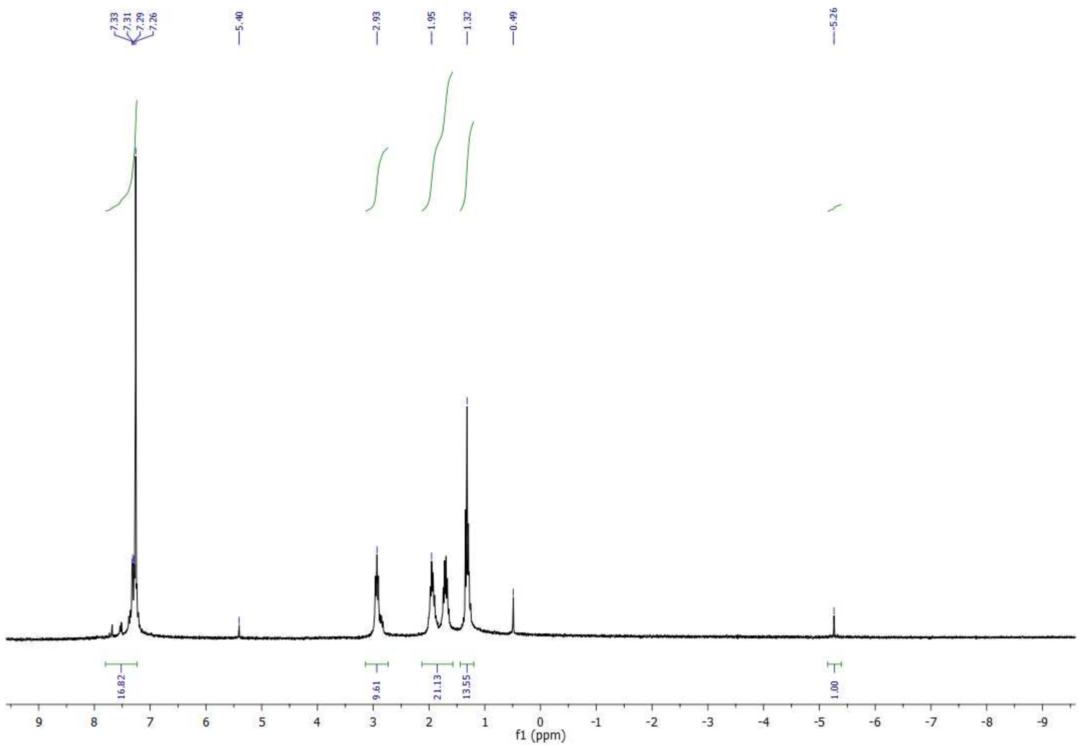

Figure A.5: ^{1}H NMR spectrum of **3-1** in $CDCl_3$.

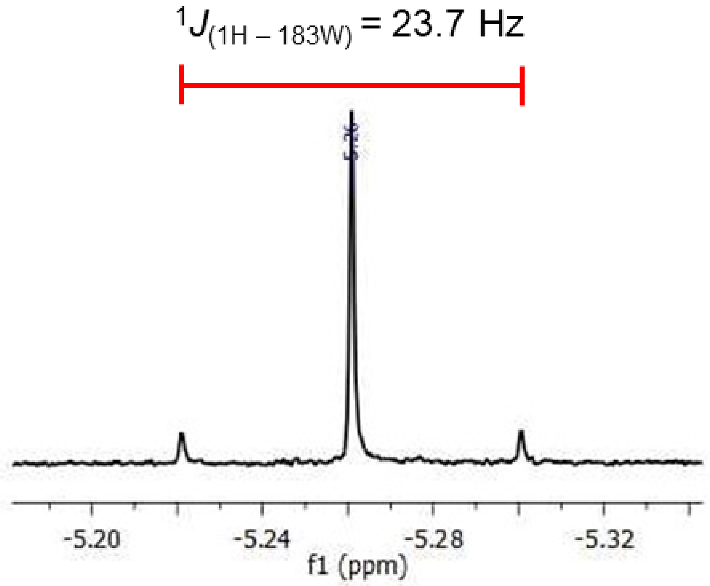

Figure A.6: The hydride resonance in the ^{1}H NMR spectrum of **3-1** in $CDCl_3$. Satellites from the ^1J coupling between ^{1}H and ^{183}W are visible at $\delta = -5.221$ ppm and $\delta = 5.300$ ppm, with $^1J =$ 23.70 Hz.

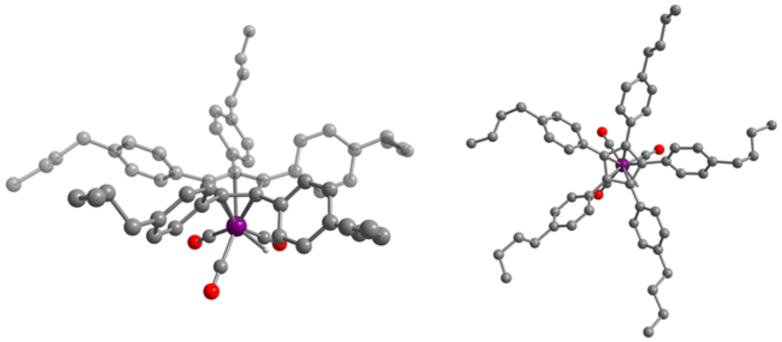

distances	
W1−C1$_{(CO)}$, Å	1.969(5)
W1− C2$_{(CO)}$, Å	1.965(5)
W1− C3$_{(CO)}$, Å	1.954(6)
W1−Cp$_{(centroid)}$, Å	2.016
C1−O1, Å	1.157(5)
C2−O2, Å	1.161(6)
C3−O3, Å	1.161(7)

angles	
C1−W1−C2, °	77.6(2)
C1−W1−C3, °	104.3(2)
C2−W1−C3, °	81.1(3)
W1−C1−O1, °	179.2(4)
W1−C2−O2, °	178.0(4)
W1−C3−O3, °	177.2(6)

Figure A.7: Selected bond distances and angles in the molecular structure of **3-1**. Purple = W, grey = C, red = O, white = H.

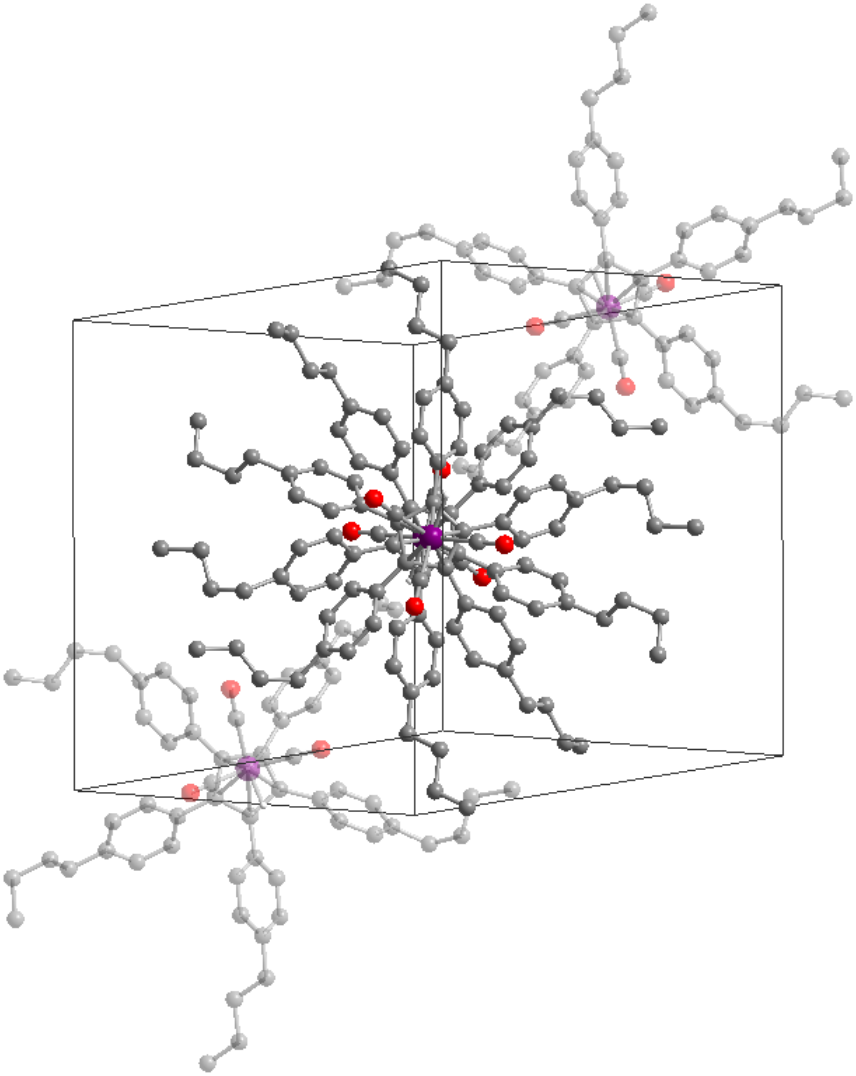

Figure A.8: Unit cell of **3-1**. Purple = W, grey = C, red = O, white = H.

APPENDIX B

SECOND APPENDIX

Compound	Dy(fc[NSi(*t*-Bu)Me$_2$]$_2$)$_2$ (**4-1**)
Formula	$C_{44}H_{76}DyFe_2N_4Si_4$
Crystal size	0.34 x 0.22 x 0.114
Crystal system	orthorhombic
Space group	*Pbca*
a, Å	20.025(4)
b, Å	19.663(4)
c, Å	24.499(5)
α , °	90
β , °	90
γ , °	90
Volume, Å^3	9646(3)
Z	8
T, K	110
Density ϱ_{calcd} , mg/m^3	1.443
$F(000)$	4336
Absorption coefficient (mm^{-1})	2.260
Θ_{min} , Θ_{max}, °	1.662, 24.998
Index ranges	$-23 \leq h \leq 23$
	$-23 \leq k \leq 23$
	$-29 \leq l \leq 29$
Reflections collected	89008
Independent reflections	8495 [R(int) = 0.0859]
Completeness to Θ °	100 %
Absorption correction	semi-empirical from equivalents
Refinement method	full-matrix least-squares on F^2
Data/restraints/parameters	8495/290/584
Final R indices [$(I > 2\sigma(I))$]	$R_1 = 0.0376$, $wR_2 = 0.0753$
R indices (all data)	$R_1 = 0.0650$, $wR_2 = 0.0947$
Largest diff peak and hole, (e Å^{-3})	1.093 and 0.902

Table B.1: Crystallographic data for **4-1**

Compound	Er(fc[NSi(*t*-Bu)Me$_2$]$_2$)$_2$ (**4-2**)
Formula	$C_{44}H_{76}ErFe_2N_4Si_4$
Crystal size	0.15 x 0.08 x 0.07
Crystal system	orthorhombic
Space group	*Pbca*
a, Å	19.794(2)
b, Å	19.822(2)
c, Å	24.603(2)
α , °	90
β , °	90
γ , °	90
Volume, Å^3	9653(2)
Z	8
T, K	110
Density ϱ_{calcd} , mg/m^3	1.448
$F(000)$	4352
Absorption coefficient (mm^{-1})	2.449
Θ_{min} , Θ_{max}, °	1.673, 19.999
Index ranges	$-19 \leq h \leq 19$
	$-19 \leq k \leq 19$
	$-23 \leq l \leq 23$
Reflections collected	81679
Independent reflections	4502 [R(int) = 0.3290]
Absorption correction	semi-empirical from equivalents
Refinement method	full-matrix least-squares on F^2
Data/restraints/parameters	4502/1008/516
Final R indices [$(I > 2\sigma(I))$]	$R_1 = 0.0742$, $wR_2 = 0.1491$
R indices (all data)	$R_1 = 0.1587$, $wR_2 = 0.1847$
Largest diff peak and hole, (e Å^{-3})	1.353 and 1.273

Table B.2: Crystallographic data for **4-2**

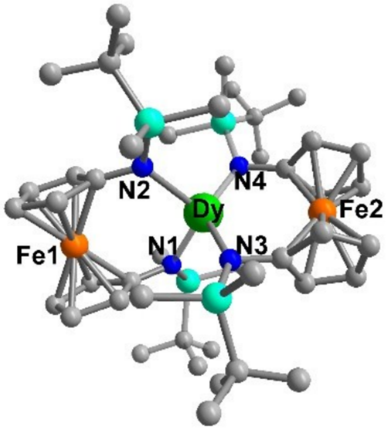

distances		
	Dy···Fe1, Å	3.792(2)
	Dy···Fe2, Å	3.368(2)
	Dy-N1, Å	2.370(4)
	Dy-N2, Å	2.338(4)
	Dy-N3, Å	2.262(4)
	Dy-N4, Å	2.252(4)
angles		
	N1-Dy-N2, °	110.5(2)
	N1-Dy-N3, °	104.2(2)
	N1-Dy-N4, °	102.7(2)
	N2-Dy-N3, °	100.3(2)
	N2-Dy-N4, °	106.5(2)
	N3-Dy-N4, °	131.9(2)

Figure B.1: Selected geometric parameters for compound **4-1**.

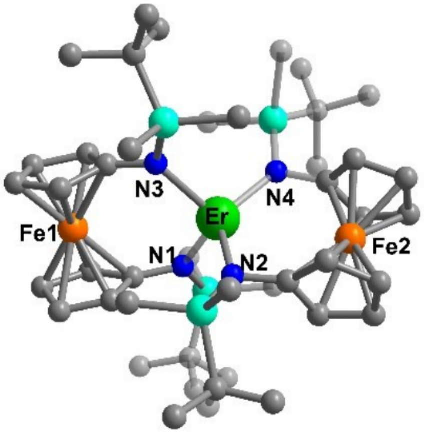

distances	
Er···Fe1, Å	3.819(5)
Er···Fe2, Å	3.498(4)
Er-N1, Å	2.27(1)
Er-N2, Å	2.22(2)
Er-N3, Å	2.29(1)
Er-N4, Å	2.21(2)
angles	
N1-Er-N2, °	104.8(6)
N1-Er-N3, °	109.6(5)
N1-Er-N4, °	104.2(6)
N2-Er-N3, °	102.2(6)
N2-Er-N4, °	126.7(6)
N3-Er-N4, °	108.7(5)

Figure B.2: Selected geometric parameters for compound **4-2**.

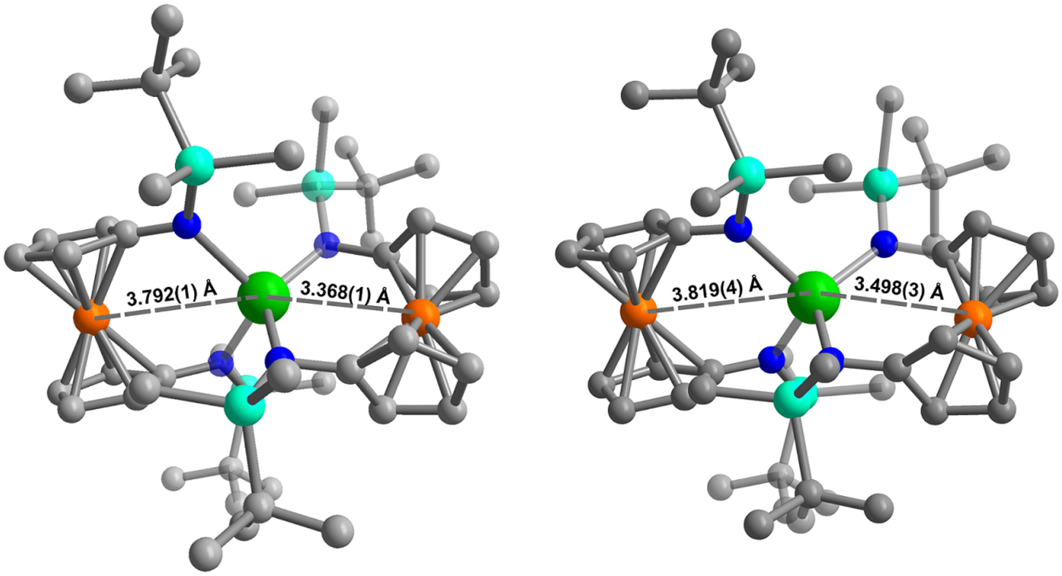

Figure B.3: Molecular structure of Dy(fc[NSi(*t*-Bu)Me$_2$]$_2$)$_2$ **4-1** (left) and Er(fc[NSi(*t*-Bu)Me$_2$]$_2$)$_2$ **4-2** (right). Green = Ln, orange = Fe, cyan = Si, blue = N, grey = C. Hydrogen atoms omitted for clarity. Ln–Fe distances are highlighted: Dy–Fe = 3.792(1) Å and 3.368(1) Å, Er–Fe = 3.819(4) Å and 3.498(3) Å.

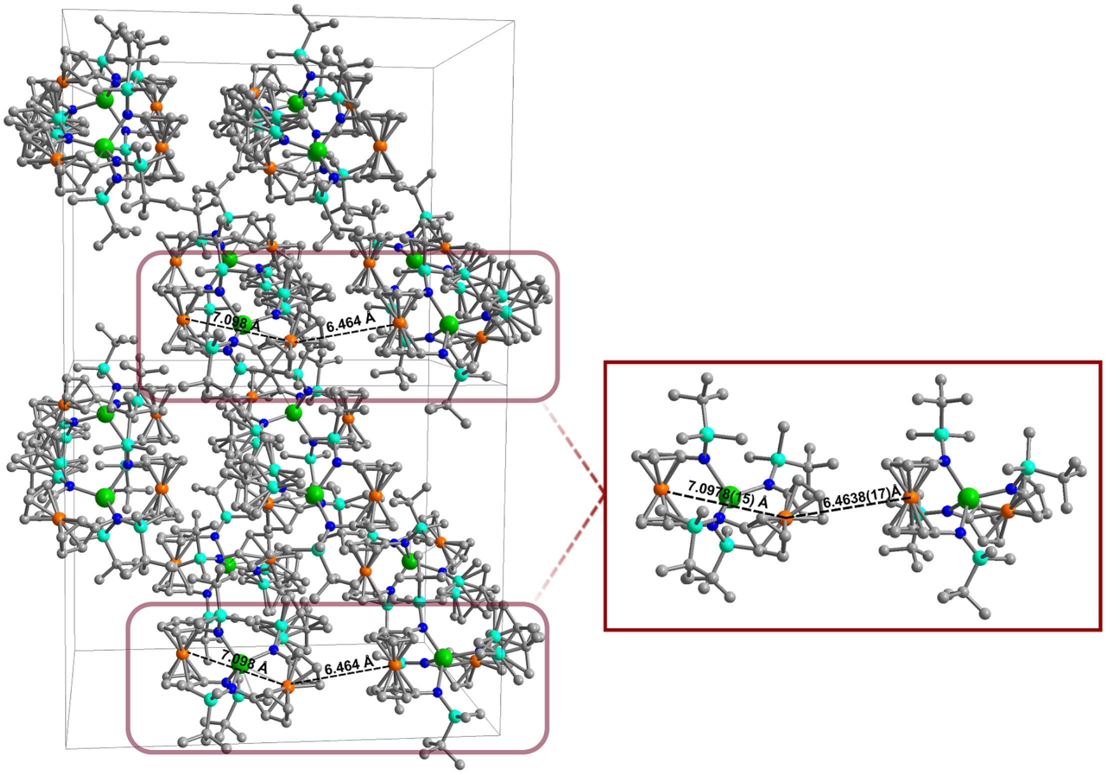

Figure B.4: Unit cell packing in **4-1**. The closest Fe···Fe contacts of 6.464(2) Å (intermolecular) and the longer Fe···Fe contacts of 7.098(2) Å (intramolecular) are highlighted.

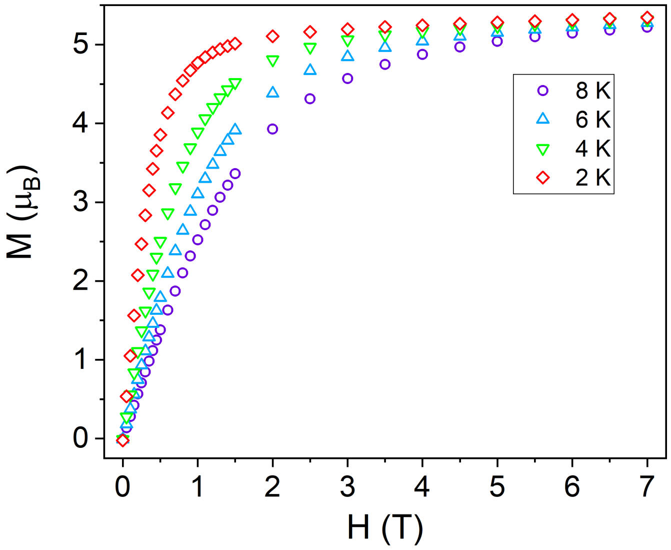

Figure B.5: Field dependence of the magnetization for **[4-1]**$^{-}$.

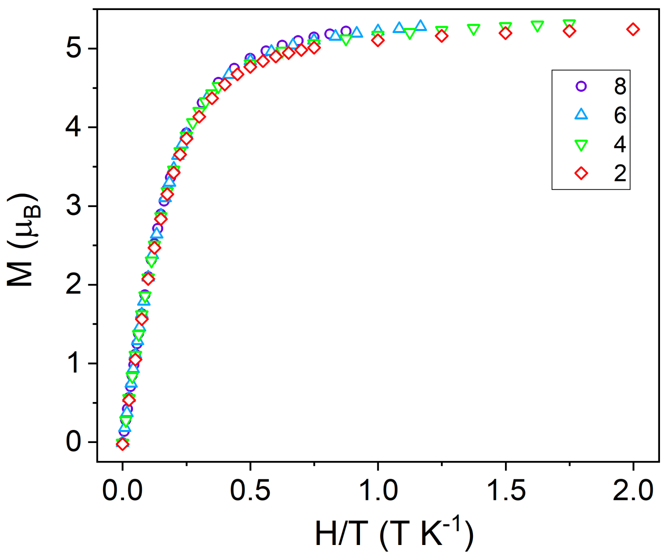

Figure B.6: Field dependence, temperature dependence of the magnetization for **[4-1]**⁻.

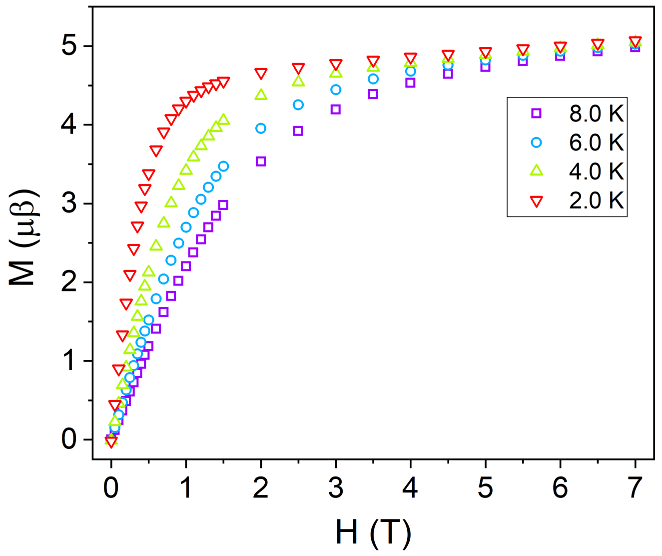

Figure B.7: Field dependence of the magnetization for **4-1**.

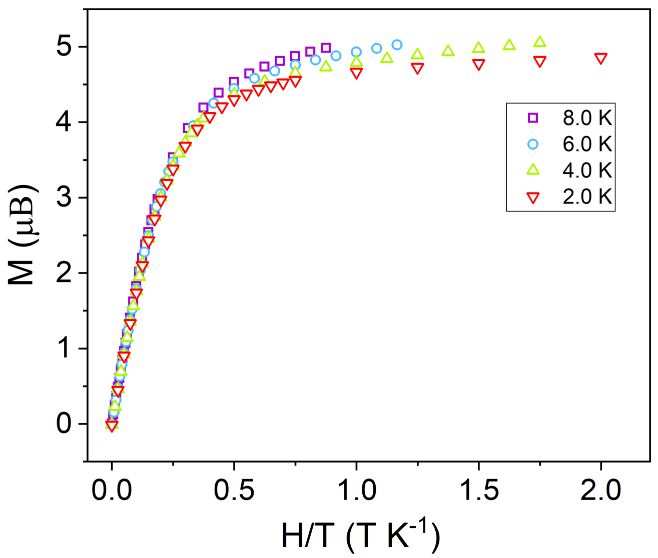

Figure B.8: Field dependence, temperature dependence of the magnetization for **4-1**.

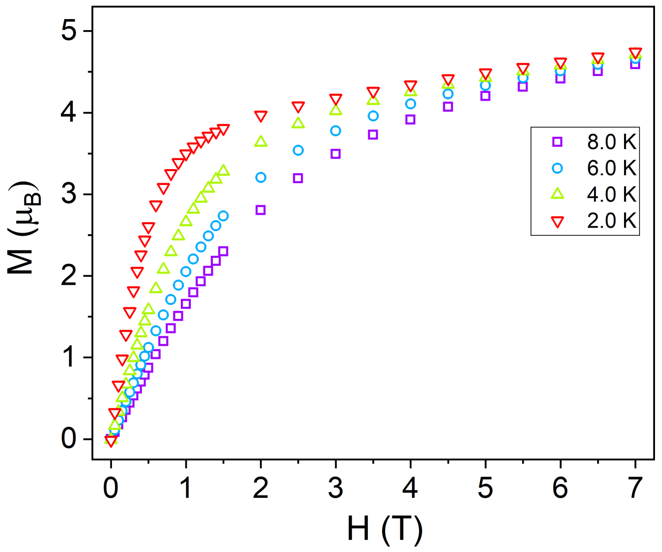

Figure B.9: Field dependence of the magnetization for **[4-1]**$^{-}$.

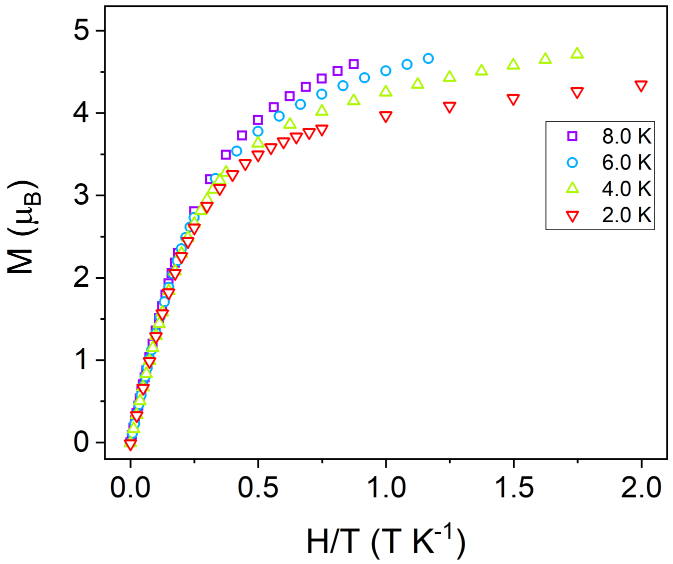

Figure B.10: Field dependence, temperature dependence of the magnetization for **[4-2]**$^-$.

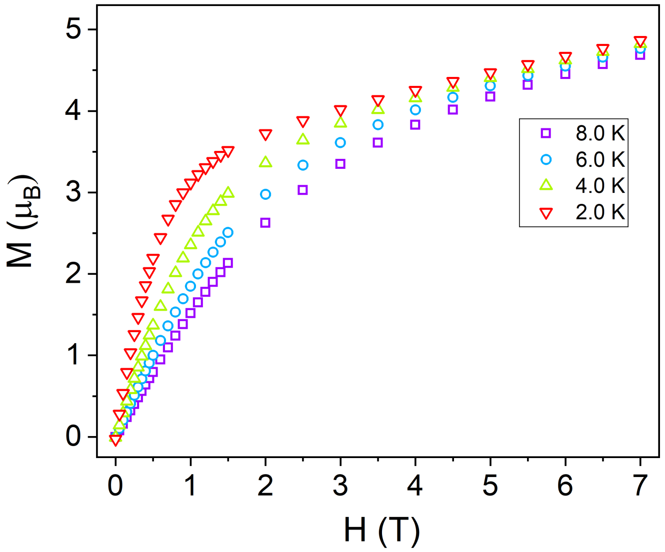

Figure B.11: Field dependence of the magnetization for **4-2**.

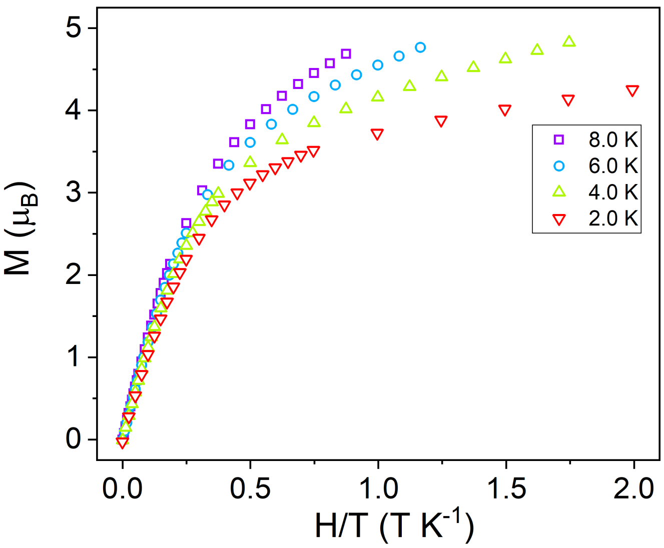

Figure B.12: Field dependence, temperature dependence of the magnetization for **4-2**.

$$\tau^{-1} = \tau_0^{-1} exp\left(\frac{-U_{eff}}{kT}\right) \quad \textbf{(linear approximation)}$$

$$\tau^{-1} = \tau_{QTM}^{-1} + CT^{n_2} + \tau_0^{-1} exp\left(\frac{-U_{eff}}{kT}\right) \quad \textbf{(eqn 1)}$$

$$\tau^{-1} = AH^{n_1}T + \tau_{QTM}^{-1} + CT^{n_2} + \tau_0^{-1} exp\left(\frac{-U_{eff}}{kT}\right) \quad \textbf{(eqn 2)}$$

$$\tau^{-1} = AH^{n_1}T + \frac{B_1}{1 + B_2H^2} + D \quad \textbf{(eqn 3)}$$

	$K(thf)_5[Dy(fc[NSi(\textit{t}\text{-}Bu)Me_2]_2)_2]$ **[1]$^-$**				$Dy(fc[NSi(\textit{t}\text{-}Bu)Me_2]_2)_2$ **1**	
dc field (Oe)	0		1000		1000	
Approximation	linear	eqn 1	linear	eqn 2/eqn 3	Linear	eqn 2/eqn 3
A (s^{-1} T^{--n1} K^{-1})	-	-	-	615	-	3.77 x 10^3
n_1	-	-	-	4	-	2
B_1 (s^{-1})	-	-	-	3.22 x 10^3	-	2.55 x 10^{14}
B_2 (T^{-2})	-	-	-	9.92 x 10^3	-	2.36 x 10^{13}
D (s^{-1})	-	-	-	162	-	0
C (s^{-1} K^{-n2})	-	0.08(1)	-	0.0018(3)	-	3.63(1)
n_2	-	5	-	7	-	5
τ_{QTM} (s)	-	5.03 x 10^{-4}	-	-	-	8.77 x 10^{-4}
τ_0 (s)	2.43 x 10^{-6}	1.63(2) x 10^{-6}	4.79 x 10^{-7}	7.3(7) x 10^{-7}	5.79 x 10^{-7}	5.0(4) x 10^{-7}
U_{eff} (cm^{-1})	**20.9**	**27.3(8)**	**35.0**	**46(2)**	**16.8**	**27.2(5)**

a) QTM terms were not included in the fitting of temperature dependence of [1]$^-$.

Figure B.13: Fitting parameters for the Dy^{3+} compounds **[4-1]$^-$** and **4-1**

	$K(thf)_5[Er(fc[NSi(t\text{-}Bu)Me_2]_2)_2]$ **[2]**$^-$	
dc field (Oe)	500 Oe	
Approximation	Linear	eqn 2/eqn 3
A (s^{-1} T^{--n1} K^{-1})	-	1.29×10^4
n_1	-	4
B_1 (s^{-1})	-	4.63×10^4
B_2 (T^{-2})	-	70.8×10^5
D (s^{-1})	-	21.2
C (s^{-1} K^{-n2})	-	$1.85(2) \times 10^{-2}$
n_2	-	9
$\tau^{-1}{}_{QTM}$	-	3.33×10^{-2}
τ_0 (s)	9.52×10^{-9}	$4(1) \times 10^{-7}$
U_{eff} (cm^{-1})	**26.9**	**29(2)**

Figure B.14: Fitting parameters for the Er^{3+} compound **[4-2]**$^-$

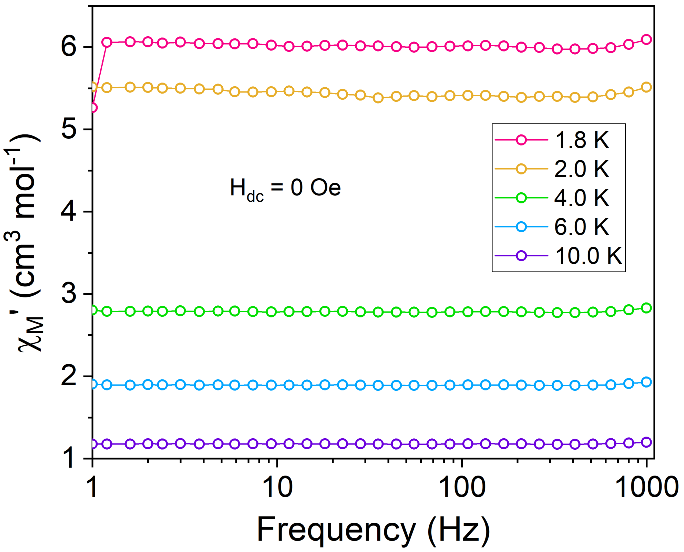

Figure B.15: Frequency dependence of the in-phase component (χ') of the ac susceptibility for **4-1** under zero dc field. Lines are a guide for the eye.

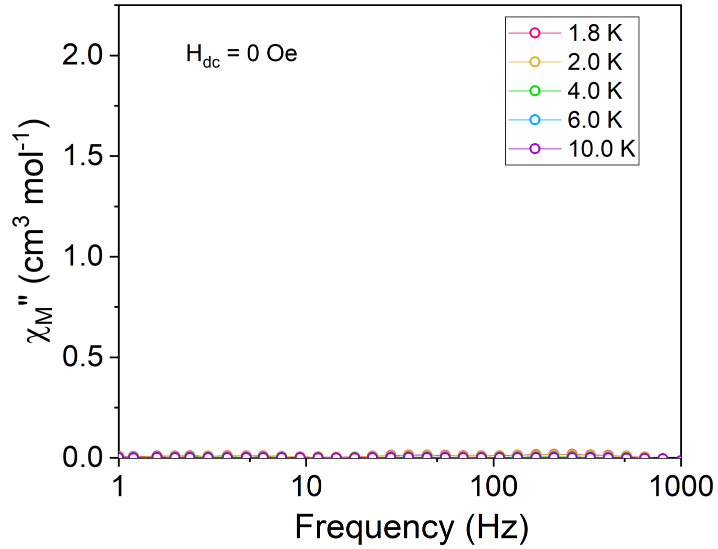

Figure B.16: Frequency dependence of the out-of-phase component (χ") of the ac susceptibility for **4-1** under zero dc field. Lines are a guide for the eye.

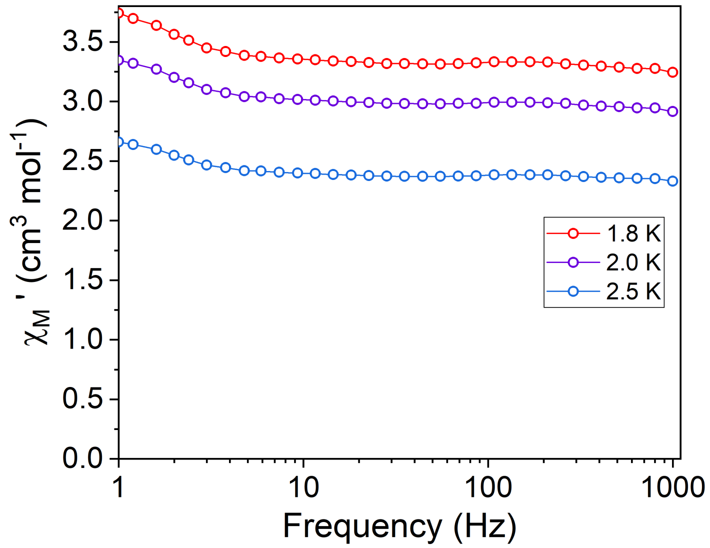

Figure B.17: Frequency dependence of the in-phase component (χ’) of the ac susceptibility for **[4-2]**$^-$ under zero dc field. Lines are a guide for the eye.

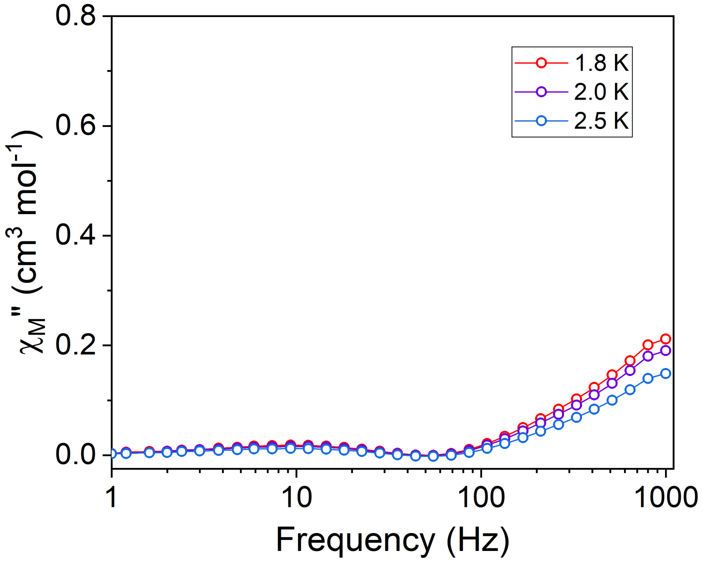

Figure B.18: Frequency dependence of the out-of-phase component (χ") of the ac susceptibility for **[4-2]⁻** under zero dc field. Lines are a guide for the eye.

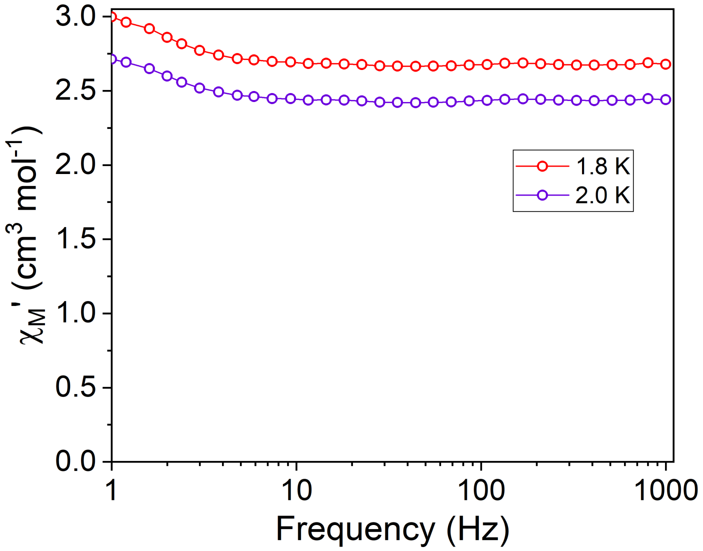

Figure B.19: Frequency dependence of the in-phase component (χ') of the ac susceptibility for **4-2** under zero dc field. Lines are a guide for the eye.

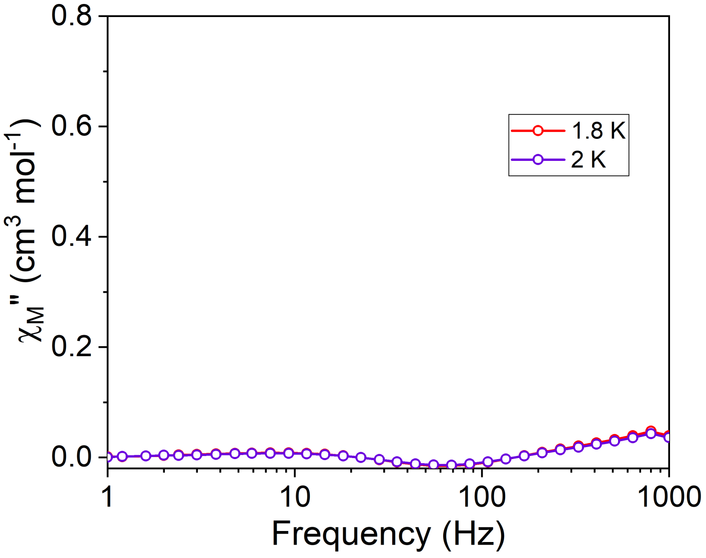

Figure B.20: Frequency dependence of the out-of-phase component (χ'') of the ac susceptibility for **4-2** under zero dc field. Lines are a guide for the eye.

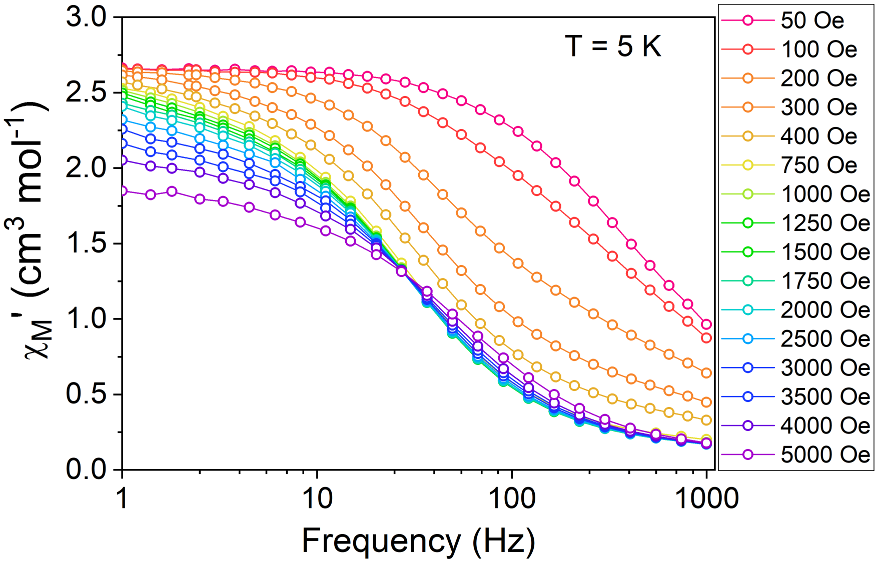

Figure B.21: Frequency dependence of the in-phase component (χ') of the ac susceptibility for **[4-1]**$^-$ at T = 5 K with a 2 Oe switching field and applied dc fields varying from 50 to 5000 Oe. Lines are a guide for the eye.

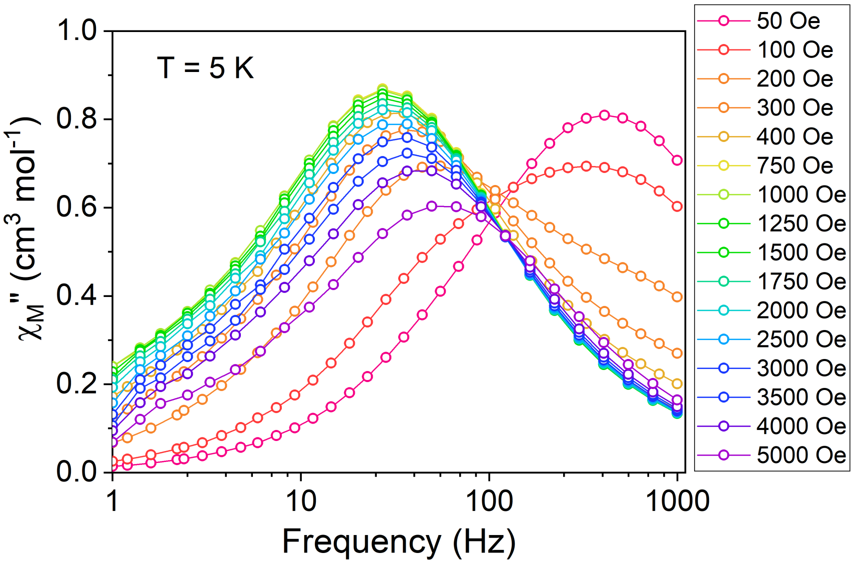

Figure B.22: Frequency dependence of the out-of-phase component (χ") of the ac susceptibility for **[4-1]**$^-$ at T = 5 K with a 2 Oe switching field and applied dc fields varying from 50 to 5000 Oe. Lines are a guide for the eye.

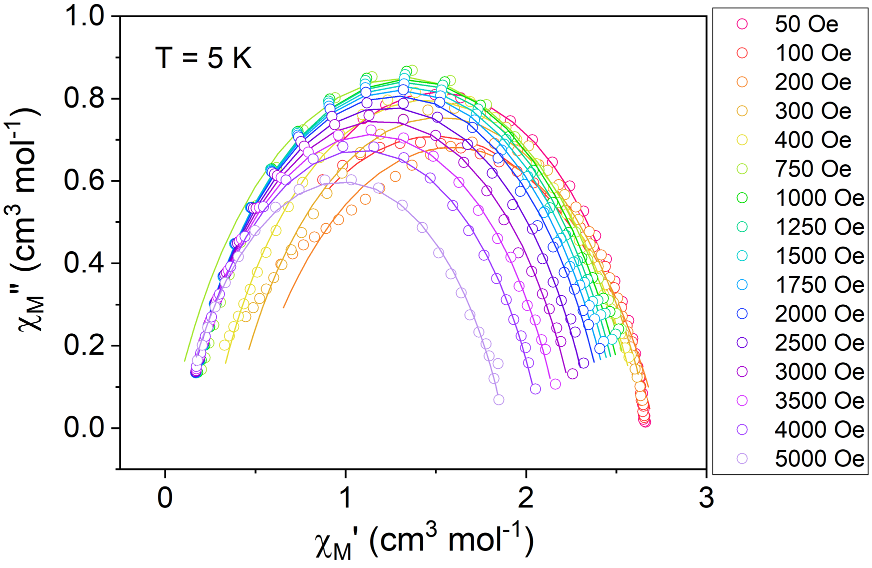

Figure B.23: Cole-Cole plots for **[4-1]**$^-$ at 5 K with various applied dc fields. Open circles are experimental data, lines are fits to the generalized Debye equation.

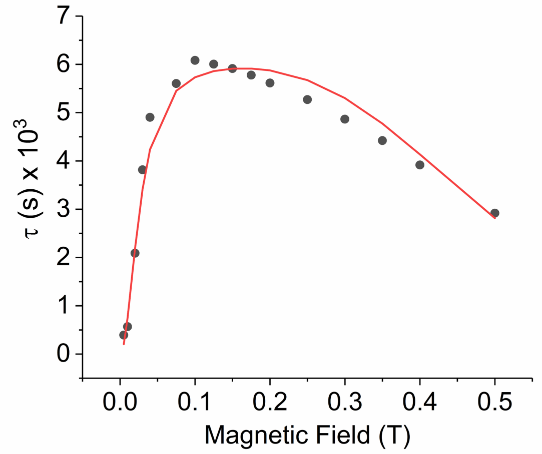

Figure B.24: Field dependence of the relaxation times τ in **[4-1]**$^-$ at 5 K. Black circles are experimental data points, red line represents the fit (see main text).

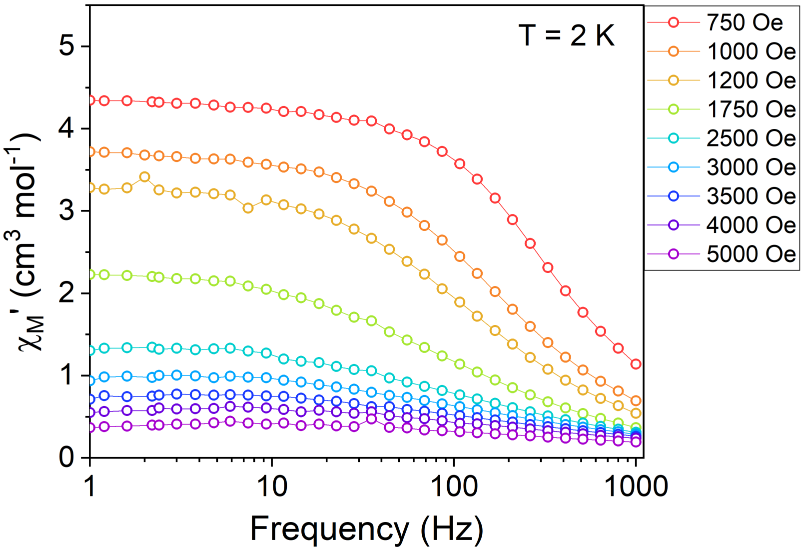

Figure B.25: Frequency dependence of the in-phase component (χ') of the ac susceptibility for **4-1** at T = 2 K with a 2 Oe switching field and applied dc fields varying from 750 to 5000 Oe. Lines are a guide for the eye.

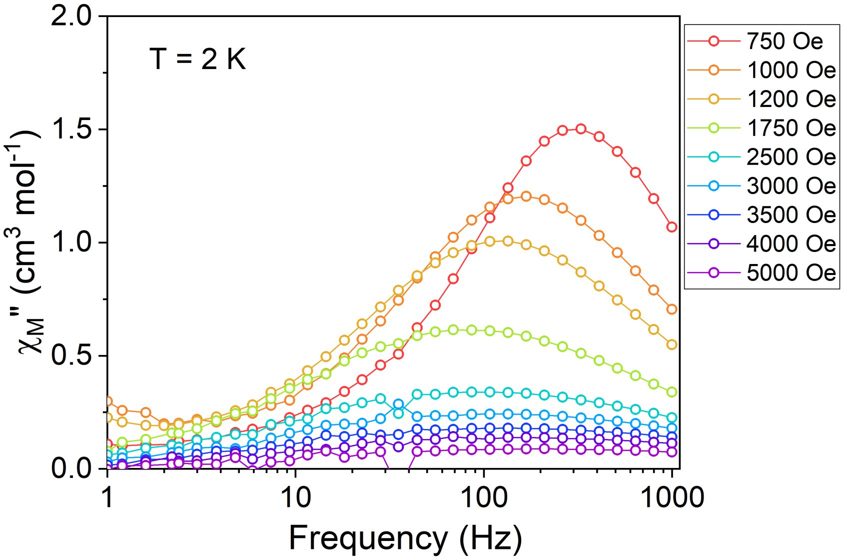

Figure B.26: Frequency dependence of the out-of-phase component (χ'') of the ac susceptibility for **4-1** at T = 2 K with a 2 Oe switching field and applied dc fields varying from 750 to 5000 Oe. Lines are a guide for the eye.

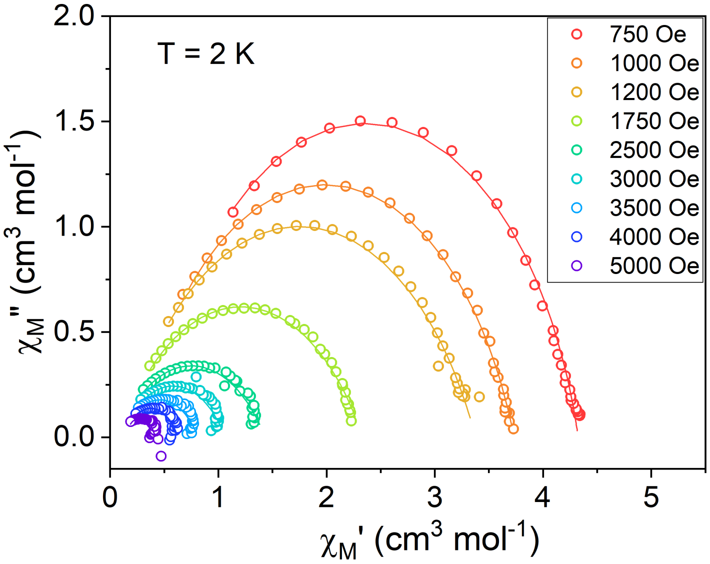

Figure B.27: Cole-Cole plots for **4-1** at 2 K with various applied dc fields. Open circles are experimental data, lines are fits to the generalized Debye equation.

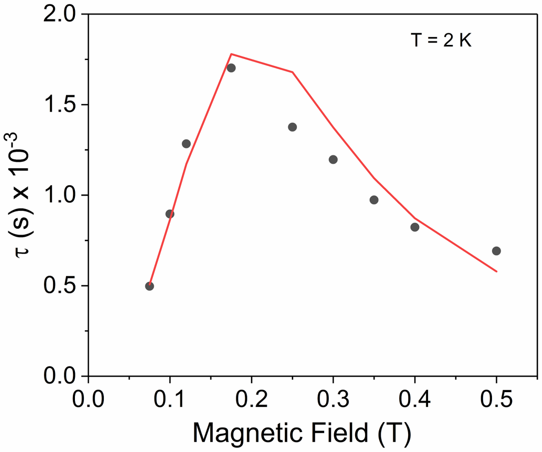

Figure B.28: Field dependence of the relaxation times τ in **4-1** at 2 K. Black circles are experimental data points, red line represents the fit (see main text).

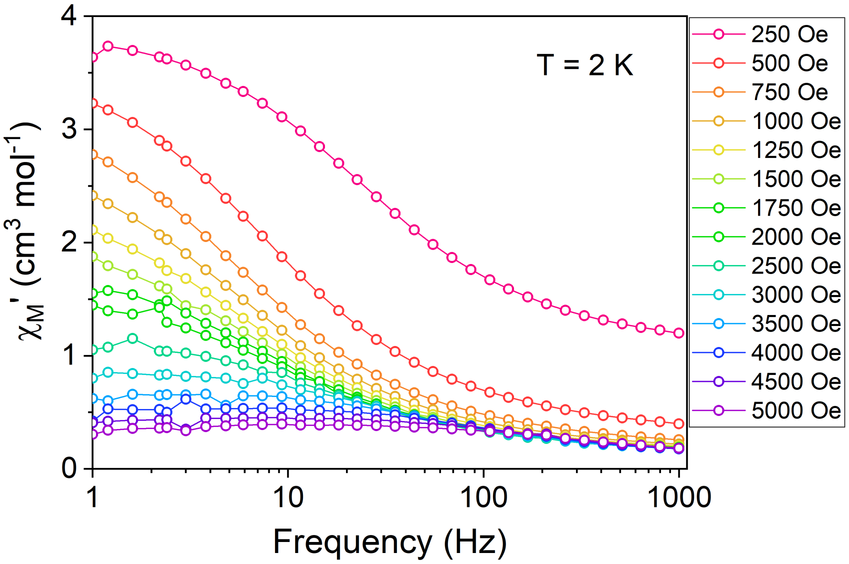

Figure B.29: Frequency dependence of the in-phase component (χ') of the ac susceptibility for **[4-2]**$^-$ at 2 K with a 2 Oe switching field and applied dc fields varying from 250 to 5000 Oe. Lines are a guide for the eye.

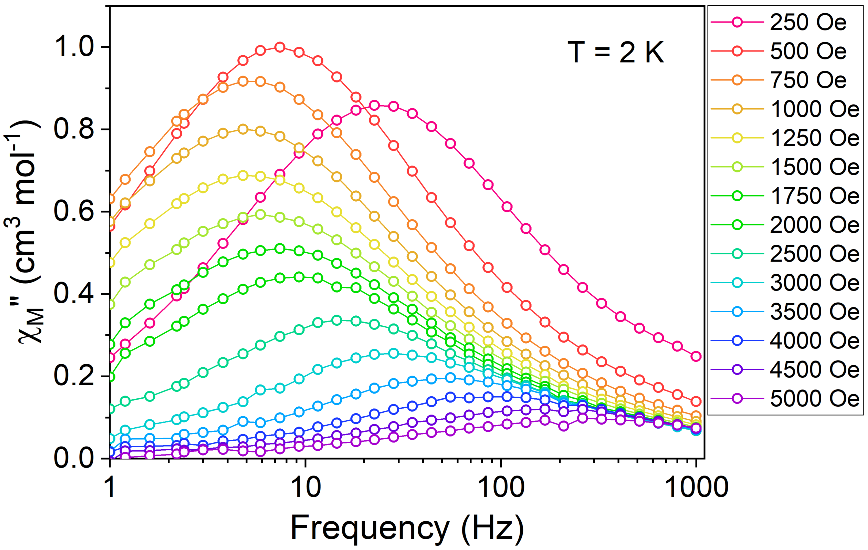

Figure B.30: Frequency dependence of the out-of-phase component (χ") of the ac susceptibility for **[4-2]**$^-$ at 2 K with a 2 Oe switching field and applied dc fields varying from 250 to 5000 Oe. Lines are a guide for the eye.

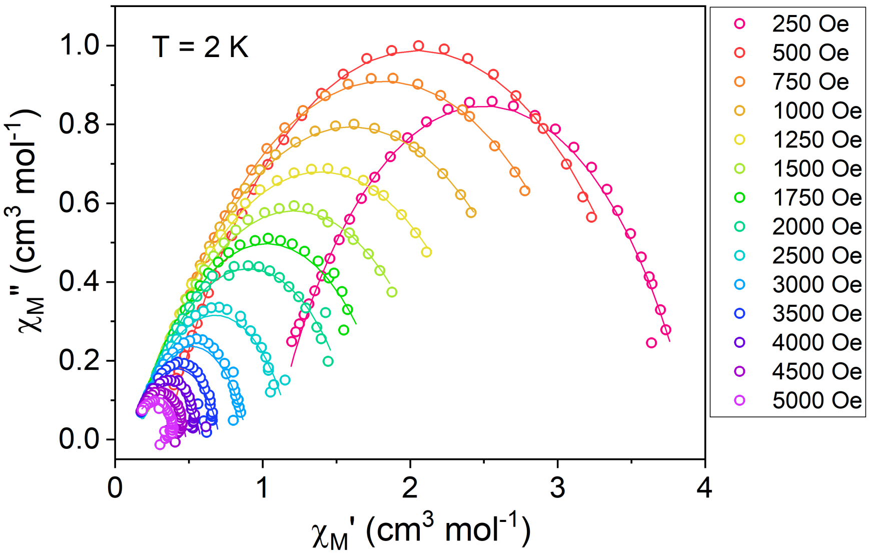

Figure B.31: Cole-Cole plots for **[4-2]**$^-$ at 2 K with various applied dc fields. Open circles are experimental data, lines are fits to the generalized Debye equation.

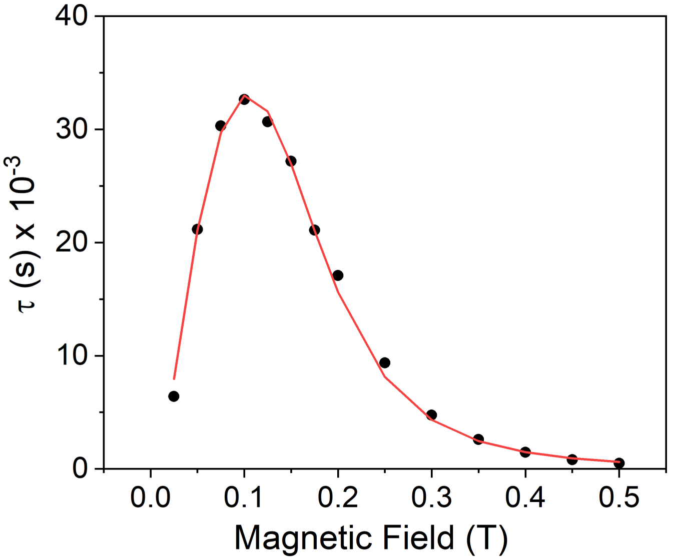

Figure B.32: Field dependence of the relaxation times τ in **[4-2]**$^-$ at 2 K. Black circles are experimental data points, red line represents the fit (see main text).

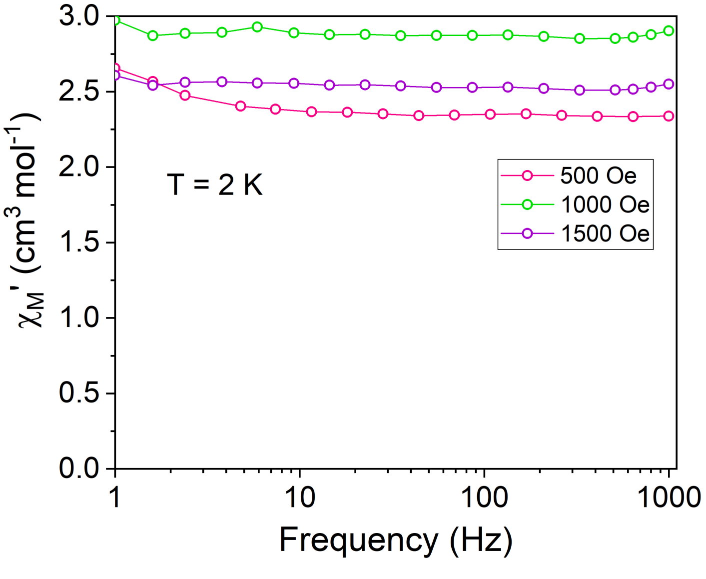

Figure B.33: Frequency dependence of the in-phase component (χ') of the ac susceptibility for **4-2** at 2 K with a 2 Oe switching field and applied dc fields varying from 500 to 1500 Oe. Lines are a guide for the eye.

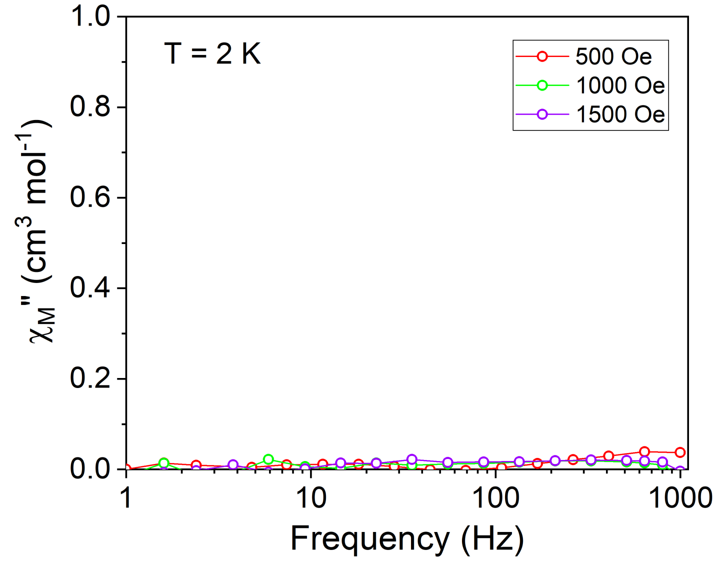

Figure B.34: Frequency dependence of the out-of-phase component (χ'') of the ac susceptibility for **4-2** at 2 K with a 2 Oe switching field and applied dc fields varying from 500 to 1500 Oe. Lines are a guide for the eye.

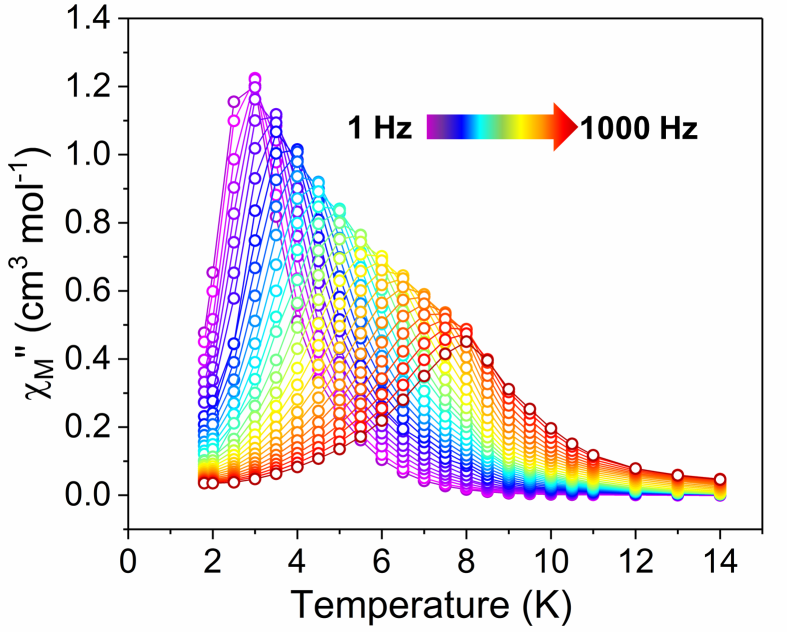

Figure B.35: Temperature dependence of the out-of-phase component (χ'') of the ac susceptibility for **[4-1]**$^-$ with a 2 Oe switching field and a 1000 Oe applied dc field (H_{dc} = 1000 Oe). Lines are a guide for the eye.

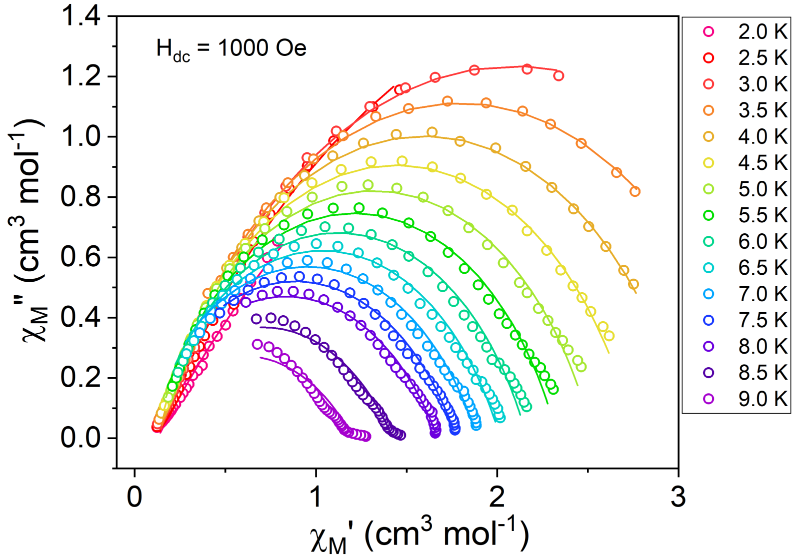

Figure B.36: Cole-Cole plots for **[4-1]⁻**, with an applied dc field of 1000 Oe (H_{dc} = 1000 Oe). Open circles are experimental data points, solid lines are fits to the generalized Debye equation.

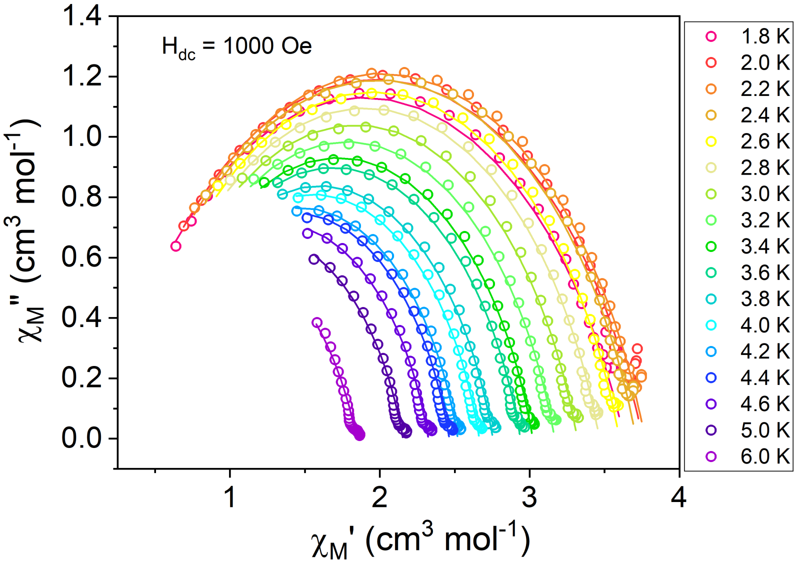

Figure B.37: Cole-Cole plots for **4-1**, with an applied dc field of 1000 Oe (H_{dc} = 1000 Oe). Open circles are experimental data points, solid lines are fits to the generalized Debye equation.

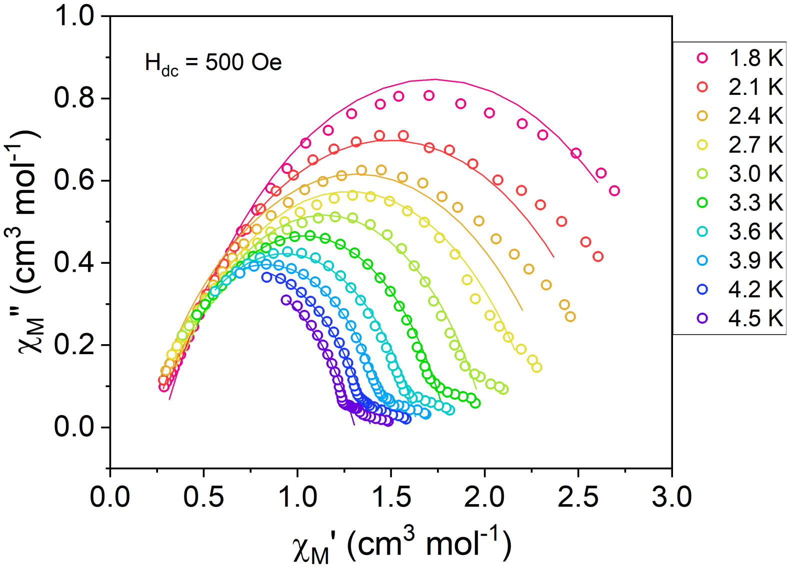

Figure B.38: Cole-Cole plots for **[4-2]**$^-$, with an applied dc field of 500 Oe (H_{dc} = 500 Oe). Open circles are experimental data points, solid lines are fits to the generalized Debye equation

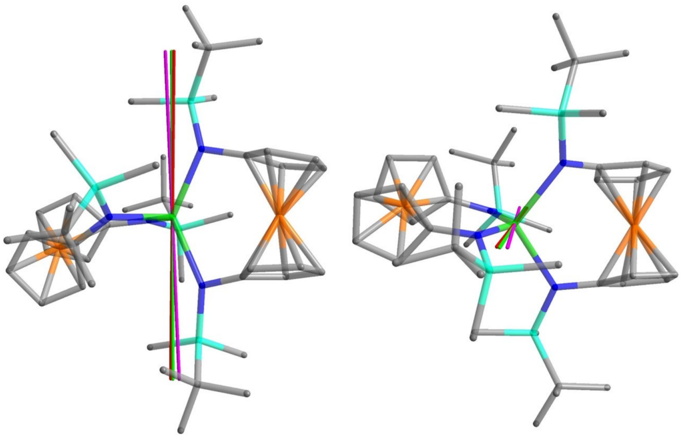

Figure B.39: Predicted orientations of the magnetic anisotropy axes in **4-1** under three scenarios using MAGELLAN (Chilton et al.): (1) red axis: assigning both Fe-Cp$_2$ units as charge neutral (Fe^{2+}), (2) green axis: assigning +1 charge to the Fe center that is closer to the Dy^{3+} ion, and (3) magenta axis: assigning the +1 charge to the Fe center that is further from the Dy^{3+} ion. (ref. N.F. Chilton, D. Collison, E. J. L. McInnes, R. E. P. Winpenny and A. Soncini, *Nat. Commun.*, **2013**, 4, 1-7)

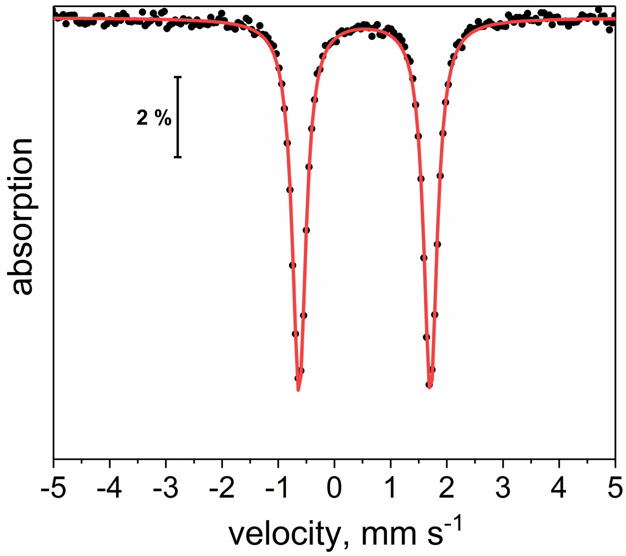

Figure B.40: ^{57}Fe Mössbauer spectrum of **[4-1]**$^{-}$ at 10 K with no external field. Isomer shift (δ) = 0.54 mm s^{-1}, quadrupole splitting (ΔE_Q = 2.34 mm s^{-1}).

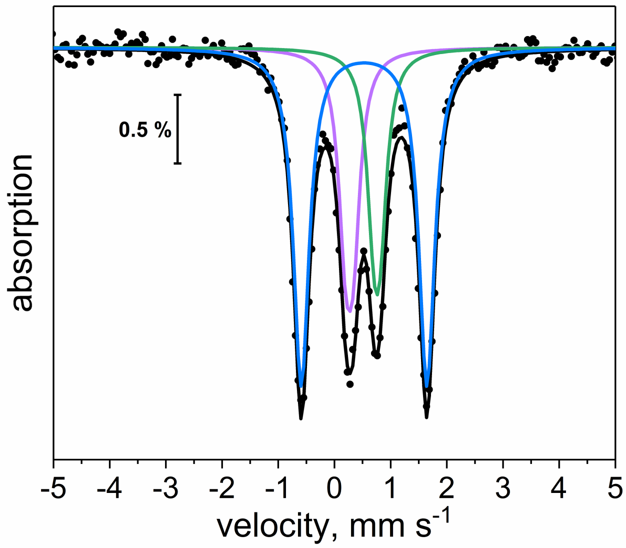

Figure B.41: ^{57}Fe Mössbauer spectrum of **4-1**, at 5 K. Black dots are experimental points. Black line is overall three-site fit. Blue, green and purple lines are the individual sub-spectra for the three-site fit

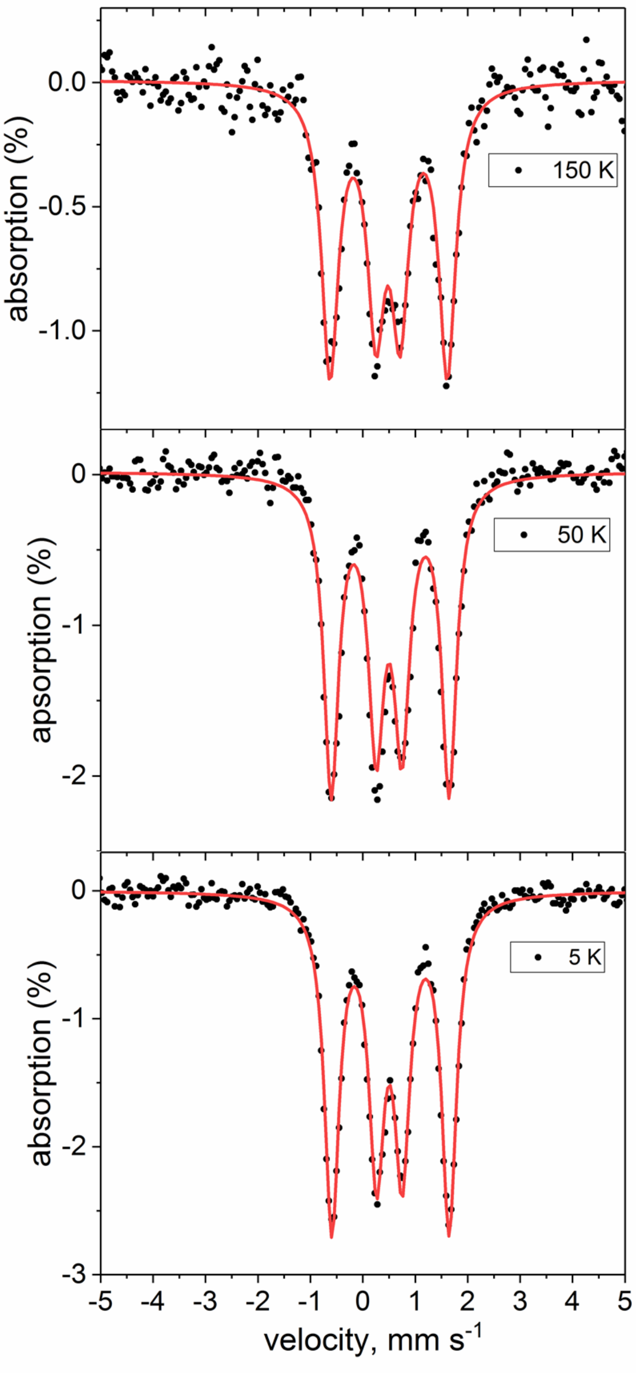

Figure B.42: ^{57}Fe Mössbauer spectrum of **4-1** at 5 K, 50 K, and 150 K. Black dots are experimental data points. Red lines are the overall two-site fits.

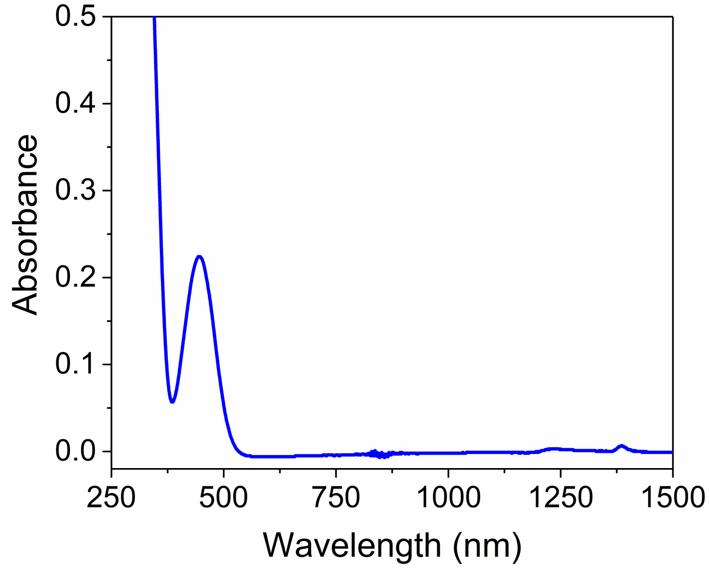

Figure B.43: UV-vis-NIR spectrum of **[4-1]**$^-$ in thf.

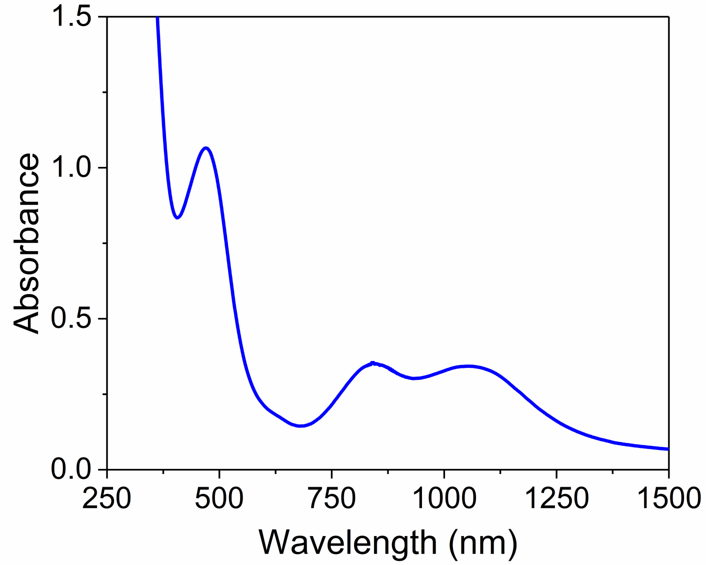

Figure B.44: UV-vis-NIR spectrum of **4-1** in thf.

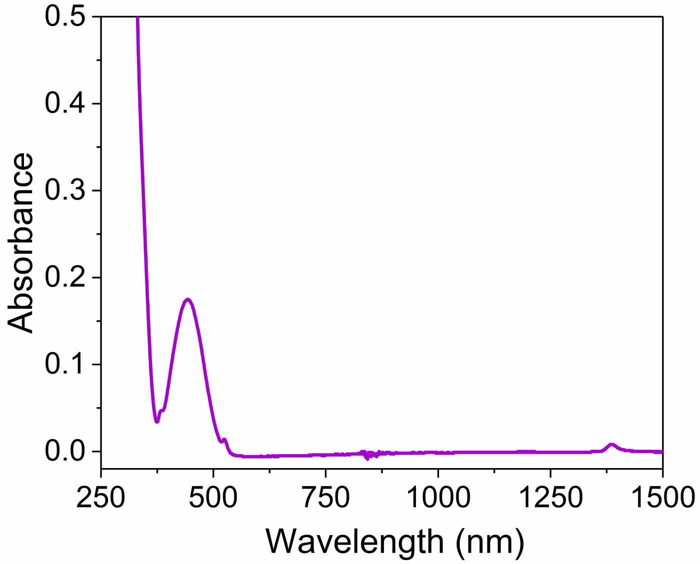

Figure B.45: UV-vis-NIR spectrum of **[4-2]**⁻ in thf.

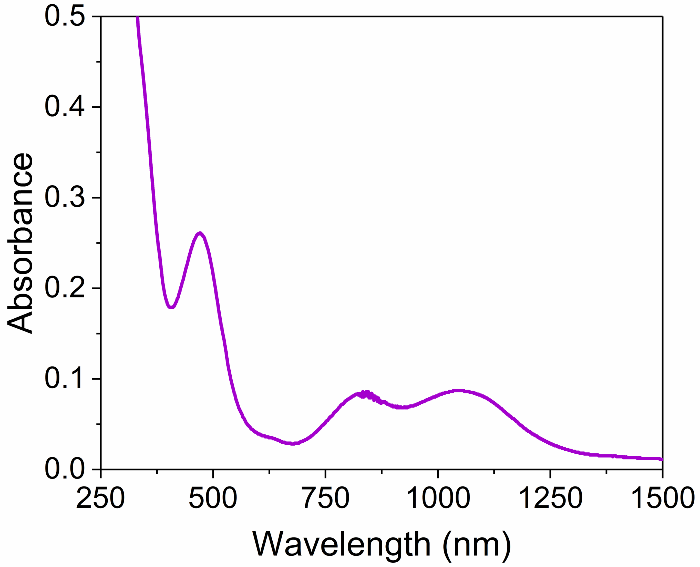

Figure B.46: UV-vis-NIR spectrum of **4-2** in thf.

APPENDIX C

THIRD APPENDIX

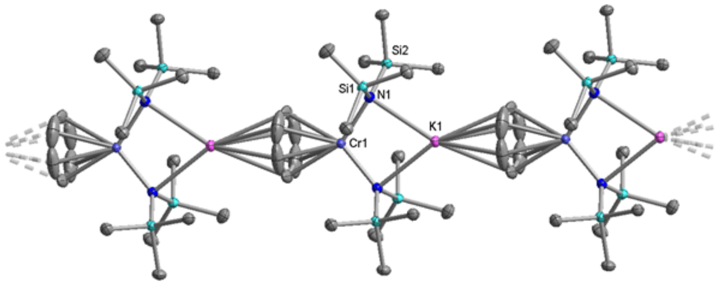

distances	
Cr1−N1, Å	2.082(3)
Cr1−Cp$_{\text{(centroid)}}$, Å	2.065
Cr1···K1, Å	3.5813(12)
Cr1···Cr1, Å	8.513
K1−N1, , Å	2.887(3)
K1−Cp$_{\text{(centroid)}}$, Å	2.866

angles	
N1−Cr1−N1, °	107.43(14)
N1−K1−N1, °	71.07(10)
Cr1−N1−K1, °	90.75(9)

Figure C.1: Selected bond distances and angles in the molecular structure of **5-1**.

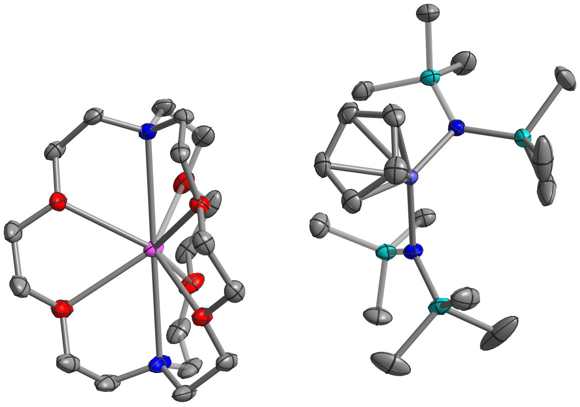

Figure C.2: Molecular structure of **5-2**. Thermal ellipsoids are set to 50 % probability.

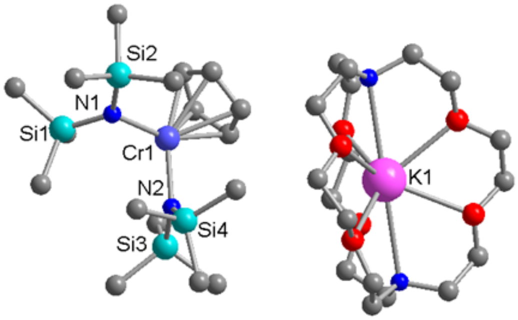

distances	
Cr1−N1, Å	2.053(3)
Cr1−N2, Å	2.069(2)
Cr1−Cp$_{\text{(centroid)}}$, Å	2.071
Cr1···K1, Å	9.5070(9)
Cr1···Cr1, Å	14.173(14)

angles	
N1−Cr1−N1, °	107.65(8)

Figure C.3: Selected bond distances and angles in the molecular structure of **5-2**.

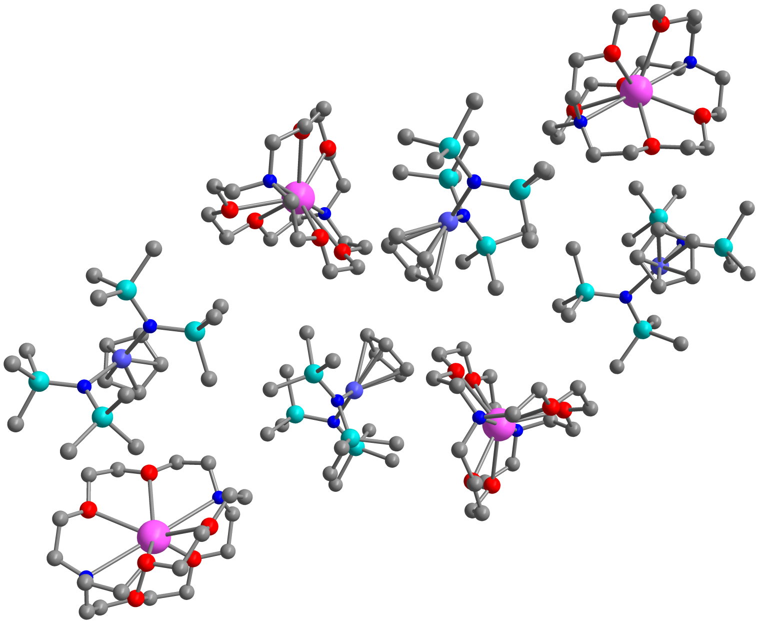

Figure C.4: Unit cell of **5-2**, containing four asymmetric units.

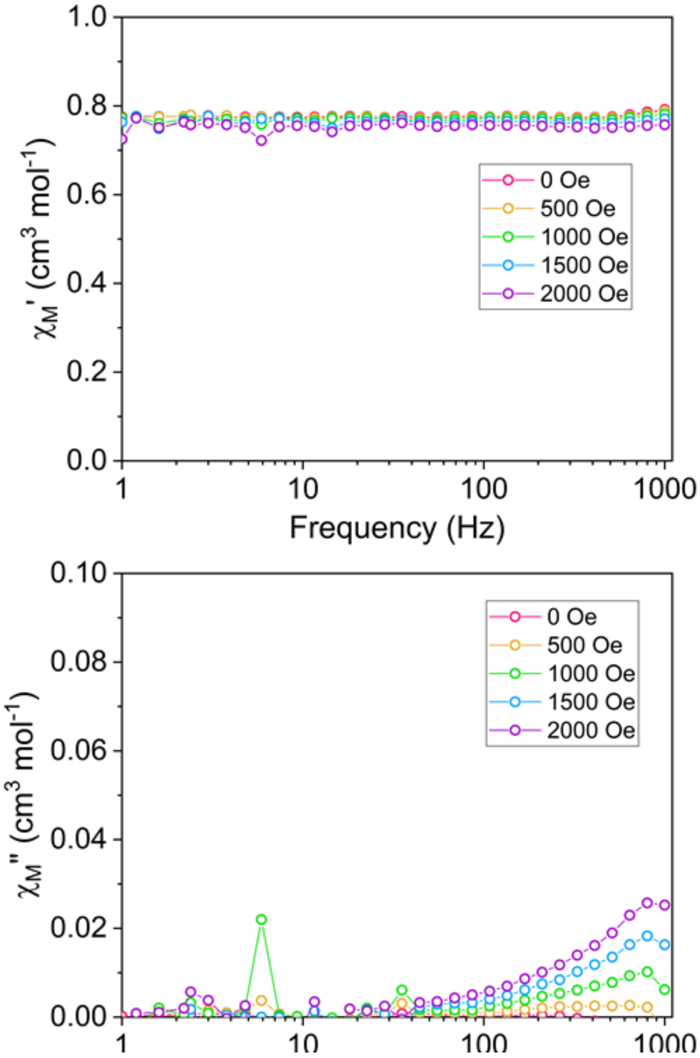

Figure C.5: The in-phase, χ_M' (top), and out-of-phase, χ_M" (bottom), components of the ac susceptibility for **5-1** at 1.8 K under dc fields from 0 Oe to 2000 Oe. Lines are a guide for the eye.

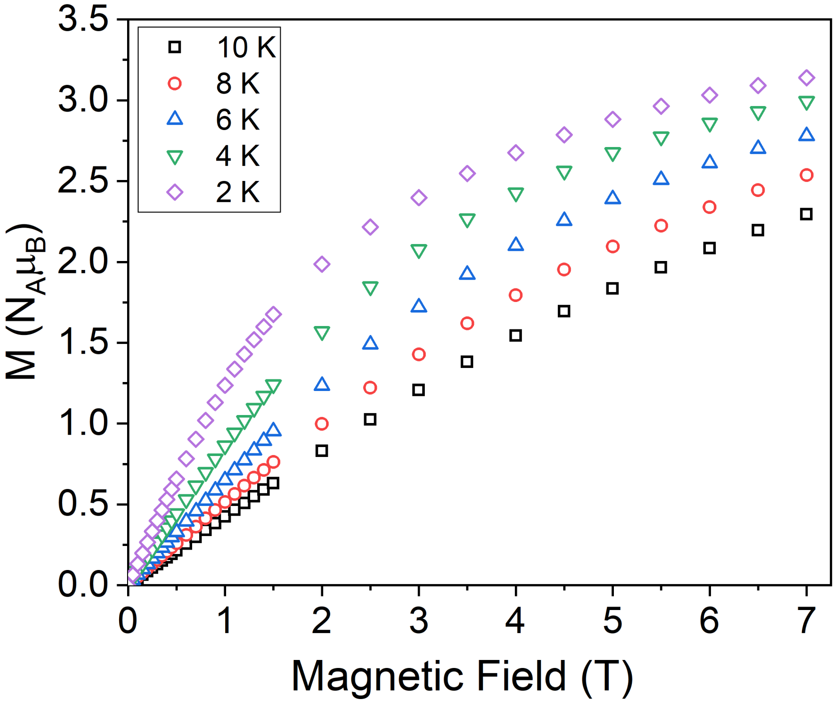

Figure C.6: Field dependence of the magnetization (*M*) for **5-1**.

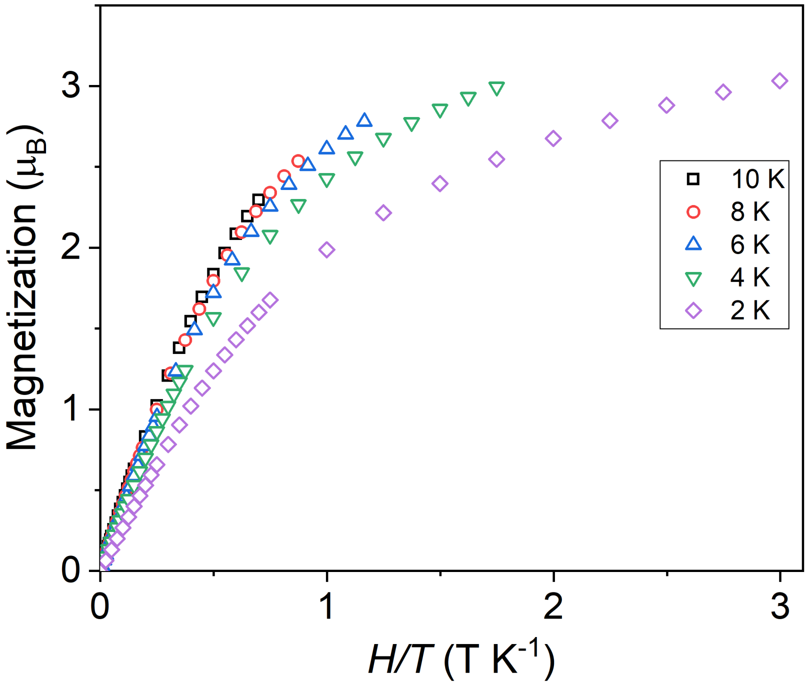

Figure C.7: Field dependence, temperature of the magnetization (*M*) for **5-1**.

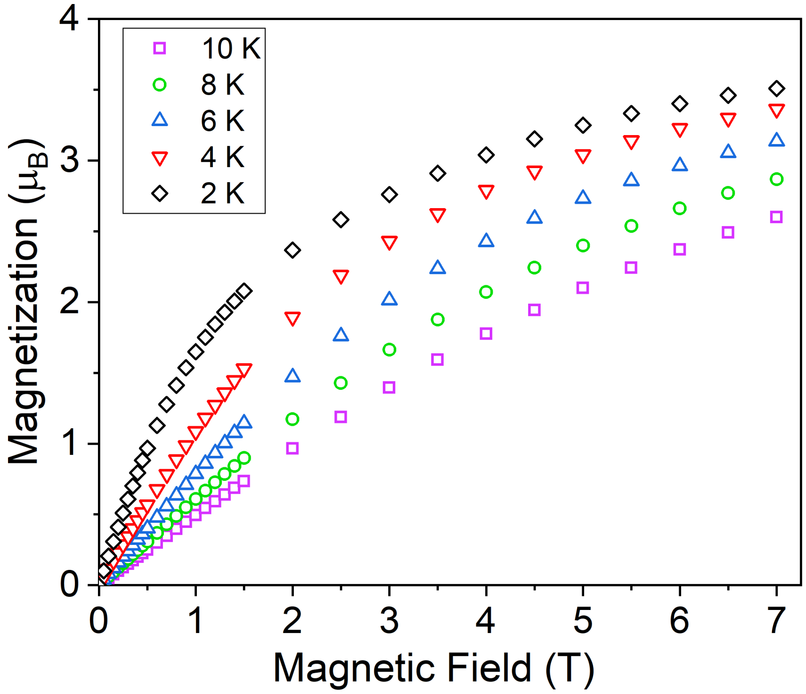

Figure C.8: Field dependence of the magnetization (*M*) for **5-2**.

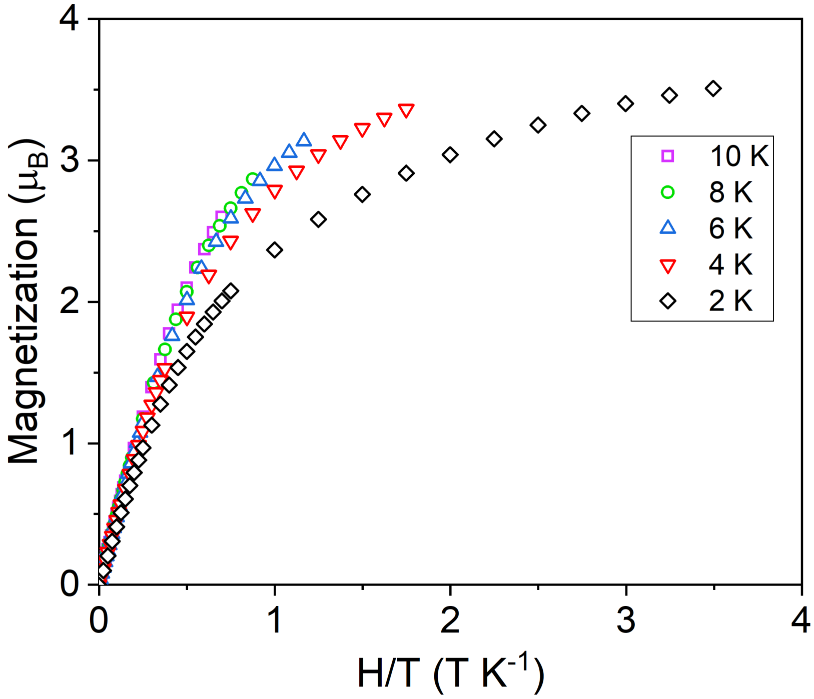

Figure C.9: Field dependence, temperature of the magnetization (*M*) for **5-2**.

APPENDIX D

FOURTH APPENDIX

Introduction to Mössbauer spectroscopy

Mössbauer spectroscopy relies on the Mössbauer effect; the recoilless emission or absorption of a γ-ray photons by a nucleus. The Mössbauer effect was first observed by Rudolph Mössbauer in 1958, earning him the Nobel prize in 1961.

An advantage of Mössbauer spectroscopy is that (narrow energy range gamma rays) it produces monochromatic electromagnetic radiation with a narrow energy spectrum and therefore can probe minor energy differences. It is used to detect slight variations in energy of interaction between the nucleus and the extra-nuclear electrons. The emission and absorption of γ-rays is related to the nuclear energy level transitions. The energy precision of a nuclear excited state can be on the order of 10^{-8} eV, an incredibly precise target to hit with a γ-ray. This value can be compared to vibrations of the nucleus that are approximately 2.5 x 10^{-2} eV/atom. If changes in vibrational energy of the nucleus occur while a γ-ray is being emitted, the energy would not be precise enough to be reabsorbed by another nucleus. The recoil effect (explained below) prevents resonance absorption. The M ossbauer effect circumvents this issue.

The Recoil Effect

According to classical mechanics, energy and momentum must be conserved. Therefore, the emission of a γ-ray of a certain momentum requires the recoil of the emitting system with equal and opposite momentum. If a photon is emitted from a nucleus of mass, *M*, with an initial velocity V_x (moving in the *x*-direction), following the γ-ray emission, the nucleus will have a new velocity $(V_x + v)$, due to the recoil effect. According to the conservation of energy:

$$E + \frac{1}{2}MV_x^2 = E + \frac{1}{2}M(V_x + v)^2 \tag{D.1}$$

Meanwhile, there will be a difference in energy between the emitted γ-ray and the nuclear transition due to the recoil energy (E_R) and the Doppler effect energy (E_D) (accounting for random thermal motion of the atoms). This energy of the emitted gamma-ray is given by:

$$E_\gamma = (E_e - E_g) - \frac{1}{2}Mv_R^2 + MV_x v_R = E_0 - E_R + E_D \tag{D.2}$$

Where the change in energy (Δ) is given by:

$$\Delta E = E_R + E_D \tag{D.3}$$

The γ-ray distribution is shifted by a value of E_R and is broadened by twice the geometric mean of the recoil energy (E_R) and the average thermal energy (E_K), in a Gaussian distribution (Figure D.1).

$$E_D = 2\sqrt{E_K E_R} \tag{D.4}$$

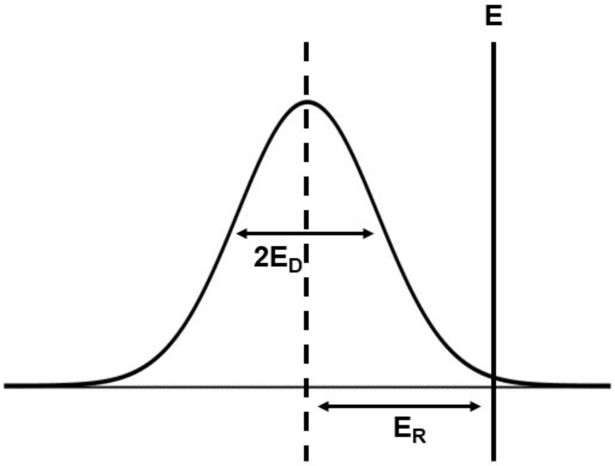

Figure D.1: Doppler and Recoil effects in M ossbauer spectroscopy.

The recoil energy (E_R) can also be expressed in terms of the energy of the γ-ray ($E\gamma$), where p is the recoil momentum of the atom and c is the speed of light ($c = 2.998x10^1 1$ mm/s).

$$E_R = \frac{1}{2}Mv^2 = \frac{(Mv)^2}{2M} = \frac{p^2}{2M} \tag{D.5}$$

By conservation of momentum:

$$p = -p_\gamma = -\frac{E_\gamma}{c} \tag{D.6}$$

Therefore:

$$E_R = \frac{E_R^2}{2Mc^2} \tag{D.7}$$

The emitted γ-ray has E_R less energy than the nuclear transition, however to be resonantly absorbed it must actually have E_R more energy than the nuclear transition to account for recoil effects. Random thermal motion of the atoms causes an energy distribution, E_D (Doppler effect). There is only a very small resonance overlap (Figure D.2 -shaded area, not to scale) between absorption and emission in which photons may be resonantly emitted and reabsorbed. This overlap region contains only about 1 millionth or less of the γ-rays (not a reliable amount).

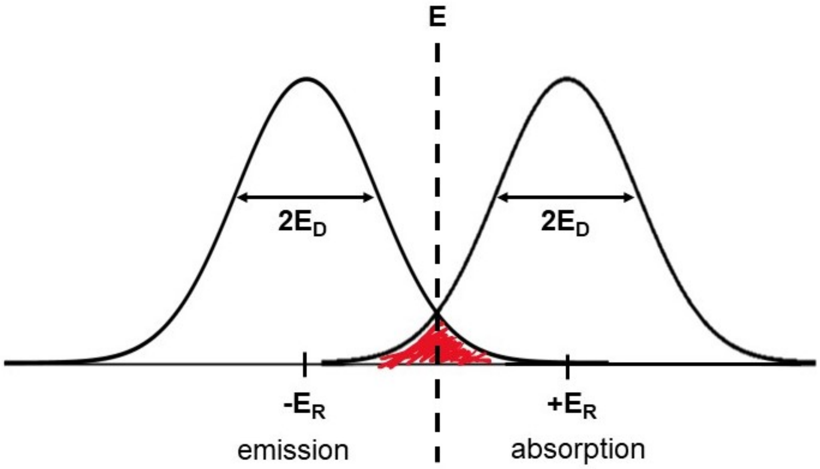

Figure D.2: Resonant absorption, not to scale.

The Mössbauer Effect

Rudolph Mössbauer discovered that the mass in Equation D.7 under certain conditions could equal the mass of the entire solid matrix, not just the individual nucleus, thereby rendering the recoil energy trivial and allowing for resonant absorption. For atoms in a solid matrix, ie. in a crystalline lattice, the momentum of the γ-ray emission is taken up by the recoil of the entire crystalline lattice, resulting in the recoil of the nucleus to be approximately zero (recoilless emission). The key to the M ossbauer effect is if the γ-ray energy is small enough, the recoil of the nucleus is too low to be transmitted as a phonon (vibration) (low probability of exciting a phonon).

In addition, Mössbauer discovered that using mechanical motion could could give the γ-rays Doppler shifts and it could be tuned to the nuclear resonance. Moving the γ-ray source towards and away from the sample (in mm/s) creates very small changes in the γ-ray energy via the Doppler effect. Fractions of the mm/s give the minute energy shifts (expand here)

The resolution in Mössbauer spectroscopy is dependent upon the presence of low-lying excited states and the the lifetime of the excited state. The number of recoil free events depends upon the energy of the γ-ray. The Mössbauer effect is only detected in isotopes with low-lying isotopes (low energy γ-rays). Additionally, the excited state must be long lived. Therefore, ideal isotopes for Mössbauer spectroscopy feature a low-lying and long-lived excited states.